Physics of molecular donor-acceptor solar cells

Correlation between interface morphology, energetics and device performance

Dissertation

zur Erlangung des
Doktorgrades der Naturwissenschaften
(Dr. rer. nat.)

eingereicht an der
Mathematisch-Naturwissenschaftlichen Fakultät
der Universität Augsburg

vorgelegt von

Julia Katharina Kraus

(geb. Wagner)

2013

Universität Augsburg
Mathematisch-Naturwissenschaftliche Fakultät

1. Gutachter:	Prof. Dr. Wolfgang Brütting
2. Gutachter:	Prof. Dr. Frank Schreiber
3. Gutachter:	Dr. Hubert Krenner
Tag der mündlichen Prüfung:	9. Juli 2013

Contents

Chapter 1

Motivation

Development of organic photovoltaics and challenges for further progress
According to studies by the International Energy Agency (IEA) it is to be expected that the global primary energy consumption will increase by about 30% within the next 25 years.[1] This rising energy demand together with the shortage of resources and a massive increase in atmospheric CO_2—considerably threatening our climate—urge us to find alternatives. Thus, the search for environment-friendly, renewable energy sources can be declared as a central task of the 21st century. Photovoltaics, i.e. the direct conversion of sunlight into electricity, represents one of the possible technologies to address this issue. Already today, the global photovoltaic industry is annually growing by over 100%—and the trend is rising.[2] At the moment, solar cells based on inorganic semiconductors dominate the market, primarily represented by crystalline or amorphous silicon. An overview of the temporal development of the highest efficiencies in various solar cell technologies is shown in Fig. 1.1—demonstrating the steep and sustaining upward trend in almost any branch of technology.[a] In the field of inorganic photovoltaics single pn-junctions based on crystalline silicon are already approaching their theoretical thermodynamic efficiency limit of approximately 33%[3]—shifting the focus of research on new technologies, particularly with respect to cost-efficient manufacturing processes. Nevertheless, solar cells provide little noticeable contribution to the energy market—mainly because of high production costs as result of complex

[a] It should be noted that the efficiencies of commercially available solar cells may partly differ substantially from the specified record values of laboratory-scale devices due to efficiency losses when upscaling to practicable area and output.

and expensive fabrication. To encounter this drawback an alternative approach is followed, which is based on a fundamentally different material class: instead of inorganic semiconductors, conjugated polymers and molecules can be used as active semiconducting materials in solar cells. These are organic substances whose semiconducting properties originate from alternating single and double bonds. Moderate material costs, fast and cheap production at low temperature as well as the possibility to produce large area flexible modules make organic photovoltaics a promising technology for thin-film solar cells including the compatibility with role-to-role processing for high volume output.[4,5]

In their simplest form, organic photovoltaic cells (OPVCs) comprise two electrodes, enclosing a light-harvesting active layer and blocking layers with total thicknesses of only a few hundred nanometers. Thanks to intensive research, power conversion efficiencies of approximately 10% can already be achieved with laboratory-scale cells.[6] However, the commercial breakthrough of organic photovoltaics as

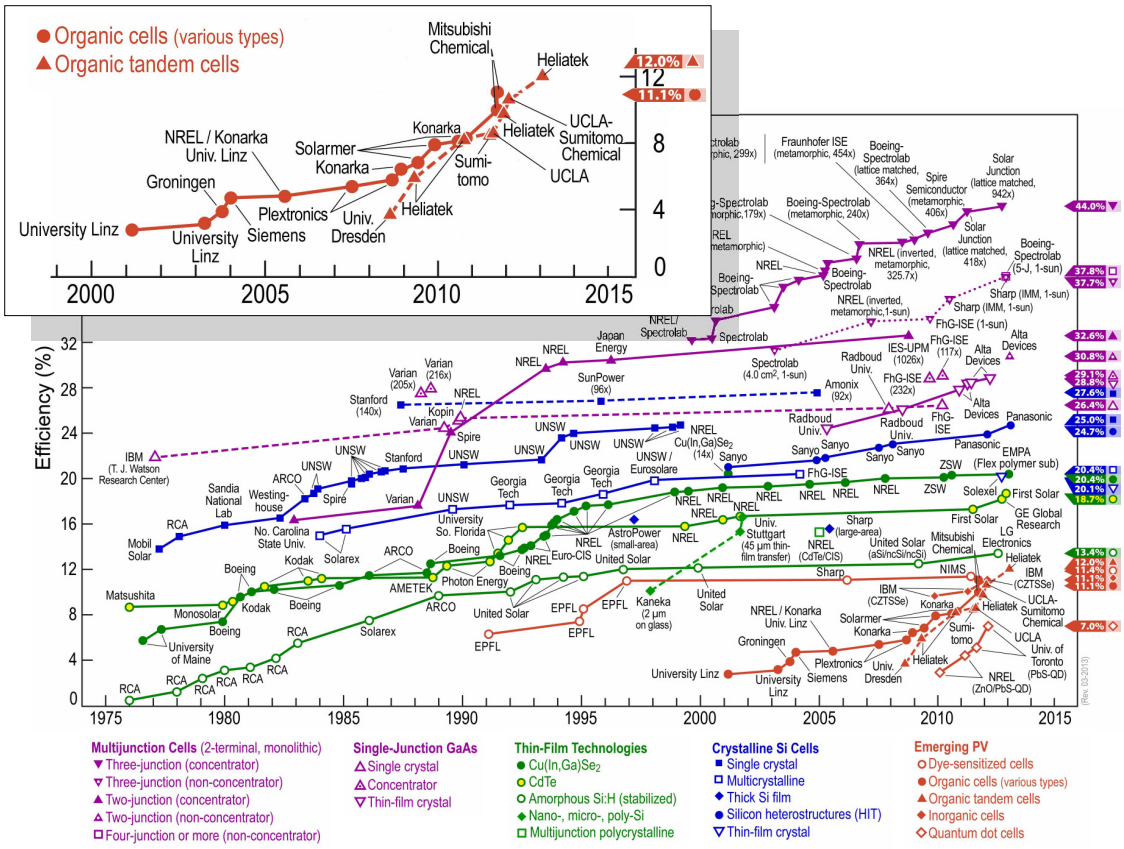

Figure 1.1.: Development of the best research-cell efficiencies of different solar cell technologies published by the National Renewable Energy Laboratory (NREL).[2] The inset shows the enlarged part of the temporal development of organic cells.

cost-efficient energy source still depends on further progress concerning challenges, amongst others, improving efficiencies in modules, enhancing long-term stability, increasing device area and solving encapsulation issues. While the first years of research on organic photovoltaics were largely dominated by trial and error experiments and material screening, further efficiency improvements require a detailed understanding of the fundamental processes occurring in organic solar cells.

The scope of this thesis is to develop a detailed understanding of the correlation between structural and electronic properties, microscopic transport phenomena and macroscopic parameters determining solar cell performance for different prototypes of organic molecular materials. In this context, organic/organic and electrode/organic interfaces will play a major role—as they crucially influence exciton dissociation, charge carrier recombination and charge extraction.
Polymeric semiconductors which are casted or printed from solution reveal strong dependence on the respective preparation condition.[7,8] While the impact of growth conditions on vacuum-processed molecular materials are similarly pronounced, this topic is less extensively investigated in literature. Apart from that, vacuum sublimation offers extended possibilities of tuning and controlling these interfaces. One goal of this thesis is to identify the relation between growth parameters and the resulting structures and morphologies between molecular materials with different shapes—either deposited subsequently forming a planar interface or simultaneously in molecular blends. Besides morphological aspects, the electronic structure of these interfaces plays an equally important role in OPVCs. While the electrode/organic contacts are responsible for charge carrier extraction, efficient exciton dissociation and charge carrier generation is decisively influenced by the organic/organic interface. Thus, all processes and device parameters are strongly dependent on adjusted energy level alignment and optimized offsets at these interfaces.

A variety of studies identified the energetics at the organic/organic interface as limiting factors for the efficiency of polymer devices. The aim in this area is to provide an experimentally validated understanding for these limitations in OPVCs based on molecular materials which allows to quantify recombination losses and work out the peculiarities of crystalline organic thin-film solar cells as compared to their polymeric counterparts. Altogether, the objective of the present thesis is to determine the true electronic structure at the relevant interfaces, to investigate the dependence of film growth conditions on structure and morphology, and finally identify correlations to device function. Concerning the material choice, pioneering work on the new donor material diindenoperylene (DIP) in combination with the fullerene C_{60} has been carried out. Both molecular species will constitute the focus material system which is used as reference throughout the thesis.

Structure of the thesis

The present work is divided into two parts, comprising theoretical basics and experimental results, and is in detail organized as follows:

Starting with an introduction into the concept of organic solar cells, **chapter 2** defines several general aspects of solar cell device physics with a special focus on fundamentals of organic semiconductors. The latter are characterized by strong intramolecular bonds but comparatively weak forces between the individual molecules and high binding energies of charge carrier pairs. These striking differences to their inorganic counterparts are the origin of a number of peculiarities such as optical excitations or charge carrier transport in organic semiconductors, which decisively determine the physics of organic solar cells.

Chapter 3 presents basic properties of the materials used in this thesis—with special emphasis on growth, structure and energetics. It is followed by a brief introduction of the experimental methods including sample preparation and applied characterization techniques.

Comprehensive studies—including structure, morphology and energetics—were performed for the heterojunction DIP/C_{60}. However, at various parts of the thesis alternative material combinations—all assigned to the class of small-molecular semiconductors—serve as comparison systems. An overview of the donor/acceptor (D/A) combinations is given in **chapter 4** and contrasts their specific properties such as growth phenomena, energetic positioning and absorption.

The organization of the subsequent experimental part follows the gradual device structure: Different interfaces are considered concerning their specific properties and their impact on the functionality of the cell. **Chapter 5** starts with the interface between anode and donor which comprises the influence of substrate temperature and different hole injection materials. The results emphasize the critical impact on the energy level alignment between anode and donor being crucial for achieving highest possible fill factors.

In organic solar cells, photogenerated charges have to be transported efficiently through the active materials to be extracted at the electrodes and contribute to a current flow. In other words, high charge carrier extraction efficiencies require acceptable electron and hole mobilities. The charge-transport properties critically depend on the degree of ordering in the thin film as well as on the density of chemical and structural defects. As mobility studies within DIP films—especially in diode configuration—are very limited, this topic will be addressed in **chapter 6**.

Chapter 7 is dedicated to the D/A interface: Studies on different material combinations emphasize the strong correlation between interface morphology and solar cell performance. Stacked as well as mixed layers are examined and reveal the vital impact on interfacial structure—both traced back to growth conditions but also to

the molecular shape of the constituents. Moreover, electronic states at the D/A interface play a major role for limiting mechanisms in organic solar cells, especially concerning the open-circuit voltage (V_{oc}). In this context, temperature dependent measurements of V_{oc} and impedance data serve as observables to assess recombination losses in the device. Apart from that, photothermal deflection spectroscopy and electroluminescence measurements are performed to detect the spectroscopic signature of the charge transfer state.

Finally, the influence of top contact variation will be presented in **chapter 8**. Amongst others, the effect of different exciton blocking layers and their impact on device degradation will be shown. The studies emphasize the protective effect of a widely-used exciton blocking layer—independent of its role as exciton diffusion barrier.

This thesis was supported by the German Research Foundation within the Priority Programme SPP 1355, focusing on *Elementary Processes in Organic Photovoltaics* (DFG Schwerpunktprogramm 1355 "Elementarprozesse der Organischen Photovoltaik"[9]). The interdisciplinary research within this program was carried out in close collaboration with university research groups in Berlin, Tübingen and Würzburg—contributing to the present work by enriching investigations on structural and electronic properties as well as microscopic transport phenomena. Essential results of these cooperative studies will be included where necessary for the overall understanding.

Part I

Physical background and methods

Chapter 2

Device physics of organic solar cells

In the following chapter several aspects of solar cell device physics will be briefly presented. Subsequently, a short introduction into the fundamentals of organic semiconductors will cover their binding behavior, the peculiarities of excitation and charge carrier transport as well as some aspects concerning the organic/organic and metal/organic interface. Thereafter, basics of organic solar cells will be explained, including the donor/acceptor concept, the role of the charge transfer state and some fundamental loss mechanisms.

2.1. Solar cell basics

The basic property common to all photovoltaic cells is that they convert sunlight into electrical power. Independent of the type of solar cell, this is achieved by light-induced creation of an electron-hole pair inside an active layer, followed by its dissociation into free charge carriers. The electrical behavior of any solar cell can be best described by its current-voltage (j-V) characteristics, including the most relevant parameters. Under dark conditions, the j-V curve resembles a diode characteristic with a rectifying behavior. When illuminating the solar cell, an additional contribution to the net current is provided by the generated charge carriers, *viz.* the photocurrent density j_{ph}. Thus, the dependence of current density j on the applied voltage V of an illuminated solar cell can be described by the

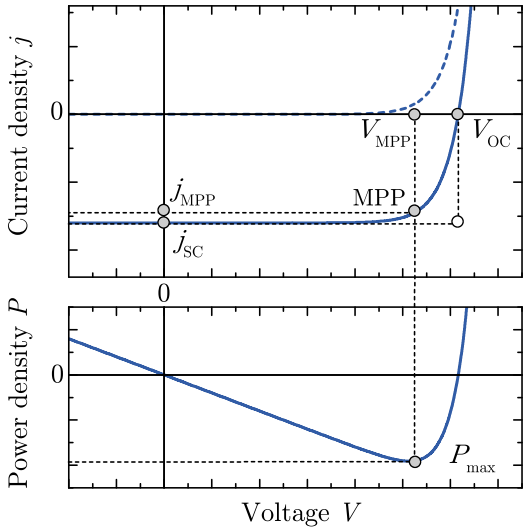

Figure 2.1.: Typical j-V characteristics of an idealized solar cell in the dark (dashed line) and under illumination (solid line). The short-circuit current density (j_{sc}) and open-circuit voltage (V_{oc}) are shown. The maximum output power density P_{max} is given by the rectangle $j_{\mathrm{MPP}} \cdot V_{\mathrm{MPP}}$, defining the maximum power point MPP.

Shockley equation, extended by j_{ph}:

$$j(V) = j_0 \left[\exp\left(\frac{eV}{nk_{\mathrm{B}}T} \right) - 1 \right] - j_{\mathrm{ph}}, \tag{2.1}$$

where j_0 is the dark saturation current, e the elementary charge, n the diode ideality factor and k_{B} Boltzmann's constant.[10]

The upper part of Fig. 2.1 depicts the simulated j-V characteristics of an ideal solar cell in dark (dashed line) and under illumination (solid line). The product of current density and voltage results in the power density shown in the lower graph of Fig. 2.1. It is in the fourth quadrant, i.e. the voltage regime between 0 and V_{oc}, where the cell generates power. For voltages above V_{oc}, charge carriers are injected into the device and power is consumed. This is the regime where light-emitting diodes are operated and where also in some organic solar cells electroluminescence is detectable as will be shown in Sec. 7.2.3. Marked parameters as the open-circuit voltage V_{oc}, the short-circuit current density j_{sc} as well as the resultant parameters fill factor FF and power conversion efficiency η are discussed in the following.

2.1.1. Open-circuit voltage

The open-circuit voltage V_{oc} is defined as the voltage at which the net current under illumination vanishes. As the total current can be seen as superposition of dark and light current, V_{oc} is reached when the photocurrent is entirely compensated by the dark recombination current which is carried by recombination of injected charge carriers without light exposure. From Fig. 2.1 it becomes clear that V_{oc} marks the voltage beyond which power is consumed rather than generated by the device. In OPVCs, the open-circuit voltage is determined by the energy levels of the used active organic semiconductors as will be discussed in Sec. 2.3.2.

2.1.2. Short-circuit current

The photocurrent shifts the diode curve towards the negative current regime with the short-circuit current j_{sc} being the intersect with the negative part of the current axis (see Fig. 2.1). Accordingly, j_{sc} can be detected under short-circuit condition without external voltage ($V = 0\,\mathrm{V}$). In this context, it has to be mentioned that the maximum photocurrent is usually not reached at j_{sc} but only at higher internal fields at additional negative bias. However, a prevalent simplification considers j_{ph} to be constant and equal to j_{sc}, even though a field dependence of the photocurrent is necessary to precisely describe most organic solar cells. Moreover, a commonly observed intersection of dark and light curves under forward bias cannot be explained by a constant photocurrent. Even though it was found that the field dependence of j_{ph} can be ascribed to both dissociation of Coulombically bound excitons and extraction of the resulting free charges, its exact origin is still part of ongoing research.[11] The magnitude of j_{sc} depends on the number of photons which are absorbed by the solar cell. To cover a largest possible part of the sunlight infrared absorbers have been applied to organic solar cells to realize optimized light harvesting.[12,13]

2.1.3. Fill factor

As can be seen from Fig. 2.1, V_{oc} and j_{sc} specify the points on the j-V curve between which the product of current and voltage is negative and the cell delivers power. The point of highest possible power output P_{max} is denoted as maximum power point (MPP). This occurs at some voltage V_{MPP} and the corresponding current density j_{MPP} and designates the operating point of the solar cell (see Fig. 2.1). The ratio of the maximum power density P_{max} and the product of V_{oc} and j_{sc} defines

the fill factor FF as

$$\mathrm{FF} = \frac{V_{\mathrm{MPP}} \cdot j_{\mathrm{MPP}}}{V_{\mathrm{oc}} \cdot j_{\mathrm{sc}}} \tag{2.2}$$

which describes the "squareness" of the j-V curve.

On the way to highest possible efficiencies, most approaches pursue the strategy to maximize V_{oc} and j_{sc} while the fill factor is taken for granted. Yet, besides V_{oc} and j_{sc}, the overall device efficiency depends linearly on the fill factor. In inorganic solar cells, fill factors are usually in the range of 75% to 88%,[6] whereas organic solar cells often suffer from low fill factors with typical values between 60% and 70% hardly reaching 75%, which still leaves room for improvement.[14] Among others, reasons for low fill factors can be found in high series resistances as will be discussed in Sec. 2.1.6.

2.1.4. Power conversion efficiency

The power conversion efficiency η of a solar cell is the maximum achievable output power as a fraction of the incident light power density I_{L}:

$$\eta = \frac{V_{\mathrm{max}} \cdot j_{\mathrm{max}}}{I_{\mathrm{L}}}. \tag{2.3}$$

By using Eq. (2.2), η can be expressed as

$$\eta = \frac{V_{\mathrm{oc}} \cdot j_{\mathrm{sc}} \cdot \mathrm{FF}}{I_{\mathrm{L}}}, \tag{2.4}$$

underlining the need to simultaneously maximize V_{oc}, j_{sc} and FF for getting efficient devices.

Since the sensitivity and thus the conversion efficiency of solar cells strongly depend on the spectrum of the light source $I_{\mathrm{L}}(\lambda)$, standard test conditions have been defined including a designated spectrum with an incident power density of $100\,\mathrm{mW/cm^2}$.[15] The reference spectrum is a simulated AM 1.5 (AM: air mass) global spectrum (cf. Fig. 2.2) which corresponds to an angle of incidence of solar radiation of 48° relative to the surface normal of the earth.

2.1.5. External quantum efficiency

The external quantum efficiency (EQE)—also known as incident photon to current efficiency (IPCE)—is another measure of the performance of a solar cell. In contrast to the power conversion efficiency, which is an integral quantity over all

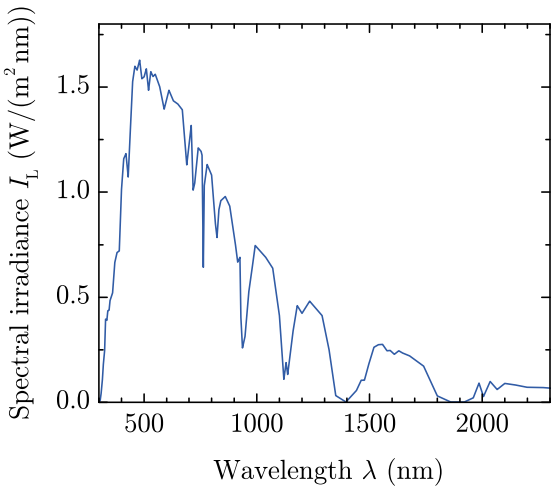

Figure 2.2.: Spectral irradiance of the AM 1.5 g standard terrestrial solar spectrum. Data taken from Ref. 16.

wavelengths, the EQE is a spectral measure and is defined as the ratio of the number of charge carriers collected by the solar cell to the number of incident photons of a given energy. The wavelength dependence is mainly a result of the absorption spectrum of the solar cell but also of spatially inhomogeneous photovoltaic response: the efficiency of charge carrier transport to the electrodes can depend on the position where these charges have been generated, i.e., where the photon was absorbed inside the device.[17] This is closely related to interference effects causing standing waves inside the thin organic layers.

The EQE can be determined from a wavelength dependent measurement of the short-circuit current

$$\mathrm{EQE}(\lambda) = \frac{hc}{e\,\lambda} \cdot \frac{j_{\mathrm{sc}}(\lambda)}{I_{\mathrm{L}}(\lambda)}, \tag{2.5}$$

where c is the speed of light and λ the wavelength.

In contrast to the internal quantum efficiency η_{int}, the EQE accounts for reflection losses but can be converted into η_{int}, if only the fraction of the actually absorbed photons are considered:

$$\eta_{\mathrm{int}} = \frac{\mathrm{EQE}(\lambda)}{1 - R(\lambda) - T(\lambda)}, \tag{2.6}$$

with $R(\lambda)$ denoting the fraction of reflected light and $T(\lambda)$ the fraction of transmitted light.

2.1.6. Equivalent circuit

In order to figure out the relation between device modification and its impact on performance it can be helpful to make use of a model to fit the measured j-V curves. The equivalent circuit model as shown in Figure 2.3 (a) was originally derived for the electrical simulation of inorganic solar cells but is commonly adapted to organic photovoltaics.[18,19] This very simple equivalent circuit consists of a current source (accounting for the photocurrent density j_{ph}) and a diode (representing the dark current density $j_{\mathrm{dark}}(V)$) connected in parallel. Based on this model the net current density of a solar cell under illumination can be approximated by a superposition of $j_{\mathrm{dark}}(V)$ and j_{ph} as was already introduced in the previous section by Eq. (2.1).

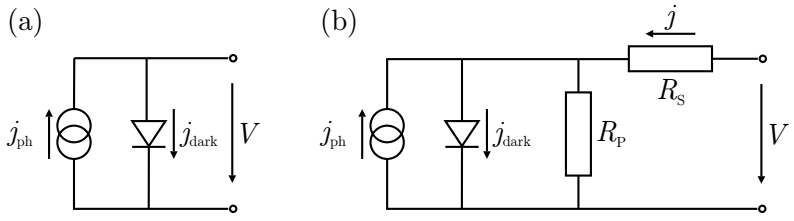

Figure 2.3.: (a) Equivalent circuit of an ideal solar cell consisting of a current source generating j_{ph} in parallel with a diode, which generates the dark recombination current j_{dark}. (b) Equivalent circuit of a real device including series resistance R_{S} and shunt resistance R_{P}.

However, in real devices the equivalent circuit has to be extended by two parasitic resistances (cf. Fig. 2.3 (b)); a specific series resistance $R_{\mathrm{S}}A$ accounting for the voltage drop at the contacts and a specific parallel resistance $R_{\mathrm{P}}A$ as consequence of leakage currents (A denotes the area of the cell). Consequently, the internal voltage V' has to be modified by the voltage drop at the series resistance, as $V'(V) = V - j(V)R_{\mathrm{S}}A$ and an additional current contribution j_{P} caused by the shunt has to be taken into account with $j_{\mathrm{P}} = V'/R_{\mathrm{P}}A$. When both parasitic resistances are included, the diode equation (2.1) then takes the form

$$\begin{aligned} j(V) &= j_0 \left\{ \exp\left[\frac{eV'(V)}{nk_{\mathrm{B}}T} \right] - 1 \right\} + j_{\mathrm{P}} - j_{\mathrm{ph}} \\ &= j_0 \left\{ \exp\left[\frac{e\,(V - j(V)R_{\mathrm{S}}A)}{nk_{\mathrm{B}}T} \right] - 1 \right\} + \frac{V - j(V)R_{\mathrm{S}}A}{R_{\mathrm{P}}A} - j_{\mathrm{ph}}. \end{aligned} \tag{2.7}$$

In order to visualize the influence of n, j_0, $R_{\mathrm{S}}A$ and $R_{\mathrm{P}}A$ on the shape of j-V characteristics, simulations have been performed based on Eq. (2.7) with varying parameters. The impact of n on the dark and light j-V characteristics is shown

in Fig. 2.4 (a). Especially the fill factor of the j-V curve is negatively affected by high values of n. The ideality factor is connected to the slope of the exponential curve, where an ideal diode shows an ideality factor of $n = 1$. Compared to ideal devices, the dark current of real cells usually depends more weakly on bias with n typically lying between 1 and 2.[20] As will be further discussed in Sec. 7.2.4, ideality factors larger than unity can be assigned to recombination currents.[21]

The dark saturation current j_0 is given by the current density in reverse direction of the diode in dark. Figure 2.4 (b) graphically illustrates the influence of the reverse saturation current j_0 on device characteristics and points out that smaller values of j_0 shift the j-V curve to the left resulting in lower V_{oc}. However, the short-circuit current is not affected by j_0. The crucial dependence of V_{oc} on the dark saturation current will be discussed in more detail in Sec. 7.2.1. At this point, it has to be mentioned that in real devices the exponential increase of dark current above the onset voltage depends both on the diode ideality factor as well as on the dark saturation current. Thus, a separate analysis of n and j_0 as it is shown here is only a simplified representation visualizing the impact of both parameters as if they could be viewed in isolation from each other.

Figure 2.5 illustrates how the extrinsic behavior of the cell is affected by varying $R_{\mathrm{S}}A$ and $R_{\mathrm{P}}A$. As can be seen from (a), the addition of a simple series resistance has a tremendous effect on the fill factor, while the short-circuit current is almost unaffected by $R_{\mathrm{S}}A$ until it becomes very large. The greatest influence of the curve is observed near the open-circuit voltage. However, $R_{\mathrm{S}}A$ does not affect the V_{oc} value itself since, at open circuit, the overall current flow through the device is zero. A first approximation of the series resistance can be received from the slope of the j-V curve at V_{oc}. Reasons for non-vanishing values of $R_{\mathrm{S}}A$ can be found in additional lead resistances of the electrodes, contact resistances at the electrode/semiconductor interface or the resistance of the semiconductor itself.[22]

The effect of a finite parallel resistance can slightly reduce V_{oc} but mainly affects the fill factor, as shown in Fig. 2.5 (b). In an ideal device, the specific parallel resistance is infinite ($R_{\mathrm{P}}A = \infty$). Deviations may originate from leakage currents bypassing the cell or shunt currents through small short paths. The slope of the j-V curve near the short-circuit current can serve as a first approximation of $R_{\mathrm{P}}A$.

It can be seen that both parasitic resistances, separately or combined, reduce the fill factor but have minor influence on V_{oc}. An expression for the open-circuit voltage can be derived by neglecting the influence of $R_{\mathrm{S}}A$ and $R_{\mathrm{P}}A$, setting the

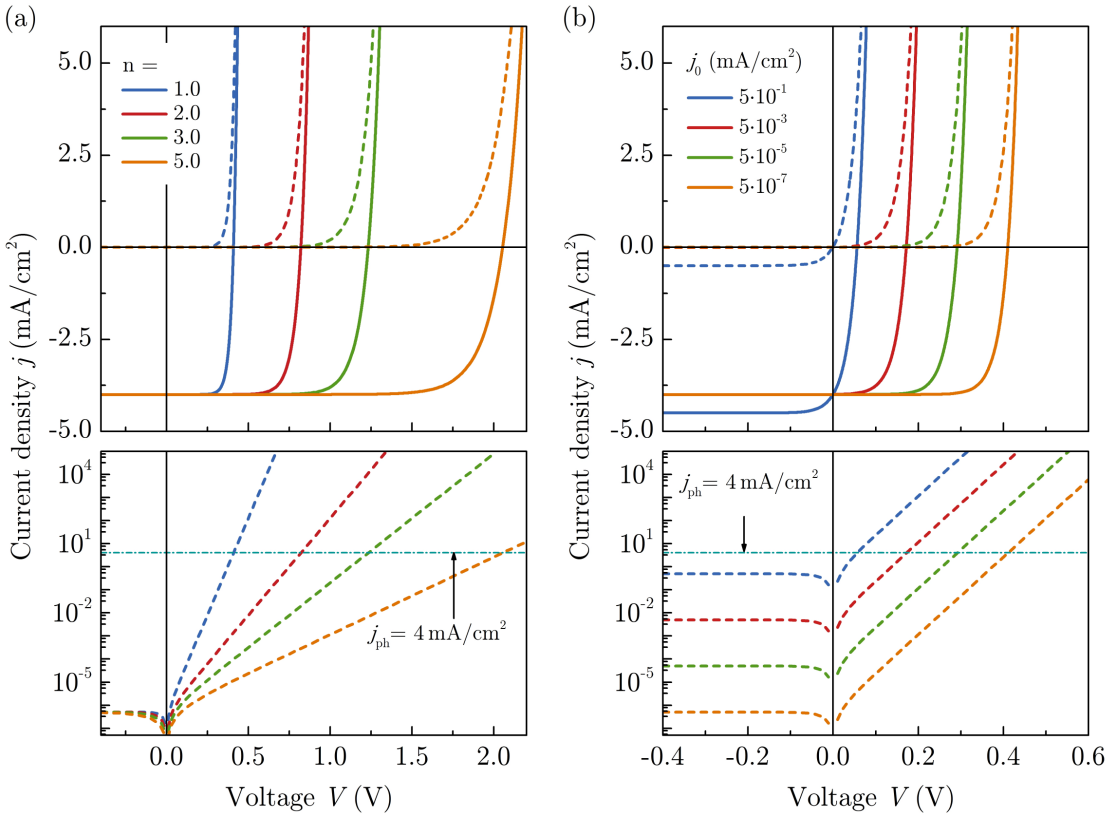

Figure 2.4.: Effect of (a) the ideality factor n and (b) the dark saturation current j_0 on the j-V characteristics of a solar cell. The upper parts show the simulated j-V curves under illumination (i.e., in consideration of a photocurrent j_{ph}, solid lines) and in dark (dashed lines) while the lower parts depict the logarithmic plot of the dark j-V characteristics. Unless otherwise indicated, the following parameters have been used for simulation: $R_{\mathrm{S}}A = 0$, $R_{\mathrm{P}}A = \infty$, $\mathrm{T} = 300\,\mathrm{K}$, $j_0 = 5 \cdot 10^{-7}\,\mathrm{mA/cm^2}$, $n = 1$, $j_{\mathrm{ph}} = 4\,\mathrm{mA/cm^2}$.

ideal equation (2.1) to zero and solving for the voltage:

$$V_{\mathrm{oc}} = n\frac{k_{\mathrm{B}}T}{e}\,\ln\left(\frac{j_{\mathrm{ph}}}{j_0} + 1\right). \tag{2.8}$$

From this it can be expected that—apart from j_{sc}—the parameters with the largest impact on V_{oc} are j_0 and n as demonstrated in Fig. 2.4.[21]

Besides the above described comparatively straightforward model, several authors report on more complex approaches to refine the simulation. One important work was done by Sokel and Hughes, who numerically analyzed the photoconductivity in insulators by taking diffusional forces and their impact on charge extraction into account.[23] Comparisons to experimental data indicate that diffusion plays an

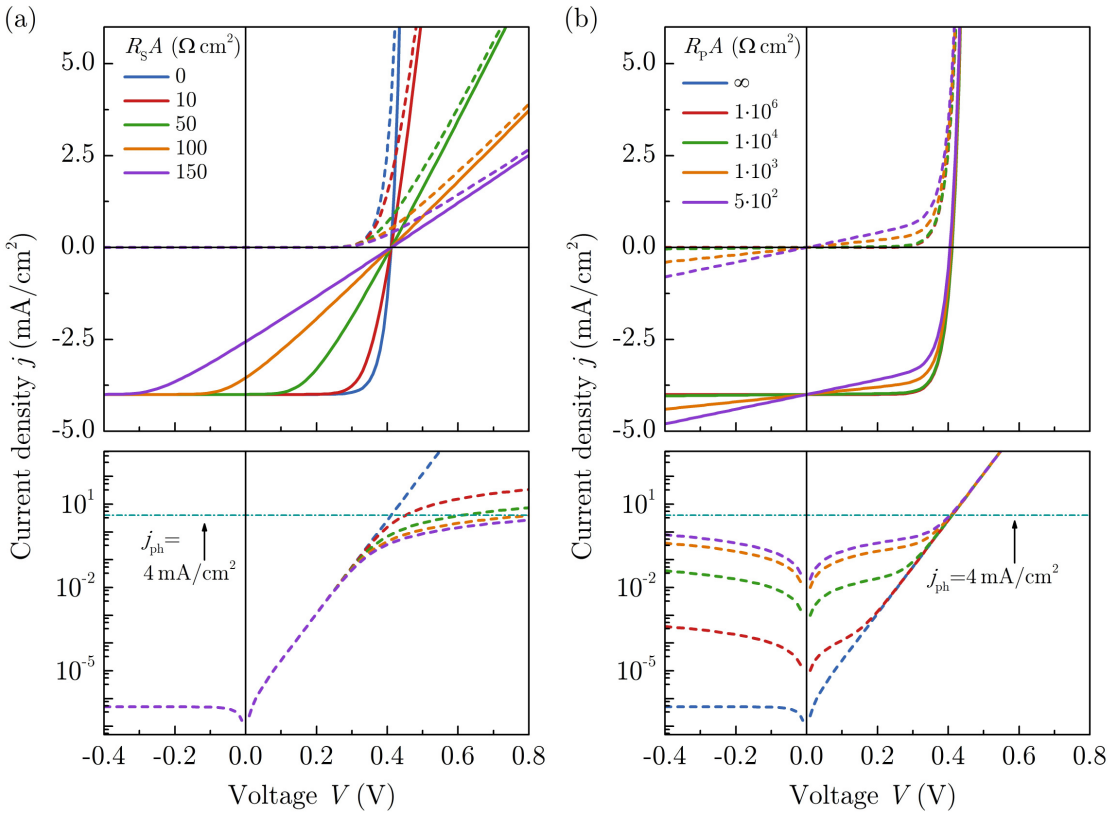

Figure 2.5.: Effect of (a) the specific series resistance R_SA and (b) the specific parallel resistance R_PA on the j-V characteristics of a solar cell. The upper parts show the simulated j-V curves under illumination (i.e., by accounting for a photocurrent j_{ph}, solid lines) and in dark (dashed lines) while the lower parts depict the logarithmic plot of the dark j-V characteristics. Unless otherwise indicated, the following parameters have been used for simulation: $j_0 = 5 \cdot 10^{-7}$ mA/cm^2, $n = 1$, T = 300 K, $R_PA = \infty$, $R_SA = 0$, $j_{ph} = 4$ mA/cm^2.

important role for the photocurrent—especially at low effective fields.[24] By means of rate equations for electron transfer, probabilities for charge carrier recombination and accounting for field-dependent photocurrents new models are developed to address the peculiarities of organic photovoltaic devices.[11,25–28] Based on charge extraction as calculated by Sokel and Hughes combined with a field dependent polaron pair dissociation after Onsager and Braun,[29,30] Mihailetchi *et al.* could explain the experimentally observed photocurrent in reverse direction.[24] Yoo *et al.* reported on a refined equivalent circuit model containing an additional shunt resistance and an additional diode to represent light intensity dependent behavior of the cells.[18] However, a more complex device modeling would go beyond the scope of this thesis and thus simulation and fitting is limited to the above introduced gen-

eral approach. In order to exclude elusive effects—caused, e.g., by field-dependent photocurrents—the application of the model will be restricted to dark characteristics in this thesis. This approach is justifiable as it was found that changes in light characteristics are linked to significant changes in the dark j-V curves.

2.2. Organic semiconductors

2.2.1. General aspects

Within the large variety of organic solids, organic semiconductors have aroused increased interest in recent years, as they can be termed as the heart of organic electronics. They are generally categorized into two major classes, *viz.* polymers and molecular materials (often referred to as "small molecules") both having carbon as main constituent.[31] This thesis will focus on the latter. The most obvious difference is their size which, in turn, determines the manufacturing technique of thin films: polymers can consist of a huge amount of repeating units with length scales of up to a few hundred nanometers and are usually deposited by solvent-based spin-coating and printing techniques. Small molecules are typically no more than a few tens of nanometers in scale and can be thermally evaporated.

Organic semiconductors are characterized by the presence of conjugation, i.e., alternating single and double bonds between neighboring carbon atoms, being responsible for the formation of a delocalized π-electron system.[32] While σ-bonds, which are formed by sp^2-hybridization of carbon atoms, form the molecular backbone of the molecule, the remaining p_z-orbitals lead to the formation of additional π-bonds (see Fig. 2.6 (a)). If single- and double-bonds alternate, a conjugated π-electron system is built up where the electron density is delocalized over the whole molecule.

A widespread building block of many organic semiconducting small molecules is benzene (C_6H_6), which is composed of six C-atoms in a ring, with one hydrogen atom attached to each carbon. The orbitals of the valence electrons of the C-atoms are schematically depicted in Figure 2.6 (b): three sp^2-orbitals of one carbon atom form two σ-bonds to the neighboring C-atoms and one σ-bond forms the bonding to the respective hydrogen atom (left out for the sake of clarity). The remaining p_z-orbital is directed perpendicularly to the internuclear axis and contains one unpaired electron. In the case of benzene the bonding molecular π-orbitals are doubly occupied, respectively. For this reason they form the highest occupied molecular orbital (HOMO) of the ground state while the antibonding π^*-orbitals represent the lowest unoccupied molecular orbital (LUMO) (Fig. 2.6 (c)). Due to

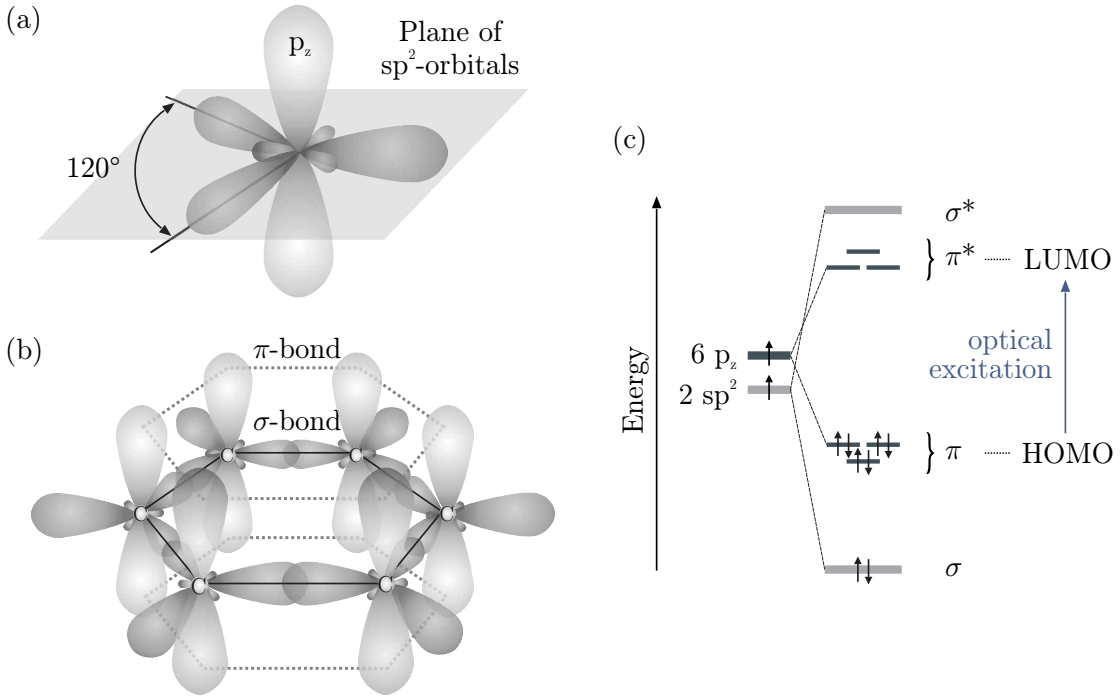

Figure 2.6.: Schematic sketch of the sp^2-hybridization (a) and the formation of σ- and π-bonds in benzene (b). (c) Energy level diagram illustrating the bonding and antibonding molecular orbitals in benzene. The lowest electronic excitation is between the bonding π-orbital and the antibonding π^*-orbital.

the weaker orbital overlap of the p_z-orbitals, the π-π^* splitting is smaller compared to the splitting of the σ-orbitals, making the π-electron system responsible for most electronic and optical properties in conjugated molecules. The size of this energy gap E_g typically lies in the range of 1.5 to 3 eV, which makes the material semiconducting and leads to light absorption or luminescence in the visible, near infrared or near ultraviolet range of the electromagnetic spectrum.[33] The size of the band gap can be varied by the extent of the conjugated π-electron system allowing for chemical tailoring to alter their properties.

While the intramolecular stability of the molecules or polymer chains is mainly governed by covalent σ-bonds, comparatively week Van der Waals forces are responsible for the cohesion within a molecular solid.[32] They are based on dipole forces between electrically neutral molecules and significantly determine mechanical and thermodynamic material properties.

2.2.2. Optical excitations in organic molecules

Optical transitions

The basic optical transitions in an organic semiconductor are illustrated based on a simplified energy level diagram depicted in Fig. 2.7. As already mentioned above, molecular crystals show weak intermolecular forces as compared to the much more significant intramolecular covalent bonds. Thus, the electronic transitions inside an organic molecular crystal can directly be deduced from those of its free molecules.[32] In general, electronic states are divided into singlet and triplet states which can be distinguished by the total spin state of the molecule. The absorption of light leads to a transition from the ground state S_0 to the excited state S_1. Relaxation can take place via fluorescence, i.e., a direct radiative transition from S_1 to S_0, which is spin allowed leading to excited state lifetimes on the order of nanoseconds. By contrast, a radiative transition from T_1 to the ground state S_0 (phosphorescence) is spin forbidden, and hence the triplet state has lifetimes in the range of milliseconds. As the transition from singlet to triplet involves a change of spin, the so-called intersystem crossing (ISC) is normally forbidden, however, becomes partially allowed by spin-orbit coupling.

For a comprehensive description of the electronic transitions in a molecule, the electronic excitation would have to be completed by vibrational and rotational

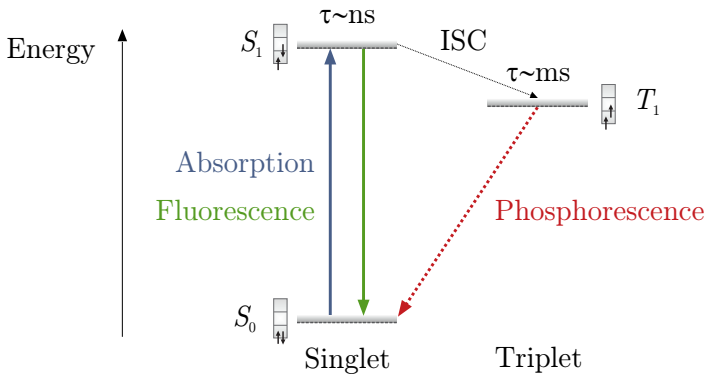

Figure 2.7.: Schematic energy level diagram of an organic molecule illustrating the most important transitions between the electronic ground state S_0, the first excited singlet state S_1 and triplet state T_1. The direction of the small arrows visualize the spin orientation of the most weakly bound π-electrons. By absorption of light, an electron can be lifted to the excited electronic state S_1. A radiative decay back to the ground state can either take place via fluorescence from the excited singlet state or via phosphorescence from the triplet state.

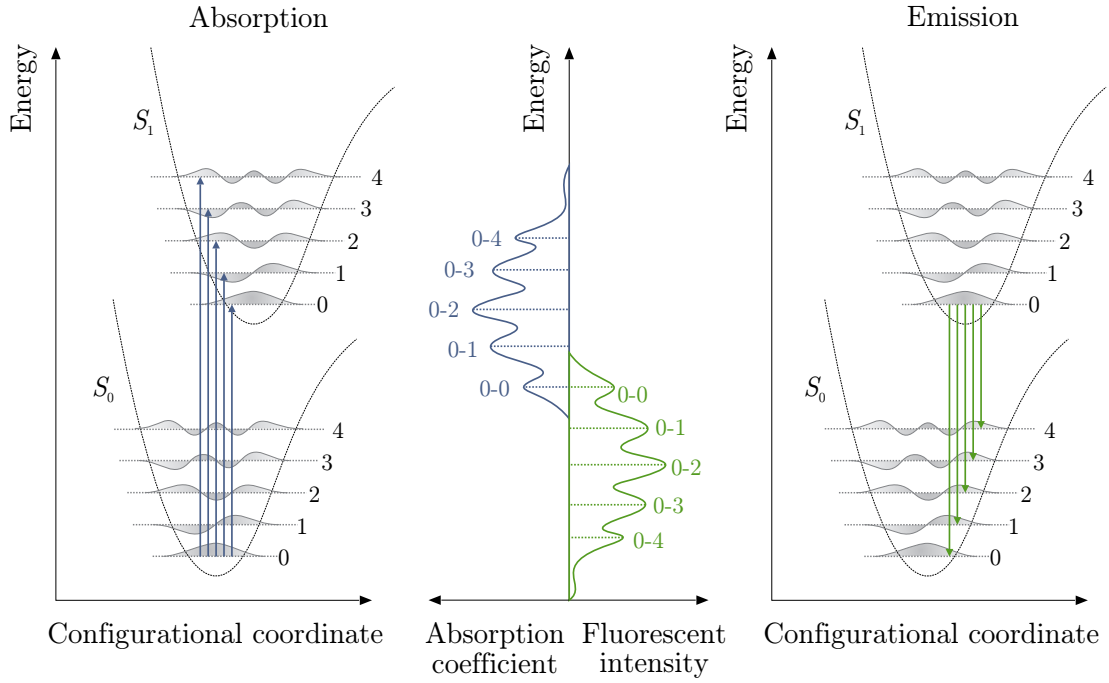

Figure 2.8.: Potential energy curves of the ground (S_0) and excited (S_1) state with the corresponding wavefunctions of the vibrational energy levels. The vertical arrows indicate optical transitions from S_0 to the vibrational level of S_1 in case of absorption (blue) and from S_1 to vibrational levels of S_0 in case of fluorescence (green). The curves in the middle depict the resulting absorption and emission spectra illustrating the vibronic progression according to the Frank-Condon principle.

components of the molecule's wavefunction.[b] While all three contributions have to be regarded in gases and liquids, the rotational part can be neglected in solids as a consequence of their restricted rotational degrees of freedom. The formation of vibronic progression in absorption and emission spectra is illustrated in Fig. 2.8 by means of the potential energy diagrams of the electronic ground and excited states S_0 and S_1. Due to the deformation of the molecule as a consequence of electronic excitation, the potential curves are usually affected by a shift in the nuclear coordinate. Upon absorbing a photon a transition from the lowest vibrational level of the electronic ground state to a vibrational level of the excited state takes place (see left part of Fig. 2.8). The selection rules for these vibrational transitions are described by the Franck-Condon principle, which states that the probability of a transition is the higher, the more intense the overlap of the vibrational wave functions of the two involved transitions is.[34–36] By means of non-radiative recombination, the

[b] In a quantum-mechanical description the Born-Oppenheimer approximation allows for the separation of all three components since the mass of the nuclei significantly exceeds the electron mass.

molecules relax to the lowest vibrational level of the excited state. This process occurs on time scales in the picosecond range and is called "internal conversion". From the lowest vibrational level of the excited state, de-excitation takes-place to one of the vibronic levels of the electronic ground state (see right part of Fig. 2.8). This results in a vibronic progression of both the absorption and emission spectra and their mirror symmetry to each other as schematically illustrated in Fig. 2.8. As a consequence of the non-radiative relaxation process within the excited state, the emission spectrum is red-shifted in comparison to the absorption spectrum (Stokes-shift).

Excitons

The striking difference between organic semiconductors and their inorganic counterparts can be found in the way of charge generation. Organic solar cells belong to the class of so-called "excitonic solar cells" (including dye-sensitized solar cells and polymer solar cells).[37,38] In conventional semiconductors, electron-hole pairs exhibit binding energies far below $k_\mathrm{B}\,T$ ($\approx 25\,\mathrm{meV}$ at room temperature), as high dielectric constants of typically around 12–16 lead to screened Coulomb interaction. Thus, weakly bound electron-hole pairs (Mott-Wannier excitons) are generated upon light absorption, which can easily be separated into free charge carriers by thermal energy. By contrast, absorption of photons in organic solar cells leads to the formation of Frenkel excitons (i.e., excited quasiparticles which can be seen as electrostatically-bound electron–hole pairs). Reasons for this are two-fold:
Firstly, comparatively low dielectric constants of organic semiconductors ($\approx$ 3–4) lead to strong Coulomb attraction between the respective electron and hole, which results in high exciton binding energies of the order of 0.1 to 2 eV.[39,40] In order to escape from this attractive interaction, the separation must be sufficiently large. The equalization between both energies defines the Coulomb radius

$$r_\mathrm{C} = \frac{e^{\,2}}{4\pi\varepsilon\varepsilon_0 k_\mathrm{B} T}\,, \tag{2.9}$$

where ε_0 is the permittivity of free space. The Coulomb radius r_C typically amounts to approximately 20 nm.
Secondly, weak Van der Waals interactions between the individual molecules result in a small Bohr radius of the relevant charge carrier r_B. In a semiconductor with hydrogen-like wave functions, r_B of the lowest electronic state can be determined to[41]

$$r_\mathrm{B} = r_0\,\varepsilon\frac{m_\mathrm{e}}{m_\mathrm{eff}}, \tag{2.10}$$

where $r_0 = 0.53$ Å is the first Bohr radius of an electron of the hydrogen atom, m_e the mass of the electron and m_{eff} the effective mass of the electron in the semiconductor. The larger the effective mass and the lower the value of the dielectric constant, the smaller is the Bohr radius.

By means of these two measures, one can give a rule for the occurrence of excitonic behavior: if $r_C > r_B$, excitonic properties are observed and excitons are formed upon light absorption rather than free electron-hole pairs.[42] This fundamental difference is schematically illustrated in Fig. 2.9: for inorganic semiconductors, the Bohr radius $r_{B,IOSC}$ is much larger than the Coulomb radius $r_{C,IOSC}$—while the Coulomb radius $r_{C,OSC}$ in organic semiconductors exceeds the Bohr radius $r_{B,OSC}$ by far, resulting in excitonic behavior.

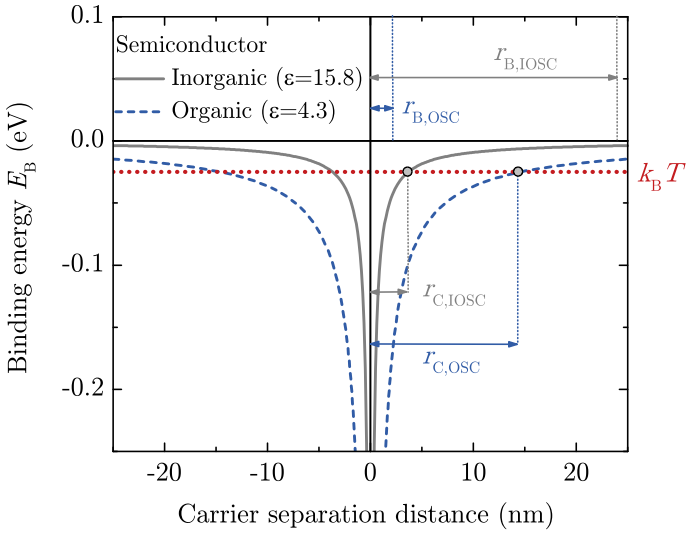

Figure 2.9.: Schematic representation of the fundamental differences between conventional semiconductors (properties marked as IOSC) and excitonic semiconductors (which include organics, properties marked as OSC). The calculations assume Coulomb's law with the positive charge at 0 nm and assume a permittivity of C_{60} of $\varepsilon_{OSC} = 4.3$[43] and Germanium of $\varepsilon_{IOSC} = 15.8$,[44] standing exemplarily for organic and inorganic semiconductor, respectively. The relevant distinction has to be made between the size of the wavefunction ($r_{B,IOSC} \approx 24$ nm,[45] $r_{B,OSC} \approx 2$ nm[46]) and the width of the Coulomb potential well at $k_B T$ (r_C).

2.2.3. Charge carrier transport in organic semiconductors

Charge carrier transport can be considered as key factor for the functionality of organic semiconductor devices. Thus, balanced electron and hole mobilities are

decisive to control the position of charge carrier recombination in OLEDs, because imbalanced charge transport lead to accumulation of charges inside the device or electroluminescence quenching when charge carriers recombine close to the metallic interface—both leading to a loss in efficiency.[47] In OPVCs—as will be shown in Sec. 2.3.1—dissociated charge carriers have to be efficiently transported towards the electrodes in order to contribute to the photocurrent. Moreover, the realization of high charge carrier mobilities is a necessary prerequisite for practical applications of OFETs. However, one of the remaining key questions is whether charge carrier transport occurs via hopping between localized states or via band transport similar to inorganic semiconductors. The answer to that question critically depends on the degree of order in the solid.

Band versus hopping transport

Long-range order and periodicity of covalently bound inorganic crystals lead to delocalized electronic states and wide bands with bandwidths of few electron Volts, allowing for band transport at high mobilities of up to $10^3\,\mathrm{cm^2/Vs}$ (see Fig. 2.10). Similarly, the intermolecular transport of organic single crystals[48,49] or highly ordered crystalline organic semiconducting films[50] can be described as band-like transport as long as temperature is sufficiently low. However, weak van der Waals forces which keep the individual molecules together lead to less pronounced electronic interaction between molecular orbitals of adjacent lattice sites as compared to inorganic crystals. As a consequence narrow bands arise with bandwidths on the order of a few hundred milli-electron Volts.[51]

When the organic molecules do not crystallize in an ordered fashion but form amorphous films, the absolute values of molecular energies are randomly distributed as a result of the spatial variation of the surrounding polarization.[52] Consequently, HOMO and LUMO states are localized on each molecule with narrow intermolecular bandwidths smaller than $0.1\,\mathrm{eV}$.[53] Thus, the electronic structure of a disordered organic solid mostly resembles that of a single molecule with localized states instead of well-defined bands. Free charge carriers are—similar to excitons—localized to single molecules or few repetition units of a polymer and thermally activated hopping is the prevailing transport mechanism. Not infrequently, mobilities in disordered organic semiconductors are found to be lower than $10^{-5}\,\mathrm{cm^2/Vs}$, and hence, again several orders of magnitude below those of organic crystals ($\mu \approx 1$–$10\,\mathrm{cm^2/Vs}$).[54] Electrons, which are injected into the material or generated by photoexcitation, occupy the LUMO of the organic semiconductor. The formed anion polarizes its molecular surrounding, and the charge in combination with the geometric distortion of the molecule is referred to as negative

"polaron". Vice versa, holes are occupying the HOMO and are—together with their electronic polarization—considered as positive polarons.[32] The energetic distribution of the hopping sites can be best described by a Gaussian function, and emphasizes that HOMO and LUMO do not exactly describe energies of a band edge, which is different to their inorganic equivalent of valence and conduction band, respectively.

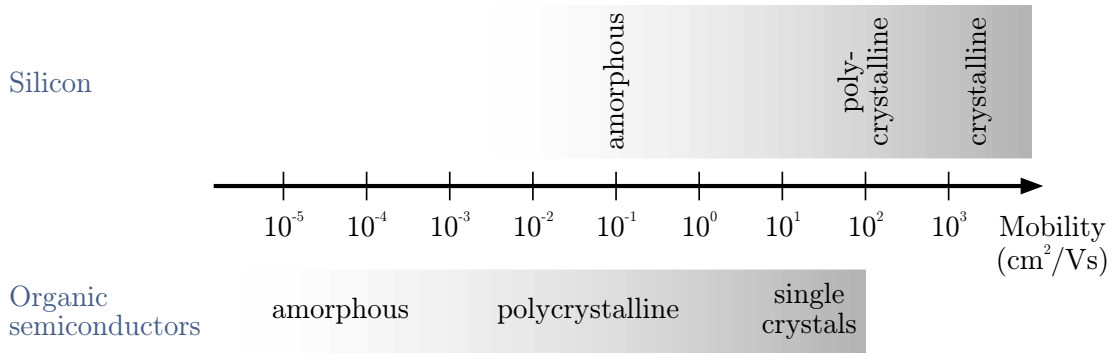

Figure 2.10.: The charge carrier mobility in organic semiconductors strongly depends on the extent of disorder—on the whole, however, values are considerably lower compared to silicon. Illustration adopted from Ref. 55.

Factors influencing charge carrier transport in organic semiconductors

The distinctive parameter describing the transport properties of a particular material is the charge carrier mobility μ, which is defined as the proportionality factor between drift velocity ν_d and applied electric field F ($\nu_\mathrm{d} = \mu \cdot F$). There are many factors influencing μ, including temperature, molecular packing, the degree of disorder, traps, electric field and charge-carrier density[56]—some of them are briefly addressed in the following.

Temperature Band transport in inorganic semiconductors is based on the motion of delocalized plane waves in broad bands. It is limited by scattering with acoustic phonons which results in the reciprocal temperature dependence of the mobility ($\mu \propto T^{-3/2}$),[c] i.e., the mobility decreases with increasing temperature.[57] By contrast, polaron-hopping in organic semiconductors is a thermally activated process. Thus, transport is improved with higher temperatures providing sufficient energy to overcome the barriers formed by energetic disorder. The temperature

[c] Only at very low temperature the scattering from phonons die out and scattering from charged defects lead to an opposite temperature behavior of $\mu \propto T^{3/2}$.

dependence of the mobility is often described by an Arrhenius law:

$$\mu(F) \propto \exp\left(\frac{-E_\mathrm{a}}{k_\mathrm{B}T}\right), \tag{2.11}$$

with an activation energy E_a on the order of approximately 0.3–0.5 eV.[54] In contrast to the empirical relation given by Eq. (2.11) Monte Carlo simulations by Bässler showed a non-Arrhenius temperature dependence of the mobility at low fields:[58]

$$\mu(F) \propto \exp\left[-\left(\frac{2\sigma}{3k_\mathrm{B}T}\right)^2\right], \tag{2.12}$$

where σ is the width of the Gaussian DOS (see below).

Electric field In single crystals, a field dependence is observed only in ultrapure crystals where an increase in electric field leads to reduced mobilities.[56] By contrast, disordered materials show an increase in mobility at high fields, which can be described by

$$\mu(F) \propto \exp\left(\gamma\sqrt{F}\right), \tag{2.13}$$

with the field activation parameter γ.[59] This so-called Poole-Frenkel like behavior describes the modification of a Coulomb potential in the presence of an electric field F, which lowers the energy barrier for charge carrier hopping in direction of the field by $\gamma\sqrt{F}$ as illustrated in Fig. 2.11 (a).

Disorder There are many factors influencing the energetic disorder of an organic semiconducting film, which is related to fluctuations in strength of interactions between adjacent molecules. Among others, disorder can be influenced by the substrate, its temperature or film thickness which changes the degree of order (see Ref. 56 and references therein). In this context, another aspect influencing charge carrier transport can by found by grain boundaries: It was shown by Horowitz and Hajlaoui that the mobility in polycrystalline films increases linearly with grain size.[62] Hopping transport in organic systems with energetic and spatial disorder was first described by Bässler by means of the Gaussian disorder model.[58] His analysis is based on Monte Carlo simulations using Miller-Abrahams hopping rates[63] and considers a Gaussian density of states distribution with a disorder parameter σ on the order of 100 meV (see Fig. 2.11 (b)).

Charge carrier density However, an extension to the Gaussian disorder model for hopping transport became necessary when it was observed that the mobility

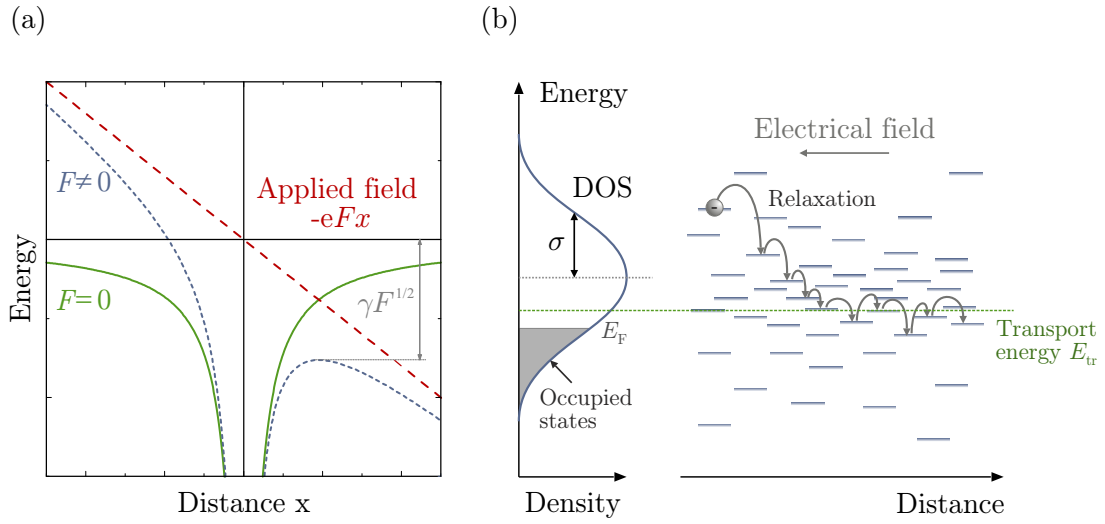

Figure 2.11.: (a) Coulombic potential well in the presence of an electric field F illustrating the Poole–Frenkel effect. The Coulomb potential barrier is reduced by $\gamma F^{1/2}$ in the direction of the field (after Ref. 60). (b) Charge transport by hopping within an energetic landscape of localized states described by a Gaussian density of states (DOS) with a disorder parameter σ. Upon injection or photoexcitation, the charge carrier relaxes to states with lower energy. Steady-state charge transport takes place around a transport energy E_{tr} which is mainly determined by temperature and disorder (after Ref. 61).

additionally depends on the concentration of charge carriers in disordered organic semiconductors.[64] This requirement was met by the so-called multiple trapping and release model, which is based on the concept of transport energy.[65,66] As schematically depicted in Fig. 2.11 (b) charge carrier transport under steady-state condition is described by hopping around the transport energy E_{tr}. As the charge carrier density in the system is increased, the distance between E_{F} and E_{tr} is reduced. Thus, more states are provided which are accessible to mobile charge carriers finally leading to an increase in mobility.[67] Reviews by Jaiswal *et al.*[57] and Braun[68] give summaries of the most common models and equations relating to transport in disordered systems.

Molecular packing It was shown that the amplitude of the transfer integrals—one of the major parameters governing the transport properties—is extremely sensitive to molecular packing.[69] Thus, large mobility anisotropy can be found in ordered OSCs: depending on the molecular orientation π-orbital overlap can vary significantly with different directions. Along the plane of π–π stacking more efficient charge transport is found resulting in higher mobilities (see Fig. 2.12).

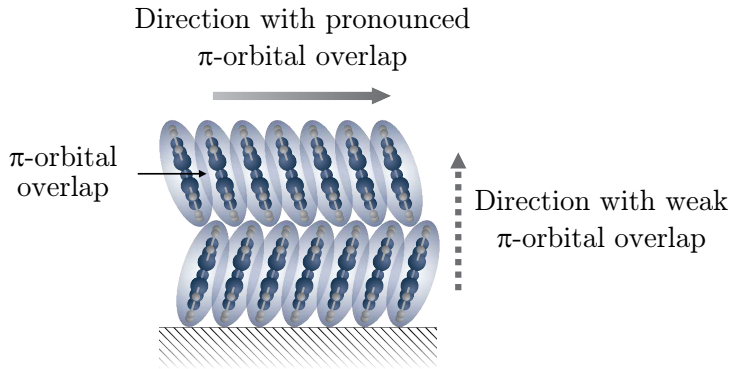

Figure 2.12.: Illustration of anisotropic charge carrier transport in a molecular crystal as result of varying degree of π-orbital overlap in different directions. Schematic redrawn from Ref. 55.

Charge carrier traps Transport properties are particularly affected by charge carrier traps. Based on their microscopic origin, one distinguishes between extrinsic traps due to impurities or chemical defects and intrinsic traps caused by structural inhomogeneity.[70] Impurities act as traps if their frontier orbitals are situated within the energy gap of the pure material. While shallow traps are characterized by a trapping energy on the order of $k_\mathrm{B}T$ (making thermal detrapping possible), trapping energies larger than $k_\mathrm{B}T$ identify deep traps. In order to prevent or reduce unintentional contamination, most of the materials used throughout this thesis have been purified by gradient sublimation. Besides impurities, charges can also be trapped by structural defects within the organic layer. In polycrystalline organic semiconducting films the major contribution to structural defects is formed by grain boundaries which limit the overall transport properties of the film.

Measurement of charge carrier mobility

The suitable macroscopic quantity for charge carrier transport in an organic semiconductor device is the current density j, which is related to the mobility as

$$j = e\rho_0\nu_d = e\rho_0\mu F. \tag{2.14}$$

This expression highlights the significance of the charge carrier density ρ_0 on the magnitude of the current, as the intrinsic carrier density is usually close to zero in organic semiconductors with large energy gaps. Aside from photogeneration, high carrier densities inside an organic film can be generated by injection of charges across the contacts. Ideally, the contact between electrode and semiconductor can be considered as ohmic, i.e., it is characterized by sufficiently small injection barriers. In this case, the current is limited by a build up of space charge inside the

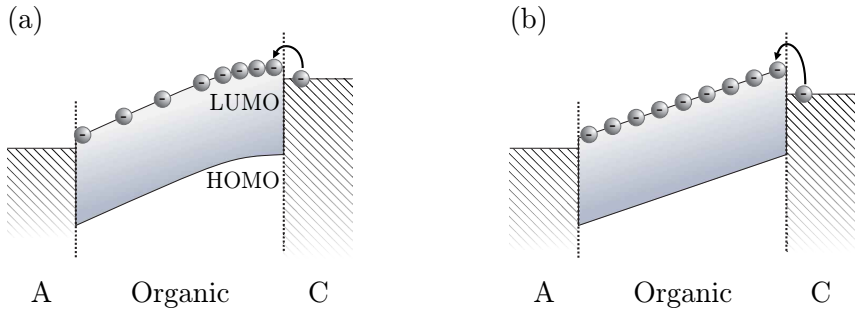

Figure 2.13.: Comparison of the local dependence of electron density in an electron-only device (both cathode (C) and anode (A) are low work function materials) with (a) space-charge limited current (SCLC) and (b) injection-limited current. Schematic is leaned to Ref. 32.

semiconductor—in contrast to injection-limited current as result of high energetic barriers (see schematic illustration in Fig. 2.13).

The theory of space-charge-limited current (SCLC) can be used as a simple tool to determine the mobility of an organic semiconductor in an experimental configuration which is relevant for the respective device.[71–74] In the absence of any trapping effects the current density carried by one type of charge carriers is given by the Mott-Gurney equation[75]

$$j_{\mathrm{SCLC}} = \frac{9}{8}\varepsilon_{\mathrm{r}}\varepsilon_0\mu\,\frac{\mathscr{V}^2}{d^3}, \tag{2.15}$$

where ε_{r} and ε_o are the dielectric constants of the material and vacuum, respectively and d the thickness of the active layer. The applied bias V has to be corrected for the built-in potential V_{bi} arising from the difference in work function of the contacts, so that $\mathscr{V} = V - V_{\mathrm{bi}}$.

However, SCLC currents cannot automatically be assumed to be present in any kind of organic semiconducting film: Especially π-conjugated polymers—in contrast to purified molecular semiconductors[76,77]—do not always fulfill the necessary requirement that the intrinsic bulk free carrier density is much less than the carrier density injected by the electrodes.[78] Instead, Poole-Frenkel-like currents are sometimes observed.[37,79] In order to measure SCLC of hole- or electron-only devices, the injection of one type of charge carrier has to be suppressed by large injection barriers.[74,80]

For a field-dependent mobility of the form of Eq. (2.13), Murgatroyd found an

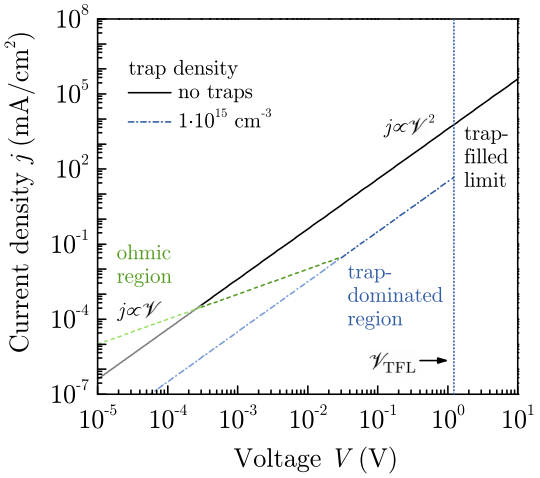

Figure 2.14.: Simulated limits for a j-$\mathscr{V}$ curve with discrete trap states, which considerably decrease the current in the trap-dominated region.

empirical approximation including the field activation parameter γ:[81]

$$j_{\mathrm{SCLC}}^{(\mathrm{PF})} \approx \frac{9}{8}\varepsilon_{\mathrm{r}}\varepsilon_0\mu_0\frac{\mathscr{V}^2}{d^3}\exp\left(0.891\cdot\gamma\sqrt{\mathscr{V}/d}\right). \tag{2.16}$$

When plotting the j-$\mathscr{V}$ characteristics on a double logarithmic scale, the field-dependent mobility in the absence of traps shows a characteristic upward bending of the curve.

Generally, the Mott-Gurney equation (2.15) applies only for the special case of a trap-free semiconductor. However, in the general case there are charge carrier traps which can lead to a substantial reduction of current by several orders of magnitude.[76] If considering an energetically discrete trap level E_{trap} with a trap density N_{t} the j-$\mathscr{V}$ curve can be described by two limiting cases: At low current densities j is dominated by the influence of traps and the current-voltage behavior is formally identical with the trap-free case but with an effective mobility μ_{eff}:

$$j = \frac{9}{8}\varepsilon_{\mathrm{r}}\varepsilon_0\mu_{\mathrm{eff}}\frac{\mathscr{V}^2}{d^3} \tag{2.17}$$

with

$$\mu_{\mathrm{eff}} = \mu\cdot\theta, \tag{2.18}$$

whereas θ depends on the quotient of the density of traps and the total number of molecules[d], $N_{\mathrm{t}}/N_{\mathrm{c}}$, and the trap level E_{trap} (E_{trap} expresses the energy between

[d]Strictly speaking, N_{c} denotes the density of states at the transport level—which can be equated with the density of molecules in organic semiconductors. Based on a bulk density of 1.35 g/cm^3

the trap and the corresponding transport level of the charge carrier):[83]

$$\theta^{-1} = 1 + \frac{N_\mathrm{t}}{N_\mathrm{c}} \exp\left(\frac{E_\mathrm{trap}}{k_\mathrm{B}T}\right). \tag{2.19}$$

With increasing voltage, traps will become filled and free carriers are introduced which cannot be trapped any more. This can be seen in a steep increase in current at the so-called trap-filled limit voltage $\mathscr{V}_\mathrm{TFL} = eN_\mathrm{t}d^2/2\varepsilon_0\varepsilon_r$. Both limiting cases are simulated in Fig. 2.14 for a 100 nm thick layer of DIP with the following parameters: $\mu = 10^{-2}\,\mathrm{cm^2/Vs}$, $\varepsilon_r = 4$, $N_\mathrm{c} = 2 \cdot 10^{21}\,\mathrm{cm^{-3}}$ and $E_\mathrm{trap} = 0.5\,\mathrm{eV}$ with different trap densities N_t as indicated in the legend. The lines represent only the limit of trap-dominated current with $\theta \ll 1$ and the trap-filled limit with $\theta \approx 1$ as well as the transition voltage. A mathematically correct description of the transition region would require numerical simulations as can, e.g., be found in Ref. 84. Additionally, the figure shows the ohmic region at low voltages which is characterized by a current $j \propto \mathscr{V}$. From the simulation it becomes obvious that a proportionality of $j \propto \mathscr{V}^2$ is not sufficient to presume a trap-free SCLC behavior.

However, charge carrier traps with an energetically discrete trap level are rather unusual in disordered systems. Instead, traps are generally found to be distributed in energy and are gradually filled with increasing electric field. This leads to an increase in current which is faster than quadratic up to the point when all traps are filled.[85] Based on an exponential trap distribution, the so-called trap-charge limited current (TCLC) is given by

$$j_\mathrm{TCLC} = N_\mathrm{C}\,\mu\,e \left(\frac{\varepsilon_\mathrm{r}\varepsilon_0\,l}{N_\mathrm{t}e\,(l+1)}\right)^l \left(\frac{2l+1}{l+1}\right)^{l+1} \frac{\mathscr{V}^{l+1}}{d^{2l+1}}, \tag{2.20}$$

with the parameter $l = E_\mathrm{trap}/k_\mathrm{B}T > 1$ derived from the trap distribution.[71,84,86]

From the different characteristic equations for $j(\mathscr{V})$ it becomes obvious that voltage-dependent current measurements can be used to determine the prevailing transport mechanism. However, in addition to the voltage-dependence of the current, the dependence on the thickness provides an alternative possibility for distinction. If the current is injection limited, the electric field between the electrodes is homogeneously distributed and the current density at a certain applied field is independent of the thickness. For trap-free SCLC—be it with or without field dependent mobility—the current at constant applied field scales with d^{-1} as can be deduced from Eq. (2.15) and (2.16). Finally, space-charge limited current with a distribution of traps—measured at constant field—scales with d^{-l} with $l > 1$.[84,86]

(cf. Ref. 82) and a molar mass of 400.47 g/mol, N_c of DIP results in $\approx 2 \cdot 10^{21}\,\mathrm{cm^{-3}}$.

2.2.4. Metal/organic and organic/organic interfaces

Organic electronic devices usually consist of a multiple layer stack of organic films and conducting electrode materials, where the fundamental electronic processes, charge carrier transport as well as injection and extraction of charges take place. Hence, analyzing and controlling the electronic structures of these metal/organic and organic/organic interfaces form the basis of understanding and improving the performance of organic devices.

The work function Φ_{sc} of a semiconductor is defined in the same way as the work function Φ_{m} of a metal: it is the energetic difference between the Fermi level E_{F} and the vacuum level E_{vac} ($\Phi = E_{\mathrm{vac}} - E_{\mathrm{F}}$), even if there are no electrons at the Fermi level. However, electrons fill the energy levels following Fermi-Dirac statistics which legitimates the validity of this concept. The electron affinity of a semiconductor χ_{sc} is defined as the difference between the LUMO and the vacuum level, and the ionization potential $\mathrm{IP}_{\mathrm{sc}}$ is by definition the energy separation between HOMO and vacuum level. Due to polarization effects the values of $\mathrm{IP}_{\mathrm{sc}}$ and χ_{sc} deviate from those of an isolated molecule. For an illustration of the terms used in this context see Fig. 2.15 (a).

Metal/organic interfaces

In the early beginnings of organic electronics, contacts between organic semiconductors and metals were often described by assuming an alignment of both vacuum levels.[87] The assumption of this so-called Mott-Schottky limit was based on the peculiarity of organic solids to be composed of self-contained molecular units with putatively little interaction with a metal. However, it turned out that disregarding physico-chemical phenomena may lead to strong deviations between measurements and their theoretical predictions. That means separately determined values of Fermi level, ionization potential and electron affinity have to be taken with care as any possible interfacial dipoles may change the energetic positions considerably in some cases.[88] Figure 2.15 (b) illustrates the Mott-Schottky case with its two fundamental concepts: a common vacuum level at the interface as well as Fermi level alignment in the bulk resulting in band bending within the space charge layer of the semiconductor. The more general case including a finite vacuum level shift Δ is schematically depicted in Fig. 2.15 (c).[89–91]

This shift in vacuum level has its origin in the formation of an interface dipole, which might result from charge transfer across the interface, the presence of permanent dipoles, image charges, interfacial chemical reaction, and other types of rearrangement of electronic charge.[53,93] It should be noted that even if band bending

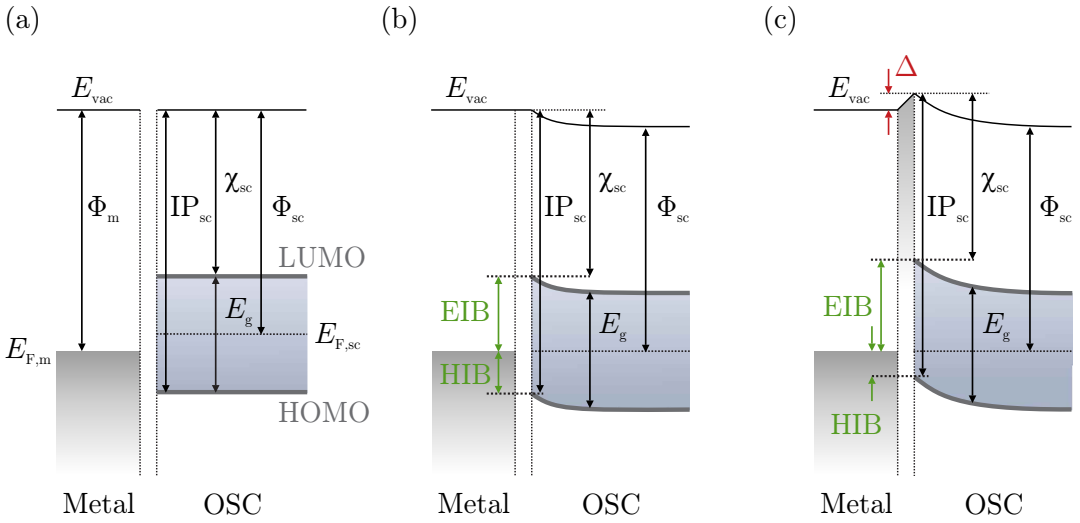

Figure 2.15.: Models for energy level alignment between a metal and an organic semiconductor (OSC). (a) Energy diagram before contact, (b) Mott-Schottky model assuming vacuum level alignment at the interface and band bending with Fermi level alignment and (c) realistic model including vacuum level shift Δ at the interface (E_{vac}: vacuum level, IP_{sc}: ionization potential, χ_{sc}: electron affinity, Φ_m/Φ_{sc}: work function of metal and semiconductor, E_g: HOMO-LUMO bandgap, HIB/EIB: hole/electron injection barrier. Schematic redrawn from Ref. 92).

is considered in this picture and observed in various cases,[94] it does not necessarily take place in undoped organic semiconductors due to the absence of free charges in an intrinsic, wide-gap and purified material.[95]

As consequence of a vacuum level shift the barrier heights have to be modified by the amount of Δ. By definition, a positive value of Δ corresponds to a rise in vacuum level by the deposition of organic material. The hole and electron injection barriers (HIB and EIB) are consequently modified as

$$\text{HIB} = \text{IP} - \Phi_m - \Delta \tag{2.21}$$

$$\text{EIB} = \Phi_m - \chi_{sc} + \Delta = E_g - \text{HIB} \tag{2.22}$$

Neglecting the vacuum level shift at the interface may therefore lead to incorrect predictions of carrier injecting properties within devices with a metal/organic interface.[92,96] This effect can even be very pronounced as Δ can take values of up to 1 eV.[90]

Another phenomenon which may occur at metal/organic interfaces is the so-called "Fermi level pinning".[97] It appears if the Fermi level of the substrate approaches the energy of the LUMO or HOMO level of the semiconductor. In this

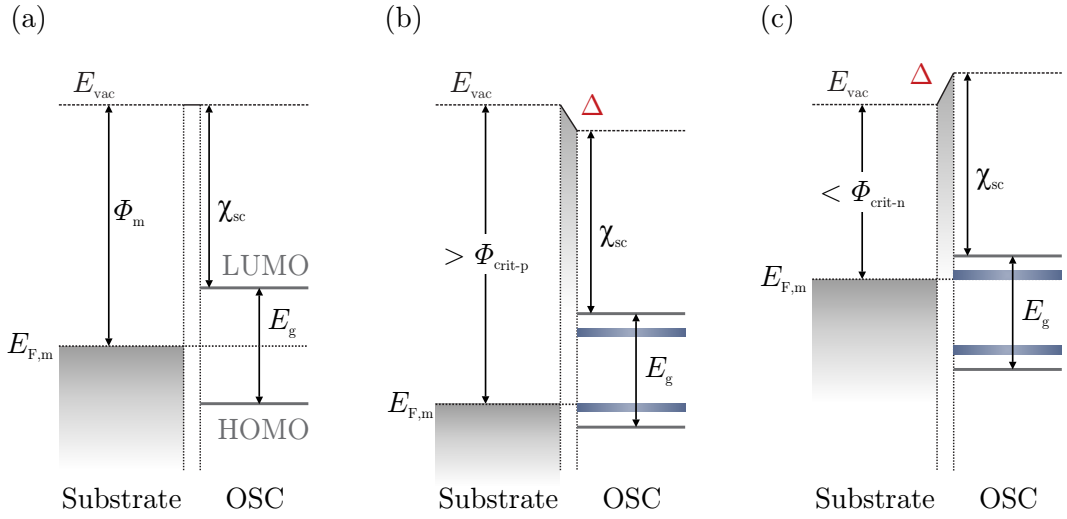

Figure 2.16.: Schematic energy level diagrams visualizing Fermi level pinning at the interface between an organic semiconductor (OSC) and a conducting substrate with (a) vacuum level alignment, (b) positive vacuum level shift and (c) negative vacuum level shift due to molecular charge transfer states or polaron levels (redrawn from Ref. 88).

case charges are transfered across the interface resulting in the formation of an interface dipole Δ. Thus, the Fermi level of the conducting substrate is "pinned" at the energy of charge transfer induced states, which are near the LUMO or HOMO of the semiconductor. Consequently, the Fermi level of the substrate remains within the energy gap of the semiconductor. This means, that in the Fermi level pinning regime, the magnitude of Δ scales linearly with the work function of the substrate.[88] A graphical representation of this phenomenon is depicted in Fig. 2.16: Starting from the initial situation without interfacial dipole (Fig. 2.16 a) an increase of the substrate's work function Φ above a critical value Φ_{crit-p} leads to the formation of positive polarons at the interface, which entails a pinning of the Fermi level at this position—accompanied by an interface dipole Δ (Fig. 2.16 b).[88] The same phenomenon can be observed when the work function of the substrate falls below a critical value Φ_{crit-n}. In that case, negative polarons are formed and Δ changes its sign (Fig. 2.16 c).

Organic/organic interfaces

As will be discussed in the next chapter, strongly bound excitons in OPVCs are usually dissociated at an interface between two organic materials. From this fact it becomes clear, that—besides the metal/organic interface—the electronic structure of organic/organic interfaces plays an equally important role. In a very common

description, the same considerations as for the metal/organic interface regarding a possible vacuum level shift can be applied to the internal organic interfaces. The investigation of a variety of different material combinations showed that, in general, the magnitude of Δ is found to be smaller than in the case of organic/metal interfaces.[53] As a result, vacuum level alignment at organic/organic interfaces was assumed in the majority of cases and interface dipoles were neglected for a long time. However, recently it was found that following the simple Schottky-Mott limit by assuming a common vacuum level may lead to heavily distorted energetic conditions at organic/organic interface.[98,99] The authors report on small but finite interface dipoles observed for a variety of organic heterojunctions. The studies emphasize the importance and inevitability of experimental determination of interface energetics in order to get reliable values for the energy levels—even though the number of pertinent studies is still limited.

2.3. Physics of organic solar cells

The characteristic properties of organic semiconductors, as briefly introduced in chapter 2.2, certainly determine the properties of the device they are applied to. The virtually infinite variety of materials offers the possibility of tailoring the molecules according to the desired electrical and chemical properties.[100,101] Weak inter-molecular forces of organic semiconductors allow for large-scale manufacturing techniques like solvent-based spin-coating and printing techniques or thermal evaporation at relatively low temperature. Since organic molecules and polymers typically exhibit high absorption coefficients almost complete light absorption can be achieved within only a few hundred nanometers,[102] which reduces the material consumption and allows for light-weight and flexible devices accompanied with low-cost fabrication.

The beginning of organic electronics can be traced back to the early 20$^{\text{th}}$ century, when the dark and photo conductivity in benzene derivatives was discovered.[103–105] However, the applicability and thus the research on this topic was very limited for a long time. With the discovery of electroluminescence in molecular crystals in the 1960s[106,107] and the conductivity of doped semiconducting polymers in the 1970s[108,109] the field of organic semiconductors greatly gained importance. It was around the same time that energy conversion utilizing organic semiconductors in photovoltaic cells has been under investigation.[17] After poor success with metal-organic Schottky junctions, a seminal step towards more efficient organic photovoltaic cells was made by Tang in 1986,[110] who laid the foundation for effective exciton-dissociation with the invention of the donor/acceptor heterojunc-

tion concept. Inspired by this promising discovery—these first bilayer solar cells reached efficiencies of around 1 %—organic photovoltaics have been the subject of active research over the past 25 years, and has recently received increased interest by the industrial sector.[111] Nevertheless, some pioneering innovations had been necessary to encourage the breakthrough of organic photovoltaics. These are the donor/acceptor concept and the bulk heterojunction approach, as will be introduced in the following.

2.3.1. The donor/acceptor concept

In inorganic solar cells, photons with energy exceeding the band gap of the semiconductor are absorbed and are directly present as free electron-hole pairs. High dielectric constants and efficient carrier screening lead to low exciton binding energies as was demonstrated in Sec. 2.2.2. Thus, thermal energy at room temperature is sufficient to dissociate the exciton into a free electron-hole pair which is spatially separated by the pn-junction. By contrast, the working mechanism of organic semiconductors is markedly different, most importantly due to the excitonic nature of photo-excitations in organic semiconductors (see Sec. 2.2.2). Application as photovoltaic materials thus requires strategies for an efficient dissociation of excitons. In this context, the introduction of a second organic semiconductor layer has proven extremely successful.[110] To enable photo-induced charge transfer between both partners appropriate energy level alignment has to be fulfilled, with one material acting as electron-donor (D) and the other as electron-acceptor (A). For an efficient exciton dissociation it has to be energetically favorable for the electron to be transfered to the LUMO of the acceptor or for the hole to the HOMO of the donor material, respectively. Figure 2.17 depicts a simple energy level diagram of this situation. It includes the ionization potential IP, which is the energy required to remove an electron from the HOMO to the vacuum level, and the electron affinity χ being the energy released when filling the LUMO with an electron. For this simplified schematic, the donor and acceptor films are stacked on top of each other and sandwiched between two electrodes. This configuration is called *planar heterojunction* with an internal field V_{bi} which is built up by the difference in work function of the anode Φ_{A} and cathode Φ_{C}. Taking into account any vacuum level shifts that may occur at the interfaces (cf. Sec. 2.2.4), the built-in potential results in $e\,V_{\mathrm{bi}} = \Phi_{\mathrm{A}} - \Phi_{\mathrm{C}} + \sum \Delta$.

In order to make dissociation of the strongly bound exciton energetically favorable, the energy gain has to be larger than the exciton binding energy. Thus, an offset of the HOMO and LUMO levels of a few hundred milli-electron Volts is believed to be necessary for efficient charge transfer.[112] Strictly speaking, the exciton

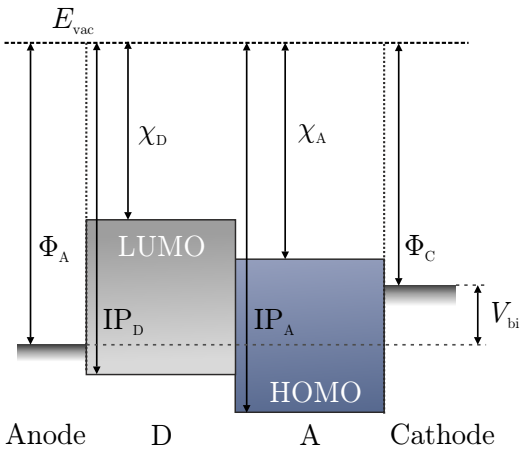

Figure 2.17.: Energy level diagram of an organic heterojunction. IP_D (IP_A) and χ_D (χ_A) denote the ionization potential and the electron affinity of the donor (acceptor) molecular layer, respectively. Φ_A and Φ_C are the work functions of the anode and the cathode and V_{bi} denotes the built-in voltage. For simplicity, possible interface dipoles have not been considered in the schematic.

dissociation is successful as long as the exciton energy is larger than the energy of the electron-hole pair after charge transfer, which is called polaron pair or charge transfer (CT) complex.[113]

During the past years, research on organic solar cells has developed a general picture of the individual steps from light absorption to photocurrent generation, schematically illustrated in Fig. 2.18.[74]

(a) The absorption of a photon with an energy exceeding the band gap of the semiconductor excites an electron to the LUMO of the organic material and creates a Coulombically bound exciton—either in the donor or in the acceptor material.

(b) The created excitons diffuse towards the D/A interface. As Frenkel excitons are electrically neutral, this process is not driven by an electrical field but can be regarded as a random process based on concentration gradients.[114]

(c) If an exciton reaches the interface, it can dissociate by charge transfer into an electron on the LUMO of the acceptor and a hole on the HOMO of the donor. In certain material combinations this charge transfer is reported to be extremely fast on the time scale of a few tens of femtoseconds[115] and thus much faster than any competing processes such as photoluminescence.

(d) Even though the exciton is dissociated into an electron residing on the acceptor and a hole on the donor, they are still Coulombically bound[116] and have to be

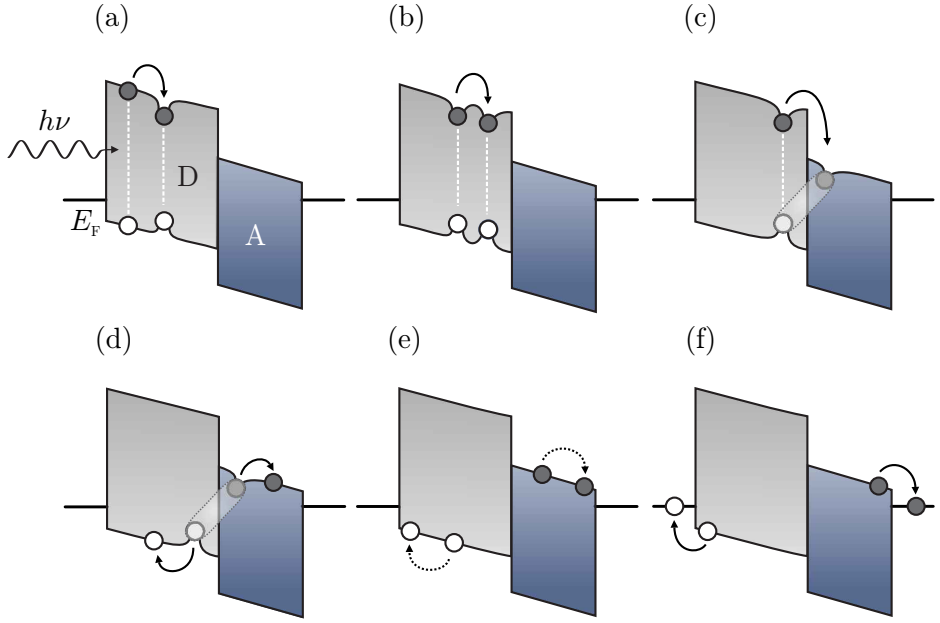

Figure 2.18.: Schematic of individual processes from light absorption to photocurrent generation in a planar heterojunction solar cell by means of a simplified energy diagram, which depicts the HOMO and LUMO levels of donor (D) and acceptor (A) sandwiched between the Fermi levels E_F of the electrodes. (a) Absorption of a photon with energy $h\nu$ in the donor material and subsequent exciton generation. (b) Exciton diffusion towards the D/A interface. (c) Exciton dissociation by electron transfer to the LUMO of the acceptor. (d) Separation of Coulombically-bound electron-hole pair. (e) Charge carrier transport to the electrodes. (f) Charge carrier collection at the contacts.

separated what ultimately leads to free charges.

(e) Once the polaron pair is dissociated, charges can be transported to the respective electrodes—a process which is driven by the internal field.

(f) Following charge carrier transport towards the electrodes, electrons and holes can be extracted by cathode and anode, respectively—finally leading to a photocurrent.

Especially step (c) and (d), i.e., exciton dissociation and charge carrier separation, is not yet fully understood and subject of ongoing research. The formation of an intermediate CT complex seems to be generally accepted but for a detailed description of the procedure one has to consider a manifold of charge-separated states or energy transfer.[114] Section 2.3.2 will provide a closer look into the energetics of the CT complex and its impact on V_{oc}.

The internal quantum efficiency—being a measure of the overall charge genera-

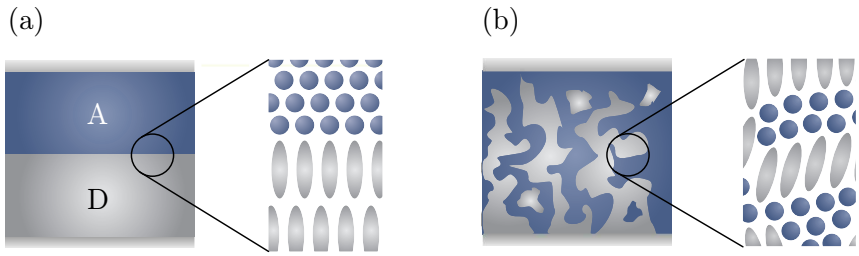

Figure 2.19.: Schematic device configuration of typical organic solar cells: (a) Bilayer device with planar heterojunction (PHJ) and (b) blend layer of donor and acceptor forming a bulk heterojunction (BHJ). The D/A interface of the PHJ is restricted to the two-dimensional area between both materials, while in the BHJ the D/A interface is distributed over the whole volume.

tion process—can be written as a product of the single efficiencies[117]

$$\eta_{\text{int}} = \eta_{\text{Abs}} \cdot \eta_{\text{ED}} \cdot \eta_{\text{CT}} \cdot \eta_{\text{CC}} \tag{2.23}$$

whereas η_{Abs} and η_{ED} denote the absorption and exciton diffusion efficiency, respectively. The exciton dissociation and charge carrier separation, i.e., steps (c) and (d), are merged into a charge-transfer efficiency η_{CT} just as the two final steps, *viz.* charge carrier transport and extraction, which are represented by a charge collection efficiency η_{CC}.

The typically high absorption coefficients of organic semiconductors allow for almost complete light absorption for sufficiently thick organic layers, and thus, high values of η_{Abs}.[102] As mentioned above, suitable D/A interfaces guarantee for charge transfer on comparatively short time scales yielding high charge-transfer efficiencies η_{CT} approaching unity.[4] Provided that charge carrier mobility is sufficiently high, η_{CC} in a two-layered photovoltaic cell can be close to 100 %.[118] However, the main limiting factor is given by η_{ED}. It is determined by the exciton diffusion length L_{D}, being the average distance an exciton can travel before it decays back to its ground state. Values for L_{D} are typically in the range of a few nanometers only for molecular materials.[102,119,120] With typical absorption coefficients of $\alpha \approx 10^5\,\text{cm}^{-1}$,[102] the optical absorption length which is required for absorbing a significant fraction of the incident light can be estimated to be around 100–200 nm. With that typical exciton diffusion lengths lie far below the values for the film thickness, which leads to a large fraction of lost excitons not being able to reach the D/A interface in a planar heterojunction solar cell (PHJ, see Fig. 2.19 (a)). To overcome this exciton diffusion bottleneck, the donor and acceptor materials can be mixed together to enlarge the D/A interface and to minimize the distance an exciton has to travel to be dissociated. As the dissociating interface is extended over the entire bulk of the

blend, this concept is called *bulk heterojunction* (BHJ, schematically depicted in Fig. 2.19 (b)). Since this strategy has been first demonstrated by Hiramoto *et al.* for a blend of a metal-free phthalocyanine as donor and a perylene derivative as acceptor material,[121] it was successfully adopted to a multitude of other material combinations.[102,122–127]

The BHJ concept was also applied to polymeric solar cells which benefit from an interpenetrating network formed from phase-segregated polymer:polymer[122] or polymer:small molecule[123] blends. Similar to mixtures of molecular materials, the bicontinuous network of polymers provides spatially distributed interfaces enabling efficient photogeneration of charges. For solution processed solar cells, the invention of the BHJ concept presents a further benefit: For fabricating a planar heterojunction, it has to be ensured that the second layer does not dissolve and remove the first one. Deposition of both donor and acceptor at once solves this problem and facilitates the fabrication techniques.

While exciton dissociation can be strongly improved by mixing donor and acceptor, continuous percolation paths—i.e. continuous paths of the same material to the respective electrode—should be available inside the blend. Only by this, successful charge carrier extraction can be warranted. Thus, controlling the morphology of the bulk heterojunction is one of the key factors for high performing solar cells. Besides these two extreme cases of planar and mixed heterojunction, there are several other possibilities to design the interface between donor and acceptor, as can be seen in Fig. 2.20. Starting from the planar architecture (a) the effective interfacial area can be increased by creating a roughened (b) or an interdigitated interface (c). The BHJ architecture can vary from homogeneous molecular mixtures (d), phase-separated systems (e) or films with compositional gradient (f). A further improvement can sometimes be achieved by the use of a planar-mixed heterojunction (PM-HJ) concept (g), which can be considered as a combination of a strictly planar heterojunction and a mixed-layer bulk heterojunction within the

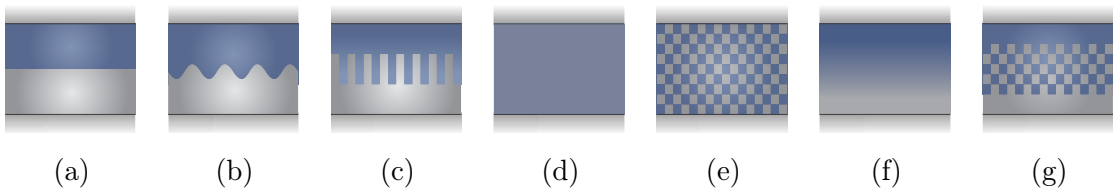

Figure 2.20.: Different architectures for solar cells. (a) Planar heterojunction (PHJ). (b) D/A heterojunction with rough interface. (c) Interdigitated D/A interface. (d) Bulk heterojunction (BHJ) with molecular mixture. (e) Phase-separated BHJ. (f) Gradient heterojunction. (g) Planar mixed heterojunction (PM-HJ).

same structure and is known to unify the benefits of both concepts.[125] Thus, it takes maximum advantage of the unhindered charge carrier collection properties of neat organic layers, and the improved exciton dissociation properties of mixed films.

2.3.2. Role of charge transfer state on the open-circuit voltage

As already introduced in the previous section, charge transfer complexes are bound electron-hole pairs at the donor/acceptor heterointerface (see Fig. 2.21 (a)). The CT state acts as intermediate between an initial exciton state and the final charge-separated state, where the hole in the donor and the electron in the acceptor are independent of one another. There is an ongoing discussion about the precise microscopic nature of the CT state (whether it is localized or delocalized) and the question if it is Coulombically bound or not.[114,128] Among the points for discussion there is, for example, the debate about the height of the binding energies of excitons and charge transfer states, E_B^{exc} and E_B^{CT}, respectively (see Fig. 2.21 (a)). The exciton binding energy is typically defined as the potential energy difference between the two dissociated charge carriers inside the same material (transport gap ${E_t}^e$) and the exciton (optical gap E_g).[116] There are several investigations about the magnitude of E_B^{exc}, which is found to be in a wide interval ranging from less than 0.1 eV to more than 1 eV.[130–134] Due to the increased distance of electron and hole, when going from the exciton to the charge transfer state, E_B^{CT} is expected to be lower than the exciton binding energy with typical values in the range of 0.1 eV to 0.5 eV.[19,74,135–137]

In any case, it is indisputable that these CT states play an important role for the photovoltaic performance: In its role as precursor state to free charge carriers, CT formation and the efficiency of its dissociation strongly determine the short-circuit current while the energy of the charge transfer state ultimately sets the maximum achievable open-circuit voltage. In the following, a short introduction is given on the relation between maximum open-circuit voltage and CT state energy. A detailed review on the role of the charge transfer state in organic solar cells can, e.g., be found in Refs. 116, 128 and 138.

[e] The transport gap is defined as the distance between HOMO and LUMO edges[129] as the motion of single charge carriers takes place in the π and π^* orbitals.

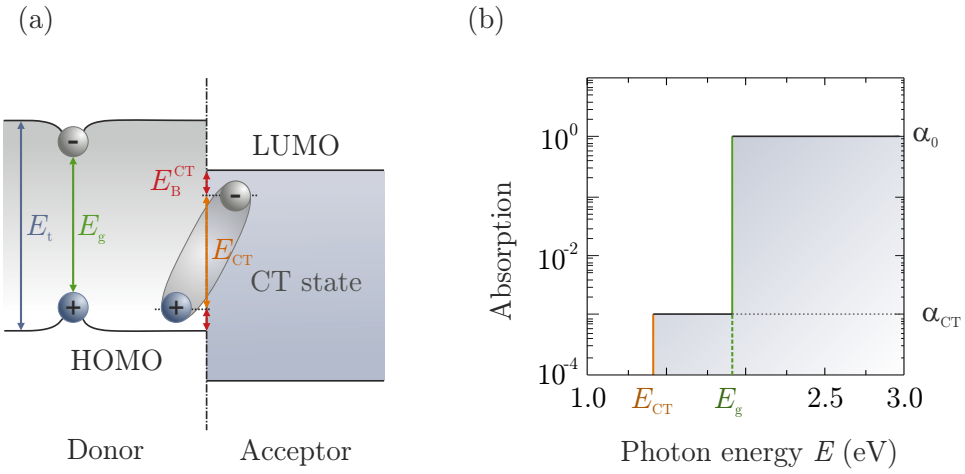

Figure 2.21.: (a) Schematic illustration of the formation of a charge transfer (CT) state with energy E_{CT} including binding energies for the exciton $E_B^{exc} = E_t - E_g$ and CT state E_B^{CT}. (b) Step-like absorption in a D/A heterojunction solar cell. In addition to the absorption α_0 of photons with energy exceeding the optical energy gap E_g, absorption from the CT state α_{CT} already takes place for photon energies above E_{CT}.

Upper limit of the open-circuit voltage

Initial studies on the origin of V_{oc} assigned its magnitude to the difference in the work function of anode and cathode.[139,140] However, this first theory was only approved for non-ohmic contacts[141] and thereupon replaced by an alternative approach: For polymeric solar cells it has been shown convincingly that there is a direct relation between V_{oc} and the energy-level offset at the D/A heterojunction, i.e., in first order approximation the difference between the HOMO level of the donor and the LUMO level of the acceptor.[4,142] If the binding energy of the CT state is considered, V_{oc} is related to the energy of the intermolecular CT state resulting from exciton dissociation. A quantitative correlation between V_{oc} and the intermolecular HOMO-LUMO gap was empirically identified by Scharber *et al.*, which applies to a variety of material combinations with PCBM as acceptor:[100] $e\,V_{oc} = \left(\left|E_{HOMO}^{donor}\right| - \left|E_{LUMO}^{acceptor}\right|\right) - 0.3\,\text{eV}$, whereas the relevant energies were determined by cyclic voltammetry. A similar equation was proposed by Rand *et al.*, who replaced the empirical factor of 0.3 eV by the Coulomb binding energy of the bound electron-hole geminate pair.[19] Moreover, Veldman *et al.* predict an upper limit for V_{oc} to be approximately 0.6 eV below the lowest optical band gap energy of either donor or acceptor based on empirical results, which attribute ca. 0.5 eV to a loss from E_{CT} to $e\,V_{oc}$ and a minimal driving force of ca. 0.1 eV to effectively populate the CT state.[113] Very recently, Wilke *et al.* explicitly determined the HOMO-LUMO gap by means of ultraviolet and inverse photoemission

spectroscopy for a variety of different donor/acceptor combinations.[98] Compared to calculated HOMO-LUMO gaps from literature values of individual components their studies have the decisive advantage to consider any possible interfacial dipoles at the organic/organic interface, providing reliable values for a certain material combination. The comparison with corresponding solar cell characteristics reveal an almost constant energy loss of 0.5 eV for all material pairs when comparing the experimentally determined HOMO-LUMO gap with V_{oc}. A comprehensive study including a variety of molecular D/A combinations will be shown in Sec. 7.2.1.

These empirical relations already emphasize the significance of the CT state energy with regard to the upper limit of V_{oc}. Apart from empirical observations, an estimate of the fundamental losses during the conversion from radiative to electrical energy can be applied to derive an upper limit for V_{oc}. The basis for these calculations has been framed in 1961 in a seminal work by Shockley and Queisser[143](SQ). Their thermodynamic analysis is basically focused on the principle of detailed balance between a semiconductor with a certain energy gap E_{g} situated at the surface of earth which is in thermal equilibrium with the photon flux from the sun—both assumed as black bodies, though at largely different temperatures. Recently, Vandewal *et al.* demonstrated that the principle of detailed balance also determines the relation between photon detection and emission in organic solar cells.[142] Thus, they showed that electroluminescence and photovoltaic external quantum efficiency spectra are related to each other following the detailed balance approach. Charge generation and recombination in this kind of bulk heterojunction devices is determined by the charge transfer state at the interface between donor and acceptor. The CT state can even be detected in electroluminescence under forward bias[144] and was found to be decisive for an upper limit of V_{oc}, as was already predicted by empirical relations introduced above.

Important theoretical calculations about the subject of detailed balance were recently carried out by Rau *et al.* who could relate the external quantum efficiency of charge generation $\mathrm{EQE_{PV}}$ of a solar cell to its electroluminescence quantum yield $\mathrm{EQE_{EL}}$ caused by recombination of charge carriers according to the following equation:[145]

$$j_0\,\mathrm{EQE_{EL}}(E) = e\,\mathrm{EQE_{PV}}(E)\cdot\Phi_{\mathrm{BB}}(E). \tag{2.24}$$

This means that the generation of free charge carriers $\mathrm{EQE_{PV}}(E)\cdot\Phi_{\mathrm{BB}}(E)$ (with $\Phi_{\mathrm{BB}}(E)$ being the ambient black-body spectrum) is balanced by a recombination flux of free charge carriers if the system is in equilibrium. Herein, j_0 denotes the dark saturation current as already introduced as prefactor in the ideal Shockley diode equation (2.1). A detailed theoretical treatment can be found in Refs. 145 and 146.

Based on this analytical ground, Vandewal *et al.* found that some modifications referring to the electronic structure have to be included when adapting the SQ limit from inorganic homojunction solar cells to organic heterojunction solar cells. Thus, the decisive energetic state for photon emission is not the primary singlet exciton of one material but—instead—the photoexcitation of the CT state has to be considered. Indeed, they found the following expression for the open-circuit voltage[147]

$$V_{\mathrm{oc}} = \frac{k_{\mathrm{B}}T}{e} \ln\left(\frac{j_{\mathrm{sc}}}{j_0} + 1\right), \tag{2.25}$$

whereas j_{sc} and j_0 are assessed by accurate measurements of $\mathrm{EQE_{PV}}$ and $\mathrm{EQE_{EL}}$. As in the original work by Shockley and Queisser, their findings are based on the assumption that under open-circuit condition the injected current which causes the emitted radiation flux must be equal to j_{sc} given by the number of absorbed photons. Here, the injection current is described by the ideal diode equation (2.1). Recently, Gruber *et al.* applied this model to OPVCs based on diindenoperylene and C_{60}.[148] As illustrated in Fig. 2.21 (b), key parameters entering the model are, apart from the optical gap of the absorber material E_{g}, the energy E_{CT} and relative absorption strength α_{CT} of the CT state. The studies show how the solar cell characteristics—especially V_{oc}—are affected by different parameter values.

Concerning the experimental determination, CT states have been observed by photoluminescence,[149–152] where additional peaks could be assigned to radiative CT recombination, or electroluminescence[144,153,154] as result of charge injection.[f] Moreover, the existence of the CT state can be proven by photocurrent generation resulting from its specific absorption[155,156] or photothermal deflection spectroscopy (PDS).[157] In general, CT states are characterized by weak absorption and emission intensities, requiring sensitive spectroscopic techniques. Within this work, PDS was used to assess the energy and absorption coefficient of the CT state of a specific D/A combination as will be subject of Sec. 7.2.2.

Recombination as limiting factor for the open-circuit voltage

In the previous section it was shown that $e\,V_{\mathrm{oc}}$ is ultimately limited by the energy of the charge transfer state E_{CT}, however, with a discrepancy of several 100 meV.[113,156] Following the theoretical calculations by Shockley and Queisser[143] and the reciprocity theorem of Rau *et al.*[3,145] the difference could be assigned to recombination of electrons and holes in the organic semiconductor. While the radiative annihilation of charge carriers determines the efficiency of OLEDs, recombination losses

[f] Note that within some of these references the expression "exciplex" can be identified with CT state.

have been identified as the main factors limiting efficiency of organic solar cells[148] and are subject of current research.

Once a photon has been absorbed within the active layer of a solar cell, the formed exciton has to bypass several recombination possibilities on its way from dissociation into free charge carriers, transport and finally to a successful extraction of charges at the contacts. Those recombination events might either be radiative or non-radiative; both occurring in parallel. While radiative recombination is associated with the release of photons, the energy transfer in a non-radiative recombination event involves the simultaneous release of many phonons (resulting from high exciton binding energies in organic semiconductors, cf. Sec. 2.2.2). This process occurs with a small probability but becomes more likely if intermediate states—often provided by impurities—facilitate the transition by splitting the relaxation into several steps with each of these steps involving a smaller number of phonons.[158] From this it becomes obvious that non-radiative bulk recombination can be reduced by minimizing the number of impurities. However, states inside the gap of the semiconductor cannot be avoided at the interface to the metal contacts because of the homogeneous distribution of states within the metal. To minimize the amount of surface recombination, so-called exciton-blocking layers can be introduced as spacer between semiconductor and metal (see Sec. 3.1.4).

In contrast to non-radiative recombination its radiative counterpart cannot be avoided as long as the semiconductor shall maintain its probability to absorb light. This is based on the principle of detailed balance which states that every microscopic process in a system must be in equilibrium with its inverse process, as long as the system is in thermodynamic equilibrium.[3] Under the assumption of negligible non-radiative recombination and by defining radiative recombination as the only fundamental loss process the detailed balance principle allows to calculate the ultimate efficiency limit of a solar cell.

However, it was found that radiative recombination—to which recombination should be restricted for maximum obtainable V_{oc}[143]—is just a small fraction of the total recombination.[148] Thus, the relation between open-circuit voltage of an excitonic solar cell at finite temperature and its CT energy given in Ref. 159 can be generalized[148] to

$$V_{\mathrm{oc}}(T) = \frac{E_{\mathrm{CT}}}{e} - \Delta V_{\mathrm{OC}}^{\mathrm{rad}}(T) - \Delta V_{\mathrm{OC}}^{\mathrm{non-rad}}(T). \tag{2.26}$$

It was shown by Gruber *et al.* that temperature dependent measurements of V_{oc}—as will be subject of Sec. 7.2.1—can serve to determine E_{CT}. By means of the modified SQ theory an upper limit of V_{oc} for a given D/A combination can be determined. Furthermore, temperature dependent measurements can be applied to

quantify recombination losses and enable the quantitative access to non-radiative and radiative recombination.[148]

Classification of different recombination mechanisms

In the following, some definitions and different mechanisms associated with recombination will be given.

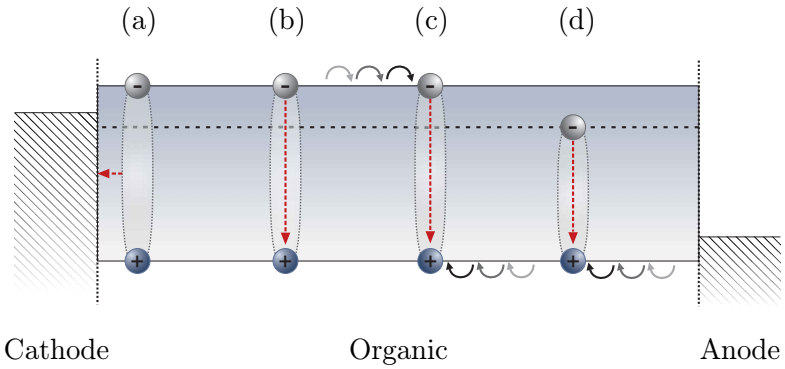

Figure 2.22.: Schematic illustration of different recombination mechanisms inside an organic semiconductor device. (a) Non-radiative surface recombination, (b) monomolecular recombination of a geminate polaron pair, (c) second-order bimolecular recombination of a non-geminate polaron pair (Langevin-type), and (d) first order bimolecular recombination of a free hole with a trapped electron (SRH-type, sometimes also referred to as monomolecular recombination if the order of reaction is crucial for denomination as described in text).

Geminate versus non-geminate recombination As was already introduced above, surface recombination—usually being of non-radiative nature—seems to be unavoidable whenever organic films are in close proximity to adjacent metal contacts (Fig. 2.22 (a)). Apart from the classification into radiative and non-radiative, recombination may be grouped into two categories, namely geminate and non-geminate recombination. If an electron-hole pair has been arisen from the dissociation of one exciton, it is called a "geminate pair", which is still bound by Coulomb interaction (Fig. 2.22 (b)). Thus, the corresponding recombination of a geminate polaron pair which stems from the same precursor state is called geminate recombination. By contrast, recombination of dissociated carriers generated by two different absorption events is known as non-geminate recombination (Fig. 2.22 (c) and (d)). Before two oppositely charged carriers can decay by non-geminate recombination, they have to diffuse to each other as far as their Coulomb capture

radius. This diffusion process usually slows down the recombination kinetics and generally leads to faster processes during geminate recombination as compared to non-geminate recombination. While geminate recombination is reported to occur on a time scale of the order of hundreds of picoseconds up to 100 ns,[160–164] typical time scales for non-geminate recombination are reported to range into the microsecond to millisecond regime.[116,135]

Monomolecular versus bimolecular recombination Geminate and non-geminate recombination are often equated with "monomolecular" and "bimolecular" recombination, respectively. However, these are terms which require precise definition as they are sometimes used differently. In some publications monomolecular and bimolecular are defined in terms of the recombination rate order depending on the incident light intensity I_L.[165] The probability of any recombination event is based on the initial step where electrons and holes have to find each other. Very generally, the recombination rate R can be considered as being proportional to the product of electron density n_e and hole density n_h:

$$R \propto n_\mathrm{e} \cdot n_\mathrm{h}. \tag{2.27}$$

In this case, monomolecular recombination is used as a synonym for any first-order process ($\kappa = 1$, $R_\mathrm{mono} \propto n_\mathrm{e} \cdot n_\mathrm{h}(I_\mathrm{L})$ or $R_\mathrm{mono} \propto n_\mathrm{e}(I_\mathrm{L}) \cdot n_\mathrm{h}$), while bimolecular recombination is equated with a second order reaction ($\kappa = 2$, $R_\mathrm{bi} \propto n_\mathrm{e}(I_\mathrm{L}) \cdot n_\mathrm{h}(I_\mathrm{L})$). Annihilation between two oppositely charged carriers which recombine through a trap state (Shockley-Read-Hall, SRH recombination[166,167]) is called monomolecular, even if both charges originate from different absorption events, i.e., forming a non-geminate pair (see Fig. 2.22 (d)). The reason which makes SRH recombination a first-order process is the observation of a time delay between the capture of the first charge and the second charge. That leads, e.g., to a reservoir of trapped electrons with which mobile holes can recombine and defines a rate constant of $R_\mathrm{SRH} \propto n_\mathrm{e,trap} \cdot n_\mathrm{h}(I_\mathrm{L})$.[165]

In other publications[116,168–170] the terms are defined in a mechanistic (or chemical) sense—independent of the specific rate order. In this case, bimolecular refers to a reaction involving two molecular entities, which makes it synonymous with non-geminate. Accordingly, monomolecular is identified with geminate recombination.[171]

CT state recombination Concerning the recombination of a CT state, it can either be of geminate (monomolecular) or non-geminate (bimolecular) nature.[138] If the CT complex originates from a singlet exciton as result of a photoinduced

excitation either in the donor or acceptor, the decay takes place by a first-order geminate (monomolecular) recombination.[24] In contrast, two free and oppositely charged polarons can recombine via an intermediate CT state. As both charge carriers were generated independently of one another and do not originate from the same geminate pair, the recombination mechanism is of second-order (non-geminate/bimolecular).[172,173] The recombination itself can either occur via direct transition from the CT excited state to the ground state or via charge carrier back transfer to the initial molecule.[128]

Identification of different recombination mechanisms The SRH theory is commonly used to describe recombination dynamics when trapped charges take part in the recombination process. When recombination is independent of trap states, bimolecular recombination dynamics in low-mobility materials are usually described by the Langevin model,[174,175] where the rate limiting step is the diffusion of free carriers towards each other in their mutual Coulomb field.[g] A practical identification of the dominant recombination mechanism can be obtained by the dependence of the short-circuit current density j_{sc} on incident light intensity I_{L}:

$$j_{\mathrm{sc}} \propto (I_{\mathrm{L}})^{\alpha}, \tag{2.28}$$

with the scaling exponent α usually ranging between 0.85 and 1.[176] However, the interpretation of α varies in literature and is subject of recent debates.[177–179] Prior to a critical discussion of that issue, it had been widely supposed that an exponent of $\alpha \approx 0.5$ hints to second-order bimolecular recombination, whereas for first-order processes a linear relation between photocurrent and light intensity ($\alpha = 1$) is expected.[180–183] The argument is based on the following consideration starting with the general continuity equation for electrons

$$\frac{\mathrm{d}n_{\mathrm{e}}}{\mathrm{d}t} = G_0(I_{\mathrm{L}}) - R_{\mathrm{mono}}(I_{\mathrm{L}}) - R_{\mathrm{bi}}(I_{\mathrm{L}}), \tag{2.29}$$

where G_0 denotes the generation rate of bound polaron-pairs which is proportional to the light intensity. As shown above and with the assumption of $n_{\mathrm{e}} = n_{\mathrm{h}}$, the recombination rates can be expressed as

$$R_{\mathrm{mono}}(I_{\mathrm{L}}) = k_{\mathrm{mono}} \cdot n_{\mathrm{e}}(I_{\mathrm{L}}) \tag{2.30}$$

and

$$R_{\mathrm{bi}}(I_{\mathrm{L}}) = k_{\mathrm{bi}} \cdot (n_{\mathrm{e}}(I_{\mathrm{L}}))^2. \tag{2.31}$$

[g] Following the Langevin theory, the general formulation of a second order recombination rate is specified to $R_{\mathrm{Langevin}} = \gamma n_{\mathrm{e}} n_{\mathrm{h}}$ with γ being the Langevin recombination strength $\gamma = \frac{e}{\varepsilon\varepsilon_0}\mu$.

For steady state analysis, i.e. $\frac{\mathrm{d}n_\mathrm{e}}{\mathrm{d}t} = 0$, it follows from Eq. (2.29) that

$$G_0(I_\mathrm{L}) = R_\mathrm{mono}(I_\mathrm{L}) + R_\mathrm{bi}(I_\mathrm{L}). \tag{2.32}$$

At this point the relation to the current is established by assuming a direct proportionality between drift current and density of charges ($j \propto n_\mathrm{e}$).

In the case of pure monomolecular recombination $G_0(I_\mathrm{L}) = k_\mathrm{mono} \cdot n_\mathrm{e}(I_\mathrm{L})$ which means that $n_\mathrm{e}(I_\mathrm{L}) \propto G_0(I_\mathrm{L})$ and, hence, $j \propto I_\mathrm{L}$. This linear dependence of the current on light intensity implies an exponent of $\alpha = 1$. Assuming pure bimolecular recombination the generation rate becomes $G_0(I_\mathrm{L}) = k_\mathrm{bi} \cdot (n_\mathrm{e}(I_\mathrm{L}))^2$ and $n_\mathrm{e}(I_\mathrm{L}) \propto \sqrt{G_0(I_\mathrm{L})}$. It follows that $j \propto \sqrt{I_\mathrm{L}}$, which implies a sublinear behavior with $\alpha = 0.5$.

Reasons leading to $\alpha < 1$ could be space charge effects resulting from mobility differences,[28,184] charge carrier extraction distance[185] or recombination via interfacial states between donor and acceptor or at the interface to the electrode.[177,186] Others report about a transition from first-order recombination at j_sc to bimolecular recombination at V_oc as a result of increasing charge carrier density with increasing voltage.[165] However, it has been shown that a direct proportionality between photocurrent and illumination intensity can be observed despite the losses exclusively being of bimolecular origin,[178,187–189] which limits the usage of steady-state measurements to reliably determine the dominant loss mechanism. Recently, the diode ideality factor has been found to serve as suitable parameter to be interpreted in terms of the prevailing recombination mechanism as will be discussed in Sec. 7.2.4.

Chapter 3

Materials and experimental methods

The following chapter introduces the organic materials which were used in the scope of this thesis. They are presented in the order they appear in the stack of the device, i.e., beginning with different hole injection layers through diverse active semiconductors to exciton blocking layers and organic metals. Afterwards, the techniques of sample preparation are presented. Beside organic solar cells the fabrication of organic light-emitting diodes and organic field-effect transistors is briefly explained as they serve as supplementary devices at certain points. Finally, different experimental methods for device characterization are introduced in short.

3.1. Materials for organic electronic devices

3.1.1. Substrates

All solar cells and light-emitting diodes shown in this thesis are fabricated on commercially available glass substrates covered with approximately 130 nm of indium tin oxide (ITO, purchased first from Merck, Darmstadt (GER) later from Thin Film Devices, Anaheim (CA); sheet resistance in both cases $< 20\,\Omega$/sq.). ITO is a widely used anode in OPVCs and OLEDs as it is at the same time conducting and transparent. Transistors are built on substrates based on highly p-doped silicon (100)-wafers (specific resistance $\rho < 0.1\,\Omega$cm) covered with 320 nm thermally grown oxide.

3.1.2. Hole injection layers

The use of intrinsically conducting polymers as electrode and hole injection layer (HIL) is a common method in the area of optoelectronic devices. The most widely used species of this class is based on aqueous dispersion of poly(3,4-ethylenedioxythiophene)(PEDOT) and poly(styrenesulfonate) (PSS) (PEDOT:PSS, see Fig. 3.1 for chemical structure). Due to its PSS content the pH value lies in the range between 1.5 and 2.5.[190] The essential property of this π-conjugated polymer is good film-forming quality, moderately high conductivity (approximately $10\,\mathrm{S\,cm^{-1}}$), high visible-light transmission, and relatively good stability.[191] Moreover, PEDOT:PSS has a smoothing effect on ITO, whose rough surface would otherwise result in small parallel resistances or even short circuits through the cell.[192] Three different PEDOT:PSS containing formulations were used—differing in their work functions:[193] Clevios$^{\mathrm{TM}}$ P AI4083 (designated as PEDOT, work function $\Phi \approx 5.0$–$5.2\,\mathrm{eV}$,[194] commercially available), Clevios$^{\mathrm{TM}}$ HIL1.3 (designated as HIL1.3, work function $\Phi \approx 5.4$–$5.9\,\mathrm{eV}$,[194] commercially available) and Clevios$^{\mathrm{TM}}$ HIL1.3 N (designated as HIL1.3 N, work function expected to be similar to HIL1.3 but with different pH value, not commercially available) (all obtained from Heraeus Clevios GmbH, Leverkusen, Germany).

Alternatively, the self-doping polymer poly(thiophene-3-[2-(2-methoxyethoxy)-ethoxy]-2,5-diyl) (sulfonated solution sold under the trademark Plexcore$^{\mathrm{TM}}$ OC RG-1200, purchased from Sigma Aldrich, designated as Plexcore in the scope of this thesis) has been used for some comparative studies on hole injection layers. It is characterized by a work function of $\Phi \approx 5.1$–$5.2\,\mathrm{eV}$ and reduced acidity predicting decreased electrode degradation.[195]

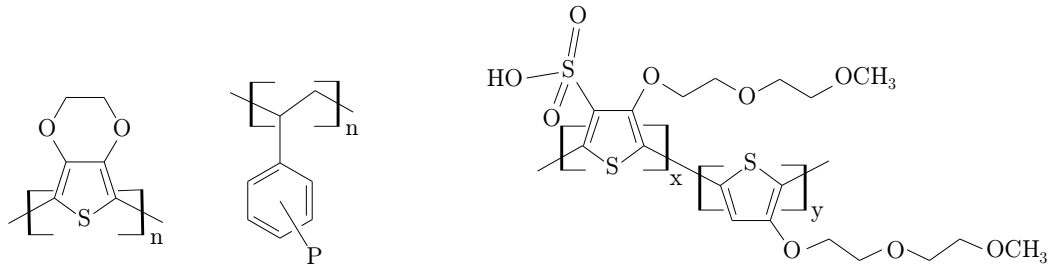

PEDOT PSS Plexcore

Figure 3.1.: Chemical structure of PEDOT:PSS and Plexcore.

3.1.3. Active organic semiconductors

In principle, the almost infinite variety of organic materials enables an unlimited possibility of different material combinations for the application in organic electronic devices. From this multitude only a few molecular species have been selected in the framework of the collaborative project—with the system DIP/C_{60} being the central material combination in the present thesis. All others mainly serve as objects of comparison in terms of morphology as well as structural and energetic aspects. The chosen materials are diindenoperylene (DIP), Buckminster fullerene (C_{60}), sexithiophene (6T), copper-phthalocyanine(CuPc), perfluorinated CuPc (F_{16}CuPc) and pentacene (Pen). From the different molecular shapes of the chosen materials—being spherical such as C_{60}, disk-shaped like CuPc or rod-like as DIP, 6T and Pen—different film growth scenarios are expected. Moreover, the materials cover a wide range of energy levels, as will be shown in chapter 4.

Diindenoperylene

Diindenoperylene (DIP, $C_{32}H_{16}$) is a polycyclic aromatic hydrocarbon consisting of two indeno-groups attached to the central perylene-core (Fig. 3.2 (a)). The molecule has a planar shape with dimensions of approximately 18.4 Å × 7 Å and a molecular weight of 400.48 g/mol.[196] First syntheses of the material date back to the 1930s[197] and even if it was subject of detailed structural[82,198–200] and optical investigations,[201,202] DIP has only recently gained attention as possible active material in organic photovoltaic devices. It has been shown that DIP exhibits almost balanced transport of electrons and holes along the c' direction in single crystals[203] and thin films[204] and remarkably high exciton diffusion lengths of up to 100 nm[205]—although the magnitude of the exciton diffusion length and its unique determination in thin films is still under discussion.[119,120,206] The transition dipole moment of the fundamental molecular absorption is aligned along the long molecular axis.

Structural investigations showed that DIP single crystals appear in two different bulk phases: A triclinic low-temperature phase and a monoclinic high-temperature phase. Both reveal a herringbone-type structure (see Fig. 3.2 (b)) with the phase transition taking place at $T \approx 403\,\mathrm{K}$.[203,207] For the present studies the growth behavior in thin films is of more significance. It is determined by the interplay between molecule/substrate and molecule/molecule interaction potentials.[208] With SiO_2 as substrate DIP forms polycrystalline films consisting predominantly of the high-temperature phase, however, there are two common orientations with respect to the substrate: At high substrate temperature molecules are oriented almost upright with their long axis tilted by an angle of $\varphi \approx 17\,^\circ$ to the surface normal

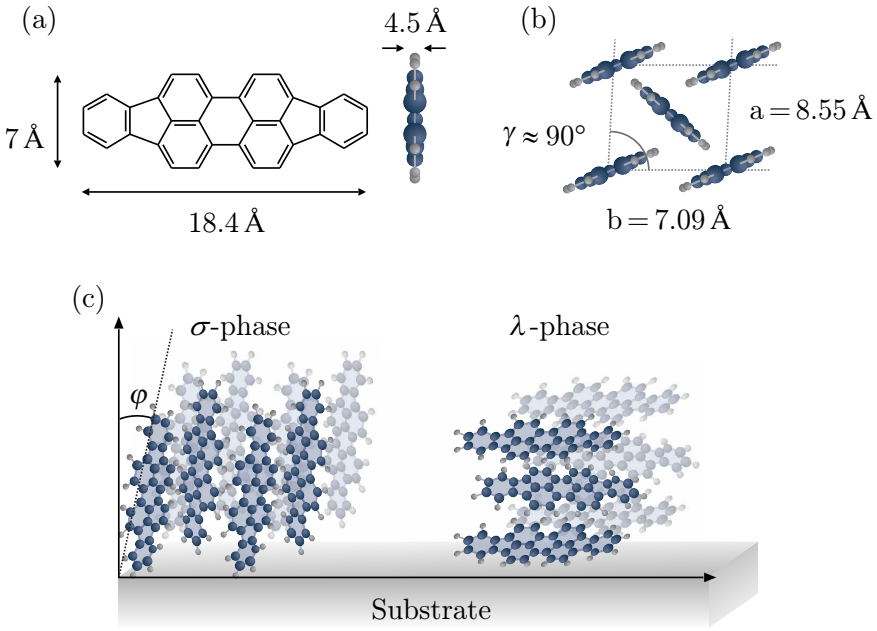

Figure 3.2.: (a) Structure and dimensions of the DIP molecule. (b) Two-dimensional projection of a possible arrangement of DIP high-temperature phase in a DIP unit cell (herringbone-structure). (c) Growth scenarios of DIP thin films in σ- and λ-orientation (both belong to the high-temperature phase) on silicon oxide. The σ-phase is characterized by almost upright standing molecules with an angle of $\varphi \approx 17\,^{\circ}$ to the surface normal. In contrast, the λ-phase describes molecules oriented nearly parallel to the substrate.[82]

(denoted as σ-phase, see left part of Fig. 3.2 (c)).[82,198] At lower substrate temperatures or on metal substrates the high-temperature phase remains stabilized, but molecules are found to be oriented nearly parallel to the substrate (denoted as λ-phase[h], see right part of Fig. 3.2 (c)).[82,209] The different molecular orientations markedly affect the ionization potential of DIP films, which is found to be 0.4 eV lower for the λ-phase as compared to the σ-phase.[210,211]

The structure and morphology of DIP grown on substrates which are relevant for device fabrication were investigated under the effect of different substrate temperatures and are presented in Sec. 5.1. It was further shown that DIP exhibits exceptionally high structural order in evaporated thin films,[82,198] which, in turn, confirms the large exciton diffusion length as there is a correlation between structural coherence length and exciton diffusion length.[212] Concerning its application as donor in organic solar cells, the main advantage of DIP can be found in its high

[h]It is conventional to designate σ- and λ-structures as "phase", even though they both belong to the high-temperature phase and are only differently oriented on the substrate. A less misleading designation would be σ- and λ-orientation.

ionization potential and the favorable energy level alignment with the acceptor C_{60} from which high open-circuit voltages are expected. Recently, DIP was also successfully employed as molecular acceptor material in organic solar cells combined with the thiophene derivatives poly(3-hexylthiophene) and α-sexithiophene.[213] DIP was purchased from two different suppliers (S. Hirschmann, Univ. Stuttgart, Germany and W. Schmidt, Institut für PAH Forschung, Germany) and purified twice by gradient sublimation.

Buckminsterfullerene

After preliminary theoretical predictions of its existence Buckminsterfullerene (C_{60}) was finally synthesized in 1985.[214] The spherical molecules with diameter of 7.1 Å[215] (see Fig. 3.3) were found to crystallize in face-centered cubic (fcc) arrangement.[216] At room temperature, C_{60} molecules undergo an uncorrelated rotation around their crystal sites which freezes at temperatures below 90 K.[217]

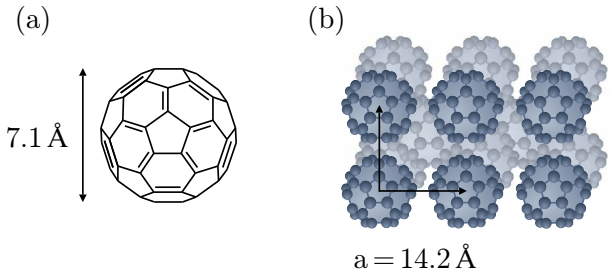

Figure 3.3.: (a) Structure of the C_{60} molecule and (b) fcc packing of C_{60} (after Ref. 218).

Concerning its application in organic solar cells, the low lying LUMO of C_{60} provides sufficient driving force for successful exciton dissociation in combination with a variety of donor materials. Charge transfer to various conjugated polymers has been reported to be ultrafast, i.e. on the order of tens of femtoseconds[115] and high electron mobilities exceeding 1 $cm^2/V\,s$ were found in field-effect transistors.[219] Moreover, it is assumed that the isotropic nature of the fullerene positively affects the orientation factor in exciton diffusion and charge transfer. The large delocalized π-electron system results in a comparatively high dielectric constant of $\varepsilon = 4.4 \pm 0.2$[43,220–222] which, in turn, stabilizes the charge transfer state formed upon exciton dissociation.[223] All these energetic, structural and electronic properties contribute to the success of the fullerene and its derivatives as acceptor material. For the application in this work, C_{60} was purchased from Creaphys, Germany, purified twice by gradient sublimation.

Copper-phthalocyanine

Phthalocyanines are a class of macrocyclic compounds with an alternating nitrogen-carbon ring structure. The central metal ion can be replaced in a broad range (e.g. Fe, Zn, Pb or Cu), which allows for a certain degree of tunability. Copper-phthalocyanine (CuPc, $C_{32}H_{16}CuN_8$), or—to be precise—protonated copper-phthalocyanine (H_{16}CuPc, see Fig. 3.4 (a)) is a blue dye with many applications in color industry, such as paper, plastics or textile dyeing. For several years it has been a rather popular organic semiconductor[224,225] for the use as donor in organic solar cells[226,227] as interlayer in OLEDs[228] or for ambipolar charge transport in OFETs.[229–231] Thin films of CuPc mainly appear in two different kinds of polymorphs, the α and β-phase, even though many more can be found apart from thin films.[232]

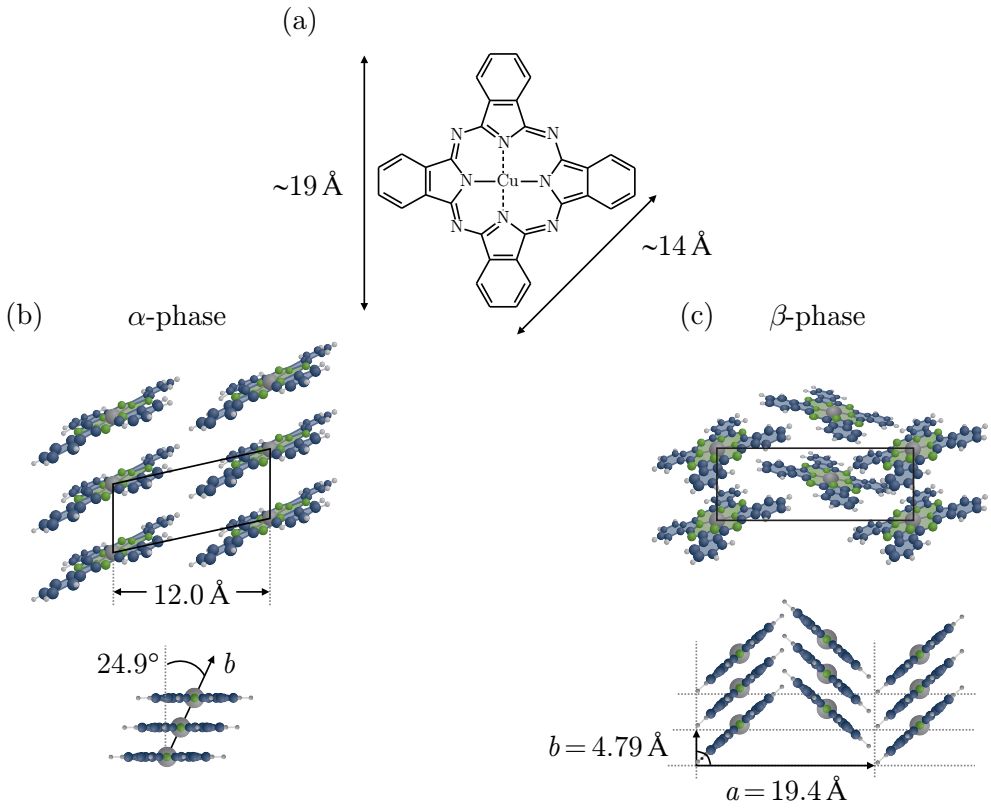

Figure 3.4.: (a) Structure and dimensions of the CuPc molecule.[233] Crystal packing of two different polymorphs of CuPc: (b) Triclinic α-phase showing parallel stacks with one molecule per unit cell.[234] (c) Monoclinic β-phase exhibiting a herringbone arrangement[235]—the lower part shows the diagrammatic projection visualizing the relative orientation of the phthalocyanine molecules.[236]

For a long time it has been assumed that α-CuPc would crystallize—according to many other phthalocyanines—in a herringbone structure.[237] However, it was shown that CuPc α-phase has a triclinic structure with one molecule per unit cell (see Fig. 3.4 (b)).[234] On most substrates CuPc molecules in the α-phase stand almost upright with a lattice spacing perpendicular to the substrate of $d_\perp = 12.0$ Å. While the α-phase is predominant at room temperature, β-phase[236] is found for high temperature growth or post-annealed films.[238] It exhibits a herringbone structure as visualized in Fig. 3.4 (c).

For CuPc it was found that the ionization potential of standing and lying CuPc phases differ by a value of 0.40 eV.[239] The energetic position of the HOMO level of CuPc grown on PEDOT was recently determined by Wilke *et al.*; they propose a growth scenario according to which the first monolayer of CuPc molecules at the direct interface to PEDOT lies flat on the substrate. With increasing film thickness (≈ 10 nm) the orientation of the molecules changes to standing with an ionization potential of 4.8 eV.[240]

CuPc has been purchased from Sigma Aldrich as sublimation grade and was additionally purified once by gradient sublimation.

Perfluorinated copper-phthalocyanine

Perfluorinated copper-phtalocyanine (F_{16}CuPc, also known as hexadecafluoro-copper-phthalocyanine) is the fluorinated counterpart of CuPc with the hydrogen atoms being completely substituted by fluorine (see Fig. 3.5(a)). According to the current status thin films of F_{16}CuPc appear in two different polymorphs—depending on the film thickness. When grown on SiO_2 the first monolayers appear as β_{bilayer}-structure with upright standing molecules stacked in columns (see Fig. 3.5(b)) and a corresponding out-of-plane lattice spacing of $d_\perp = 14.1$ Å.[241] The β_{bilayer}-phase is similar to the α-phase of H_{16}CuPc. Thicker films consist of the β-phase with a herringbone arrangement (see Fig. 3.5(c)) and an out-of-plane lattice spacing of $d_\perp = 14.3$–14.9 Å.[242] Moreover, the thickness-dependent polymorphism is accompanied by a change in morphology and optical properties.[243,244] F_{16}CuPc was purchased from Sigma Aldrich and purified twice by gradient sublimation.

Pentacene

Pentacene (Pen, $C_{22}H_{14}$) is a planar rod-shaped molecule consisting of five benzene rings (see Fig. 3.6 (a)). In contrast to DIP it is a well-known substance for application in organic devices[31] and has been studied intensely due to its relevance for OFETs.[245] It crystallizes in a herringbone structure and shows a remark-

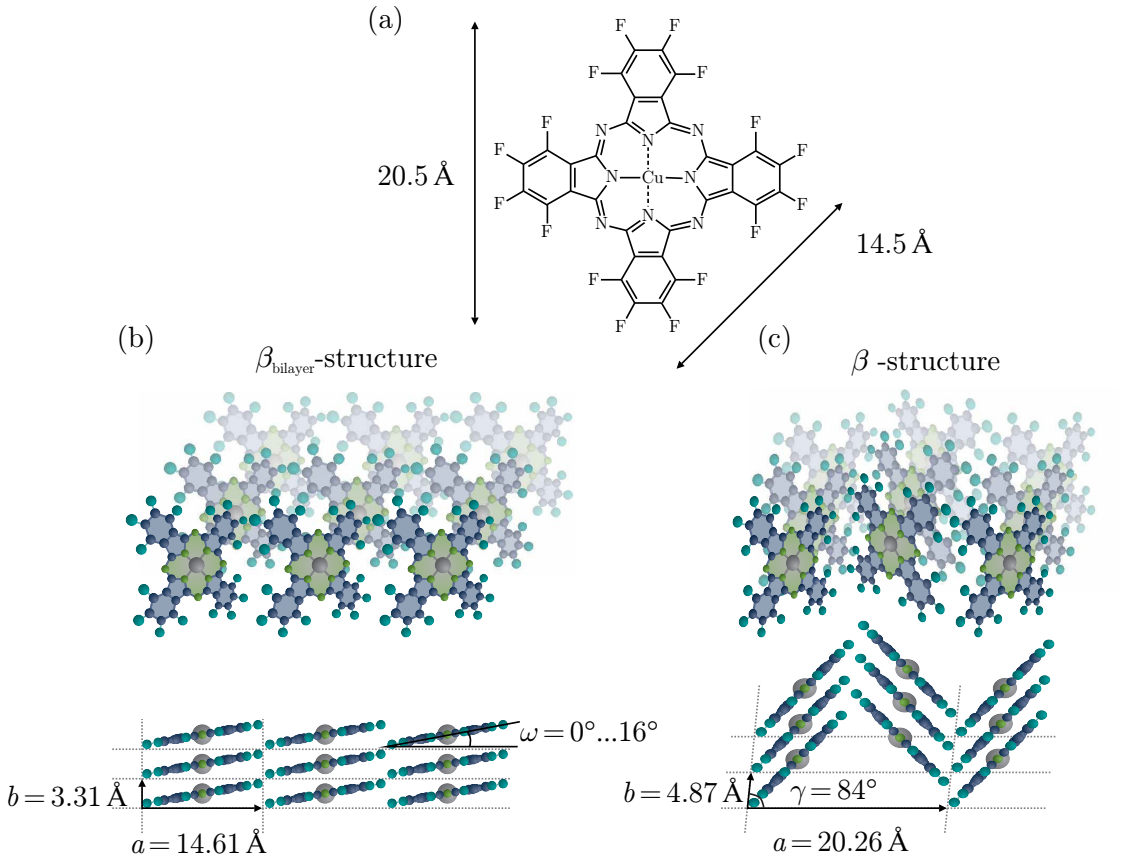

Figure 3.5.: (a) Structure and dimensions of the $F_{16}CuPc$ molecule. (b) Crystal packing of two different polymorphs of $F_{16}CuPc$: (b) β_{bilayer}-phase showing parallel stacks with one molecule per unit cell and (c) β-phase exhibiting a herringbone arrangement with two molecules per unit cell—the lower parts show the schematic top view visualizing the relative orientation of the phthalocyanine molecules.[241]

able appearance of two structures—namely a "thin-film" and a "bulk structure"—coexisting above a certain thickness.[246,247] In contrast to DIP the transition dipole moment of the HOMO-LUMO is oriented along the short axis of the molecule.[202] Pen was purchased from Sigma Aldrich and used without further purification.

α-sexithiophene

α-sexithiophene (α-6T, $C_{24}H_{14}S_6$, Fig. 3.6 (c)) has been intensively studied both as representative for fundamental properties of π-conjugated semiconductors[248–250] as well as for its specific application in electronic devices.[213,251] The planar molecules crystallize in a herringbone structure (see Fig. 3.6 (d)) with four molecules per unit cell. Similar to the high-temperature phase of DIP, 6T molecules are found to

appear in two different orientations—either lying flat or standing upright on the substrate—depending on deposition rate, substrate temperature and film thickness.[252] A coexistence of molecules standing upright on their long molecular axis and molecules lying flat on the substrate was found in ultra-thin films grown on SiO_2.[253] In thicker films (larger than one monolayer) all α-6T molecules stand perpendicularly on the substrate. The material was purchased from Sigma Aldrich and purified twice by temperature gradient sublimation.

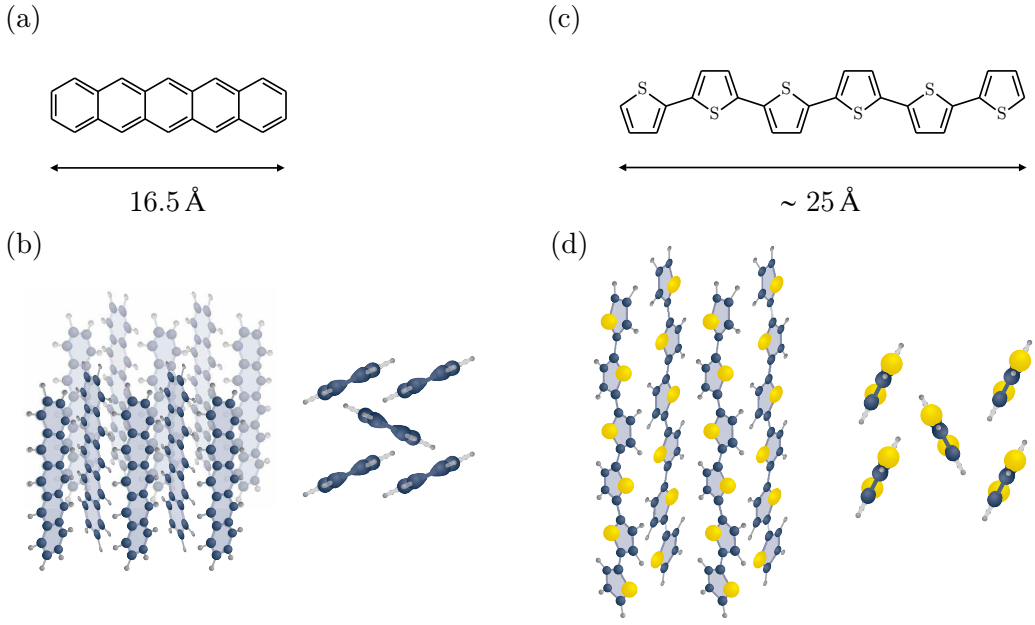

Figure 3.6.: Structure and dimension of (a) Pentacene and (c) α-sexithiophene. (b) Sketch of the herringbone structure of the "thin film"-phase of Pen—the right part shows the schematic top view visualizing the relative orientation of the Pen molecules.[254,255] (d) Schematic of the herringbone structure formed by α-6T.[252]

3.1.4. Exciton blocking layers

In order to avoid electrical losses inside an organic solar cell caused by the interface between acceptor and the adjacent metallic cathode, the following requirements on the interface have to be met: For an unhindered charge carrier flow, dissociated electrons have to be extracted by the cathode without energetic barrier. On the other hand, it was shown in Sec. 2.3.2 that non-radiative recombination of charge carriers at the aluminum interface has to be avoided—as parasitic exciton quenching near a metal surface represents a well-known loss mechanism.[256] An established approach to address these requirements on the acceptor/cathode interface is the

insertion of an exciton blocking layer (EBL). The beneficial effect of this interlayer on solar cell performance has been demonstrated by various studies, all describing its property to prohibit quenching of excitons at the electrode and to act as diffusion barrier for Aluminum (Al) and as a protection layer to eliminate the creation of Al-induced defect states in C_{60}.[257–260] A detailed study on this topic will be shown in Sec. 8.

Bathocuproine

The most common exciton blocking material in OPVCs is Bathocuproin (2,9-dimethyl-4,7-diphenyl-1,10-phenanthroline (BCP), see Fig. 3.7 (a)). It satisfies the requirements to efficiently prevent exciton quenching at the metallic cathode as it features a large bandgap of $E_g = 4.7\,\text{eV}$.[95] When used in OPVCs based on C_{60} as acceptor, the bandgap of BCP is considerably larger than E_g of the adjacent C_{60}, which hinders exciton transfer to the BCP layer. At the same time, the huge bandgap makes the material transparent across the solar spectrum and thus, BCP serves the purpose of a spacer between photoactive region and metallic cathode. While the offset energy between the LUMO levels of C_{60} and BCP is a decisive factor of the exciton blocking effect of BCP, unhindered electron transport to the cathode has to be guaranteed preferably without any increase in series resistance. From thickness-dependent measurements it was found that electron transport through BCP mainly occurs via defect states below the LUMO of BCP, which are induced by evaporating the metal top contact and which enable electron transport from C_{60} to the cathode (see schematic picture in Fig. 3.7,(b)). BCP was purchased from Sigma Aldrich as sublimed grade and used without further purification.[192, 261]

Naphthalene-tetracarboxylic-dianhydride

Apart from the well-known and widely used BCP, NTCDA (napthalene-tetracarboxylic-dianhydride, see Fig. 3.7 (a)) was studied as exciton blocking material. From literature it is stated that NTCDA can be used as extremely thick EBL (with thicknesses between 600 nm and 2 µm) without degrading the cell performance.[264–266] Utilizing thicker films would bring the advantage of a successful protection against metal diffusion. In contrast to the electron transport via damage-induced defect states as found in BCP, electron transport in NTCDA is supposed to occur in the absence of damage as its LUMO of ca. 4.0 eV[263] is approximately aligned with that of C_{60}.[262] A schematic picture of the different transport mechanisms as supposed by Lassiter *et al.* is shown in Fig. 3.7 (b) and (c).

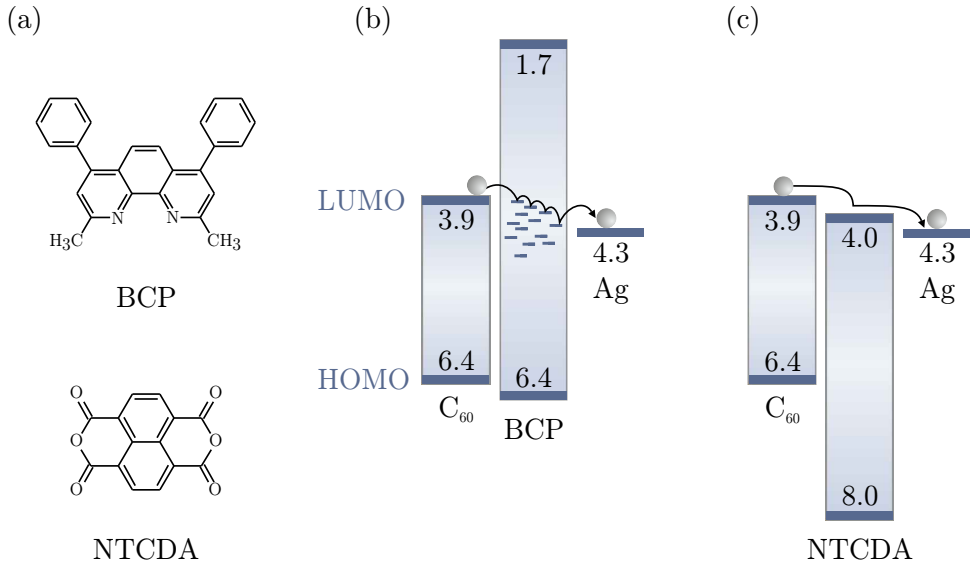

Figure 3.7.: (a) Chemical structures of the exciton blocking layers BCP and NTCDA. Electron transport mechanism (b) via damage-induced defect states in BCP and (c) through the LUMO level as found in NTCDA (after Ref. 262). HOMO and LUMO positions of BCP and NTCDA are taken from Refs. 95 and 263, respectively. The HOMO level of C_{60} is taken from UPS measurements as will be shown in Sec. 7.1.1, while the LUMO is calculated with a transport gap of 2.50 eV.[98]

Lithium-fluoride

As alternative to BCP or NTCDA, small amounts of lithium-fluoride (LiF) can be incorporated between photoactive layer and aluminum cathode. Photoelectron spectroscopy studies showed that the work function of the metal surface can be considerably reduced by the deposition of LiF.[267] From OLEDs it is known that the insertion of LiF directly below the cathode leads to lower turn-on voltages and higher efficiencies which were attributed to a reduction of the interface barrier for electron injection.[268–272] An overview of the proposed mechanisms to explain enhanced electron injection when applying LiF/Al cathode in OLEDs can be found in Ref. 273. Brabec *et al.* could show that this strategy leads to an enhancement of both FF and V_{oc} in OPVCs,[274] most likely due to a dipole formation induced by LiF leading to charge transfer across the interface. The strong interfacial dipole results from a comparable strong intrinsic molecular dipole moment of LiF.[275] However, the exact role of this buffer layer is still under discussion.[276] Besides its property to lower the electron injection barrier, LiF is known to improve device stability and lifetime. It was found that a thin LiF buffer layer below the Al electrode considerably suppresses oxygen penetration into the underlying photoactive layer which ensures improved environmental stability.[277,278] Because of its insulating proper-

ties, LiF can only be inserted as very thin layer—with thicknesses of approximately 5 Å—which does not completely cover the surface and thus, limits its protective role against oxygen and moisture.[279]

3.1.5. Top contact materials

For the metallic top contacts of the solar cells and OFETs either Al ($\Phi_{Al} \approx 4.3\,eV$[4]), Calcium (Ca, $\Phi_{Ca} \approx 2.9\,eV$[280]) or Samarium (Sm, $\Phi_{Sm} \approx 2.7\,eV$[281]) is used. Ca and Sm are highly reactive metals and have to be protected against early oxidation by an Al capping layer.

To realize unipolar hole transport, top contacts of TTF-TCNQ (Tetracyanoquinodimethane-tetrathiafulvalene, see Fig. 3.8) are used. TTF-TCNQ is an organic metal with highly conducting properties and belongs to the class of molecular charge-transfer salts. They consist of an electron donor and acceptor whose electrostatic attraction is responsible for the cohesion of the molecular complex.[282] The work function of TTF-TCNQ is estimated to be between 4.6 and 4.8 eV[283] and, thus, comparable to the value for gold (Au, $\Phi_{Au} \approx 5.0\,eV$[284]). However, it was found in OFETs based on a variety of organic semiconductors that Au allows both for electron and hole injection while the use of TTF-TCNQ prevents electron injection and enables unipolar hole transport.[285] This fact can be attributed to different interfacial behavior as the diffusion of evaporated Au atoms might lead to damages inside the organic layer and thus to modified energy level alignment. In contrast, TTF-TCNQ is deposited by thermal evaporation at comparably low evaporation temperatures between 50 and 100 °C. This leads to a damage-free interface to the adjacent organic film, and prevention of interdiffusion and undesirable interface dipole formation.[231]

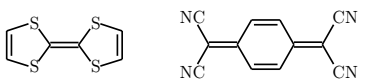

TTF TCNQ

Figure 3.8.: Chemical structure of TTF and TCNQ.

3.2. Sample preparation

3.2.1. Fabrication of solar cells and light-emitting diodes

The following section explains the basic steps for the fabrication of small molecule OPVCs and OLEDs as illustrated in Fig. 3.9. Device configuration and fabrication of both types of devices do not differ from each other in their essential features, which makes a common explanation reasonable.

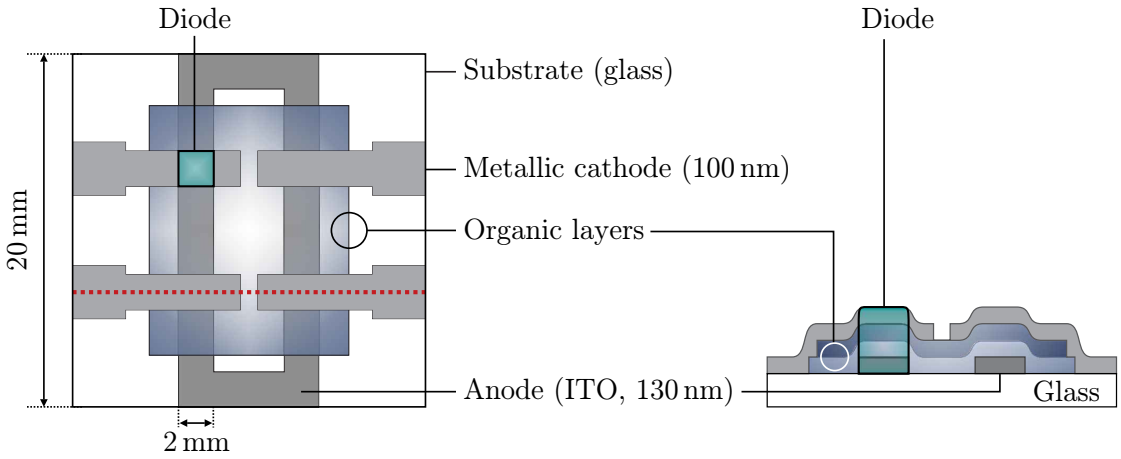

Figure 3.9.: Schematic illustration of the OPVC and OLED device geometry. The left picture shows the top view of the configuration: four diodes are located on one substrate with an active area of $2 \times 2\,\mathrm{mm}^2$ respectively. The red dotted line marks the position of the cross section depicted on the right hand side. The active organic semiconductors are either deposited on top of each other for a layered structure or simultaneously to obtain mixed films.

Anode preparation

All solar cells are fabricated on glass substrates covered with ITO. The device area is defined by the overlap of anode and cathode, which results in four diodes each with an area of $A = 2 \times 2\,\mathrm{mm}^2$. For that purpose the ITO layer is patterned in a photolithography process in cleanroom atmosphere: Cleaned substrates are covered with photoresist by spin coating. After drying, the substrates are exposed to UV light through shadow masks and the photoresist is subsequently developed. Uncovered parts of ITO are then removed by an etching process in hydrochloric acid and the remaining photoresist is lifted off with acetone. Prior to further

processing, substrates are subsequently cleaned in ultra sonic bath with acetone and isopropanol and blown dry with nitrogen.

Deposition of hole injection layer

For improved energetic alignment between the anode work function and the HOMO of the adjacent organic film, an approximately 30 nm thick layer of HIL is spin cast onto the ITO and dried on a hot plate under clean room atmosphere. Besides its role to adjust the energy levels to the organic layer, the HIL smoothens the ITO surface and thus prevents electrical shorts between both electrodes. In order to remove any residues and to improve the wettability for the aqueous suspension of the polymer, UV/Ozone or an oxygen plasma treatment is implemented prior to spin coating.[286] After the drying process samples are transferred from cleanroom to a nitrogen filled glovebox.

Thermal evaporation of organic semiconductors

For deposition of the active organic semiconductors the substrates are transferred to an evaporation chamber with a base pressure of typically 1–3 $\times$ 10^{-7} mbar. A vacuum transfer system enables the samples to be transferred without air exposure. Figure 3.10 shows a schematic sketch of an evaporation chamber, where the materials are thermally evaporated from quartz crucibles. Several effusion cells inside one chamber enable the simultaneous evaporation of different materials for molecular blends or doping experiments. The actual layer thickness is in situ monitored by quartz crystal microbalances. Deposition rates are controlled via the temperature of the crucibles and are usually set between 0.2 and 0.5 Å/s. Heating the substrates during material deposition can be realized by a halogen lamp placed in a copper block which is mounted above the sample holder. For substrate heating a graphite plate is placed on the backside of the glass substrate which allows to set substrate temperatures up to ca. 120 °C. However, thermal coupling is not always uniform over the whole area which leads to variations in temperature of approximately $\pm$10 °C. In contrast to spin coating which impedes lateral structuring of the film, the evaporation technique allows to apply deposition masks. Hence, the area of organic semiconducting layers can be restricted which minimizes leakage currents.

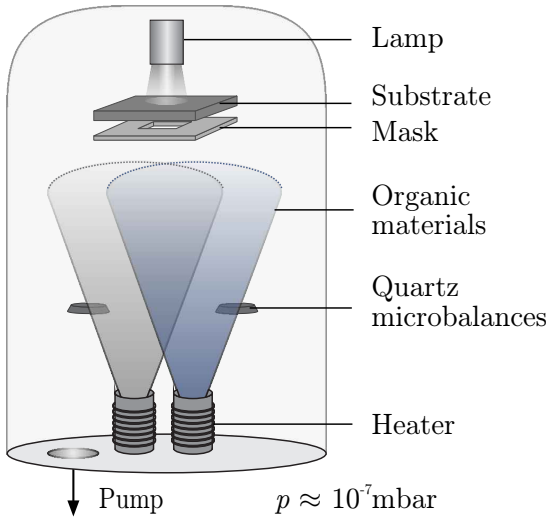

Figure 3.10.: Schematic sketch of an evaporation chamber used for deposition of small molecular organic semiconductors.

Top contact deposition

For the deposition of top contact materials, OPVCs were—without exposure to air—transferred to a different evaporation chamber. Usually the cathode consists of a metal layer with total thickness of approximately 100 nm. It may either consist of pure Al or several tens of nanometers of Ca or Sm covered with Al. Metal deposition is realized through a shadow mask, yielding the device structure schematically illustrated in Fig. 3.9 whereas the active area of $2 \times 2\,\mathrm{mm}^2$ is defined by the overlap between the patterned anode and the cathode. While Al is evaporated out of boron nitride crucibles, Ca and Sm can be evaporated from tungsten basket heaters as they directly sublime without melting (evaporation rates of approximately 1 Å/s). Prior to cathode deposition a few nanometers (typically 5–10 nm) of BCP or NTCDA might be used as exciton blocking layer—alternatively, small amounts (typically few Ångstroms) of LiF can be used. The organic metal TTF-TCNQ is thermally evaporated from effusion cells with thicknesses of typically 150–300 nm (evaporation rates of approximately 1 Å/s), as a conductive layer is formed only after a certain layer thickness.[283]

Encapsulation

Organic materials are by nature comparatively susceptible to degradation from oxygen and moisture, which diffuses into the active layers and oxidizes the organic material—especially under illumination. Moreover, it is known that oxygen and water also react with the Al cathode due to its low work function.[287] A common

way to protect organic electronic devices from oxygen and moisture is realized with an air-tight encapsulation. For this purpose, an impermeable cover glass is attached to the substrate by using a UV curable epoxy containing microspheres. It creates a protective cavity which is filled with inert gas when the procedure is carried out inside the glovebox.

3.2.2. Fabrication of field-effect transistors

Thin-film transistors were prepared on highly doped silicon wafers with 320 nm thermally grown oxide acting as gate electrode and gate dielectric, respectively. A sketch of the OFET layout can be seen in Fig. 3.11. An additional layer of the insulating alkane tetratetracontane (TTC, $C_{44}H_{90}$, 10 nm) was used as passivation layer.[204,288] The reason for the application of this passivation layer can be found in its property to spatially separate the transport channel from trap states on the SiO_2 surface to obtain a trap-free insulator/semiconductor interface and to enhance the crystallinity of the organic semiconductor.[289] TTC is deposited by thermal evaporation with sublimation temperatures around 100 °C (evaporation rate approximately 0.1 Å/s) and subsequently annealed at 60 °C for 120 minutes in nitrogen atmosphere, which drastically reduces the surface roughness.[231] TTC was purchased from Sigma Aldrich and was used without any further purification. A detailed study on the application of TTC in organic field-effect devices can be found in Ref. 289. To realize unipolar electron and hole transport, top contacts of Ca and

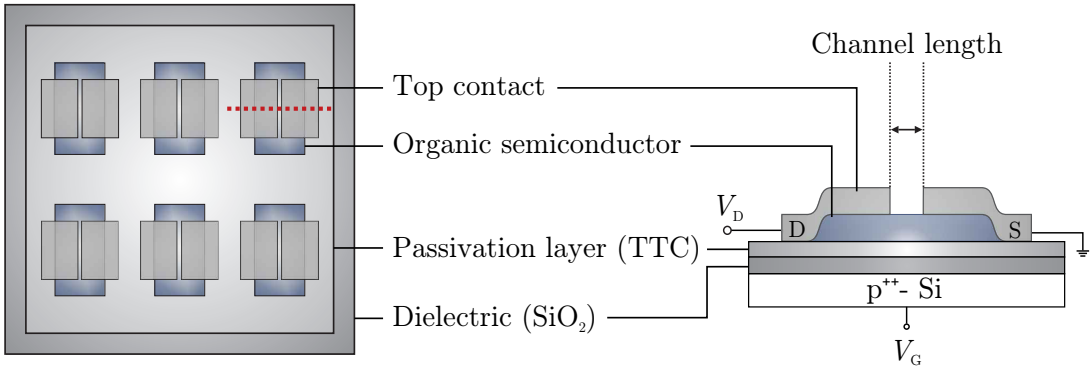

Figure 3.11.: Schematic device geometry of a top contact OFET. The left picture shows the top view of the configuration: six transistors are located on one substrate with channel lengths between 50 µm and 150 µm. The red dotted line marks the position of the cross section depicted on the right hand side. Top contacts form source (S) and drain (D) of the transistor and the bottom of the highly p-doped Si wafer acts as gate. V_D and V_G stand for the drain and gate voltage, respectively.

TTF-TCNQ are used, respectively. Source and drain contacts were evaporated through a shadow mask with various channel lengths in the range of 50 µm to 150 µm. In OFETs a 25 nm thick layer of an organic semiconductor is deposited on top of the passivated substrates. A description of the working principle of OFETs can, e.g., be found in Ref. 290.

3.3. Characterization techniques

3.3.1. Current-voltage measurements

Steady-state j-V characteristics were recorded using a source measure unit (Keithley 2400 sourcemeter or Keithley 236 SMU) in dark and under white light illumination. Two different light sources were used for illumination, noted at the respective measurement. One source is a white LED (Luxeon LXHL-NWE8) at an intensity of approximately 54 mW/cm^2. As the illumination conditions do not fulfill the AM 1.5 g standards, values for power conversion efficiencies are not specified when the LED is used for illumination (spectrum depicted in Fig. 3.12 (a)). Instead, emphasis is placed on the comparability of the samples prepared within one series. The other light source is a xenon high pressure lamp (Oriel 150W) with filters to simulate the AM 1.5 g solar spectrum (see Fig. 3.12 (b)). The illumination intensity was approved by a calibrated silicon reference cell (RERA systems, PV Measurement Facility, Radboud University Nijmegen, area 1×1 cm^2). Nevertheless, as the perfect homogeneity of the light beam cannot be guaranteed, the power conver-

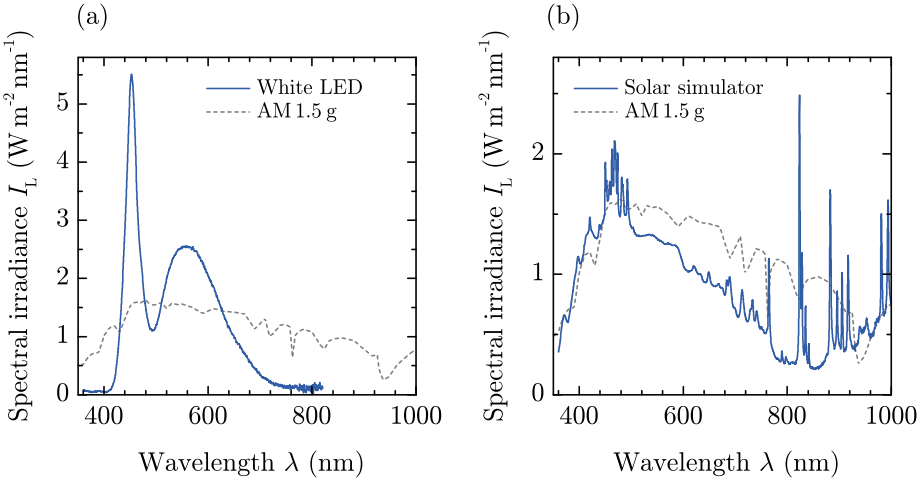

Figure 3.12.: Spectrum of (a) the white LED and (b) the used solar simulator—both compared to the AM 1.5 g standard spectrum.

sion efficiency of solar cells with an area smaller than the reference cell are slightly overestimated—however, comparable with each other. In order to achieve solar cell characteristics which are independent of the precise shape of the spectrum, the difference between the simulated and the AM 1.5 g solar spectrum would have to be considered by a spectral mismatch factor,[15] which is not done in this study. However, the focus of this research is not on the comparison of absolute efficiencies of solar cells but rather on changes induced by different morphologies, growth conditions, or the substitution of one material by another. As devices to be compared are measured under similar conditions, the observed tendencies in cell characteristics are still relevant. In addition to the characteristics at 1 sun (100 mW/cm^2), intensity dependent measurements are enabled by different neutral density filters which attenuate the incident light intensity of the solar simulator. All measurements are either performed in nitrogen atmosphere, under vacuum condition or on encapsulated devices. A photodiode (Gigahertz) is used to additionally record the photocurrent of the emitted light (this applies especially for OLEDs or solar cells which are driven in forward direction). Its sensitivity is either adjusted to the human eye's wavelength dependent sensitivity (in this case, the light intensity correlates to the luminance L), or it is equipped with a radiometric filter, which—as opposed to the photometric filter—does not account for the spectral sensitivity of the human eye. Sweeping the voltage and simultaneously recording current and photocurrent is done with a Keithley 2612 dual-channel sourcemeter.

3.3.2. Temperature dependent measurements

j-V curves in dependence on temperature were measured in vacuum using a liquid-nitrogen-cooled cryostat (Cryovac). To prevent exposure to air, the sample holder can be loaded inside the glovebox and sealed prior to transfer. The temperature control within the cryostat is performed by adjusting the flow rate of nitrogen and by simultaneously heating with a resistive heater. This allows an adjustment of temperatures between approximately 350 and 130 K. Measurements at different temperatures were carried out from high to low temperature in steps of 10 K. The cryostat is equipped with two temperature sensors; one measures the actual temperature at the device and a second one detects the temperature of the sample chamber. The temperature controller adjusts the set temperature according to the second detector—however, the real device temperature is read from the sensor in close proximity to the sample. At each set temperature a j-V curve is recorded in dark and under illumination. Measurements in light were realized by using a white LED.

3.3.3. Photoluminescence

Photoluminescence (PL) measurements were carried out with an Edinburgh Instruments double-monochromator setup equipped with a Xe high pressure lamp and two monochromators both on the excitation and detection part, enabling improved energetic resolution. The emission signal can either be detected by a Photomultiplier or an InGaAs detector, overall covering a wavelength range between approximately 300 and 1800 nm. In addition to the monochromatic excitation of the Xenon lamp, light from an external laser can be coupled into the setup. Measurements have been performed at the Chair for Experimental Physics II, Universität Augsburg. Samples for PL were prepared as single layers of one material or mixed films of two materials—directly evaporated on glass substrates without top contacts. The samples were not encapsulated and measurements were performed under ambient atmosphere.

3.3.4. Electroluminescence

For a direct determination of the energy of the CT state via electroluminescence (EL) measurements, highly sensitive detection systems for the presumably weak signals are needed. For the majority of systems under consideration CT signals are expected to be in the near-infrared region. Preliminary EL measurements have been performed with a non-cooled photomultiplier system as was used for PL measurements. The setup allows for an external electrical connection of the samples inside the light-tight system. In order to significantly lower dark current, EL measurements have been carried out with an alternative setup at the Chair for Experimental Physics I, Universität Augsburg, which is equipped with a liquid-nitrogen cooled CCD camera (PyLoN:100BR, Princeton Instruments) with a spectral sensitivity in the wavelength range of approximately 300–1000 nm. Alternatively, a liquid-nitrogen cooled InGaAs photodiode array can be used to cover the spectral range above 1000 nm. All EL measurements are performed on encapsulated solar cells, driven by an external manually controlled voltage source.

3.3.5. Optical absorption

Optical absorption spectra were obtained from transmission measurements of organic films grown on transparent substrates using a Varian Cary 50 UV-Vis spectrophotometer at the Chair for Solid State Chemistry, Universität Augsburg, with a spectral range from 280 to 1000 nm.

3.3.6. Atomic force microscopy

Atomic force microscopy (AFM, sometimes also referred to as *Scanning force microscopy*) was first introduced in 1986[291] and is a popular technique to record a sample's surface topography with lateral resolution on the nanometer scale. The measurement technique is based on the deflection of a cantilever as a result of attractive or repulsive forces between a tip and the surface of the sample when brought in close proximity. Typically, the deflection is optically measured by means of a laser beam which is reflected from the cantilever and detected by a 4-quadrant photo detector. A schematic drawing of the basic principle is depicted in Fig. 3.13. Based on this general mechanism, there are a number of different operating modes, however, in most cases a feedback mechanism is used to adjust the distance between tip and sample. Precise adjustments of the distance and accurate scanning of the surface is usually enabled by piezo crystals.

AFM data are acquired under ambient conditions with an Autoprobe CP-Research microscope from ThermoMicroscopes operated in tapping mode, where the cantilever oscillates close to its resonance frequency. The data is analyzed with the freely available software Gwyddion.[292]

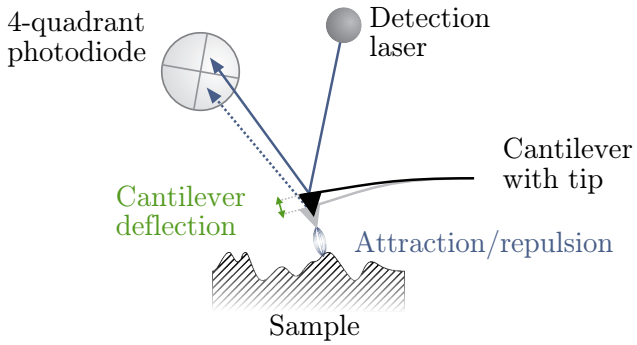

Figure 3.13.: Schematic illustration of the basic principle of an atomic force microscope. The technique is based on the deflection of a cantilever as a result of attractive or repulsive forces between tip and sample, which is optically detected by a laser beam.

3.3.7. Photothermal deflection spectroscopy

Photothermal deflection spectroscopy (PDS) is a highly sensitive technique to measure optical absorption and was first introduced in 1979.[293] A detailed description of this measurement technique can be found in Ref. 294. It is based on local heating of the sample by absorption of light and the subsequent change in refractive index

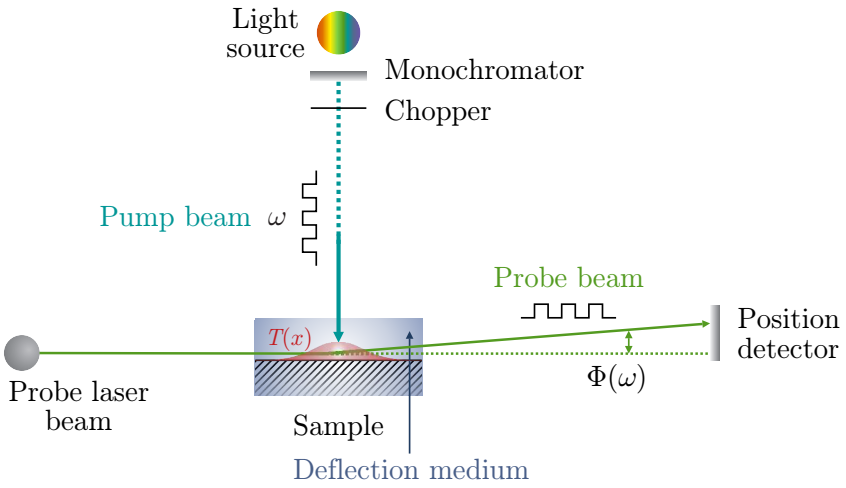

Figure 3.14.: Schematic illustration of the setup and working principle of photothermal deflection spectroscopy. A periodically modulated pump beam leads to a wavelength-dependent excitation of the sample which, in turn, results in heating of the surrounding medium ($T(x)$). A probe laser beam detects the subsequent change in refractive index and gives a highly sensitive measure for the absorption.

of the surrounding medium (cf. Fig. 3.14). Usually, the excitation is obtained by a modulated monochromatic pump beam which is locally heating up the sample in consequence of non-radiative relaxation. As a result, the surrounding medium is warmed up and leads to a periodical change of the temperature dependent refractive index. These changes are subsequently detected by a probe laser beam which passes through the surrounding medium and whose magnitude of deflection $\Phi(\omega)$ is a measure for the wavelength-dependent absorption of the sample. PDS can be used to directly measure subgap absorption features of doped and undoped inorganic[295] or organic semiconductors.[296] The measurements were carried out at the Chair for Experimental Semiconductor Physics II, Walter Schottky Institut, Technische Universität München.

3.3.8. X-ray scattering

X-ray scattering (XRS) is a common technique to determine the structural properties of any kind of crystalline or poly-crystalline material. Here, only the basic concepts are introduced which are necessary for the interpretation of measurement data. Details about this method can, e.g., be found in Ref. 297. XRS is based on scattering of electromagnetic waves impinging on a periodic structure and can be measured in various experimental geometries.

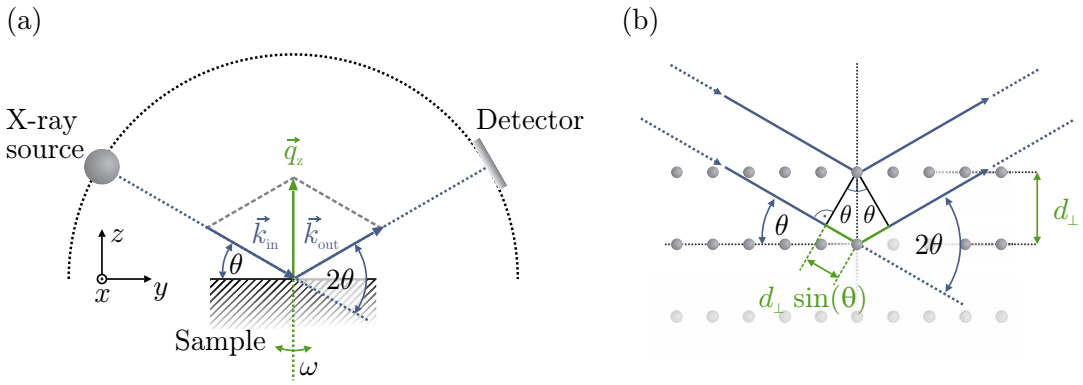

Figure 3.15.: (a) Principle of X-ray reflectivity (XRR), visualizing the scattering geometry with the wave vector of the incident and reflected beam, $\vec{k}_{\text{in}}$ and $\vec{k}_{\text{out}}$, respectively, and the momentum transfer $\vec{q}_z$. Bragg reflections are recorded by varying the angle θ while ω is varied to determine the mosaicity in rocking-scans. (b) Schematic illustration of the Bragg relation, where $d_\perp$ corresponds to the out-of-plane lattice spacing.

Within the present work, mainly X-ray reflectivity (XRR) has been applied which is based on the detection of a specularly reflected beam of X-rays. The schematic setup of an XRR experiment is depicted in Fig. 3.15 (a). The monocromatic incident X-ray beam (with wave vector $\vec{k}_{\text{in}}$) encloses an angle θ with the sample surface. A detector, mounted at an angle $2\,\theta$ to the incident beam, records the reflected beam with wave vector $\vec{k}_{\text{out}}$. On the assumption of elastic scattering, the wavenumbers of incoming and reflected beam have to be equal: $\left|\vec{k}_{\text{in}}\right| = \left|\vec{k}_{\text{out}}\right| = 2\,\pi/\lambda$. As a result, the momentum transfer $\vec{q} = \vec{k}_{\text{out}} - \vec{k}_{\text{in}}$ is oriented along the surface normal with the z component

$$q_z = \frac{4\,\pi}{\lambda}\,\sin\theta \tag{3.1}$$

being the only non-zero component.

Organic molecules which grow as crystalline thin films show a periodic variation of electron density in the out-of-plane direction, where the X-ray beam is scattered. For constructive interference at the crystal planes the change in path length has to be an integer multiple n of the X-ray wavelength λ. According to the Bragg condition, this constraint can be expressed as

$$2\,d_\perp \cdot \sin\theta = n\,\lambda. \tag{3.2}$$

This geometric relation is visualized in Fig. 3.15 (b). Bragg peaks are analyzed by means of the peak center position q_z and the full width at half maximum (FWHM)

of the peak, Δq_z. The corresponding out-of plane lattice spacing is determined as

$$d_\perp = 2\,\pi/q_z, \tag{3.3}$$

whereas a lower limit for the vertical domain size is given by[82]

$$D = 2\,\pi/\Delta q_z. \tag{3.4}$$

When a certain angle θ fulfills the Bragg condition a so-called rocking-scan allows to determine the mosaicity of the crystallites. It is measured by keeping the absolute momentum transfer q_z fixed at resonance position while tilting the sample holder by a small angle ω. Typically, the FWHM is determined from a rocking-scan which reflects the average misorientation of the crystallites.

While specular X-ray scattering probes the out-of-plane structures of a sample, grazing incidence X-ray diffraction (GIXD) is used to probe the lateral in-plane crystal structure of a sample and is carried out using small angles of incidence θ.

All XRS measurements were conducted by our cooperation partners from Eberhard Karls Universität Tübingen (group of Prof. Frank Schreiber). XRR measurements were performed on a GE/Seifert X-ray diffractometer ($CuK_{\alpha 1}$ radiation with $\lambda = 1.541\,\text{Å}$, multilayer mirror, and double bounce compressor monochromator) under ambient conditions. GIXD measurements were performed on the X04SA beamline at the Swiss Light Source, Paul Scherrer Institut, Villigen, Switzerland (12 keV photon energy).

3.3.9. Ultraviolet photoelectron spectroscopy

Photoelectron spectroscopy is an experimental technique to determine the energetic structure of the occupied electronic states of a material and, thus, provides a common technique to directly probe the energetic position of the occupied levels in organic semiconductors.[298] It is based on the photoelectric effect, i.e., the emission of electrons from matter as a result of light absorption. Ultraviolet photoelectron spectroscopy (UPS) uses UV light with energy $h\nu$ for the excitation which is just enough for the emission of valence electrons. A spectrometer measures the kinetic energy E_{kin} of the photoelectrons which are emitted from the sample. In order to avoid unwanted scattering processes with air molecules the processes has to take place under ultra-high vacuum. A scheme of the setup is shown in Fig. 3.16 (a).

Figure 3.16 (b) displays the relevant energy levels in the sample (left side) and in the spectrometer (right side)—and their relation to each other. The exemplary sample describes a semiconducting material with a certain occupied density of

states and a Fermi level E_F located inside the band gap. Due to the electrical contact between sample and analyzer, the Fermi levels are aligned. With the knowledge of the excitation energy $h\nu$ and the spectrometer's work function Φ_spec, the binding energy E_B can be calculated from the measured quantity E_kin by

$$E_\mathrm{B} = h\nu - E_\mathrm{kin} - \Phi_\mathrm{spec}. \tag{3.5}$$

The spectrum over the binding energies allows for the construction of a valence region spectrum, which is independent of the sample's work function Φ_sample. The HOMO can be identified from the low binding energy onset which reflects the fastest electrons directly emitted from the edge of the occupied DOS. The value of Φ_sample is determined by the secondary electron cut-off (SECO), which is given by secondary electrons with low energies enabling them to just escape from the sample. It is recorded by applying an additional potential $e\,V_\mathrm{bias}$ to separate the secondary electrons emitted from the sample from those which are generated by the impinging electrons inside the analyzer.

In-situ measurements of subsequently deposited films of dissimilar materials provide information about metal/organic and organic/organic interfaces as they play a crucial role in the performance of thin-film devices.[53,299,300] This implies, in turn, that literature values of transport levels can only serve as rough guide because possibly occurring effects like interfacial dipoles or band bending cannot be taken into account.[301] Moreover, the exact values of work function and HOMO position strongly depend on the precise preparation conditions,[88] the respective substrate[302] or molecular orientations.[211,239,303] Thus, for reliable values of energy levels it is indispensable to determine both HOMO and LUMO for a certain material composition in combination with the relevant substrate as it was, e.g., done by Wilke *et al.* with DIP/C_{60} deposited on ITO/PEDOT.[98]

UPS measurements shown in this thesis were performed at two different facilities: measurements concerning the study of the influence of PEDOT:PSS heating during DIP evaporation were obtained at beamline BL8B of the Ultraviolet Synchrotron Orbital Radiation facility (UVSOR) of the Institute for Molecular Science (IMS), Okazaki, Japan. Spectra were recorded with a hemispherical energy analyzer (VG, ARUPS 10) with 40 eV photon energy. The SECO was recorded with the sample biased at −12 V. Sample transfer between preparation chamber (base pressure 1×10^{-7} mbar) and analysis chamber (base pressure 4.5×10^{-10} mbar) was done without breaking UHV conditions. All other UPS spectra were recorded by our cooperation partners from Humboldt Universität Berlin (group of Prof. Norbert Koch). Measurements of top contact modifications were performed using a helium discharge lamp producing fixed excitation energy of 21.22 eV (He I) and

a Phoibos 100 hemispherical energy analyzer. All other spectra were recorded at the endstation SurICat at the synchrotron radiation source BESSY II–HZB and recorded with a hemispherical energy analyzer (resolution set to 100 meV) with 35 eV photon energy. In both cases SECOs were measured with the sample biased at −10 V. Sample preparation for UPS experiments was carried out under conditions comparable to those for the fabrication of solar cells.

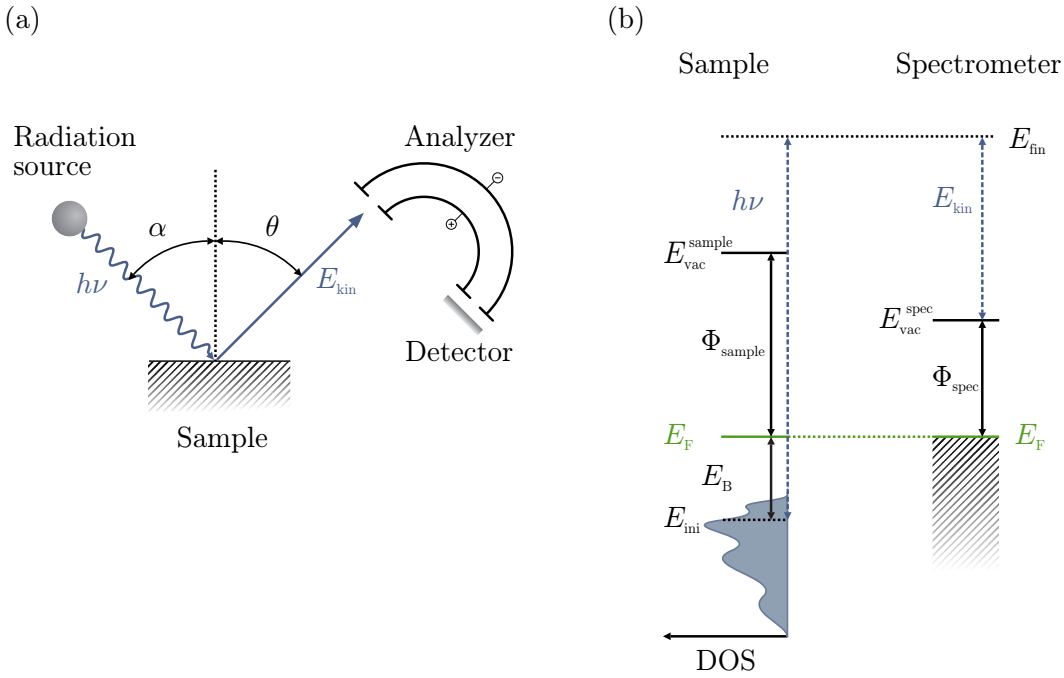

Figure 3.16.: (a) Principle of a photoelectron spectroscopy measurement after Ref. 304. A sample is irradiated with monochromatic light of energy $h\nu$, impinging under an angle α. The kinetic energy E_{kin} of the electrons which are emitted from the sample under an angle θ is recorded by a hemispherical analyzer combined with an electron detector system. The whole setup is mounted inside a UHV chamber. (b) Schematic illustration of the relevant energy levels in a photoelectron spectroscopy measurement. The left part is related to the energetics of the semiconducting sample with a certain density of states (DOS) and the right part describes the energy levels of the spectrometer. E_{ini} and E_{fin} describe the initial and final state of the photoelectron, respectively. As the sample is in electrical contact with the spectrometer, the Fermi levels E_{F} are aligned. $E_{\mathrm{vac}}^{\mathrm{sample}}$ and $E_{\mathrm{vac}}^{\mathrm{spec}}$, Φ_{sample} and Φ_{spec} are the vacuum levels and work functions of sample and spectrometer, respectively. The binding energy E_{B} is referenced to E_{F}.

3.3.10. Impedance spectroscopy

Static versus dynamic resistance - the definition of impedance

Impedance spectroscopy (IS) is a powerful non-destructive method for the characterization of dynamics of bound or mobile charges in the bulk or interfacial region of solid or liquid materials.[305] In contrast to the steady state measurement of j-V curves, IS provides a differential technique: By superimposing an alternating voltage $V_{\mathrm{ac}}(t) = V_0 \cdot \sin(2\pi f \cdot t)$ with small amplitude V_0 atop of the bias voltage V_{dc}, the operation point is moved along the j-V curve which leads to an alternating current $j_{\mathrm{ac}}(t) = j_0 \cdot \sin(2\pi f \cdot t + \varphi)$, with a phase shift φ (see Fig. 3.17). In complex

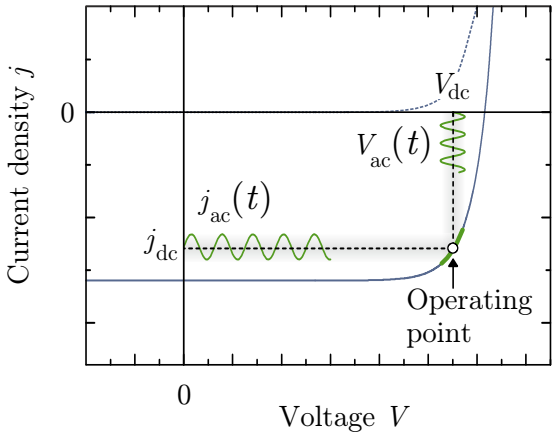

Figure 3.17.: Simulated j-V characteristics of a solar cell. The bias voltage V_{dc} specifies an operating point of the impedance spectroscopy measurement. A superimposed sinusoidal voltage V_{ac} leads to a small distortion along the j-V curve and with it to a small alternating current density j_{ac}.

notation, the alternating voltage $\hat{V}_{\mathrm{ac}}$ and current $\hat{j}_{\mathrm{ac}}$ can be written as:

$$\hat{V}_{\mathrm{ac}}(t) = V_0 \cdot \exp\left(\mathrm{i} \cdot 2\pi f \cdot t\right) \tag{3.6}$$

$$\hat{j}_{\mathrm{ac}}(t) = j_0 \cdot \exp\left(\mathrm{i} \cdot 2\pi f \cdot t + \mathrm{i}\varphi\right) \tag{3.7}$$

According to Ohm's law, the complex impedance $\hat{Z}(t)$ is defined as the ratio of complex voltage and current:

$$\hat{Z}(t) \equiv \frac{\hat{V}_{\mathrm{ac}}(t)}{\hat{j}_{\mathrm{ac}}(t)} = \mathcal{R}e(\hat{Z}) + \mathrm{i} \cdot \mathcal{I}m(\hat{Z}) = Z' + \mathrm{i} \cdot Z'' \tag{3.8}$$

$$= |\hat{Z}| \cdot \exp\left(\mathrm{i}\varphi\right) \tag{3.9}$$

with the real part Z' and imaginary part Z''.
The modulus[i] $|\hat{Z}|$ and phase angle φ are given as

$$|\hat{Z}| = \sqrt{(Z')^2 + (Z'')^2} \tag{3.10}$$

$$\varphi = \arctan\left(\frac{Z''}{Z'}\right). \tag{3.11}$$

There are several other quantities related to impedance, however, with the admittance $\hat{Y}(f)$ being one of the most significant ones for semiconductor devices. $Y(f)$ is defined as

$$\hat{Y}(f) \equiv \frac{1}{\hat{Z}(f)} = G + \mathrm{i}\,2\pi f \cdot C, \tag{3.12}$$

with the conductance $G(f)$, which reveals the dielectric loss

$$\frac{G(f)}{2\pi f} = \frac{1}{2\pi f}\frac{Z'}{(Z')^2 + (Z'')^2}, \tag{3.13}$$

and the capacitance

$$C(f) = \frac{1}{2\pi f}\frac{-Z''}{(Z')^2 + (Z'')^2}. \tag{3.14}$$

In the field of organic electronic devices, IS is employed to investigate charge transport and relaxation processes. Sequences occurring on different time scales can be discerned and information about carrier and field distribution inside the device is obtained.[307]

Impedance measurements in Augsburg were performed using a frequency response analyzer (Solartron SI 1260 Impedance/Gain-Phase Analyzer) combined with a dielectric interface (Solartron 1296). The setup allows frequency sweeps covering a range from 10^{-2} to 10^{7} Hz. The amplitude of the AC voltage is set to 100 mV rms for all measurements. The frequency response analyzer measures magnitude and phase of the complex impedance, from which all other quantities can be calculated. IS measurements carried out at the Universitat Jaume I de Castellón, Spain (Group for Photovoltaic and Optoelectronic Devices, Prof. Juan Bisquert) were performed with Autolab PGSTAT-30 equipped with a frequency analyzer module applying a small voltage perturbation of 100 mV rms. To minimize sample degradation during measurement, the devices under test have either been encapsulated or measurements were performed inside the glove box. Typically, bias-voltage sweeps were performed starting from low bias while frequency sweeps were carried out starting from high frequency.

[i] In this work, "modulus" is used in its mathematical sense—not to be confused with the physical parameter "modulus" defined as $M = \mathrm{i}\,2\pi f \cdot C_\mathrm{g}\,Y^{-1}$ with C_g as the geometrical capacitance—as it is, e.g., used in Ref. 306.

Equivalent circuit and data presentation

According to the different quantities related to impedance, representation of impedance data may vary depending on emphasis. The representation in the complex impedance plane ($-Z''$ vs. Z') is called "Nyquist plot". Plotting the magnitude $|Z|$ and the phase angle φ of the impedance versus logarithm of frequency is known under the name "Bode plot". In the present thesis, measurement data is addi-

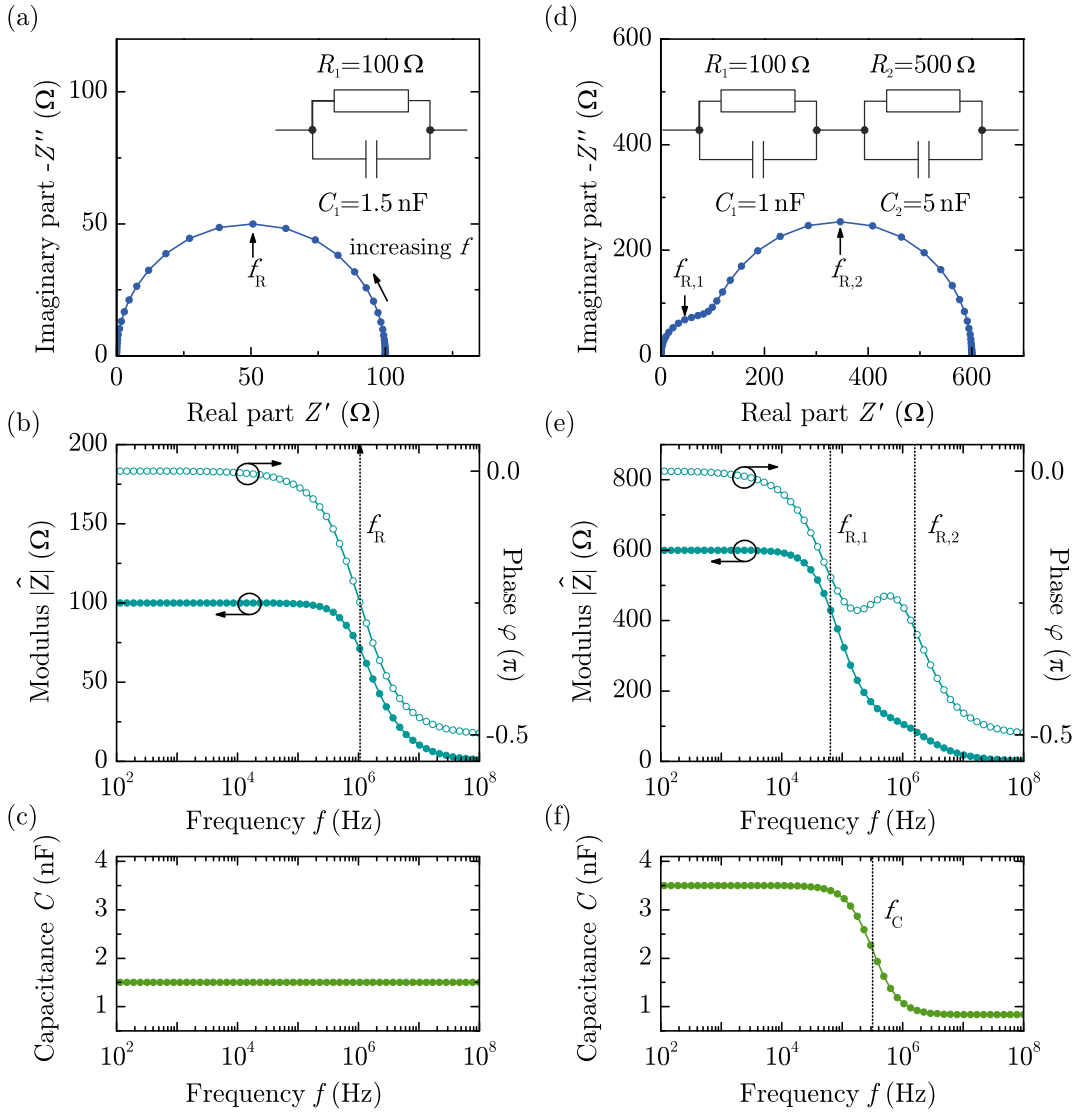

Figure 3.18.: Equivalent circuits consisting of (a) one RC and (d) two RC elements including the values used for simulation. Figures (b) and (e) depict the frequency dependent magnitude $|\hat{Z}|$ and phase φ of the impedance of one and two RC elements, respectively. Capacitance-frequency (C-f) plots are shown in (c) for one RC element and in (f) for two RC elements.

tionally presented in form of capacitance vs. frequency (C-f) and capacitance vs. voltage (C-V) scans. Data analysis and fitting was performed using the ZView™ simulation software.[308] By means of equivalent circuits, the device can be modeled and measurement data can be traced back to physical properties.

Single RC element

A single semiconducting layer stacked between two conducting electrodes can most simply be modeled by a resistor R which represents its conductivity and a capacitor C which is characterized by its dielectric constant ε. Both are connected in parallel to an RC element. Thus, the complex impedance for a single layer device can be calculated as follows:
A resistor with resistance R has the impedance

$$\hat{Z}_{\mathrm{R}} = R\,, \tag{3.15}$$

and a capacitor with the capacitance C has the complex impedance

$$\hat{Z}_{\mathrm{C}} = \frac{1}{\mathrm{i}\omega C}\,, \tag{3.16}$$

with the angular frequency $\omega = 2\pi f$.
If both are combined in parallel (for equivalent circuit see Fig. 3.18 (a)) the total impedance of the RC element $\hat{Z}_{\mathrm{RC}}$ is—according to Kirchhoff's law—given by

$$\frac{1}{\hat{Z}_{\mathrm{RC}}} = \frac{1}{\hat{Z}_{\mathrm{R}}} + \frac{1}{\hat{Z}_{\mathrm{C}}} \tag{3.17}$$

and with Eq. (3.15) and (3.16)

$$\hat{Z}_{\mathrm{RC}} = \frac{1}{\frac{1}{R} + \mathrm{i}\,2\pi f\,C}\,. \tag{3.18}$$

The simulated characteristics of the modulus $|\hat{Z}|$ and phase φ of the impedance are shown in Fig. 3.18 (b). In the limit $f \to 0$ the influence of the capacitor vanishes and the current flows through the resistor, resulting in the DC resistance $R_1 = 100\,\Omega$ and a phase angle of $\varphi = 0$. Coming to higher frequencies, the real part of the impedance decreases due to the dielectric "opening" of the capacitor, whereas the imaginary part increases. This behavior is reflected in a phase angle approaching $-\pi/2$. In between these limiting cases the current flows through both the capacitor and resistor. The frequency where both currents are equal and the imaginary part of the impedance reaches its maximum is the relaxation frequency f_{R} of the RC

element.[309] It is given by

$$f_{\mathrm{R}} = \frac{1}{2\pi}\frac{1}{R_1\,C_1}. \tag{3.19}$$

Two RC elements in series

Connecting two RC elements in series leads to an equivalent circuit schematically drawn in Fig. 3.18 (d). If their relaxation frequencies f_{R} are sufficiently different, two separated semicircles are observed in the Nyquist plot. In the present case, the relaxation frequencies are $f_{\mathrm{R},1} \approx 1.6 \cdot 10^6\,\mathrm{Hz}$ and $f_{\mathrm{R},2} \approx 0.6 \cdot 10^5\,\mathrm{Hz}$ for the first and second RC element, respectively, leading to slightly overlapping semicircles. At low frequencies the current flows through the resistors, resulting in a modulus $|\hat{Z}|$ of $R_1 + R_2 = 600\,\Omega$ and a phase angle of $\varphi = 0$ (see Fig. 3.18 (e)). Increasing the frequency leads to a decrease in phase and modulus, which corresponds to the slow process with relaxation frequency $f_{\mathrm{R},1}$. The fast process characterized by $f_{\mathrm{R},2}$ becomes noticeable at higher frequencies. In between these two distinctive limits the impedance behaves as if the system would consist of the $\mathrm{R_1C_1}$ element connected in series with the resistance R_2. In the high frequency limit a displacement current passes through both capacitors.

The difficulty in interpreting impedance data often lies in the inconclusive correlation between single elements of the equivalent circuit and the corresponding part of the device and its physical behavior. One possible strategy is to make use of geometrical capacitances calculated from the dimensions of the layers, whose magnitude often give first indication of the underlying physical origin:

$$C_{\mathrm{g}} = \frac{\varepsilon_{\mathrm{r}}\varepsilon_0 A}{d}. \tag{3.20}$$

While the capacitance of a single RC element is constant over the entire frequency range (see Fig. 3.18 (c)), the capacitance of the double RC circuit features a step (see Fig. 3.18 (f)), which can be interpreted as follows:
First, the impedance can be calculated as

$$\begin{aligned}\hat{Z} &= \hat{Z}_{\mathrm{R_1C_1}} + \hat{Z}_{\mathrm{R_2C_2}}, &(3.21)\\ &= \frac{1}{\frac{1}{R_1} + \mathrm{i}\,2\pi f\,C_1} + \frac{1}{\frac{1}{R_2} + \mathrm{i}\,2\pi f\,C_2},\\ &= \frac{R_1 + R_2 + \mathrm{i}\,2\pi f\,R_1R_2(C_1 + C_2)}{1 - 4\pi^2 f^2\,R_1R_2C_1C_2 + \mathrm{i}\,2\pi f\,(R_1C_1 + R_2C_2)}. &(3.22)\end{aligned}$$

With that, the admittance is given as

$$\hat{Y}(f) = \frac{1}{\hat{Z}(f)} = \frac{1 - 4\pi^2 f^2\, R_1 R_2 C_1 C_2 + \mathrm{i}\, 2\pi f\, (R_1 C_1 + R_2 C_2)}{R_1 + R_2 + \mathrm{i}\, 2\pi f\, R_1 R_2 (C_1 + C_2)} \tag{3.23}$$

According to Eq. (3.12) the capacitance of the double RC circuit can then be expressed as

$$C(f) = \frac{\mathcal{I}m(\hat{Y}(f))}{2\pi f}, \tag{3.24}$$

$$= \frac{R_1^2 C_1 + R_2^2 C_2 + 4\pi^2 f^2\, R_1^2 R_2^2 C_1 C_2 (C_1 + C_2)}{(R_1 + R_2)^2 + 4\pi^2 f^2\, R_1^2 R_2^2 (C_1 + C_2)^2} \tag{3.25}$$

For high frequencies the capacitance reaches the plateau value

$$\lim_{f \to \infty} C(f) = C_{\mathrm{hf}} = \frac{C_1 C_2}{C_1 + C_2}, \tag{3.26}$$

which is simply the total capacitance of both capacitors in series. In contrast to the resistivity-independent C_{hf}, the low frequency limit of the capacitance depends on R_1 and R_2 and equals

$$\lim_{f \to 0} C(f) = C_{\mathrm{lf}} = \frac{R_1^2 C_1 + R_2^2 C_2}{(R_1 + R_2)^2}, \tag{3.27}$$

which can be approximated by $C_{\mathrm{lf}} \approx C_2$ in case of a large difference between both resistances, e.g., $R_2 \gg R_1$. The transition between both regimes occurs at the relaxation frequency[310]

$$f_{\mathrm{C}} = \frac{1}{2\pi} \cdot \frac{R_1 + R_2}{R_1 R_2\, (C_1 + C_2)}, \tag{3.28}$$

which can accordingly be simplified to

$$f_{\mathrm{C}} \approx \frac{1}{R_1\, (C_1 + C_2)} \tag{3.29}$$

for $R_2 \gg R_1$.
Thus, the relaxation frequency f_{C} can be seen as a measure for the ratio of the two resistors in the double RC circuit.[311] If both RC elements can be assigned to a specific layer inside the device, it is possible to give a statement about the conductivity or injection behavior.

The constant phase element

As can be seen from Fig. 3.18 (d), two RC elements in series lead to two semicircles in the Nyquist plot. If the time constants are similar, both semicircles overlap and collapse into one single, distorted arc. What makes the interpretation of such a distorted semicircle even more difficult is the fact, that in real devices the ideal case of a perfect arc is rather rare. Instead, one often finds depressed semicircles—even for single RC elements. In order to account for this kind of distortion, a so-called constant phase element (CPE) can be included into the equivalent circuit instead of a pure capacitor. In the literature different equations for the impedance were proposed.[312–314] According to Lasia, $\hat{Z}_{\mathrm{CPE}}$ is given as[314]

$$\hat{Z}_{\mathrm{CPE}} = \frac{1}{Q}(\mathrm{i}\,2\pi f)^{-\alpha}. \tag{3.30}$$

α and Q are independent of frequency with $0 < \alpha < 1$ and Q being a constant. The parameter α is a measure for the degree of "depression" of the semicircle. The case $\alpha = 1$ recovers a perfect capacitor, which is reflected in a perfect semicircle in the Nyquist plot.

For a CPE in parallel to a resistor with resistance R_{P} (see Fig. 3.19 (a)), the effective capacitance can be calculated from the parameters Q, α and R_{P} according to[315]

$$C_{\mathrm{eff}} = \frac{(Q \cdot R_{\mathrm{P}})^{1/\alpha}}{R_{\mathrm{P}}}. \tag{3.31}$$

In Fig. 3.19 (b) it is demonstrated how smaller values of α lead to stronger deviation from the ideal case.

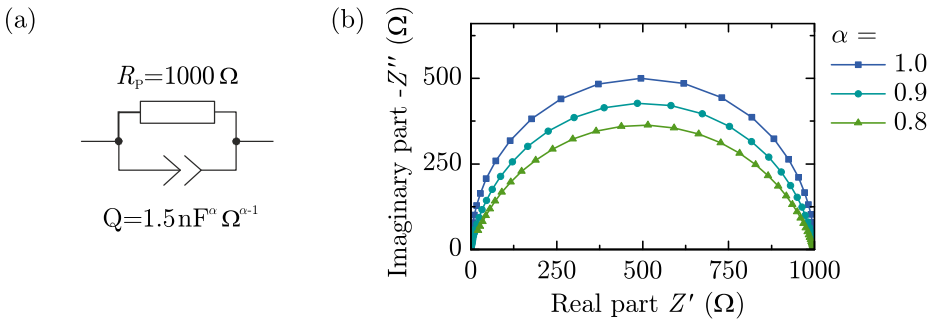

Figure 3.19.: (a) Equivalent circuit and (b) simulated impedance data of a constant phase element with different values for α connected in parallel with a resistor.

Part II

Results and Discussion

Chapter 4

Overview of investigated material combinations

The material matrix

As was shown in Fig. 2.20 there are many different solar cell architectures conceivable to increase the effective D/A interfacial area. However, it is not to be expected that all these morphologies can be realized with one single material combination. Rather, it can be assumed that the choice of the active semiconductors determines the specifics of the D/A interface—in planar as well as in bulk heterojunctions. Starting from this premise, a choice of prototypical small molecular materials is investigated within the framework of the collaborative project. Besides their suitability in planar and bulk heterojunction solar cells, structural and energetic studies form the primary focus of the joint research. The chosen materials are copper-phthalocyanine (CuPc), diindenoperylene (DIP), pentacene (Pen) and sexithiophene (6T) as donor combined with the acceptors perfluorinated CuPc (F_{16}CuPc) or the fullerene C_{60}. Due to the position of its energy levels, DIP can act both as donor and acceptor. The molecules are representatives of different classes of organic semiconductors that are already in use or were considered as promising candidates for molecular OPVCs. Within the context of the cooperational research with the project partners at the universities of Tübingen, Würzburg and Berlin, a schematic overview of the investigated material combinations was developed in the form of a material matrix. Highlighting DIP/C_{60} as central system of the present thesis, it is depicted in Fig. 4.1—a version including Perfluoropentacene can be found in Ref. 316.

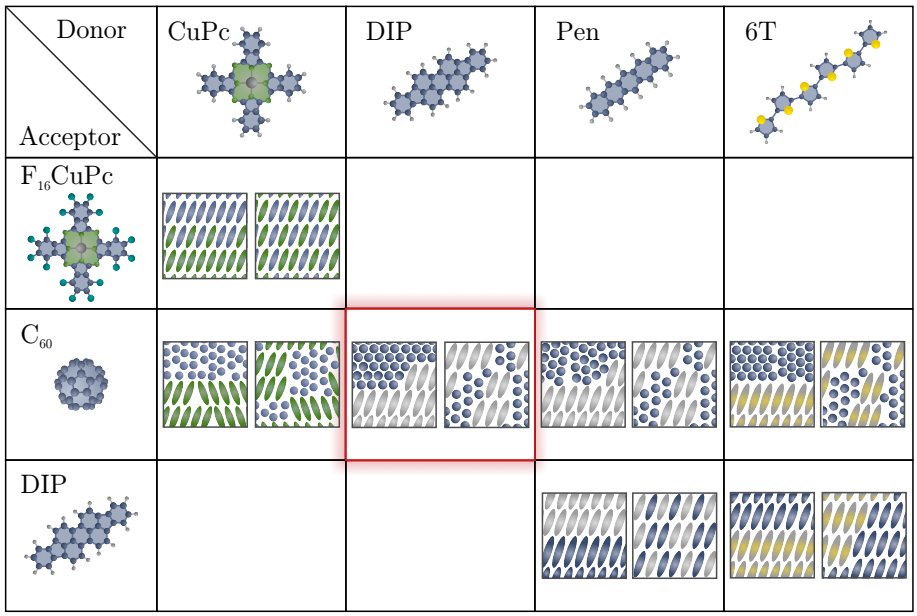

Figure 4.1.: Material combinations studied in the scope of the research project, classified according to their role as acceptor or donor in the solar cell. For each material combination the planar stacking and mixing scenario is depicted as a sketch—variations with growth temperature are not included in this overview. Note that a comprehensive study—including structure, morphology and energetics—was performed for the material system DIP/C_{60}, while all other combinations serve as comparative study to specific questionings or are only given for completeness.

Growth phenomena

Concerning the growth behavior in bulk heterojunctions, the key question is if both compounds intermix on a molecular level or if they phase-separate. The material matrix comprises sketches of the different growth and mixing scenarios. Please note that structural investigations with 6T and Pen have not been part of this thesis and results are only given for completeness. Corresponding studies can be found in Refs. 317 and 318 published by project partners. A clear summary of structural investigations covering most of the material systems is given in Refs. 200 and 319. The materials can be classified according to their shape: while C_{60} is a spherical molecule, the phthalocyanines are disk-shaped and DIP, 6T and Pen have rod-like appearance. Depending on the shape, different film growth scenarios can be expected: Depositing them on top of each other, results in different growth effects such as templating, graded interfaces, enhanced crystallization or smoothing—as demonstrated in Ref. 200. Mixing them for BHJ structures may either lead to phase separation or solid solution (statistical mixing).

Energetic positioning

As can be seen from Fig. 4.2, the materials cover a wide range of energy levels which are responsible for their classification as donor and acceptor materials. However, this classification is very specific, as the nature of a material—being a donor or an acceptor—depends mainly on the choice of the partner. Some of the materials have been energetically investigated within the research project, which was mainly enabled by project partners in Berlin. All other values are taken from literature as listed in Tab. 4.1. The values have to be taken as rough guide as the determination depends strongly on the way of preparation, the substrate as well as on exact measurement conditions. Moreover, it has been shown that the energetic position of molecular levels of organic molecules can depend crucially on the orientation of the molecules on a surface due to different ionization potentials for standing and lying molecules with respect to the substrate's surface.[303] As already mentioned above, DIP can either act as donor with respect to C_{60} and the other fluorinated materials, while it is an acceptor when combined with 6T. Apart from favorable energy level alignment this special position is enabled by its bipolar transport properties[204] and results in high open-circuit voltages in devices combining 6T or P3HT[j] with DIP as acceptor.[213]

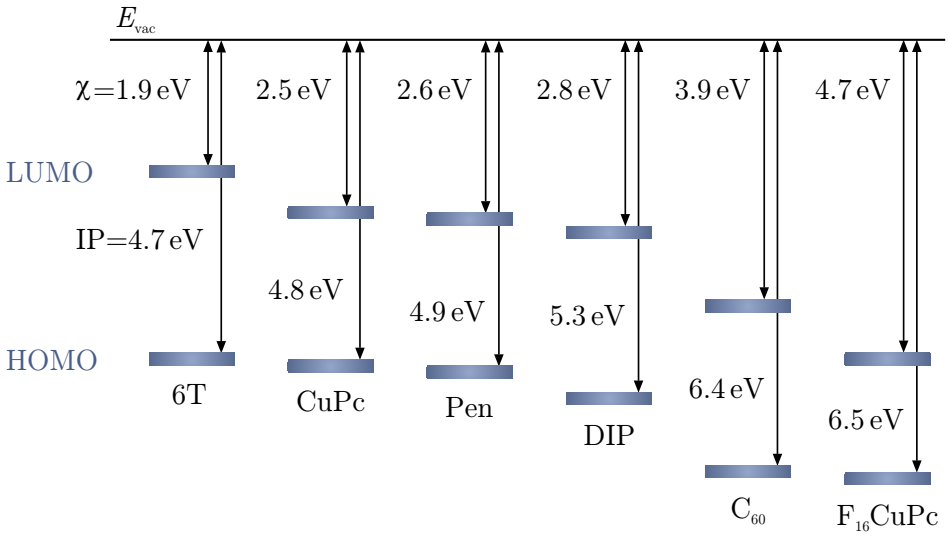

Figure 4.2.: Energies of the HOMO and LUMO levels for the investigated materials—sorted according to increasing value of IP. Energetic positions of HOMO and LUMO are given as reported in literature and summarized in Tab. 4.1.

[j]P3HT (Poly(3-hexylthiophene-2,5-diyl)) is a π-conjugated polymer and one of the most common donor materials in the field of polymer OPVCs.

Table 4.1.: Energies of HOMO and LUMO levels for the investigated materials as reported in literature.

Compound	LUMO (eV)	HOMO (eV)	Ref.
CuPc	2.5[i]	4.8[ii]	240
Pen	2.6[iii]	4.9[ii]	320
6T	1.9[iv]	4.7	98
DIP	2.8[v]	5.3[vi]	98
C_{60}	3.9[v]	6.4	98
F_{16}CuPc	4.7[vii]	6.5[ii]	321

[i] The LUMO of CuPc is estimated by adding a transport gap of 2.3 eV[39] to the HOMO.
[ii] Molecules oriented in a standing fashion.
[iii] The LUMO of Pen is estimated by adding a transport gap of 2.2 eV[95] to the HOMO.
[iv] The LUMO of 6T is estimated from the optical gap of 6T ($E_g = 2.4$ eV) and the relation between optical gap and transport gap, both found in Ref. 134.
[v] The HOMO and LUMO of DIP and C_{60} were recently determined by UPS/IPES experiments within the framework of the interdisciplinary project yielding similar transport gaps for DIP and C_{60} of 2.55 eV and 2.5 eV, respectively.[98]
[vi] This work.
[vii] The LUMO of F_{16}CuPc is estimated by adding a transport gap of 1.8 eV[129] to the HOMO.

Absorption properties

Apart from energy level alignment, efficient light harvesting of the active semiconductors plays an important role for the performance of a solar cell. It is obtained by high absolute values of the absorption coefficient—preferably covering a wide range of the solar spectrum including the red and near-infrared region—but also by complementary absorption behavior of both materials. Figure 4.3 depicts absorption spectra of the used materials calculated from transmission measurements on transparent substrates. Light absorption in complementary wavelength regimes can only be observed for the combination of C_{60} with CuPc or Pen—in all other cases relatively large spectral overlap provides less favorable conditions for high degrees of absorption over the entire solar spectrum.

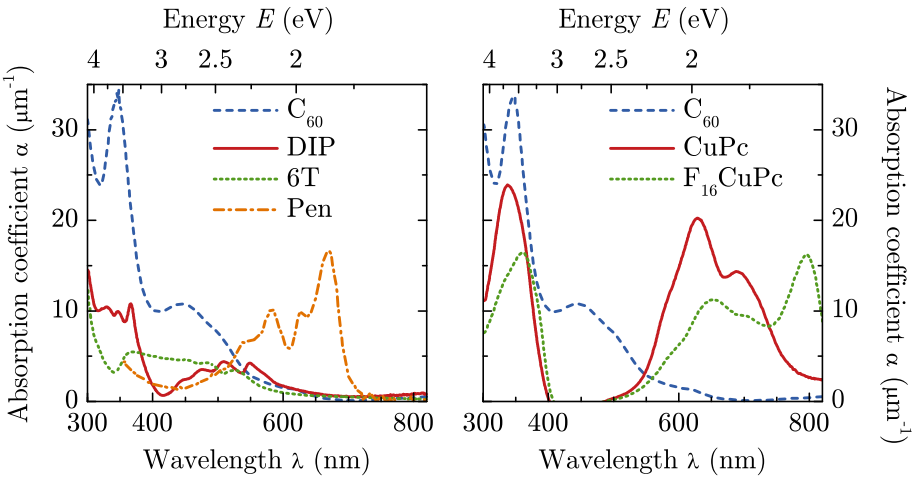

Figure 4.3.: Absorption spectra of the invesigated materials. The spectra are calculated from transmission measurements on transparent substrates.

General remark on the structure of the experimental part

In the present thesis, the main focus is on the DIP/C_{60} material combination which is comprehensively studied with regard to structural, energetic and electronic properties. The other material combinations serve as comparative systems concerning specific questionings.

The experimental part is organized as follows: Comparable with a virtual walk through the cell, the different interfaces are considered concerning their specific properties and their impact on the cell's functionality. Starting with the interface between anode and donor—which comprises the influence of substrate temperature and different hole injection materials—a major topic will be the donor/acceptor interface. While macroscopic investigations will present correlations between interface morphology and solar cell performance, studies of the microscopic interface will deal with the role of charge transfer complex and recombination. Finally, the influence of top contact variation will be presented, including among others the effect of different exciton blocking layers.

Chapter 5

The anode/donor interface

As was shown in Sec. 2.1.4 the power conversion efficiency of a solar cell is equally determined by j_{sc}, V_{oc} and FF. While much effort is put in the design and proper combination of innovative organic semiconductors to obtain high open-circuit voltages[213,322–326] and optimized light harvesting applying infrared absorbers,[12,13] over many years not much attention was paid to the fill factor. However, it can influence the total efficiency of a solar cell in the same way as V_{oc} and j_{sc}. Accordingly, current-voltage characteristics are frequently affected by an undesirable s-shape behavior, i.e., they show a decrease of the current close to V_{oc} and in forward direction of the diode. This effect can severely reduce the fill factor and hence the efficiency of a solar cell.[k]

5.1. The role of substrate heating

The following section will present the influence of substrate temperature on morphology and structural ordering of DIP films evaporated on solar cell relevant substrates. Moreover, the impact of substrate temperature on the energetics of the interface between anode and donor will be shown before presenting its effect on electrical characteristics of PHJ solar cells. Investigations are carried out on the material system DIP/C_{60}.

[k] The main results of this chapter have been published in Refs. 327 and 328.

5.1.1. Morphological and structural investigation

The morphology of the active layers in organic solar cells is a crucial parameter as transport properties of both excitons and free charge carriers are strongly correlated to the crystalline order of the involved materials. Figure 5.1 shows the surface topography (from AFM) of 50 nm thick DIP films evaporated on ITO-coated glass substrates covered with a hole injection layer of PEDOT, which were heated to different temperatures during evaporation. It can be seen, that the crystallinity is strongly influenced by the substrate conditions. The surface of DIP grown on the unheated substrate indicates growth of small islands with about 80 nm in diameter (see Fig. 5.1 (a)). When heating the substrate to 100 °C during evaporation the surface morphology changes from round-shaped islands to a terrace-like structure with extended crystallites (Fig. 5.1 (c)). The microstructure of the DIP film grown at 100 °C has a large surface area which is expected to be favorable for solar cells. As can be seen in Fig. 5.1 (b) DIP films evaporated at an intermediate substrate temperature of 60 °C show a surface morphology that appears in between those evaporated on unheated and 100 °C substrates.

In order to extend the morphological investigations, XRR measurements were performed to detect crystalline order and quantitatively determine the spatial coherence length of the observed structures. As explained in Sec. 3.3.8, the momentum transfer $\vec{q}$ is oriented parallel to the surface normal when detecting in specular reflectivity mode. This configuration allows to probe the electron density profile along that direction. Bragg peaks are analyzed by means of the peak center position q_z and the full width at half maximum of the peak, Δq_z. The corresponding lattice spacing is determined by Eq. (3.3), whereas a lower limit for the vertical

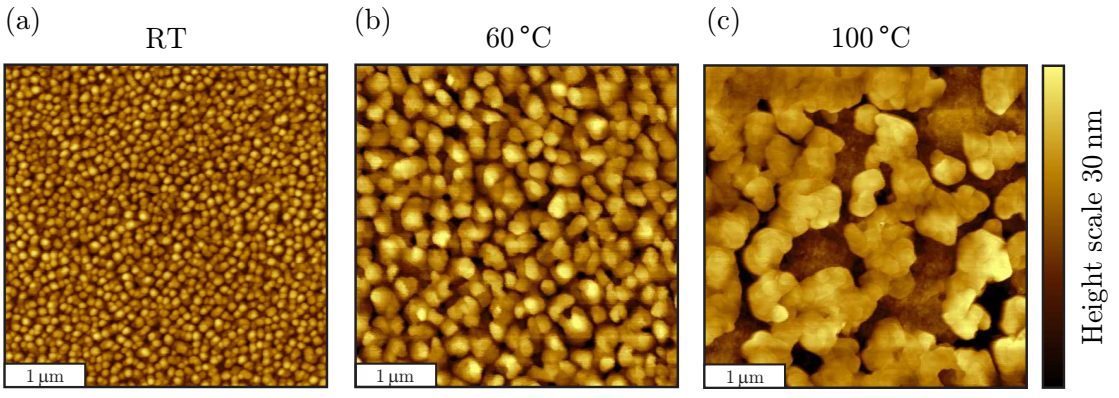

Figure 5.1.: AFM images of DIP films (50 nm) on ITO/PEDOT, evaporated at substrate temperatures of (a) RT, (b) 60 °C, and (c) 100 °C. The total image size is $4 \times 4\,\mu m^2$ in all cases.

domain size is given by Eq. (3.4). Figure 5.2 (a) shows X-ray reflectivity data of neat DIP films (40 nm) evaporated on ITO/PEDOT substrates. DIP films were deposited at substrate temperatures of RT and 100 °C. For all samples, pronounced Bragg reflections are observed at $q_z = 0.378\,\text{Å}^{-1}$, which can be associated with a DIP lattice plane spacing of $d_{\text{DIP}} = 16.6\,\text{Å}$. From this it is deduced that crystalline domains with DIP molecules standing almost upright are formed on ITO/PEDOT. As shown in Sec. 3.1.3, this can be assigned to the σ-phase, which is characterized by standing molecules tilted by $\varphi \approx 17°$ to the surface normal. The results from XRR measurements are consistent with the topographical studies already indicating highly ordered films. For elevated substrate temperatures the monomolecular steps of 16.6 Å can even be seen in line profiles of an AFM image showing the typical terrace-like structure of a DIP film (see Fig. 5.2 (b)).

One of the most decisive factors for an efficient conversion of light into electrical energy is the absorptivity of the active organic components inside the photovoltaic cell, which can strongly depend on the orientation of the molecules. The reflections in the XRR pattern at $q_z = 0.756\,\text{Å}^{-1}$ can be assigned to the (002)-peak of the DIP σ-phase. Together with the fact that the transition dipole moment of the fundamental molecular absorption is aligned along the long molecular axis of the DIP molecule, the upright standing arrangement is consistent with the low absorption

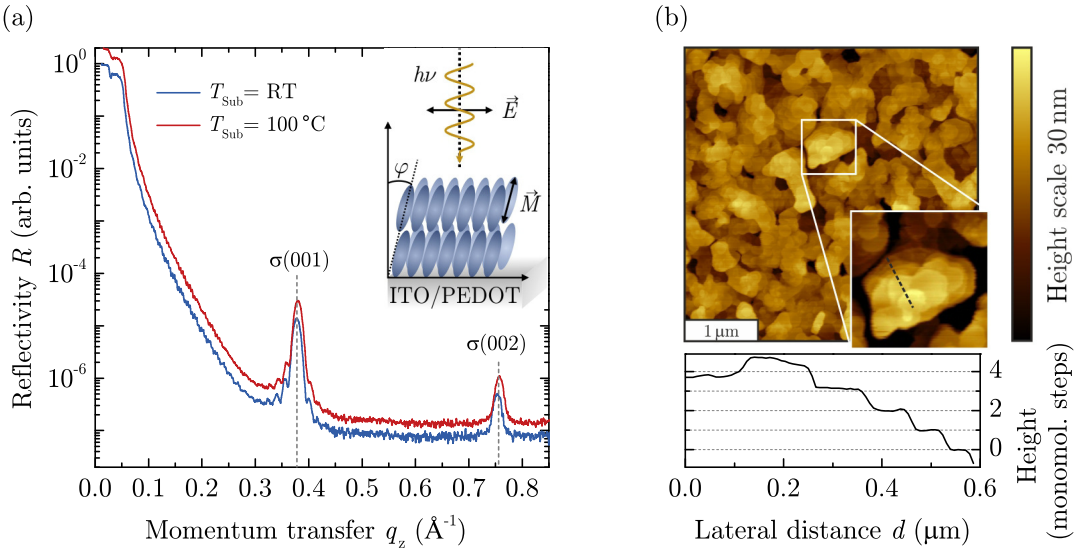

Figure 5.2.: (a) Specular X-ray reflectivity of DIP films with thickness of 40 nm evaporated on ITO/PEDOT at different substrate temperatures as indicated in the diagram. Bragg reflections at $q_z = 0.378\,\text{Å}^{-1}$ are associated with a DIP lattice plane spacing of $d_{\text{DIP}} = 16.6\,\text{Å}$ which can even be observed in line scans of a topographical picture as shown in (b) (partly taken from Ref. 327).

coefficient of neat DIP films. Thus, it is unfavorably oriented for efficient absorption of light under normal incidence as is schematically depicted in the inset of Fig. 5.2 (a). As a result, C_{60} plays a considerable role in light harvesting—this is in contrast to most of the common material combinations where the donor takes the leading part in the absorption of light. Next to the DIP(001) Bragg reflection distinct Laue oscillations can be observed, which are clear evidence for coherently ordered domains. The analysis of the peak width results in $\Delta q_z = 0.0143\,\text{Å}^{-1}$, corresponding to a coherence length of 44 nm which is approximately equal to the film thickness. This indicates that crystalline DIP domains are extended throughout the whole film—independent of substrate temperature.

5.1.2. Electronic structure

The previous section demonstrates that the morphology of DIP films is strongly influenced by substrate heating. In order to assess the influence of substrate temperature on the energy level alignment between PEDOT and the donor DIP, thickness dependent UPS investigations were performed both on heated and unheated PEDOT.

Figure 5.3 (a) and (b) show UPS spectra of heated (straight lines) and unheated (dashed lines) ITO/PEDOT covered with DIP (in each case, only the spectra of two different thicknesses are shown for clarity). The PEDOT/DIP interface energetics derived therefrom are schematically summarized in Fig. 5.4 (a) and (b) for the unheated and heated case, respectively. In order to assure successful substrate heating during evaporation, AFM images of both samples have been recorded after UPS measurement. The expected difference between round-shaped islands in case of unheated growth conditions (Fig. 5.3 (c)) and extended crystallites when the substrate was heated during DIP evaporation (Fig. 5.3 (d)) can clearly be seen—even though the particular microstructure with the remarkably large domains is not as pronounced as for thicker films shown in Fig. 5.1 (c).

The secondary electron cut-off (SECO) spectra provide information about the work function of the investigated material. According to this, the initial conducting polymer work function of PEDOT amounts to 4.75 eV. When heating the ITO/PEDOT sample, the work function is increased from 4.9 eV to 5.1 eV upon annealing.[1] This coincides with observations in literature clearly showing that an

[1]The initial work functions of both PEDOT substrates differ slightly from each other. The work function of PEDOT depends critically on the residual water content in the polymer film and is extremely sensitive to the precise preparation method. Therefore, the deviation between the work functions of unheated PEDOT films can very likely be assigned to slightly different storage times between substrate preparation and measurement.

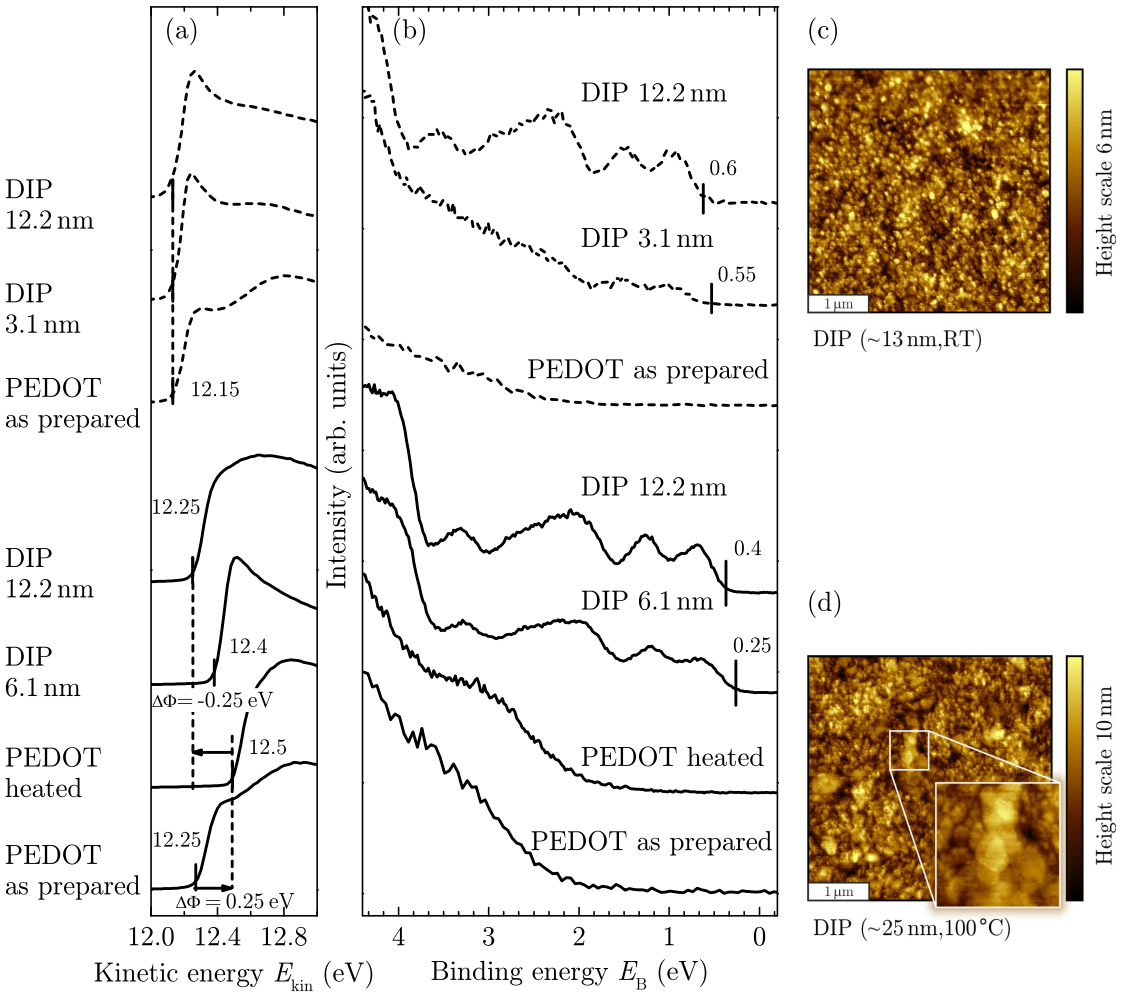

Figure 5.3.: Ultraviolet photoelectron spectra of heated (straight lines) and unheated (dashed lines) ITO/PEDOT substrates with different coverage of DIP. (a) Secondary electron cutoff (SECO) spectrum and (b) valence region spectrum. AFM images of the unheated (c) and heated (d) ITO/PEDOT/DIP sample recorded after UPS measurements—demonstrating the successful substrate heating.

annealing step of PEDOT films spin-cast onto ITO leads to an increase of its work function.[88,329] In the case of unheated PEDOT the stepwise deposition of DIP does not change the sample work function, i.e., no interfacial dipole is formed. As described in Sec. 2.2.4, this gives an indication that energy level pinning does not yet occur for this electrode work function. However, the interface energetics of DIP evaporated on heated PEDOT are different. Upon DIP deposition the sample work function changes from 5.1 eV to 4.9 eV, which can be ascribed to the formation of an interface dipole. As was introduced in Sec. 2.2.4 this observation is explained by pinning of the positive polaron level of DIP as a result of the high initial work

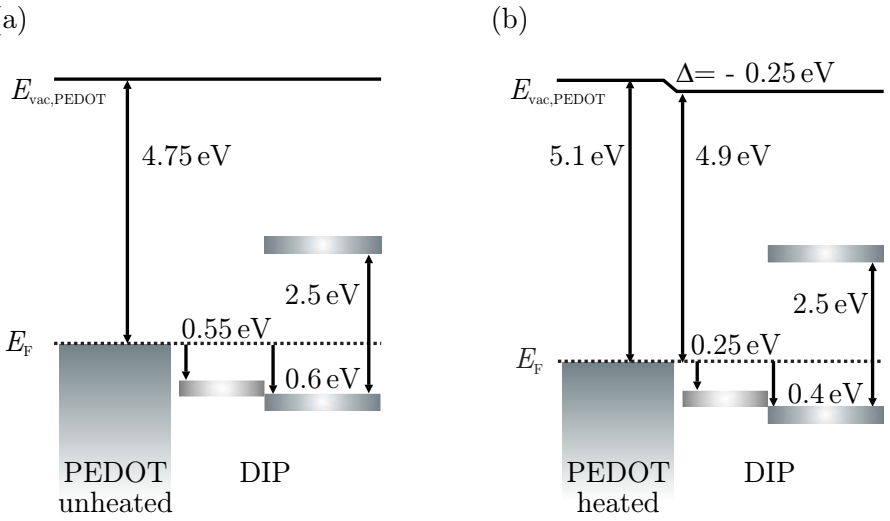

Figure 5.4.: Schematic energy level diagrams for DIP on (a) unheated and (b) heated ITO/PEDOT as derived from UPS measurements.

function of heated PEDOT, leading to positive charge carriers in the DIP layer at the PEDOT/DIP contact. Adding up the sample work function and the low binding energy onset of the DIP HOMO for the 12.2 nm bulk film yields a DIP ionization potential of $IP_{DIP} \approx 5.3\,eV \pm 0.1\,eV$.

Concerning the application in a solar cell device, the most critical parameter in the energy level diagram is the hole injection barrier (HIB), i.e., the separation between $E_{F,PEDOT}$ and HOMO level of DIP. As was shown in Sec. 3.3.9 the value of HIB can be deduced from the low binding energy onset[m] in the valence region spectra. As visualized in Fig. 5.4 the binding energy with respect to E_F amounts to 0.55 eV and 0.25 eV in the case of unheated and heated PEDOT, respectively. This result demonstrates the reduced hole injection barrier when heating PEDOT substrates during DIP evaporation.

5.1.3. Electrical characterization

To demonstrate the importance of film growth conditions, solar cells have been investigated with nominally planar heterojunctions between DIP—grown at different substrate temperatures—and C_{60} evaporated on top (with the underlying DIP film kept at room temperature). Electrical characterization has been performed by recording and analyzing j-V curves in dark and under illumination. The device preparation allows for a direct comparison between film morphology and

[m] As for hole injection the crucial energy levels are those directly at the interface, relevant values of binding energy are taken from the spectroscopy results recorded for small DIP thickness.

the resulting electrical properties in a solar cell architecture. The structure of the investigated PHJ cells is

ITO/ PEDOT/ DIP(50 nm)/ C_{60}(80 nm)/ LiF(0.3 nm)/ Al,

with DIP evaporated at substrate temperatures of RT, 60 °C and 100 °C. Results are depicted in Fig. 5.5 (a), showing the j-V characteristics under illumination (upper part) and in dark (lower part). The corresponding photovoltaic parameters are summarized in Tab. 5.1. The following discussion is focused on the shape of the j-V curves in forward bias regime—a detailed analysis with regard to photovoltaic properties of planar and bulk heterojunction solar cells will be subject of Sec. 7.1.

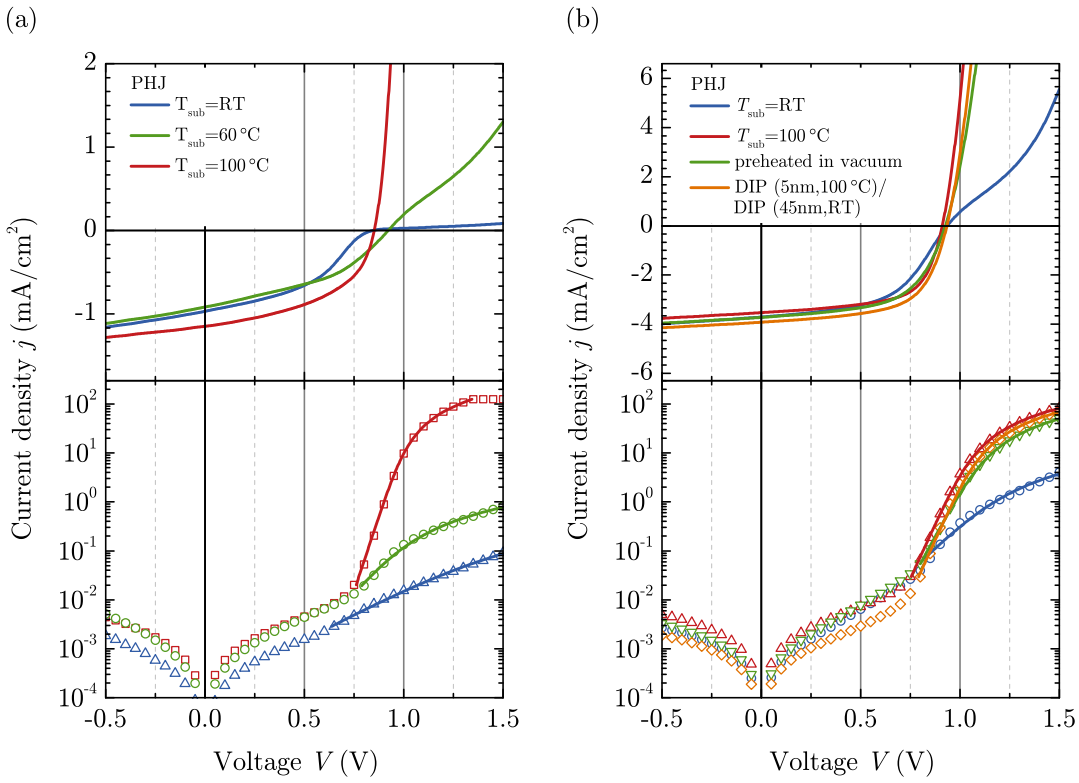

Figure 5.5.: Effect of different substrate temperatures during DIP evaporation of solar cells: (a) PHJ solar cells with ITO/ PEDOT/ DIP(50 nm)/ C_{60}(80 nm)/ LiF(0.3 nm)/ Al. (b) PHJ with ITO/ PEDOT/ DIP(50 nm)/ C_{60}(50 nm)/ BCP(5 nm)/ Al. Upper parts: j-V characteristics under simulated AM 1.5 g illumination at 100 mW/cm² (a) or under white LED illumination (b). Lower parts: Logarithmic plot of the dark j-V characteristics (open symbols). The solid lines are fits based on the modified diode equation. T_{sub} corresponds to the substrate temperature during DIP evaporation. Neat C_{60} layers are always deposited with the substrate kept at RT. Results of the fits are given in Tab. 5.1.

Table 5.1.: Open-circuit voltage V_{oc}, short-circuit current density j_{sc}, fill factor FF, specific series resistance $R_S A$, ideality factor n and dark saturation current density j_0 for PHJ solar cells with different substrate treatment during evaporation of DIP (cf. Fig. 5.5). Light illumination was realized either with a solar simulator at an intensity of one sun (first data set with LiF interlayer) or with a white LED (second data set with BCP as EBL). As the LED illumination conditions do not fulfill AM 1.5 g standards, values for power conversion efficiencies are not specified.

Substrate treatment	V_{oc} (V)	j_{sc} (mA/cm^2)	FF (%)	$R_S A$ (Ω cm^2)	n	j_0 (mA/cm^2)
PHJ cells with PEDOT as HIL and LiF as EBL (cf. j-V curves in Fig. 5.5 (a))						
T_{sub} = RT	0.84	-0.97	40.6	$1.7 \cdot 10^3$	9.1	$1.6 \cdot 10^{-4}$
T_{sub} = 60 °C	0.92	-0.92	40.9	$0.5 \cdot 10^3$	3.9	$3.8 \cdot 10^{-6}$
T_{sub} = 100 °C	0.86	-1.15	48.2	2.2	1.5	$8.6 \cdot 10^{-12}$
PHJ cells with PEDOT as HIL and BCP as EBL (cf. j-V curves in Fig. 5.5 (b))						
T_{sub} = RT	0.93	-3.7	52.8	66	4.7	$4.1 \cdot 10^{-5}$
T_{sub} = 100 °C	0.91	-3.5	62.8	4	2.0	$5.6 \cdot 10^{-9}$
preheated in vacuum	0.93	-3.7	57.8	6	2.5	$5.2 \cdot 10^{-8}$
DIP(5 nm,100 °C/45 nm,RT)	0.94	-3.9	61.0	5	2.0	$2.1 \cdot 10^{-9}$

All different substrate temperatures yield similar short circuit current densities around -1 mA/cm^2 and V_{oc} between 0.84 and 0.92 V. The most striking feature can be seen by the j-V characteristics of the device where DIP was grown at room temperature: the curve is strongly affected by an s-shape behavior. Thus, the curves under illumination show a decrease of the current close to the open-circuit voltage and above V_{oc} which reduces the fill factor of the cell. This feature decreases continuously when heating the substrate to higher temperatures during DIP deposition and vanishes completely for the device with DIP grown at 100 °C. The occurrence of the undesired s-shape in the current-voltage characteristics under illumination is correlated to suppressed forward currents being apparent already in the dark j-V characteristics, as displayed in the lower part of Fig. 5.5 (a) on a semi-logarithmic scale. Based on the general diode equation (2.7) and by neglecting the parallel resistance R_P, the forward-bias characteristics can be fitted (solid

lines) using a modified Shockley equation:[n]

$$j(V) = j_0 \left\{ \exp\left[\frac{\mathrm{e}\,(V - j(V) R_\mathrm{S} A)}{n k_\mathrm{B} T} \right] - 1 \right\}. \tag{5.1}$$

As mentioned in Sec. 2.1.6 the Shockley equation was originally applied for analyzing and parameterizing the current-voltage characteristics of inorganic pn-junction solar cells.[330] However, recently it was successfully adapted to organic solar cells as well[18,331]—even in its modified variant.[332] As was demonstrated by the simulations in Sec. 2.1.6, the slope of the j-V characteristics in the exponential regime depends on j_0 and the ideality factor n. The cell with DIP evaporated at a substrate temperature of 100 °C shows an ideality factor of 1.5. For the other substrate temperatures the determination of n is difficult as the exponential regime is not sufficiently pronounced to be fitted unambiguously. However, the most noticeable difference in the dark characteristics is the continuous decrease of series resistance when the substrate temperature during DIP evaporation is raised. As can be seen from Tab. 5.1, $R_\mathrm{S}A$ decreases by almost three orders of magnitude from 1.7 kΩ cm^2 at room temperature to 2.2 Ω cm^2 at 100 °C substrate temperature, causing the systematic decline of the s-shape in the j-V curves until completely vanishing at the highest temperature.

S-shaped solar cell characteristics have recently gained more and more attention in literature. Thus, s-shaped curves are commonly ascribed to energetic injection and extraction barriers between photoactive layer systems and electrodes.[25,333,334] In this case, s-shaped characteristics can be clearly connected to the growth temperature of the DIP layer.

As has been shown in Sec. 5.1.1 the variation of substrate temperature goes along with a pronounced change in crystallization behavior which likely influences the transport properties inside the film. On the other hand, Sec. 5.1.2 shows that annealing of PEDOT films spin-cast onto ITO leads to an increase of its work function, which yields a lowering of the hole injection barrier from the anode to the HOMO of DIP. Concerning the s-shaped characteristics of the solar cells, it is hard to distinguish the role of charge carrier injection at the electrodes and transport inside the DIP film as both might be affected by substrate heating. In order to separate both effects a comparison was made between solar cells with the following variations:

[n] This approximation is reasonable for solar cells with minimal leakage currents resulting in $R_\mathrm{P} \gg R_\mathrm{S}$.

- Substrate unheated ($T_{\mathrm{sub}} = \mathrm{RT}$)
- Substrate heated during DIP evaporation ($T_{\mathrm{sub}} = 100\,^{\circ}\mathrm{C}$)
- Substrate heated to 100 °C inside the evaporation chamber but left to cool down to RT before DIP growth
- First monolayers (5 nm) of DIP grown at $T_{\mathrm{sub}} = 100\,^{\circ}\mathrm{C}$ followed by RT growth of the remaining 45 nm of DIP

The device stack using DIP and C_{60} as photoactive materials was extended by an additional layer of the exciton blocking material BCP. Its beneficial effect on solar cell performance has already been addressed in Sec. 3.1.4 and is analyzed in more detail in Sec. 8. The following device stack was used:

ITO/ PEDOT/ DIP(50 nm)/ C_{60}(50 nm)/ BCP(5 nm)/ Al.

The j-V characteristics of the corresponding solar cells are depicted in Fig. 5.5 (b) and the cell parameters are listed in Tab. 5.1—illumination was realized with a white LED, not allowing for a correct declaration of the power conversion efficiency. All cells show open-circuit voltages slightly above 0.9 V and almost similar short-circuit currents. For devices where the substrate was heated before, during, or partly during DIP evaporation an ideality factor of $n \approx 2$–2.5 and a specific series resistance of $R_{\mathrm{S}}A \approx 4$–$6\,\Omega\,\mathrm{cm}^2$ was observed. Only for the completely unheated device $R_{\mathrm{S}}A$ is increased by a factor of more than 10, causing the s-shape of the j-V curve accompanied by a reduction in fill factor of approximately 20 %.

The corresponding AFM images are depicted in Fig. 5.6. For 5 nm DIP on heated PEDOT (Fig. 5.6 (a)), the beginning of terrace growth is visible. It is clearly distinguishable from the smooth surface of a pure ITO substrate covered with PEDOT, as can be seen from Fig. 5.6 (b). Evaporating another 45 nm of DIP—after the substrate has cooled down—leads to a morphology with small islands (Fig. 5.6 (c)) similar to the one without heated underlayer (cf. Fig. 5.1 (a)), showing that the underlying structure is not adapted. For DIP evaporation at room temperature but on a preheated PEDOT coated ITO substrate, the topography—as can be seen in Fig. 5.6 (d)—is similar to the case of a completely unheated substrate. This shows that the DIP layer morphology and crystallinity are not the primary sources of s-shaped j-V characteristics. It rather indicates that the interface energetics between PEDOT and DIP play the decisive role.

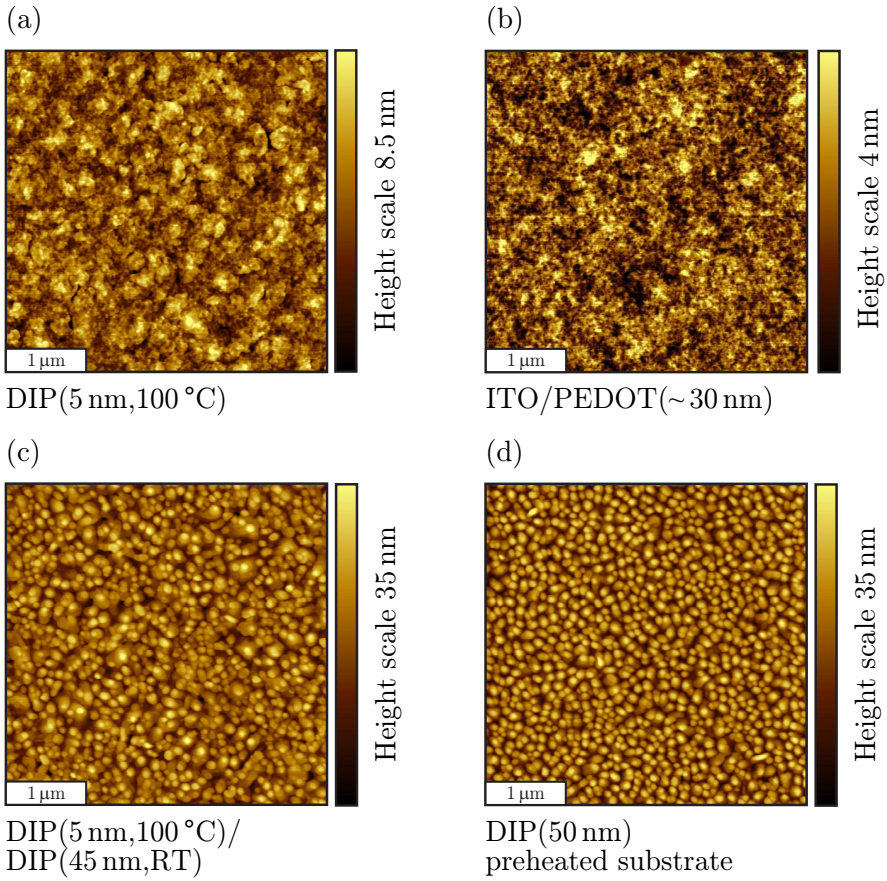

Figure 5.6.: AFM images of (a) ITO/ PEDOT/ DIP(5 nm, T_{sub} = 100 °C), (b) PEDOT(≈ 30 nm) spin coated on ITO, (c) ITO/ PEDOT/ DIP(5 nm, T_{sub} = 100 °C)/ DIP(45 nm, T_{sub} = RT) and (d) ITO/ PEDOT/ DIP(50 nm) deposited on a substrate which was preheated to 100 °C but left to cool down to room temperature before DIP growth. The total image size is $4 \times 4\,\mu m^2$ in all cases.

5.1.4. Discussion

In the previous sections the impact of substrate heating on the anode/donor interface has been investigated on the basis of DIP/C_{60} planar heterojunction solar cells. The studies emphasize the crucial influence of T_{sub} during DIP film growth on morphology, structure and interface energetics, and thus on the overall device performance including s-shaped j-V characteristics.

Recently, different aspects being responsible for the appearance of that undesired feature have been proposed. In most of the cases the s-shape is attributed to energy barriers at the contacts,[333–338] whereas the formation of these interface barriers might have different origins. Comparing drift-diffusion simulations with

experimental results Tress *et al.* emphasize the crucial role of injection barriers between hole-transport layer and donor material both in PHJ and BHJ devices.[336] They show that increasing barrier heights lead to s-shaped j-V curves with low forward currents in the case of PHJ devices, which manifests in severely reduced FFs. Gupta *et al.* ascribe the s-shape of their j-V curves to charge accumulation at the interface between the electrode and the active organic film resulting from incomplete cathode metal coverage or chemical defects at the interface.[337] Other authors report on s-shapes caused by thermally degraded PEDOT or oxidized Ca cathode leading to low conductivity and high series resistance.[338] Besides interface barriers, factors like morphology and thickness of the active layers can influence the curvature of the j-V curves of solar cell devices.[339] In addition to that, the effect of charge carrier mobility on fill factor was demonstrated in various studies.[25,340,341] By the example of PHJ solar cells based on DIP/C_{60} it was shown that substrate temperature can strongly affect the j-V curves—including the appearance of s-shaped characteristics.

Morphological investigations reveal that growth at elevated temperature leads to the formation of a cohesive network of pronounced crystalline DIP domains, yielding a large surface area that can be covered with C_{60} molecules in planar heterojunctions. The electronic structure of the PEDOT/DIP interface was investigated by means of UPS measurements. Upon annealing, the work function of PEDOT is increased from 4.9 eV to 5.1 eV. This coincides with the observation of Koch clearly demonstrating that an annealing step of PEDOT films spin-cast onto ITO leads to an increase of its work function which critically depends on the residual water content in the conductive polymer film.[88] Furthermore, it was observed that the low binding energy onset of the DIP HOMO at the interface to PEDOT amounts to 0.55 eV and 0.25 eV in the case of unheated and heated PEDOT, respectively. As this value corresponds to the hole injection barrier at the anode/donor interface, it can be concluded that an additional annealing step of PEDOT reduces the barrier for hole injection into the HOMO level of DIP. Concerning its impact on device functionality, it was shown by Campbell *et al.* that for typical organic light-emitting diodes, an energy barrier of 0.4 eV represents the transition between space-charge limited current, if the Schottky energy barrier to injection is less, and contact limited, if it is larger than that critical value.[342] Thus, it seems plausible to expect noticeable differences in device characteristics as a result of injection barriers, modified by substrate temperature.

Investigations on solar cells show that the performance of devices where DIP was grown at room temperature is seriously affected by an s-shaped behavior. By heating the substrate during or prior to DIP deposition, dark currents in forward direction are increased. This change is accompanied with a lowering of the specific

series resistance which is crucial for high fill factors and vanishing s-shapes in the current-voltage characteristics. The fact that the series resistance mainly influences the fill factor coincides with theoretical predictions by Yoo *et al.*: They show that j_{sc} as well as V_{oc} are—up to a certain point—insensitive to R_S, while the fill factor can be strongly affected.[18]

Comparing the j-V curves with the corresponding morphologies of the DIP films, it can be seen that substrate heating before DIP evaporation or during the deposition of the DIP interlayer does not lead to a similarly pronounced microstructure as found for elevated substrate temperatures. However, structural investigations indicate highly crystalline films with DIP crystallites extending throughout the entire thickness, both for unheated and heated substrate. Thus, charge carrier transport through the DIP layer is supposed to be independent of substrate temperature. The solar cell characteristics where the substrate was heated before DIP evaporation or restricted to a small fraction of the DIP film are very similar to the cell where DIP was grown at 100 °C. Together with the results from UPS measurements it can finally be stated that the decisive role of substrate heating can be mostly attributed to a reduction of the hole injection barrier between the Fermi level of PEDOT and the HOMO level of the donor material DIP. The reduced HIB is responsible for the decrease in series resistance of the solar cells whenever the substrate is heated in vacuum prior to deposition of the donor. Both, the exceptionally high structural order in a DIP film evaporated on a heated substrate as well as its favorable energy level alignment with the PEDOT electrode explain the high fill factors for this material system.

5.2. The role of hole injection layers

In the previous section substrate heating was used to manipulate the work function of the PEDOT—which was found to change the barrier height for hole injection into DIP. Another approach is the use of alternative hole injection layers, such as the PEDOT:PSS formulations HIL1.3 and HIL1.3 N as well as the polymer Plexcore. As introduced in Sec. 3.1.2 these materials cover a range of different work functions. Their influence will be shown on the basis of morphological, electronic and—most importantly—by means of electrical characterization of corresponding solar cells.

5.2.1. Morphological investigation

As a comparison to the morphological studies performed on ITO/PEDOT/DIP, similar topographical investigations have been carried out by using the alternative

hole injection layers. Figure 5.7 shows AFM images of single DIP films and DIP/C_{60} heterostructures on ITO/HIL1.3 (top row) and ITO/HIL1.3 N (bottom row) which have been evaporated at different substrate temperatures.

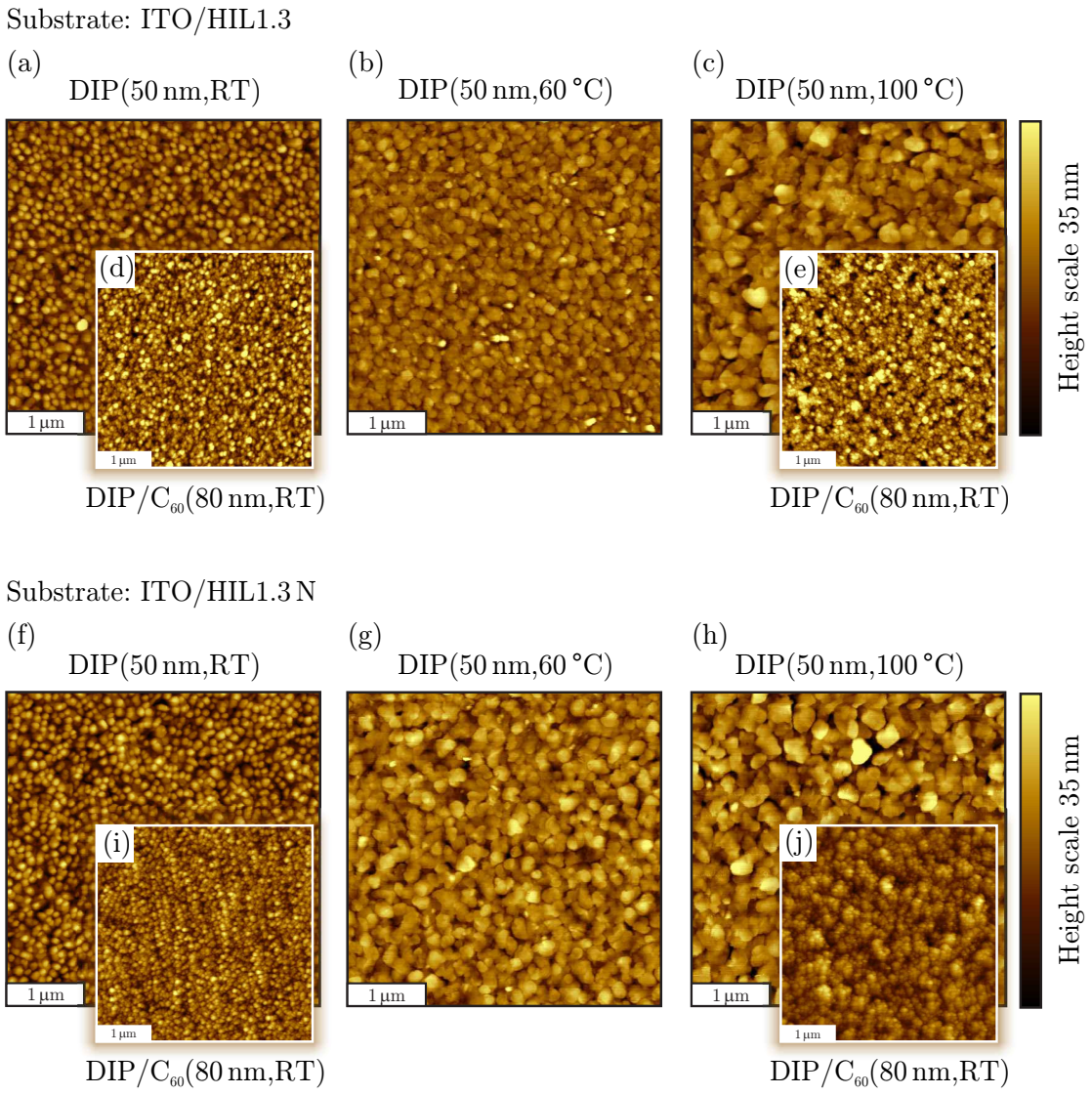

Figure 5.7.: Top row: AFM images of DIP films (50 nm) on ITO/HIL1.3, evaporated at substrate temperatures of (a) RT, (b) 60 °C, and (c) 100 °C. The insets of (a) and (c) show AFM images of C_{60} (50 nm) on ITO/PEDOT/DIP(50 nm), with DIP evaporated at substrate temperatures of (d) RT and (e) 100 °C. Bottom row: See top row but with ITO/HIL1.3 N as substrate. In all cases C_{60} is evaporated without substrate heating. The total image size is $4 \times 4\,\mu m^2$ in all cases.

Compared to ITO/PEDOT as substrate (cf. Fig. 5.1), the growth behavior on HIL1.3 and HIL1.3 N seems to be very similar; small round-shaped islands are observed when DIP is grown on unheated substrates (see Fig. 5.7 (a) and (f)) whereas the surface topography changes to a broadened structure with extended crystallites when heating the substrates (see Fig. 5.7 (c) and (h)). Intermediate substrate temperatures also induce larger crystallites, however, less pronounced. The microstructure formed at $T_{\mathrm{sub}} = 100\,^{\circ}\mathrm{C}$ is not as extensive as was observed for PEDOT, which may be due to deviations in thermal coupling to the substrate. Evaporating C_{60} on top of DIP films leads to the formation of small C_{60} domains which adapt to the underlying morphology (Fig. 5.7 (d) and (e) on HIL1.3, (i) and (j) on HIL1.3 N).[o]

5.2.2. Electronic structure

In order to investigate the energy level alignment between the alternative PEDOT:PSS containing formulations and DIP, thickness dependent UPS measurements were performed on unheated HIL1.3. The corresponding UPS spectra are depicted in Fig. 5.8 (a) and (b). The schematic energy level diagram derived therefrom is shown in Fig. 5.8 (c).

As can be determined from the secondary electron cutoff (Fig. 5.8 (a)), the work function of pristine HIL1.3 ($\Phi = 5.70\,\mathrm{eV}$) is almost 1 eV larger than the work function of unheated PEDOT and even higher than that of heated PEDOT (cf. Fig. 5.4). Upon DIP deposition the sample work function changes to 4.9 eV, which remains constant for higher DIP coverage. As explained in Sec. 2.2.4 this observation is consistent with pinning of the positive polaron level of DIP due to the high initial work function of HIL1.3. The work function reduction saturates after completion of the first two DIP monolayers, and an interface dipole of $-0.8\,\mathrm{eV}$ is caused by positive charges residing on interfacial DIP molecules. The position of the low binding energy onset of the HOMO level is located 0.3 eV below E_{F} for 1.6 nm DIP coverage while it is constant at 0.45 eV for multilayers. This can be assigned to DIP cationic species (positive polarons) present at the interface to HIL1.3, i.e., the HIL1.3/DIP contact can be considered as ohmic due to charge transfer doping of DIP.[343] The formation of an ohmic contact is visualized in Fig. 5.8 (d) and (e): Before contacting, the HOMO of DIP is situated above the Fermi level of HIL1.3 as the ionization potential of DIP is smaller than the work function of HIL1.3. Upon bringing both materials in intimate contact, the Fermi level aligns and the HIL1.3/DIP interface can be described with an accumulation of holes within a narrow region inside the DIP. Adding up the sample work function and the low binding energy onset of

[o] Corresponding morphological investigations with C_{60} evaporated on DIP with PEDOT as hole injection layer will be presented in Sec. 7.1.1.

the DIP HOMO for the 10 nm bulk film yields a DIP ionization potential which is consistent with the measurements presented on PEDOT (see Sec. 5.1.2).

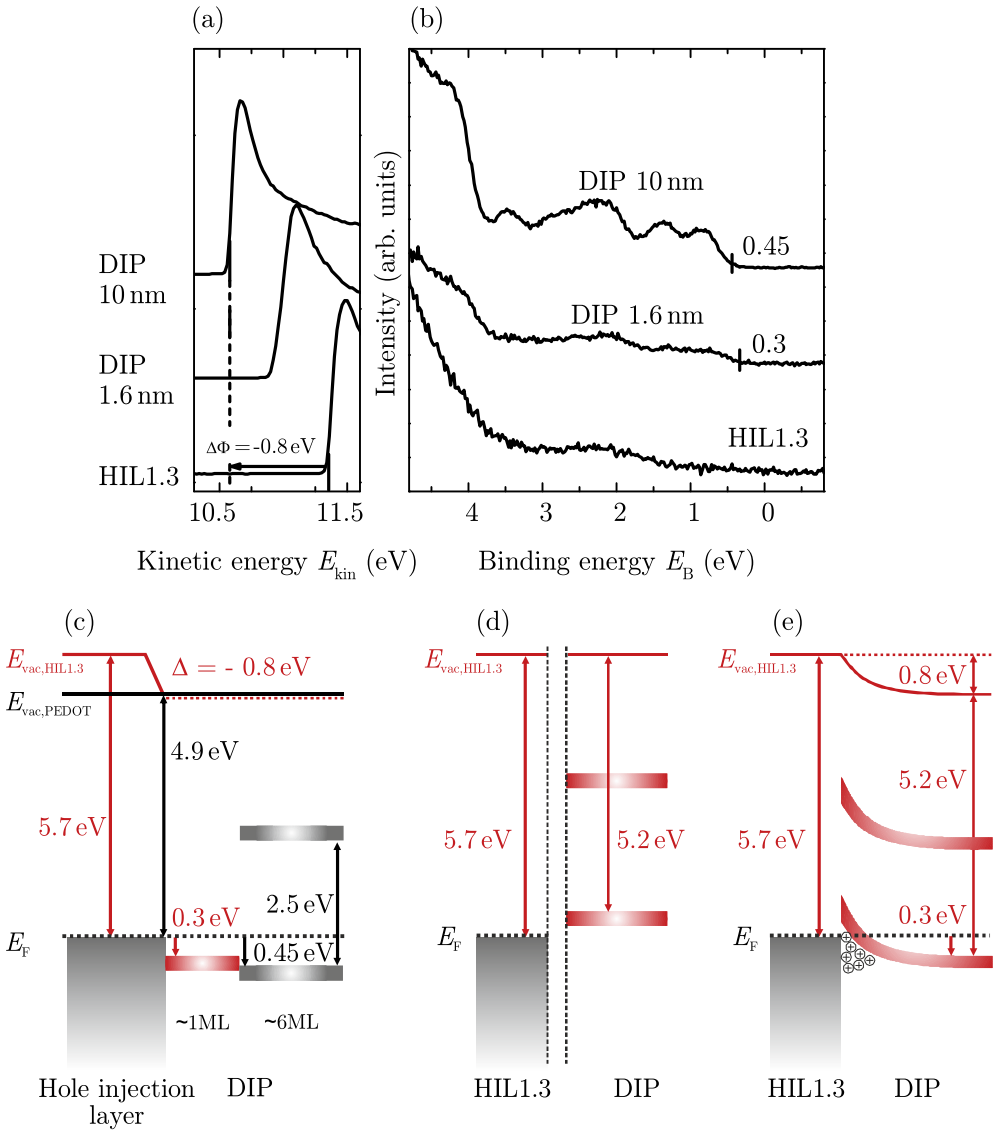

Figure 5.8.: Ultraviolet photoelectron spectra of unheated ITO/HIL1.3 substrates with different coverage of DIP. (a) Secondary electron cutoff (SECO) spectra and (b) valence region spectra (taken from Ref. 327). (c) Schematic energy level diagram of the interface between DIP and the hole injection layer HIL1.3 (red) as compared to PEDOT (black). Visualization of the formation of an ohmic contact between HIL1.3 and DIP: energetics at the interface before contact (d) and after contact (e).

5.2.3. Electrical characterization

To investigate the influence of the material used for hole injection, solar cells have been analyzed based on planar heterojunctions of DIP and C_{60}. Cells with the structure

ITO/ HIL/ DIP(50 nm)/ C_{60}(50 nm)/ BCP(5 nm)/ Al

were fabricated with DIP grown at room temperature or T_{sub} = 100 °C. HIL1.3, HIL1.3 N and Plexcore were used as hole injection layer—each of them with and without substrate heating. As work functions of HIL1.3 and HIL1.3 N are expected to be comparable, similar electronic behavior is expected for both PEDOT:PSS based formulations.

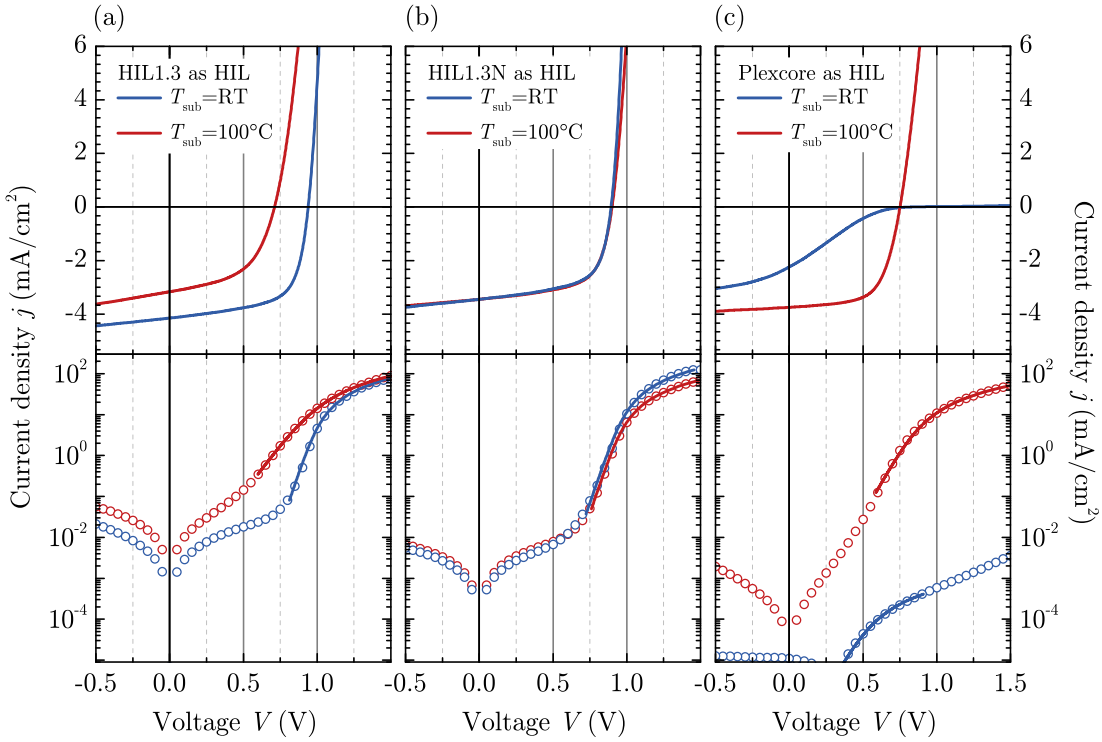

Figure 5.9.: Effect of different hole injection layers (HILs) combined with different substrate temperatures during DIP evaporation of PHJ solar cells with structure ITO/ HIL/ DIP(50 nm)/ C_{60}(50 nm)/ BCP(5 nm)/ Al and a hole injection layer of (a) HIL1.3, (b) HIL1.3 N, and (c) Plexcore. Upper parts: j-V characteristics under white LED illumination. Lower parts: Logarithmic plot of the dark j-V characteristics (open symbols). The solid lines are fits based on the modified diode equation. Neat C_{60} layers are always deposited with the substrate kept at RT. Results of the fits are given in Tab. 5.2.

The j-V characteristics in dark and under illumination are depicted in Fig. 5.9 and the photovoltaic parameters are listed in Tab. 5.2. By analogy to the analysis of PEDOT based solar cells (Sec. 5.1.3), dark j-V curves are fitted by the modified Shockley equation (5.1). The fits can be found as straight lines in the lower parts of Fig. 5.9, and fitting parameters as the specific series resistance $R_S A$ and ideality factor n are included in Tab. 5.2.

Except for the heated HIL1.3—which differ both in V_{oc} as well as in j_{sc}—the alternative PEDOT:PSS containing formulations (i.e., HIL1.3 and HIL1.3 N) show almost equal characteristic cell parameters when used as HIL, regardless of whether or not the substrate is heated during DIP evaporation. The open-circuit voltages are located between 0.90 and 0.94 V, short-circuit current densities are in the range between -3.5 and $-4.2\,\mathrm{mA/cm^2}$ and the fill factor amounts to approximately 62 to 64%. The cells show unhindered currents in forward direction which are reflected in low series resistances between 3 and $6\,\Omega\,\mathrm{cm^2}$. Compared to the morphological changes induced by substrate heating (cf. Fig. 5.7), the solar cell characteristics

Table 5.2.: Open-circuit voltage V_{oc}, short-circuit current density j_{sc}, fill factor FF, specific series resistance $R_S A$, ideality factor n and dark saturation current density j_0 for ITO/ HIL/ DIP(50 nm)/ C_{60}(50 nm)/ BCP(5 nm)/ Al PHJ solar cells with different hole injection layers (cf. Fig. 5.9). Light illumination was realized with a white LED. As the LED illumination conditions do not fulfill the AM 1.5 g standards, values for power conversion efficiencies are not specified.

Substrate treatment	V_{oc} (V)	j_{sc} ($\mathrm{mA/cm^2}$)	FF (%)	$R_S A$ ($\Omega\,\mathrm{cm^2}$)	n	j_0 ($\mathrm{mA/cm^2}$)
PHJ cells with HIL1.3 as HIL (cf. j-V curves in Fig. 5.9 (a))						
T_{sub} = RT	0.94	-4.2	64.2	3	1.7	$1.8 \cdot 10^{-9}$
$T_{sub} = 100\,^{\circ}\mathrm{C}$	0.71	-3.2	51.6	4.5	3.6	$5.3 \cdot 10^{-4}$
PHJ cells with HIL1.3 N as HIL (cf. j-V curves in Fig. 5.9 (b))						
T_{sub} = RT	0.9	-3.5	62.0	3.1	1.8	$1.2 \cdot 10^{-9}$
$T_{sub} = 100\,^{\circ}\mathrm{C}$	0.90	-3.5	62.3	6.3	1.7	$4.3 \cdot 10^{-10}$
PHJ cells with Plexcore as HIL (cf. j-V curves in Fig. 5.9 (c))						
T_{sub} = RT	0.83	-2.3	18.3	$250 \cdot 10^3$	5.3	$1.3 \cdot 10^{-6}$
$T_{sub} = 100\,^{\circ}\mathrm{C}$	0.75	-3.8	62.3	9.8	2.7	$2.4 \cdot 10^{-5}$

including the values of $R_S A$ are almost independent of T_{sub}. Moreover, the parameters are comparable to those of PHJ cells with PEDOT heated to 100 °C during or prior to DIP deposition, and BCP as EBL measured under equal conditions (cf. Fig. 5.5 (b) and Tab. 5.1). These findings emphasize the significant role of the HIL's work function and indicate that bulk effects as can be deduced from morphological variations play a minor role.

When heating HIL1.3 during DIP deposition the situation appears different; both V_{oc} and j_{sc} are reduced compared to growth at room temperature. As the morphology does not reveal any abnormalities, the reason may be modified energetics at the interface to the DIP which have not been examined in closer detail. However, it is known that ionization potentials can depend on the orientation of the molecule, which might change when deposited under substrate heating.[303] On the other hand, lying DIP molecules would be favorable for light harvesting which, in turn, would be reflected in increased current densities, which is not observed. Another possible explanation could be found in degradation of the HIL1.3 when heated to higher temperatures which might be a result of its modified composition compared to PEDOT. Concerning the reduced open-circuit voltage, increased recombination losses might play a role: It has been introduced in Sec. 2.3.2, that V_{oc} is ultimately limited by the interfacial energy gap E_{DA}—however, with additional losses due to radiative and non-radiative recombination. At the same time, recombination at the D/A interface also determines the injected current density in dark. Thus, a direct correlation between V_{oc} and the dark current characteristics is not astonishing and is quantitatively expressed by Eq. (2.25). This relation will be further discussed in Sec. 7.2.1, however, the essential outcome can be used to give a possible explanation for the reduction of V_{oc}: Apart from the series resistance R_S and the diode ideality factor n, the dark saturation current j_0 is determined when fitting the dark j-V curve by means of Shockley's equation—providing a measure for the recombination behavior within the cell. Upon heating HIL1.3 during DIP deposition, j_0 increases by five orders of magnitude. This strongly indicates enhanced recombination losses as the main cause for reduced V_{oc}—whereas its exact origin remains unclear.

When Plexcore is used as HIL the solar cell characteristics change even for both substrate temperatures. At RT the shape of the j-V curve is affected by a strong s-shape leading to a FF of only 18%. As a result of an extremely high specific series resistance of 250 kΩ cm^2, this effect can be attributed to a high injection barrier at the anode/donor interface which could at the same time explain the low leakage currents in reverse direction. For the heated case there is no s-shape observable which is reflected in high FF of 62%—however V_{oc} is reduced to similar values as obtained for heated HIL1.3. Here again, recombination losses—reflected

by comparatively high values of j_0—can, at least partly, be made responsible for the reduced V_{oc}.

5.2.4. Discussion

Investigations have been focused on different hole injection layers and their influence on morphology, interface energetics and device characteristics of DIP/C_{60} based PHJ cells. The usage of HIL1.3 and HIL1.3 N as alternative hole injection layer instead of PEDOT leads to strongly enhanced currents in forward direction, accompanied by high fill factors, even though the substrate is kept at room temperature during DIP evaporation. Energetic studies demonstrate a high initial work function of HIL1.3 ($\Phi = 5.7\,\mathrm{eV}$), leading to pinning of the positive polaron level of DIP. This results in low hole injection barriers of 0.3 eV at the interface between unheated HIL1.3 and DIP, being comparable to those found for heated PEDOT. The fact that the work function of multilayer DIP deposited on PEDOT—both heated and unheated—and HIL1.3 is almost identical ($\Phi_{DIP} \approx 4.9\,\mathrm{eV}$) allows to consider this value as the critical substrate work function for energy level pinning.

Regardless of the differences in morphology caused by varying substrate temperatures—the solar cell characteristics including the values of $R_S A$ are almost identical. This fact emphasizes the significant role of the HIL's work function rather than bulk effects. Moreover, these findings confirm the statement given in Sec. 5.1 that the reduced series resistances in devices where PEDOT was heated prior or during DIP deposition can be mainly ascribed to a lowering in hole injection barrier caused by heating up the PEDOT in vacuum. By contrast, morphological changes—and with that changes in transport behavior inside the DIP bulk—seem to play a minor role for the series resistance of solar cells.

The usage of Plexcore as alternative HIL has not proven beneficial for OPVCs based on DIP/C_{60}. With unheated substrates, extreme s-shapes appear in the j-V characteristics being indicative of inappropriate energy level alignment. Heating the substrate seems to reduce the hole injection barrier—which is reflected in high FFs—however, V_{oc} is reduced, which is traced back to enhanced recombination losses.

Apart from energy barriers as decisive factor for the occurrence of s-shaped j-V characteristics, Giebink *et al.* proposed an alternative explanation.[26] They implemented specific properties of organic heterojunctions like polaron pair generation, recombination and dissociation by means of a modified Shockley equation which shows that small built-in potentials combined with large polaron pair recombination rates lead to concavities in the j-V curves. However, as this kind of

s-shape exclusively affects the fourth quadrant of the solar cell characteristics this argumentation cannot be applied here and reduced V_{bi}—which is accompanied by a reduction of the anode work function—is not the decisive factor for the s-shape. Furthermore, misaligned transport levels of the exciton blocking layer BCP as possible explanation for s-shapes[27] can be excluded as unhindered transport with BCP/Al is observed exclusively by heating the PEDOT substrate or using an alternative HIL. Instead, all presented studies indicate that the observed s-shape of j-V curves can be attributed to the hole injection barrier at the anode/DIP interface.

Chapter 6

Charge carrier mobility inside the donor

In order to study the transport properties of holes and electrons in DIP, single-carrier devices were fabricated and examined both regarding to their current-voltage behavior as well as by impedance spectroscopy. The experimental results allow the determination of the prevailing transport mechanism and an estimation of the respective charge carrier mobility in diode configuration. Moreover, mobility measurements based on field-effect transistors reveal that purity variations between different DIP batches can have considerable impact on the solar cell performance.

6.1. Electron transport in DIP diodes

For investigating the electron mobility inside a DIP thin film, electron-only devices with the following layer structure were prepared:

Glass/ PEDOT($\approx 30\,\mathrm{nm}$)/ Al($100\,\mathrm{nm}$)/ DIP/ Al($100\,\mathrm{nm}$),

with nominal DIP film thicknesses of $d_1 = 100\,\mathrm{nm}$, $d_2 = 150\,\mathrm{nm}$, $d_3 = 200\,\mathrm{nm}$ and $d_4 = 250\,\mathrm{nm}$. Based on the comparatively low work function of Aluminum, high hole injection barriers to the HOMO of DIP are expected. The high barriers suppress hole current and enable electron-only devices. Using PEDOT as interlayer between glass and Aluminum reduces inhomogeneities at the metal/semiconductor interface, as was reported by Steyerleuthner *et al.* in Ref. 344. The authors could show that hillock-free aluminum bottom electrodes are obtained when the metal is evaporated on PEDOT—enabling smooth and stable electron currents.

6.1.1. Electrical characterization

In Fig. 6.1 the j-V characteristics of several electron-only devices are presented. According to Eq. (2.14) the current in reverse direction varies almost linearly with the applied voltage. However, the current in this voltage regime does not correlate with the DIP layer thickness as would be expected for ohmic current which is purely carried by intrinsic charge carriers. Together with the fact, that the current densities are comparatively high in reverse bias, the current flowing in the negative voltage regime can probably be attributed to above-average leakage currents, conceivable if assuming rough DIP films as well as interdiffusion of Al clusters by top contact deposition (as will be topic of Sec. 8.2). However, it has to be mentioned that there is no information about DIP film growth when deposited on ITO/PEDOT/Al as substrate.

In forward bias the current steeply increases at $V = 0\,\mathrm{V}$ not showing a pronounced turn-on voltage. From the slope of the $\log(j)$–$\log(V)$ plot (Fig. 6.1 (b)) it can be deduced that the current density j depends quadratically on V for voltages $V > 0.4\,\mathrm{V}$. As was introduced in Sec. 2.2.3 this behavior is characteristic for space-charge limited current. The absence of a region with slope exceeding two indicates that the electron transport in DIP can be regarded as almost trap free. Thus, the experimental data is fitted with trap-free SCLC as given by Eq. (2.16) with a field-dependent mobility. The fit results are shown as straight lines in Fig. 6.2 (a)—including the marked data range used for the fit. With $\varepsilon(\mathrm{DIP}) = 4$, it is found that

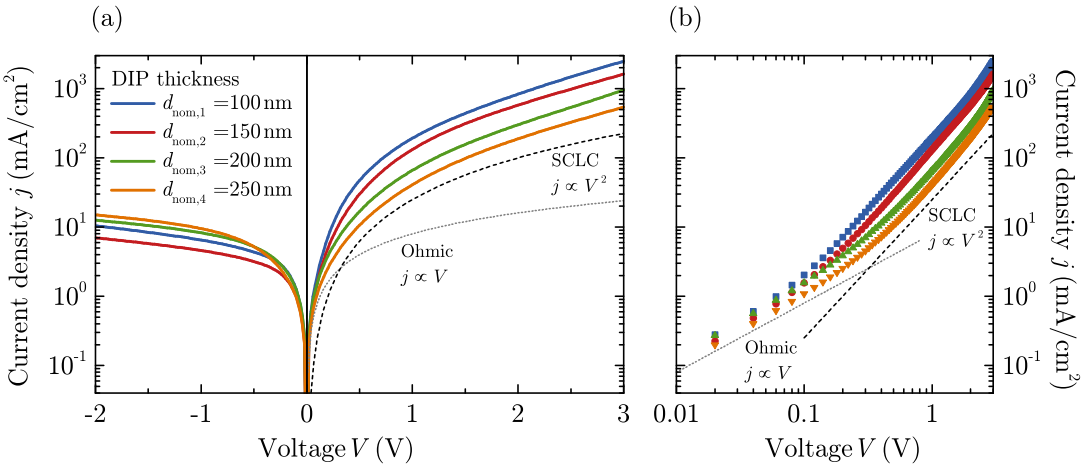

Figure 6.1.: j-V characteristics of Al/DIP/Al electron-only devices with different DIP layer thicknesses: (a) semi-logarithmic representation, (b) double-logarithmic representation. For comparison, ohmic behavior (dotted line) and bulk limited SCLC according to Eq. (2.15) (dashed line) are included.

the j-V characteristics of the devices are well described by $\mu_{e,0} = 1.8 \cdot 10^{-4}\,\mathrm{cm}^2/\mathrm{Vs}$. The remaining fitting parameters, such as the field-activation parameter γ, V_{bi} and the DIP layer thickness are listed in Tab. 6.1. The deviations between fit and data observed at high voltages might be caused by resistive heating of the samples during measurement and thermally activated charge carrier transport according to Sec. 2.2.3.

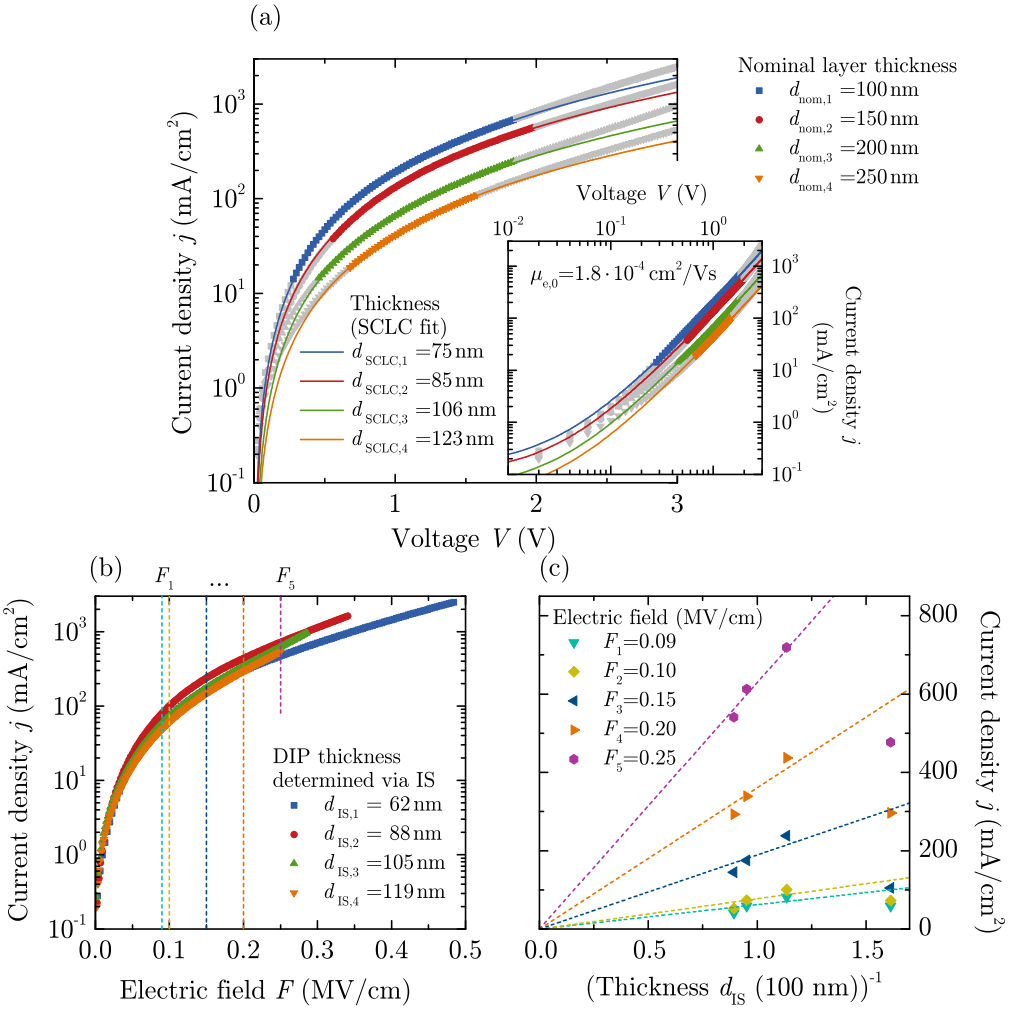

Figure 6.2.: j-V characteristics of DIP electron-only devices for several layer thicknesses. (a) Semi-logarithmic representation of measurement data (symbols) with fitted curves (straight lines) for SCLC—fitting parameters are listed in Tab. 6.1. Double-logarithmic representation is shown in the inset. The colored data mark the voltage regimes used for the fit. (b) Electric field dependence of the current density. The conversion from voltage to electric field is done by using the thicknesses as gained by impedance data (cf. Fig. 6.5). (c) Thickness dependence of the current (j versus d_{IS}^{-1}) at various constant electric fields as given in the legend.

The deviation of the fitted curves at low voltages up to approximately 0.3 V can be found in the assumptions which are entering the model: In the description of SCLC, the total current flow is determined by drift current alone while the diffusion contribution is neglected. This assumption does not hold for small voltages and deviations are expected in this region.[32] The small built-in voltage of $V_{\mathrm{bi}} = -0.002\,\mathrm{V}$ would be in good agreement with the fact, that the same material (Al) is used both as anode and as cathode. However, from the rectifying current-voltage behavior as observed for all devices it can be considered that both Aluminum electrodes show different work functions. As already mentioned in Sec. 2.2.4 this fact is relatively likely when taking different interfacial dipoles into account.

Even though the data points are well described by the fitted curves in a wide voltage range, the layer thicknesses as were given by the fit strongly differ from the nominally deposited ones. The high leakage currents in the negative voltage regime already suggest rough DIP films growing on Al substrate or interdiffusion of Al clusters during top contact deposition. Strong variances in film thickness due to inaccuracies in the determination of the tooling factor can be excluded as hole-only devices which were prepared in parallel show correct film thicknesses as were determined by impedance measurements (see Sec. 6.2). However, the thicknesses as given by the SCLC fit are in good agreement with the thicknesses determined by impedance spectroscopy as will be shown in the following section. This confirms the assumption of rough films—enhanced by the interdiffusion of Al along the grain

Table 6.1.: Analysis of electron-only devices. d_{nom}, d_{IS} and d_{SCLC} denote the nominal layer thickness and the thicknesses given by fit results based on impedance measurements and SCLC model, respectively. Besides values for the series resistance R_{S} extracted from IS data, fit parameters such as mobility μ_0, field-activation parameter γ, and built-in voltage V_{bi} are included.

d_{nom}(nm)	d_{IS}(nm)	$R_{\mathrm{S}}(\Omega)$	d_{SCLC}(nm)	
Electron-only devices (cf. j-V curves in Fig. 6.1)				
$d_1 = 100$	62*	14	76	$\mu_{\mathrm{e},0} = 1.8 \cdot 10^{-4}\,\mathrm{cm}^2/\mathrm{Vs}$ $\gamma = 4.6 \cdot 10^{-4}\,(\mathrm{cm/V})^{1/2}$ $V_{\mathrm{bi}} = -0.002\,\mathrm{V}$
$d_2 = 150$	88*	15	85	
$d_3 = 200$	105*	10	106	
$d_4 = 250$	119*	9	123	

* Due to the asymmetric behavior of the j-V and C-V-curves, thicknesses are not determined from the high-frequency plateau usually assigned to geometric capacitance. Instead, values are determined from saturation regime of C-V-measurements at reverse bias as shown in Fig. 6.5.

boundaries of polycrystalline DIP.

However, the strong differences between nominal and fitted layer thicknesses and the vanishing V_{bi}, forces to reconsider the assumption of space-charge limitation of the current. Another possibility has to be taken into account, namely the case of contact limitation. As was introduced in Sec. 2.2.3 the injection limited current depends on the electric field alone—regardless of the thickness—which would lead to overlapping curves for all thicknesses when plotted as a function of the electrical field $F = V/d_{IS}$. As shown in Fig. 6.2 (b) this is not the case. Instead there is a factor of 2 difference between the samples. In contrast to the thickness independence in the case of injection limitation, it was shown in Sec. 2.2.3 that for trap-free SCLC (with or without field-dependent mobility) the current at constant electric field scales with d_{IS}^{-1}. Apart from the thinnest sample, this condition is fulfilled over a wide range of electric fields (see Fig. 6.2 (c)) and confirms the validity of the space-charge limitation. The data points for the thinnest sample are located below the fitted curve, which can be seen as indication for an influence of the injecting contact at thicknesses $d \leq 60\,\text{nm}$.[85]

6.1.2. Impedance spectroscopy

Bias and frequency-dependent measurements of the impedance are well established techniques to probe conductivity, doping and trap states in organic semiconductors.[85] Here, it is used as complementary technique to the steady-state j-V curves in order to investigate injection barriers and potential distribution inside the device. Typical data of the complex impedance are shown in Fig. 6.3 in the form of Bode

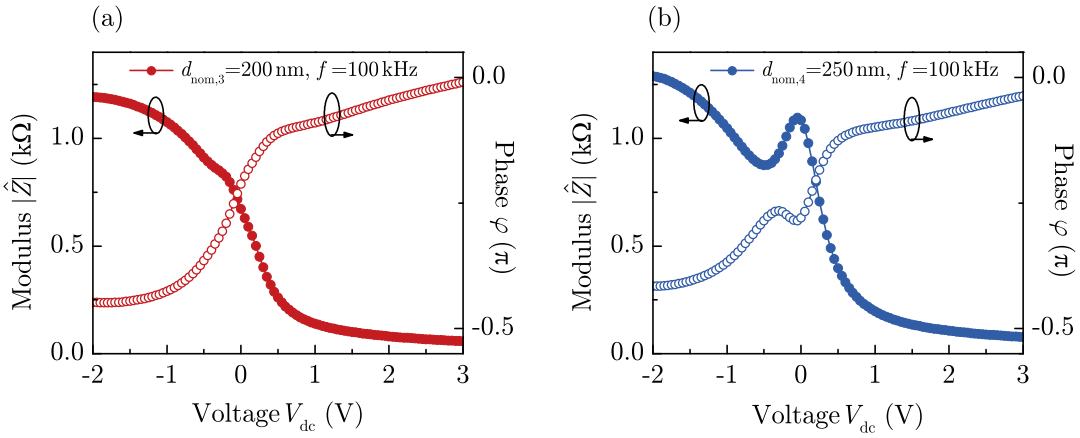

Figure 6.3.: Voltage dependent modulus $|\hat{Z}|$ and phase φ of the impedance of electron-only devices ($f = 100\,\text{kHz}$) having a DIP film thickness of (a) $d_{\text{nom},3}(\text{DIP}) = 200\,\text{nm}$ and (b) $d_{\text{nom},4}(\text{DIP}) = 250\,\text{nm}$.

plots for two electron-only devices with DIP thicknesses of (a) $d_{\mathrm{nom},3} = 200$ nm and (b) $d_{\mathrm{nom},4} = 250$ nm. At a fixed frequency of 100 kHz the applied bias voltage is varied from -2 to 3 V. The curves can be roughly divided into three regimes: For large reverse bias ($V_{\mathrm{dc}} = -2\,\mathrm{V}$) the phase φ shows a value close to $-\pi/2$ which points towards a predominantly capacitive behavior. However, as already seen in the comparatively high ohmic contribution in the reverse j-V characteristics the capacitive behavior in the negative voltage regime is limited and φ does not reach $-\pi/2$. Above $V_{\mathrm{dc}} \approx 0\,\mathrm{V}$ the modulus $|\hat{Z}|$ decreases with increasing bias voltage—while at the same time φ changes from $-\pi/2$ to 0. This can be identified with the onset of electron-injection from the top-electrode and current flowing through the device. In-between these limiting cases one additional feature appears; namely an intermediate increase in φ and simultaneous drop in $|\hat{Z}|$ in a voltage range between -1 and 0 V. This behavior indicates an ongoing capacitive response, however, with a reduced capacitive layer thickness. This feature has no equivalent in the steady-state j-V characteristics.

Even if the capacitance—determined from the complex impedance according to Eq. (3.14)—is only part of the entire impedance analysis its magnitude reflects the same behavior as observed for $|\hat{Z}|$ and φ. The variation of the real and imaginary part of the impedance were recorded at frequencies between 10 and 10^6 Hz at a range of different applied bias V_{dc}. Typical results are shown in Fig. 6.4 (a) by a C-f-plot and in (c) and (d) in the form of Nyquist plots for a device with nominal DIP thickness of $d_{\mathrm{nom},3} = 200\,\mathrm{nm}$. When the bias is strongly negative ($V_{\mathrm{dc}} = -2\,\mathrm{V}$ and $-1\,\mathrm{V}$) an almost constant capacitance is found in a wide frequency range. Compared to the j-V curve the value of capacitance corresponds to the reverse bias regime and is expected to be the geometric capacitance caused by the entire layer thickness. The representation in the complex impedance plane shows one semicircle (see Fig. 6.4 (c)). However, when V_{dc} is increased a step in the C-f curve is observed with an elevated value in the low-frequency range which relaxes to the geometric value above the relaxation frequency. The steep decrease in capacitance for bias voltages $V_{\mathrm{dc}} > 0\,\mathrm{V}$ and low frequencies marks current flow through the device—coinciding with the beginning of forward current from the j-V characteristics. As a result of different relaxation frequencies for the first and second RC element, two slightly overlapping semicircles arise in the Nyquist plot for bias voltages $V_{\mathrm{dc}} > 0\,\mathrm{V}$ (see Fig. 6.4 (d)). For detailed investigations of the experimental observations it is useful to consider an equivalent circuit (EC): From the comparison of the experimental data with the simulated curves of different ECs (see Fig. 3.18) it becomes obvious that the observed impedance behavior requires the use of two RC-elements connected in series—even though the device configuration consisting of a single organic layer sandwiched between two electrodes would suggest an EC being

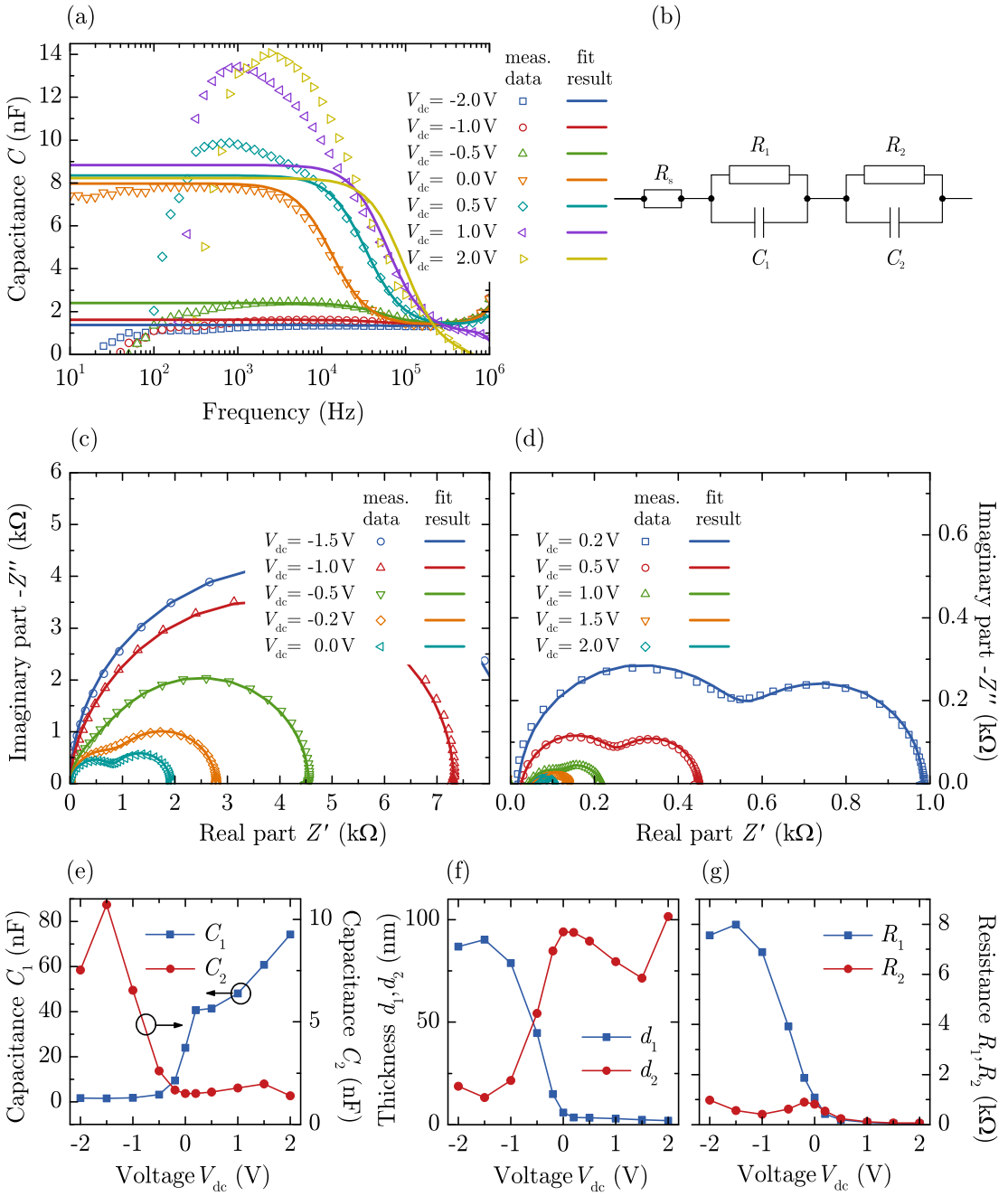

Figure 6.4.: (a) C-f-curves recorded for an electron-only device with DIP film thickness of $d_{\mathrm{nom},3}(\mathrm{DIP}) = 200\,\mathrm{nm}$ at room temperature and various applied dc bias (symbols). Data is fitted according to the equivalent circuit as shown in (b). (c) and (d) shows variations of the imaginary part, $-Z''$, of the impedance as a function of its real part, Z'. (e) Capacitances C_1 and C_2 as gained by the fit and (f) calculated thicknesses d_1 and d_2 as well as according resistances R_1 and R_2 (g).

composed of one single RC-element only. The used EC is shown in Fig. 6.4 (b). An additional series resistance R_S is included to account for a lead resistance as caused by the Al contacts. As listed in Tab. 6.1 R_S amounts to a few Ohm only which makes a subtraction of a corresponding potential drop unnecessary. Moreover, a satisfactory fit at high frequencies above $5 \cdot 10^5$ Hz is only possible if an inductance is added in order to account for the inductive properties of the cables (not shown here). The fitting results are included in Fig. 6.4 (a), (c) and (d) as straight lines. In dependence of the bias voltage, the capacitances C_1 and C_2 are shown in (e) while the corresponding resistances R_1 and R_2 are given in (g). According to Eq. (3.20) C_1 and C_2 are converted into capacitive thicknesses d_1 and d_2—depicted in (f). From the fitting results it becomes obvious that the device at negative bias can be identified by a highly resistive part of $d_1 \approx 80\,\text{nm}$ and a less resistive part of $d_2 \approx 20\,\text{nm}$. At $V_{dc} \approx -0.5\,\text{V}$ the resistance of d_1 decreases abruptly which is accompanied by a drop in the fitted value d_1 and a simultaneous increase in d_2.

One explanation is based on an internal inhomogeneity of the electric field as was reported by Berleb *et al.* for hetero-layer OLEDs.[345] The authors could show that a negative interfacial charge between hole- and electron-transporting layer lead to varying potential drop in both layers and thus to a similar observation in the impedance behavior of the sample. Following this model, the observed behavior is indicative of inhomogeneity of the potential drop across the organic layer—which would have to be a result of a positive charge being positioned around 20 nm away from the Al top contact. In contrast to the observations on hetero-layer OLEDs, there is no interface between two layers which would explain its appearance. However, it might be imaginable that interdiffusing Al atoms form clusters which lead to a charged layer in a certain depth from the organic/metal interface. A similar explanation has already been given in Ref. 346 for the occurrence of s-shaped j-V characteristics in polymer-C_{60} solar cells. The authors suggest that isolated Al clusters are formed upon cathode evaporation which lead to defects close to the organic/metal interface and change the electric field distribution in the device.

An alternative explanation for the impedance behavior of the samples might be given by the formation of a Schottky barrier inside the organic layer. In this case, a highly resistive depletion layer would be connected in series with a low resistive bulk layer of the organic semiconductor.[310] Following this model would result in a similar equivalent circuit consisting of two RC-elements in series—one assigned to the depletion layer the other associated with the bulk layer. Thus, interpretation would just differ in a sense that no interlayer charge would be present but, instead, a uniform band bending according to a Schottky contact would exist.[310] In the case of a Schottky contact, the bias voltage modulates the width of the space charge region at the contact. Mott-Schottky analysis has been used to develop a picture

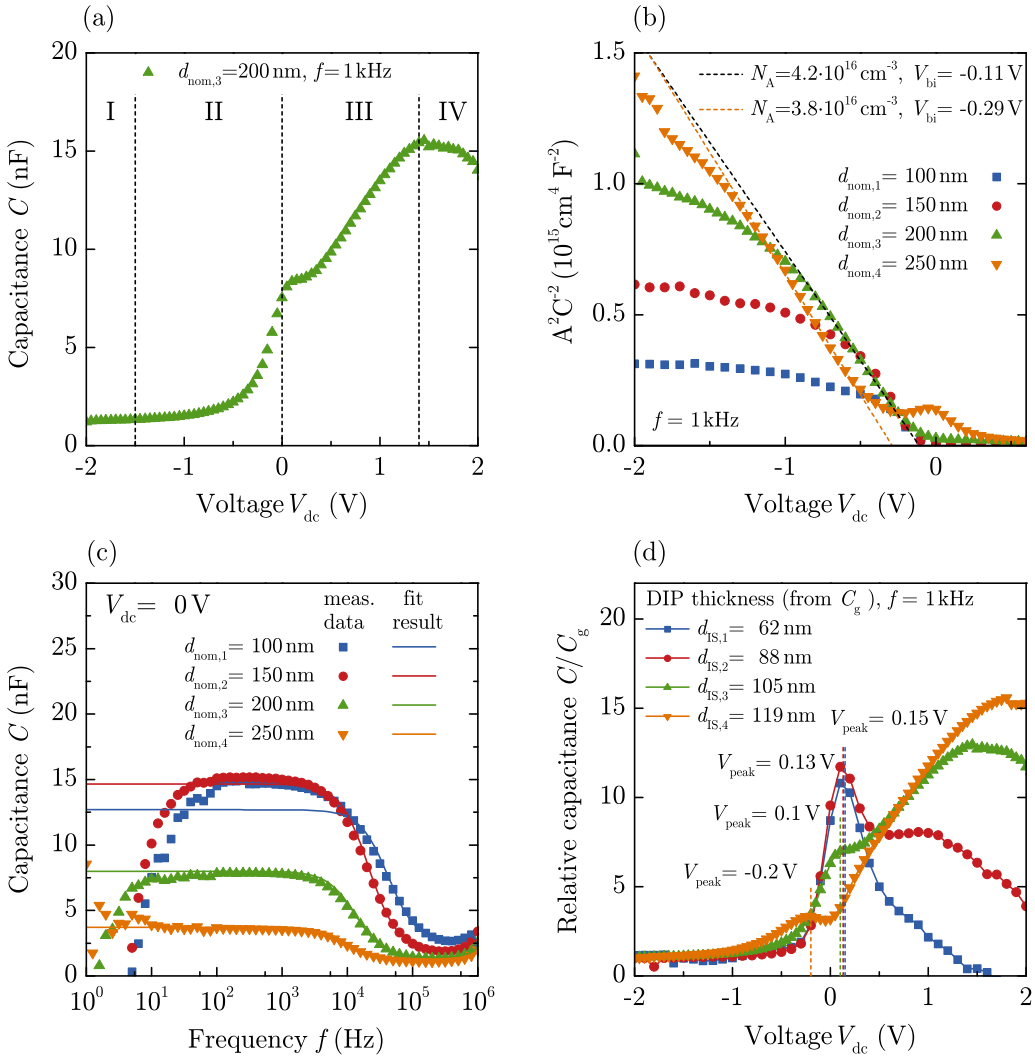

Figure 6.5.: (a) Characteristic capacitance response of the electron-only device with a layer thickness of $d_{\mathrm{nom,3}} = 200\,\mathrm{nm}$ illustrating four regions as explained in the text. (b) Mott-Schottky plot for different DIP thicknesses ($f = 1\,\mathrm{kHz}$) which exhibit straight lines from which the values V_{bi} and N_{A} are determined according to Eq. (6.2). (c) and (d) Impedance data of electron-only devices for several DIP film thicknesses. (c) C-f measurements ($V_{\mathrm{dc}} = 0\,\mathrm{V}$) and (d) C-V measurements ($f = 1\,\mathrm{kHz}$).

of the energetic relations inside P3HT:PCBM bulk heterojunction solar cells which are characterized by a Schottky junction with space charge region at the Al back contact.[347] By means of an exemplary voltage dependent impedance measurement (see Fig 6.5 (a)) the C-V-curve can typically be divided into four regions: At large reverse bias the organic layer is fully depleted and acts as a dielectric capacitor characterized by its geometric capacitance C_{g} (I). With increasing bias the width

of the depletion zone is reduced (II) up to the built-in voltage V_{bi}, where flat band condition is fulfilled. At higher voltages the depletion zone vanishes and the capacitance is governed by excess charge carriers (III). If there is sufficient current flow, the capacitance usually saturates or collapses taking even negative values (IV).[348] In region II, a doping concentration as well as a built-in voltage can easily be determined from C-V-measurements according to the Mott-Schottky analysis based on

$$C^{-2} = \frac{2(V_{\mathrm{bi}} - V)}{e\varepsilon\varepsilon_0 A^2 N_{\mathrm{A}}} \tag{6.1}$$

$$= \frac{2V_{\mathrm{bi}}}{e\varepsilon\varepsilon_0 A^2 N_{\mathrm{A}}} - \frac{2}{e\varepsilon\varepsilon_0 A^2 N_{\mathrm{A}}} \cdot V, \tag{6.2}$$

with the doping density N_{A}. By fitting a straight line to the measurement data plotted as C^{-2} versus V the built-in voltage can directly be determined from the intersect with the voltage axis while the slope gives information about N_{A}. A Mott-Schottky plot of the measured impedance data is shown in Fig. 6.5 (b) for the different DIP film thicknesses. The data show a typical linear decrease at small negative voltages. From individual fits to the curves a built-in voltage of $V_{\mathrm{bi}} \approx -0.1\,\mathrm{V}$ and a doping concentration of $N_{\mathrm{A}} \approx 4{\cdot}10^{16}\,\mathrm{cm}^{-3}$ can be determined—the thickest sample shows a slightly larger built-in voltage of $V_{\mathrm{bi}} \approx -0.3\,\mathrm{V}$. The small value of V_{bi} confirms the results from j-V measurements and the general applicability of the Mott-Schottky analysis affirms the assumption of a depletion zone caused by a Schottky contact. However, the reliability of the quantitative approach has recently been put in question by Kirchartz *et al.* in Ref. 349. The authors could show by simulations that the depletion approximation, which is an important prerequisite for the applicability of the Mott-Schottky analysis, is not readily fulfilled if the layers are too thin or the doping concentration is too low.

Up to now, the analysis of impedance measurement on electron-only devices was mainly focused on single devices. In order to compare various thicknesses, C-f curves for an exemplary bias voltage of $V_{\mathrm{dc}} = 0\,\mathrm{V}$ and C-V curves for a frequency of $f = 1\,\mathrm{kHz}$ are picked out and shown in the lower part of Fig. 6.5. From C-f behavior depicted in (c) the high-frequency plateau value at $f \approx 5 \cdot 10^5\,\mathrm{Hz}$ reflects the nominal order of thickness from thin ($d_{\mathrm{nom},1}$) to thick ($d_{\mathrm{nom},4}$), i.e., the thinnest layer corresponds to the largest capacitance while the thickest layer corresponds to the lowest capacitance. The fits of the measurement data according to the EC as shown in Fig. 6.4 (b) result in capacitances C_1 and C_2. While C_2 scales with the nominal thickness, C_1 takes a constant value corresponding to $d_1 \approx 5\,\mathrm{nm}$ for all

thicknesses.[p] This observation confirms the assumption of an inhomogeneity of the electric field caused by interdiffusion of Al clusters within a certain distance from the organic/metal interface—which is likely to be independent of the total layer thickness.

Figure 6.5 (d) depicts C-V curves of the different samples—measured at a fixed frequency of 1 kHz. The capacitance is normalized to the respective geometric value at $V_{\mathrm{dc}} = -2\,\mathrm{V}$. All curves show similar behaviors with two peaks in the capacitance before decreasing at high bias. The voltage, where the drop of C/C_{g} begins, moves towards higher values when going from the thinnest to the thickest sample—which is consistent to the j-V curves and the height of the injection currents. The thicknesses d_{IS} which can be determined from the geometrical capacitances C_{g} are listed in the diagram and Tab. 6.1. Apparently, they do not match the nominal layer thicknesses—even though one would expect from the j-V characteristics that the devices are almost completely depleted at $V = -2\,\mathrm{V}$. On the other hand, it was already mentioned that the reverse currents are comparatively high—probably as result of enhanced leakage resulting from interdiffused Al clusters or extremely rough films. This would mean that a fully capacitive behavior cannot be considered throughout the entire film thickness.

Mensfoort and Coehoorn investigated the differential capacitance of single carrier devices which show similar metal/organic/metal structures as the presented electron-only diodes.[350] They could relate the occurrence of a peak in the C-V curve at voltages below V_{bi} to the size of the barrier at the injecting electrode interface: It is shown that a distinct peak is observed when the injection barrier of at least one of the electrodes is sufficiently small. The reason for this behavior was found in the diffusion contribution to the current density. Based on the drift-diffusion model, the authors carried out simulations of different scenarios by varying V_{bi} and the height of the injection barriers. Following their approach and assuming one well-injecting electrode and an organic semiconductor of thickness d, the injection barrier at the second electrode, EIB_2, can be obtained directly from the measured position of the peak in capacitance, using

$$\mathrm{EIB}_2 = eV_{\mathrm{peak}} + \left(\ln\frac{N_{\mathrm{c}}}{n_0} - a\right) k_{\mathrm{B}}T, \tag{6.3}$$

with the volume density of molecular sites N_{c}, $a = 0.207$ and $n_0 \equiv \varepsilon k_{\mathrm{B}}T/(e^2d^2)$. As shown in Sec. 2.2.3 the density of DIP molecules can be estimated to $N_{\mathrm{c}} \approx 2 \cdot 10^{21}\,\mathrm{cm}^{-3}$. By assuming the layer thickness as given by C_{g} (d_{IS}) and the peak

[p] It has to be noted that the value of the capacitance of the second RC element cannot be easily read off from the plateau region at low frequency, as the prerequisite—namely the condition that one resistance is much smaller than the other one[85]—is not necessarily fulfilled here.

positions which are marked as vertical lines in Fig. 6.5 (d), the barrier height EIB_2 can be calculated from Eq. (6.3) and one determines values of 0.54 ± 0.05 eV for all thicknesses. Even though this value seems to be reasonable to explain the reduced electron injection in the reverse biased devices it would entail a relatively large V_{bi} when assuming a low EIB for electrons at the contact to the interface. Altogether, the peak around 0 V cannot unambiguously related to the diffusion phenomenon as described in Ref. 350. Apart from that, the authors show that V_{bi} can exceed V_{peak} by more than 0.3 V which can possibly explain the asymmetry of the j-V curves shown in Fig. 6.1.

6.1.3. Discussion

In the previous section electron transport in thin films of DIP has been investigated on the basis of electron-only devices. As both electrodes are opaque, it is not possible to prove the successful suppression of double-carrier injection by the absence of a detectable electroluminescence signal. However, mobility measurements on FETs utilizing various electrode materials suggest a clear asymmetry between the injection barriers from the Fermi level of Al to the HOMO and LUMO of DIP, which is reflected in suppressed hole injection from Al electrodes.[204] A consistent description of the layer-thickness dependence of the current density and impedance analysis may be obtained by assuming the bottom Aluminum/DIP contact to be of Schottky-type, while the top-contact seems to be ohmic. A model qualitatively illustrating this concept is depicted in Fig. 6.6 in form of a schematic energy level diagram. The electronic structure before contacting—as shown in (a)—is characterized by the Fermi level of the bottom and top Aluminum located below and above the Fermi level of DIP, respectively, which is the necessary prerequisite for a Schottky-contact formed at the bottom electrode and an ohmic contact at the top electrode. A difference in work function of both electrodes despite the usage of the same material has been found in numerous examples, as can, e.g., be seen in Ref. 351. It can be explained by the completely different metal/organic interaction—be it physisorption (i.e. van der Waals interaction), or chemisorption with certain degrees of charge transfer[352]—depending on the order of evaporation. This means, strong differences in interfacial energetics are expected when the organic is deposited onto the metal or when the metal is evaporated onto the organic, the latter often resulting in doping of the upper organic layers or interdiffusion of metal atoms or clusters into the semiconductor.[351] Moreover, the model assumes an n-type doping of the semiconductor bringing the equilibrium Fermi level closer to the LUMO level of DIP. When bringing both electrodes and the semiconductor into contact (see Fig. 6.6 (b)) a Schottky barrier is formed between DIP and

the bottom contact. A depletion layer is formed and band bending is observed in the HOMO, LUMO and vacuum level. On the other hand, the cathode contact is regarded as ohmic. If a reverse voltage is applied (see Fig. 6.6 (c)) even more electrons are removed from the semiconductor resulting in an expansion of the depletion layer and the organic becomes dielectric, explaining the capacitive behavior in the C-V- and C-f-curves at reverse bias. The modulation of the depletion layer at moderate reverse bias is reflected in the characteristic impedance behavior described by two RC-circuits and the observed Mott-Schottky behavior. Moreover, the blocking behavior of the Schottky-contact in reverse direction explains the rectifying current-voltage characteristics. An applied bias in forward direction first

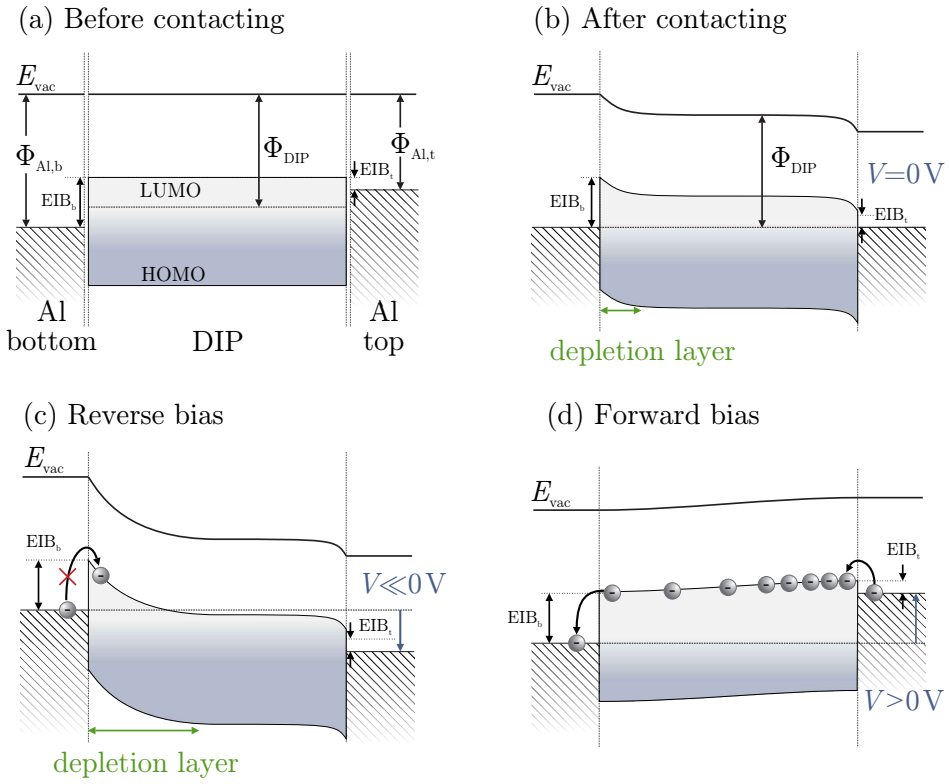

Figure 6.6.: Schematic energy diagram of the Al/DIP/Al electron-only devices. (a) Separate representation of the Aluminum bottom and top contacts with the work function $\Phi_{Al,b}$ and $\Phi_{Al,t}$, respectively. DIP is assumed to be n-type doped with a work function Φ_{DIP} defining the equilibrium Fermi level inside the semiconductor situated close to the LUMO. The differences between the Fermi level of the metal and the LUMO of DIP define the electron injection barriers at the anode EIB_b and cathode EIB_t. (b) After contacting band bending appears inside the semiconductor at the anode defining a depletion layer. (c) Reverse bias leading to an enlargement of the depletion layer. (d) Under forward bias the depletion layer completely vanishes and electrons are injected from the cathode resulting in a measurable current flow.

narrows the width of the depletion layer—at even higher forward bias electrons are injected from the cathode (see Fig. 6.6 (d)). This is accompanied by an increase in current and a collapse of the capacitance.
The model implies that in equilibrium, i.e. under zero bias voltage, the depletion layer is still pronounced, which presupposes a built-in voltage of $V_{\mathrm{bi}} \neq 0\,\mathrm{V}$. In this context, one decisive aspect has been neglected so far: No interfacial dipoles have been taken into account until now, even though their existence at the metal/organic interfaces is relatively likely as was already stated in Sec. 2.2.4 and has been shown in the previous chapter. As no quantitative statement can be given about possibly appearing interfacial dipoles, they are not included in the schematic. Nevertheless, it can be seen from Eq. (2.22), that neglecting vacuum level shifts may lead to incorrect predictions of interfacial barriers. Furthermore, taking interfacial dipoles into account would explain the appearing j-V and C-V behavior—similar to the explanation given above—however, including a vanishing V_{bi}.

6.2. Hole transport in DIP diodes

The transport properties of holes are investigated using hole-only devices consisting of a DIP film sandwiched between PEDOT and TTF-TCNQ electrodes, both having a work function close to the HOMO of DIP:

ITO/ PEDOT($\approx 30\,\mathrm{nm}$)/ DIP/ TTF-TCNQ($\approx 150\,\mathrm{nm}$),

with nominal DIP film thicknesses of $d_{\mathrm{nom},1} = 50\,\mathrm{nm}$, $d_{\mathrm{nom},2} = 100\,\mathrm{nm}$, $d_{\mathrm{nom},3} = 150\,\mathrm{nm}$, and $d_{\mathrm{nom},4} = 300\,\mathrm{nm}$ and the substrate kept at room temperature. Furthermore, hole-only devices with nominal DIP thicknesses of $d_{\mathrm{nom},1} = 100\,\mathrm{nm}$, $d_{\mathrm{nom},2} = 200\,\mathrm{nm}$, and $d_{\mathrm{nom},3} = 300\,\mathrm{nm}$ have been prepared on substrates which were heated to 100 °C during DIP evaporation. ITO/PEDOT represents the standard hole-injecting electrode for the solar cells fabricated within the scope of this work. The organic metal TTF-TCNQ has been used to enable unipolar hole transport by its high work function of approximately 4.6–4.8 eV which is expected to be large enough to prevent electron injection. The successful suppression of double-carrier injection was verified by the absence of a detectable electroluminescence signal.

6.2.1. Electrical characterization

Figure 6.7 (a) depicts the j-V characteristics of the RT hole-only devices together with simulated curves for ohmic (dotted line) and SCLC behavior (dashed line). It

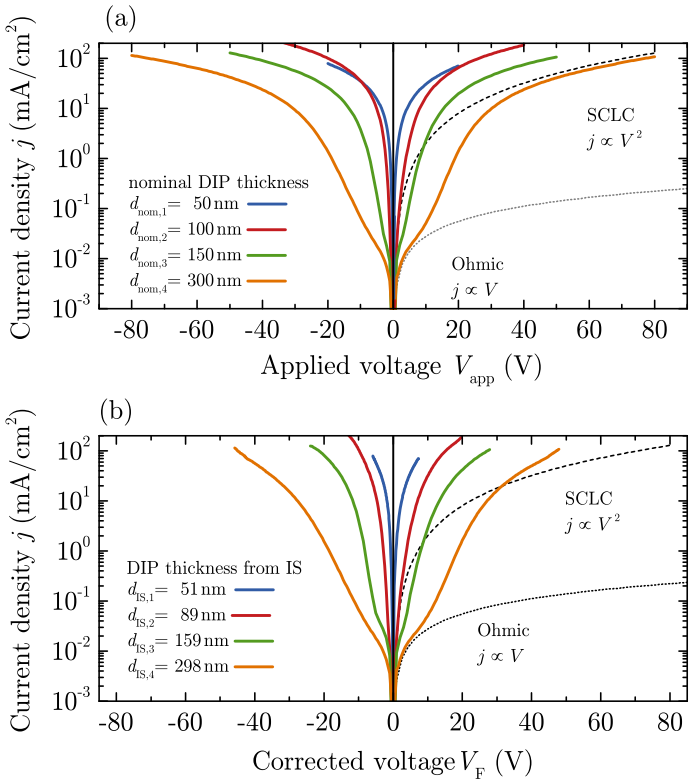

Figure 6.7.: j-V characteristics of DIP hole-only devices for several layer thicknesses (T_{sub} = RT). (a) Current density versus applied voltage V_{app} and (b) current density versus voltage corrected for potential drop at the series resistance according to $V_F = V_{app} - j \cdot R_S A$. For comparison, the bulk limited SCLC (dashed line) and ohmic current-voltage behavior (dotted line) are included.

is striking that the j-V curves are highly symmetric around $V = 0\,\mathrm{V}$, i.e. they show very similar currents in forward and reverse direction. This observation indicates similar injection conditions from both electrodes. While the reverse direction reflects the injection of holes from the top contact TTF-TCNQ, the forward direction corresponds to the injection of holes from the ITO/PEDOT bottom contact. In the following, the analysis of the data is restricted to the forward direction. As will be seen from the results of IS measurements, a comparatively high series resistance R_S has to be taken into account which is attributed to the lead resistance of ITO and TTF-TCNQ. Thus, the applied voltage V_{app} is corrected for the potential drop at the series resistance as $V_F = V_{app} - j \cdot R_S A$, whereas R_S is determined by IS measurements as will be shown in the subsequent section. The values are listed in Tab. 6.2 and the corresponding j-V_F curves are depicted in Fig. 6.7 (b). It is obvious that the effect of the series resistance is tremendous and neglecting the voltage drop at R_S would lead to unreliable data and analysis.

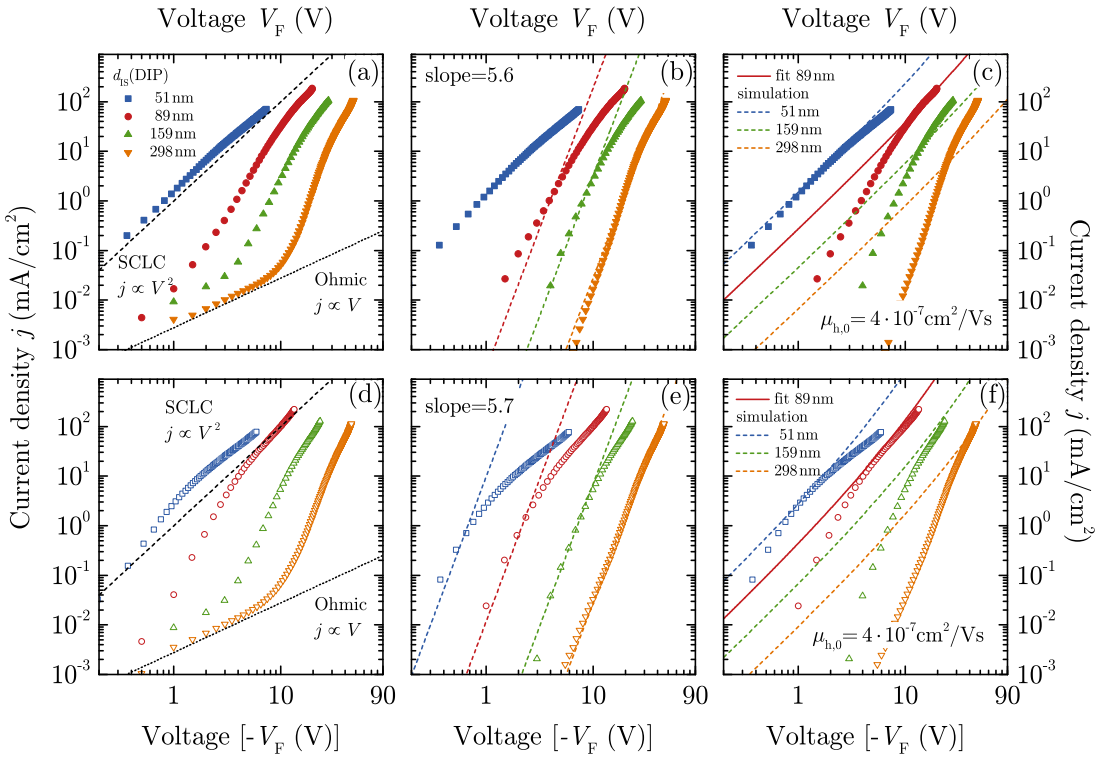

Figure 6.8.: j-V characteristics of DIP hole-only devices for several layer thicknesses (T_{sub} = RT). Top row: Double-logarithmic representation of measurement data for forward bias (a) with fits to power laws $j \propto \mathscr{V}^{l+1}$ (b) and simulated currents for SCLC (c) with parameters given in Tab. 6.2. For reverse bias analog fitting procedure is performed and data, fits and simulations are shown in (c), (d) and (e), respectively. The ohmic contribution as determined from (a) and (d) is subtracted in the subsequent diagrams, respectively.

In the double logarithmic plot of the j-V characteristics (see Fig. 6.8 (a)) three different regimes can be discriminated: At low voltages the electron current depends linearly on the bias according to Eq. (2.14). The single curves are individually fitted within this voltage region and the ohmic contribution to the current is subtracted in the further diagrams of this section. From the ohmic region an upper limit of the intrinsic carrier concentration of $\rho_0 < 9 \cdot 10^{14}\,\mathrm{cm}^{-3}$ can be calculated. The ohmic regime is followed by an increase in current density with a slope steeper than SCLC behavior. As was explained in Sec. 2.2.3, a power law behavior of the current according to $j \propto \mathscr{V}^{l+1}$ with an exponent $(l+1)$ larger than two is indicative for trap-charge limited conduction. As the trap filling takes place within a comparatively wide voltage range, discrete trap levels can be ruled out and, instead, energetically distributed trap states are expected. The transport in the third region points towards a trap-filled SCLC behavior with j depending quadratically on the voltage.

Table 6.2.: Analysis of hole-only devices. d_{nom} and d_{IS} denote the nominal layer thickness and the thickness given by fit results based on impedance measurements, respectively. Besides values for the series resistance R_{S} extracted from IS data, SCLC fit parameters such as mobility μ_0, field-activation parameter γ, and built-in voltage V_{bi} are included. Assuming an exponential distribution of traps, estimated values about charge carrier traps are listed, including the trap level E_{trap} and a trap density N_{t}.

d_{nom} (nm)	R_{S} (kΩ)	d_{IS} (nm)	SCLC forward	SCLC reverse	TCLC
Hole-only devices, $T_{\mathrm{sub}} = \mathrm{RT}$ (cf. Fig. 6.7 and 6.8)					
$d_1 = 50$	4.8	51†	$\mu_{\mathrm{h},0} = 4 \cdot 10^{-7}$ cm^2/Vs	$\mu_{\mathrm{h},0} = 4 \cdot 10^{-7}$ cm^2/Vs	
$d_2 = 100$	2.8	89†			$(l+1) \approx 6$
$d_3 = 150$	5.3	159†	$\gamma = 5.2 \cdot 10^{-4}$ (cm/V)$^{1/2}$	$\gamma = 1.8 \cdot 10^{-3}$ (cm/V)$^{1/2}$	$E_{\mathrm{trap}} = 0.12\,\mathrm{eV}$
$d_4 = 300$	7.5	298†			$N_{\mathrm{t}} \approx 7 \cdot 10^{18}\,\mathrm{cm}^{-3}$
			$V_{\mathrm{bi}} = 0\,\mathrm{V}$	$V_{\mathrm{bi}} = 0\,\mathrm{V}$	
Hole-only devices, $T_{\mathrm{sub}} = 100\,^{\circ}\mathrm{C}$ (cf. Fig. 6.10)					
			$\mu_{\mathrm{h},0} = 6 \cdot 10^{-7}$ cm^2/Vs		
$d_1 = 100$	2.8	90†			$(l+1) \approx 8$
$d_2 = 200$	3.8	174†	$\gamma = 2.6 \cdot 10^{-3}$ (cm/V)$^{1/2}$		$E_{\mathrm{trap}} = 0.18\,\mathrm{eV}$
$d_3 = 300$	5.0	269†			$N_{\mathrm{t}} \approx 3 \cdot 10^{18}\,\mathrm{cm}^{-3}$
			$V_{\mathrm{bi}} = 0\,\mathrm{V}$		

† d_{IS}(DIP) is determined from the fit results by associating the low frequency arc in the Bode plot to the DIP layer (see Fig. 6.13).

Based on these observations, the data in the medium voltage regime is fitted to Eq. (2.20) describing TCLC with an exponential distribution of traps (see Fig. 6.8 (b)). Apart from the thinnest sample all thicknesses are well described by a slope of 5.6 resulting in $l = 4.6$ and a characteristic trap energy of $E_{\mathrm{trap}} = 0.12\,\mathrm{eV}$. At high voltages, the current-voltage behavior is characterized by a flattening of the curve which indicates that the trap filling is completed. The measurement data of the sample with DIP thickness of $d_2 = 89\,\mathrm{nm}$ is fitted according to the Mott-Gurney equation (2.15) (see Fig. 6.8 (c)). The fit results in values of $\mu_0 = 4 \cdot 10^{-7}\,\mathrm{cm}^2/\mathrm{Vs}$ and $\beta = 5 \cdot 10^{-4}\,(\mathrm{cm/V})^{1/2}$—highlighting that the hole transport in DIP is worse than the electron transport. Based on the parameters given by the SCLC fit, the j-Vdependence of the remaining thicknesses have been simulated. The comparison with the experimental data (see Fig. 6.8 (c)) shows very good agreement for the thinnest sample, however, increasingly pronounced deviations for higher film

thicknesses. The same analysis has been carried out for the reverse bias regime (Fig. 6.8 (d)-(f)), which is found to result in similar behavior for the low and medium voltage regime. However, fitting and simulation in the SCLC region leads to good accordance with the layer thicknesses, nevertheless showing the same mobility $\mu_{\mathrm{h},0}$.

As was already mentioned in Sec. 2.2.3, a reliable statement about the prevailing transport mechanism can only be done by taking different parameters like the thickness dependence of the current or the dependence on electric field into account. Figure 6.9 (a) shows the electric field dependence of the current with $F = V_{\mathrm{F}}/d_{\mathrm{IS}}$. For the case of a purely injection-limited current-voltage behavior all curves would be expected to be identical over a wide range of voltages. While this is not observed for low electric fields, an approaching of the different curves can be identified for fields $F > 1.1 \cdot 10^8\,\mathrm{V/m}$ being more pronounced for thicker films. The upward bending of the curves at very high fields could possibly be assigned to a resistive heating of the sample: According to Eq. (2.11) an increase in temperature would lead to improved transport properties yielding higher currents at a constant voltage and a similar upward bending of the curve as observed here.

For sufficiently high temperature and for potential barriers which are not too high, the predominant injection mechanism proceeds via thermionic emission—whereas the barrier height is lowered by the image force effect. Crowell and Sze developed a thermionic emission-diffusion (TED) theory for current injection into low-mobility semiconductors via an injection barrier Φ_{b},[353] which gives the so-called Richardson-Schottky emission described by

$$j_{\mathrm{RS}} = A^* T^2 \exp\left(-\frac{\Phi_{\mathrm{b}}}{k_{\mathrm{B}} T}\right), \tag{6.4}$$

with the Richardson constant $A^* = 4\pi e m_0 k_{\mathrm{B}}^2/h^3$ ($= 120\,\mathrm{Acm^{-2}K^{-2}}$, m_0: free electron mass) and the barrier height lowering given by

$$\Phi_{\mathrm{b}} = \Phi_{\mathrm{b},0} - \sqrt{\frac{e^3 F}{4\pi\varepsilon_0 \varepsilon}}. \tag{6.5}$$

Strictly speaking, the equations are only valid for emission into vacuum. While they can—under certain conditions—be adopted to inorganic semiconductors, the adaptation to organic semiconductors remains challenging: due to the disorder inside the organic material, injected carriers hit upon randomly distributed energy barriers. This results in an enhanced backflow of injected carriers into the electrode which is reflected by a Richardson constant being reduced by 5–6 orders of magnitude.[84,85] In spite of a variety of attempts to adapt the model to organic

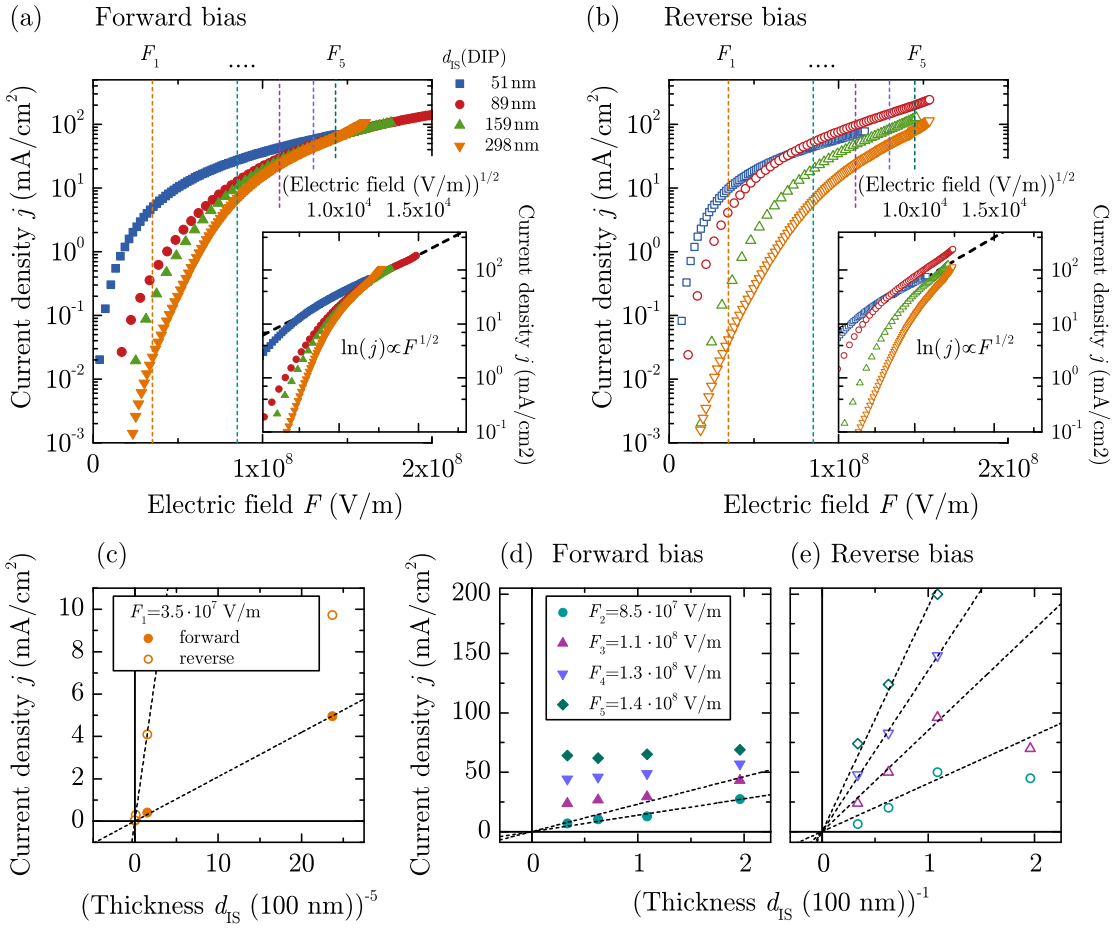

Figure 6.9.: j-V characteristics of DIP hole-only devices for several layer thicknesses (T_{sub} = RT) in the forward (a) and reverse (b) bias regime . Measurement data is presented depending on the electric field F and depending on $\sqrt{F}$ (inset). (c) Thickness dependence of the current (j versus d^{-5}) at a constant electric field of $3.5 \cdot 10^7$ V/m. (d) and (e) depict plots of j versus d^{-1} at various constant electric fields for forward (d) and reverse (e) voltage direction, respectively.

semiconductors,[354–356] an unambiguous solution is still pending. Thus, an analysis of injection limited currents is restricted to a qualitative manner.

In order to facilitate the identification of the prevailing transport mechanism of holes in DIP, the current density is plotted at different values of the electric field versus the DIP thickness. A clear proof for injection limitation would be given by constant current densities without a thickness dependence, while the current in trap-free SCLC would be proportional to d^{-1} as was the case for electron transport in DIP. The low-field data (at $F = 3.5 \cdot 10^7$ V/m) shows the current plotted versus d^{-5} (see Fig. 6.9 (c)), which is the dependence expected for TCLC with $(l+1) = 5.6$

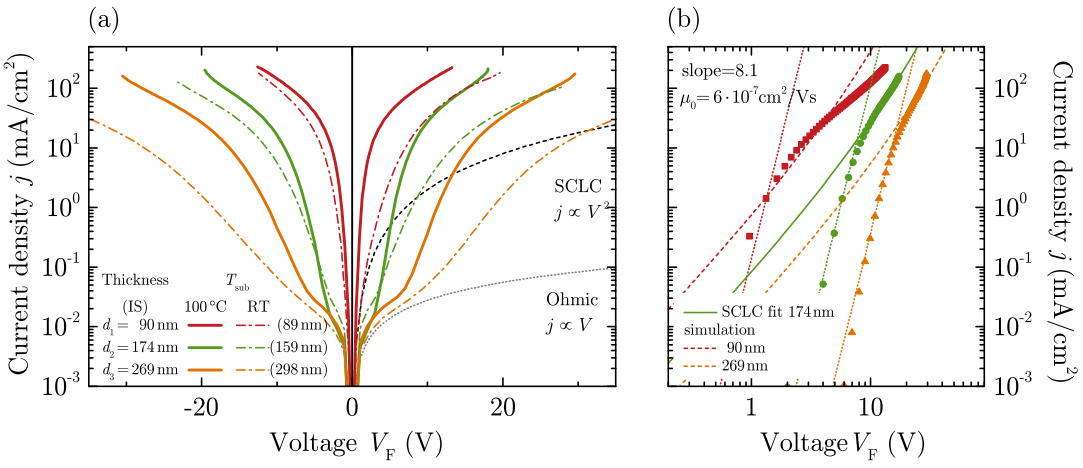

Figure 6.10.: j-V characteristics of DIP hole-only devices for several layer thicknesses with DIP deposited at substrate temperature of $T_{sub} = 100\,°C$. (a) Semi-logarithmic representation. For comparison, selected data of room temperature devices as well as simulated bulk limited SCLC (dashed line) and ohmic current-voltage behavior (dotted line) are included. (b) Double-logarithmic representation of measurement data for forward bias (symbols) with fits to power laws $j \propto \mathscr{V}^{l+1}$ (dotted lines) and simulated currents for SCLC with parameters given in Tab. 6.2 (dashed lines).

as was determined in Fig. 6.8 (b). Moreover, for purely injection limited behavior the current plotted versus the electric field should, according to Eq. (6.4) and (6.5) follow a linear dependence of $\ln(j)$ on the square root of the electric field. As depicted in the inset of Fig. 6.9 (a) this relation holds true only for high electric fields approximately above $F = 1.3 \cdot 10^8\,\mathrm{V/m}$. For electric fields $F > 8.5 \cdot 10^7\,\mathrm{V/m}$ the current is plotted versus d^{-1} (Fig. 6.9 (d)) which shows a transition between direct proportionality to thickness independence with increasing value of the electric field. However, it was ensured that the voltage region used for fitting the data according to SCLC lies below the injection limitation. For the reverse direction, there are no indications of injection limitation (see Fig. 6.9 (b)). Instead, a direct proportionality between j and d^{-1} is observed in a wide range of electric fields—at least for device thicknesses $d > 51\,\mathrm{nm}$ (Fig. 6.9 (e)).

Besides the deposition on unheated ITO/PEDOT substrates hole-only devices with DIP deposited at a substrate temperature of $T_{sub} = 100\,°C$ have been prepared. Figure 6.10 (a) depicts the current-voltage characteristics of the heated devices (straight lines) as compared to the non-heated samples (dashed-dotted lines)—in both cases the voltage is corrected for the potential drop at the series resistance as described above. Even though the layer thicknesses of the devices with $T_{sub} = 100\,°C$ are somewhat smaller than the corresponding unheated ones, there

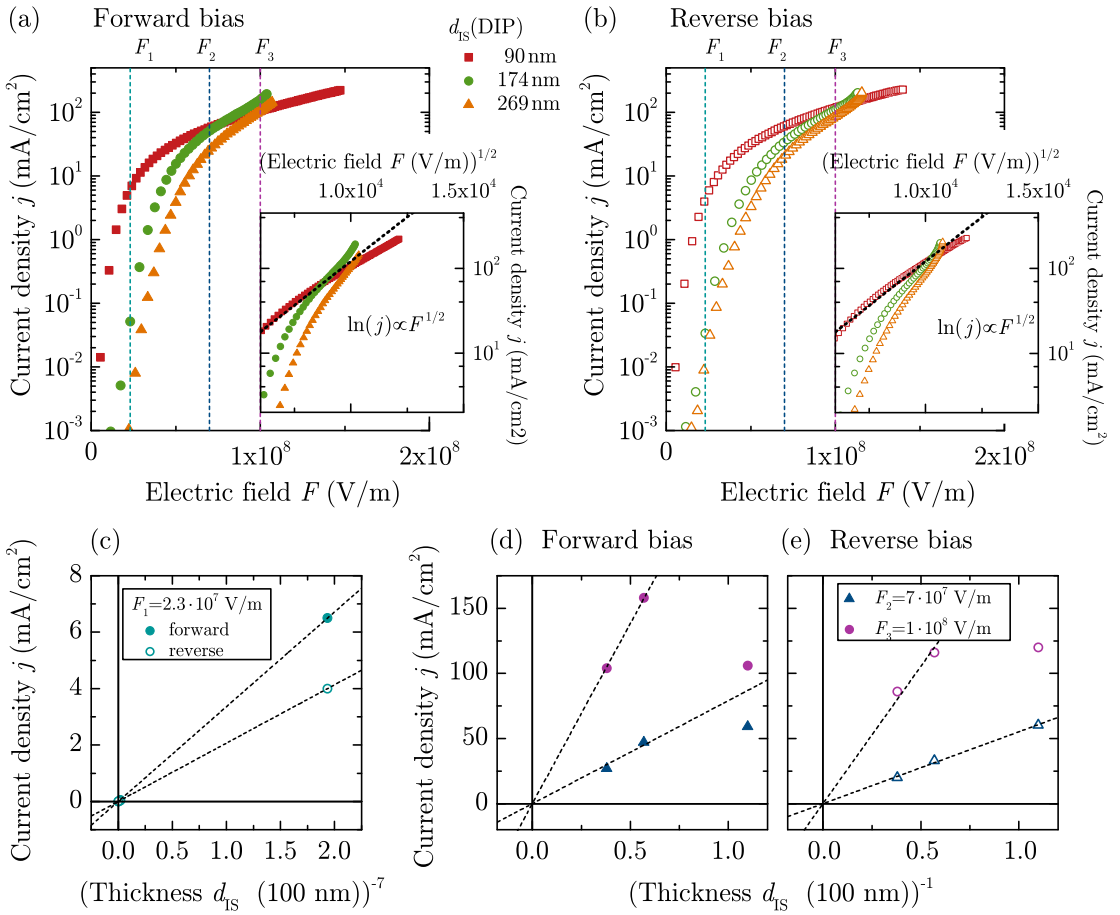

Figure 6.11.: j-V characteristics of DIP hole-only devices for several layer thicknesses in the forward (a) and reverse (b) bias regime and $T_{sub} = 100\,°C$. Measurement data is presented depending on the electric field F and depending on $\sqrt{F}$ (inset). (b) Thickness dependence of the current (j versus d^{-7}) at a constant electric field of $2.3 \cdot 10^7\,V/m$. (c) and (d) depict plots of j versus d^{-1} at constant electric fields of $7 \cdot 10^7\,V/m$ and $1 \cdot 10^8\,V/m$ for forward and reverse bias, respectively.

is a significant increase in current observable in case of the heated ones. Moreover, it is striking that in forward direction the improvements in current are more pronounced than for reverse bias—however, ending up in almost identical curve shapes being highly symmetric around $V = 0\,V$. In order to investigate the differences in more detail, a similar analysis of the j-V data is made as shown for the unheated case. After subtracting the ohmic contribution Fig. 6.10 (b) presents the data on a double-logarithmic scale, clearly characterized by two distinct areas: According to Eq. (2.20) a scaling parameter $l \approx 7$ was extracted from the low-voltage regime by a linear interpolation. For higher voltages the curve with $d_{IS,2} = 174\,nm$ is fitted according to SCLC with $\mu_{h,0} = 6 \cdot 10^{-7}\,cm^2/Vs$ and $\gamma = 2.6 \cdot 10^{-3}\,(cm/V)^{1/2}$. Based

on these values the remaining thicknesses are simulated resulting in very good description of the measurement data. For the reverse bias regime identical results are achieved (not shown here). Both, forward and reverse regime, are plotted versus the electric field as depicted in Fig. 6.11 (a) and (b), respectively. In both cases there is no overlap of the thicker layers while the thinnest sample deviates and indicates an influence of injection limitation. The latter is confirmed by the data shown in the insets: A linear relation between $\ln(j)$ and the square root of the electric field can only be found for the device with the thinnest DIP layer. At low electric fields the current is proportional to d^{-7} confirming the behavior expected for TCLC with $(l+1) = 8$ (see Fig. 6.11 (c)). The high-field data ($F_2 = 7 \cdot 10^7\,\mathrm{V/m}$ and $F_3 = 1 \cdot 10^8\,\mathrm{V/m}$ in (d) and (e) for forward and reverse bias, respectively) demonstrate the validity of trap-free SCLC with a proportionality to d^{-1} for the thicker films. Again, the deviation of the thinnest film indicate an influence of the injection current at a thickness of 90 nm, however, SCLC seems to be still the dominant mechanism. While the impact of substrate heating during DIP evaporation manifests in a simple increase in current in the reverse direction, a transition between the prevailing transport mechanism is observed for the forward bias regime: While the current for the unheated device is characterized by a considerable influence of injection limitation, the devices with $T_{\mathrm{sub}} = 100\,^{\circ}\mathrm{C}$ are dominated by SCLC, at least for thicknesses $d > 90\,\mathrm{nm}$.

6.2.2. Impedance spectroscopy

In the same way as for the electron-only devices, impedance measurements have been performed for all samples presented in the previous section. Typical data are depicted in Fig. 6.12—exemplarily shown for a hole-only device with 100 nm of DIP. In the Bode plot for a fixed frequency of 1 kHz (see Fig. 6.12 (a)) a highly symmetric behavior around $V_{\mathrm{dc}} = 0\,\mathrm{V}$ is observed: At zero applied bias, the phase takes a value of $\varphi \approx -\pi/2$ which indicates capacitive behavior. For large forward and reverse bias ($V_{\mathrm{dc}} = \pm 2\,\mathrm{V}$) φ changes to approximately 0. Compared to the j-V-curves, this transition corresponds to the onset of hole-injection either from the bottom contact (forward bias regime) or from the top contact (reverse bias regime). A similar symmetric behavior is found in the C-V curves depicted in Fig. 6.12 (b): Independent of the frequency there is a plateau around $V_{\mathrm{dc}} = \pm 0\,\mathrm{V}$ and a subsequent change in capacitance to both sides due to the injection of charge carriers. The symmetric curves point towards similar injection behavior from both electrodes—as has already been shown by the steady state current-voltage curves.

In order to determine the layer thicknesses, C-f measurements have been performed for all devices. Exemplarily, frequency-sweeps for the 300 nm device are

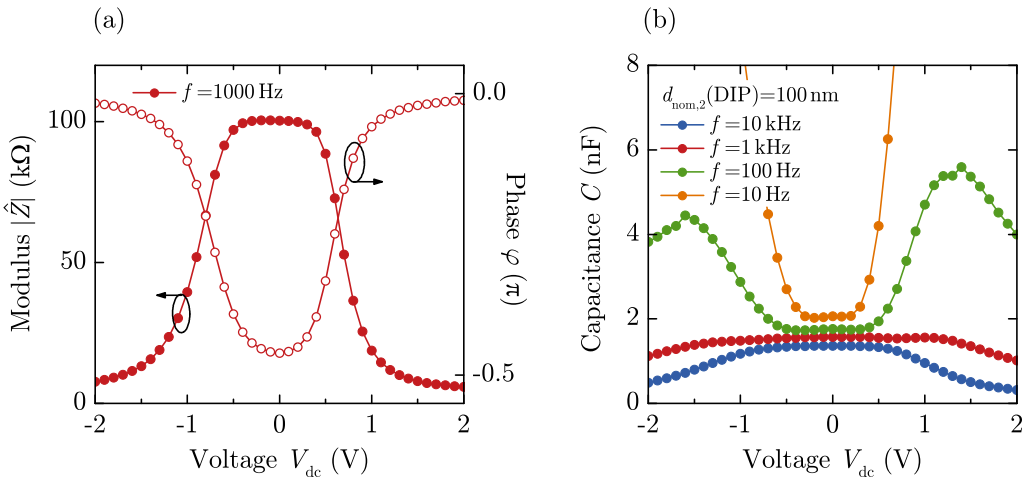

Figure 6.12.: Voltage dependent magnitude $|\hat{Z}|$ and phase φ of the impedance (f = 1 kHz) (a) and capacitance (b) of a hole-only device having a DIP film thickness of $d_{\mathrm{nom},2}(\mathrm{DIP}) = 100\,\mathrm{nm}$ grown at $T_{\mathrm{sub}} = \mathrm{RT}$.

depicted in Fig. 6.13 (a) for a variety of different bias voltages ranging from −20 V to +20 V. As can be seen from the j-V characteristics depicted in Fig. 6.7 (a) $V_{\mathrm{dc}} = -10\,\mathrm{V}$, 0 V and 10 V represent the depleted device—the current is still in the ohmic regime—while $V_{\mathrm{dc}} = \pm 20\,\mathrm{V}$ is located above the onset voltage where holes are injected and a significant increase in current can be observed. Within the ohmic voltage region the capacitance is essentially frequency-independent within a frequency range of approximately $5 \cdot 10^2$–$5 \cdot 10^4$ Hz showing a plateau value C_{g} equal to the geometric capacitance of the DIP layer. At frequencies $f > 5 \cdot 10^4$ Hz the capacitance drops down to zero, which is untypical for the given measurement setup. The high frequency regime is usually determined by parasitic effects due to contact resistances as well as inductive effects exerted by cables and is expected to be independent of the device. Thus, the observed deviations already point towards a high series resistance which governs the high-frequency part of the sweep. The increase in capacitance at low frequencies is a result of lateral conduction: Due to the crossbar device architecture without area restriction of the organic layers on the anode side there exists an additional current path through the device which lead to an additional step at low frequency as was shown in Refs. 311 and 357. This feature has not been observed for the electron-only samples, as the device setup is not based on a large-area anode but, instead, both Al electrodes are structured. Apart from the low-frequency increase observed for the hole-only devices, no additional plateau in capacitance is observed which eliminates pronounced inhomogeneities of the electric field inside the organic like band bending effects.

The data is fitted according to the equivalent circuit shown in Fig. 6.13 (b).

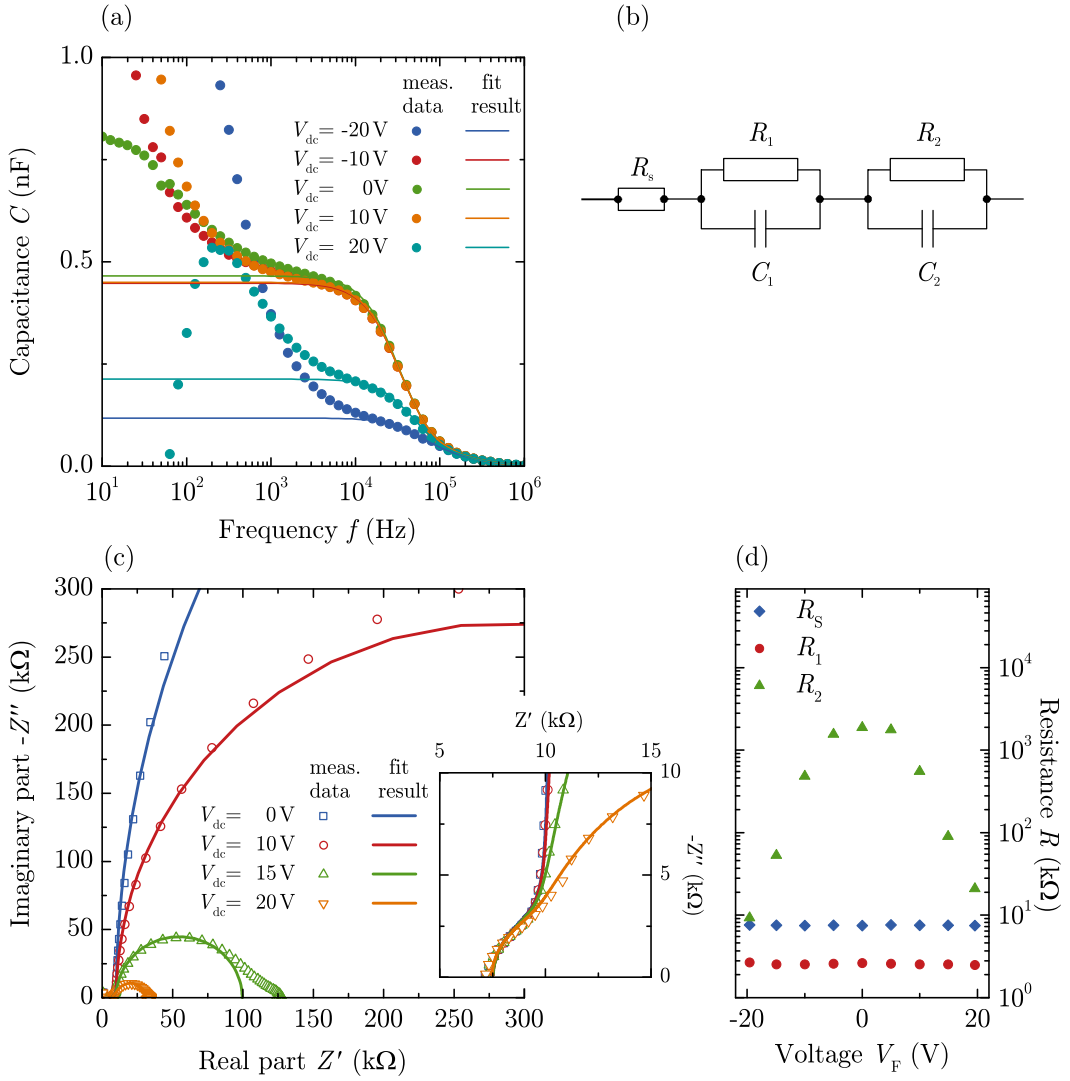

Figure 6.13.: (a) C-f-curves recorded for a hole-only device with DIP film thickness of $d(\mathrm{DIP}) = 300\,\mathrm{nm}$ at room temperature and various applied dc bias (symbols). Data is fitted according to the equivalent circuit as shown in (b). (c) Variation of the imaginary part, $-Z''$, of the impedance as a function of its real part, Z'. The inset shows the voltage independent high frequency arc which can be assigned to the TTF-TCNQ contact. (d) R_S, R_1 and R_2 as gained by the fit.

The reason for the second RC-element can be seen from the Nyquist plot depicted in (c): Besides the main arc which can be attributed to the DIP layer, and a second arc at low frequencies resulting from the lateral conductivity effects of the PEDOT electrode, there is a third arc observable in the high frequency range (see inset). This additional feature has no dependence on the applied bias and has to be considered in form of a second RC-element in the EC. The intersection of this

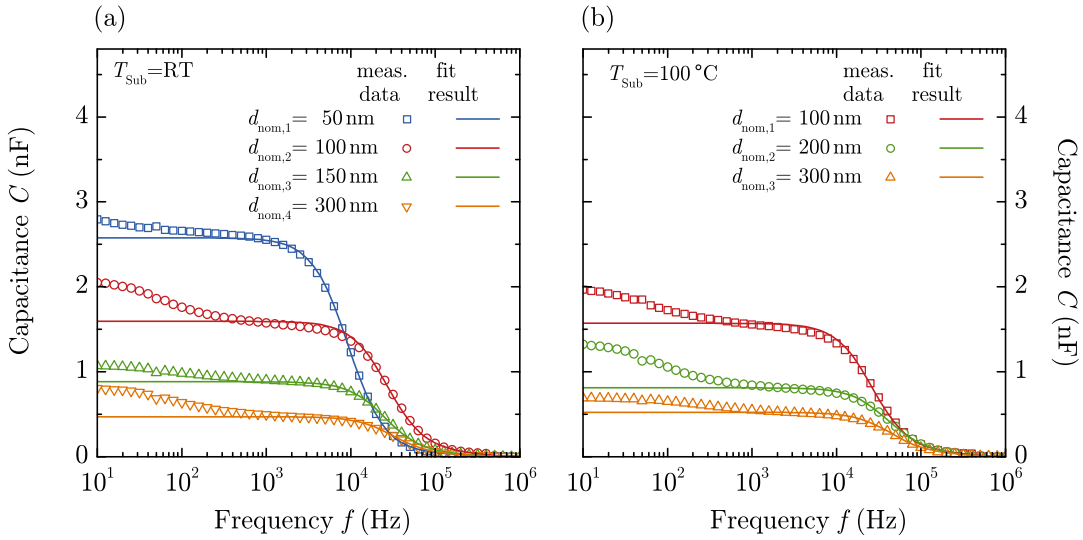

Figure 6.14.: Frequency dependent capacitance $C(f)$ of hole-only devices ($V_{dc} = 0\,V$) for several layer thicknesses; (a) without substrate heating (b) substrate temperature of $T_{sub} = 100\,°C$ during DIP deposition.

high frequency arc with the Z'-axis marks the series resistance of the device. A presentation of the resistances R_S, R_1 and R_2 is given in (d): The series resistance takes comparatively high values of $R_S \approx 7\,k\Omega$. From measurements of solar cells with ITO/PEDOT electrodes series resistances of around 75–150Ω are observed (cf. Fig. 7.28 (c)). Thus, the high series resistance can clearly be attributed to the TTF-TCNQ top contact which has to conduct the current not only transversely to the 150 nm thick film but also along the contact of the length of approximately 1 cm (cf. schematic device configuration in Fig. 3.9). Moreover, the top electrode can also be held responsible for the additional RC-element which determines the high frequency behavior. The reason can be found in the limited conductivity of TTF-TCNQ as organic metal.
In contrast to R_S and R_1, both showing almost constant values over the whole voltage range, R_2 has a voltage dependence with high values around $V_F = 0\,V$ and decreasing values for forward and reverse bias—and can thus be attributed to the DIP layer.

As a consequence of the successful assignment of the single elements forming the equivalent circuit, C_2 can be used to give information about the layer thickness. C-f curves at a bias of $V_{dc} = 0\,V$ are shown in Fig. 6.14 (a) for all RT samples and (b) for the samples with $T_{sub} = 100\,°C$. The data is fitted with the EC sketched in Fig. 6.13 (b) providing fits which are very close to the measurement in the desired frequency range between $5 \cdot 10^2$ and 10^6 Hz. Together with the series resistance R_S the thicknesses as determined from C-f fits are listed in Tab. 6.2

and are found in good agreement with the nominal layer thicknesses. For the devices with $T_{\mathrm{sub}} = 100\,^{\circ}\mathrm{C}$ the thicknesses determined by IS deviate somewhat more from the nominal layer thicknesses. This observation can be assigned to a partial desorption from the heated substrates. For a consistent analysis of the j-V curves thicknesses as determined from the C-f fits have been used as given in the previous section.

6.2.3. Discussion

In the previous sections hole transport in thin films of DIP has been investigated by studying hole-only devices—both deposited on unheated and heated substrates. Holes have been successfully injected from the ITO/PEDOT anode as well as from the TTF-TCNQ cathode. In general, the measurements reveal that the hole current in DIP is smaller than the electron current with a difference amounting to almost three orders of magnitude. This general trend has already been observed for the charge carrier transport in single crystals: while a hole mobility of $\mu_{\mathrm{h}} = 3 \cdot 10^{-3}\,\mathrm{cm}^2/\mathrm{Vs}$ has been determined, the electron mobility was reported to be almost one order of magnitude higher with $\mu_{\mathrm{e}} = 2 \cdot 10^{-2}\,\mathrm{cm}^2/\mathrm{Vs}$.[203] Mobility measurements on field effect transistors confirm these results as will be shown in the subsequent section.

It was found that the diodes suffer from high series resistances, which can predominantly be attributed to a limited conductivity of the electrode TTF-TCNQ. Thus, a potential drop at the contacts has to be taken into account. In order to assess the height of the series resistances, C-f data of the devices have been fitted according to an equivalent circuit including R_{S}. Values in the range of approximately 2–8 kΩ have been found for R_{S}, emphasizing the necessity to correct the applied voltage for this potential drop.

Generally, three different regimes could be identified from the j-V characteristics: An ohmic behavior at low voltages is followed by a filling of traps—which is identified by the current being described by a power law as expected for TCLC. A comparatively broad voltage regime for trap filling points towards traps which are distributed in energy, however, the type of distribution would require numerical simulations. Assuming an exponential distribution, a trap density of $N_{\mathrm{t}} \approx 7 \cdot 10^{18}\,\mathrm{cm}^{-3}$ with a trap level of $E_{\mathrm{trap}} = 0.12\,\mathrm{eV}$ can be estimated for the RT samples (see Tab. 6.2). For high voltages trap filling is completed and the current follows an SCLC behavior if not limited by injection. It was found that the hole current in forward direction, i.e. governed by holes injected from the ITO/PEDOT electrode, strongly depends on substrate heating: For the current density in the unheated de-

vices, the hole injection barrier plays an important role for the limiting mechanism. However, it is demonstrated that the hole current of the devices with heated substrate is no more determined by the injection property of the contact but, instead, by the bulk conduction properties of the organic material. This observation is in good agreement with the results of the previous chapter—demonstrating that the decisive influence of substrate heating can be found in lowering of the hole injection barrier—rather than the change in film morphology. The mobility in reverse direction—which is found to be limited by the transport of the organic material in both cases—increases when heating the substrate. However, the increase is only of marginal extent and, thus, it further confirms the observation that the crucial influence of substrate heating can be ascribed to a lowering of the hole injection barrier while the change in morphology plays only a minor role. In general it was found that the thickness dependence of the current provides a unique criterion to distinguish different limiting cases, even if the charge carrier mobility is characterized by a strong field-dependence. The extension of the steady-state j-V measurements to impedance spectroscopy enables the precise determination of the layer thickness, being of particular importance in the case of heated devices as a certain fraction of the molecules seem to desorb from the heated substrate. Moreover, IS data provide the possibility to determine the series resistance ascribed to a finite conductivity of ITO, PEDOT and, especially, TTF-TCNQ. Only by accounting for this potential drop reliable statements about the current-voltage behavior are possible in the first place.

To get even more reliability concerning the prevailing current limiting mechanism temperature dependent measurements together with numerical simulations would be helpful to give evidence about the type of trap distribution. Investigating a higher number of devices with different thicknesses and the usage of different contact materials would provide more precise information about the critical thickness and hole-injection barrier where a transition between contact limitation and SCLC takes place.

6.3. Impurity effects on DIP based solar cells

The purity of organic small molecular weight material used as active layer in solar cells can have a strong influence on fill factor and thus device efficiency as was revealed by studies on CuPc based solar cells.[358] To demonstrate the importance of material purity in DIP based cells, j-V curves of heated and unheated PHJ solar cells were investigated comprising DIP of different source batches. All batches have been purified twice by gradient sublimation prior to use. From a variety of batches

purchased from different companies or differing in manufacturing process, the best (named as batch 1) and worst (named as batch 2) are compared to each other in PHJ solar cells with the structure

ITO/ PEDOT/ DIP(50 nm)/ C_{60}(50 nm)/ BCP(5 nm)/ Al

with DIP deposited either on heated (T_{sub} = 100 °C) or unheated (T_{sub} = RT) substrate.

Fig. 6.15 (a) displays the j-V characteristics of the devices under illumination (upper part) and in dark (lower part). The dark curves are fitted within the exponential region by using the modified Shockley equation (5.1). Results of the

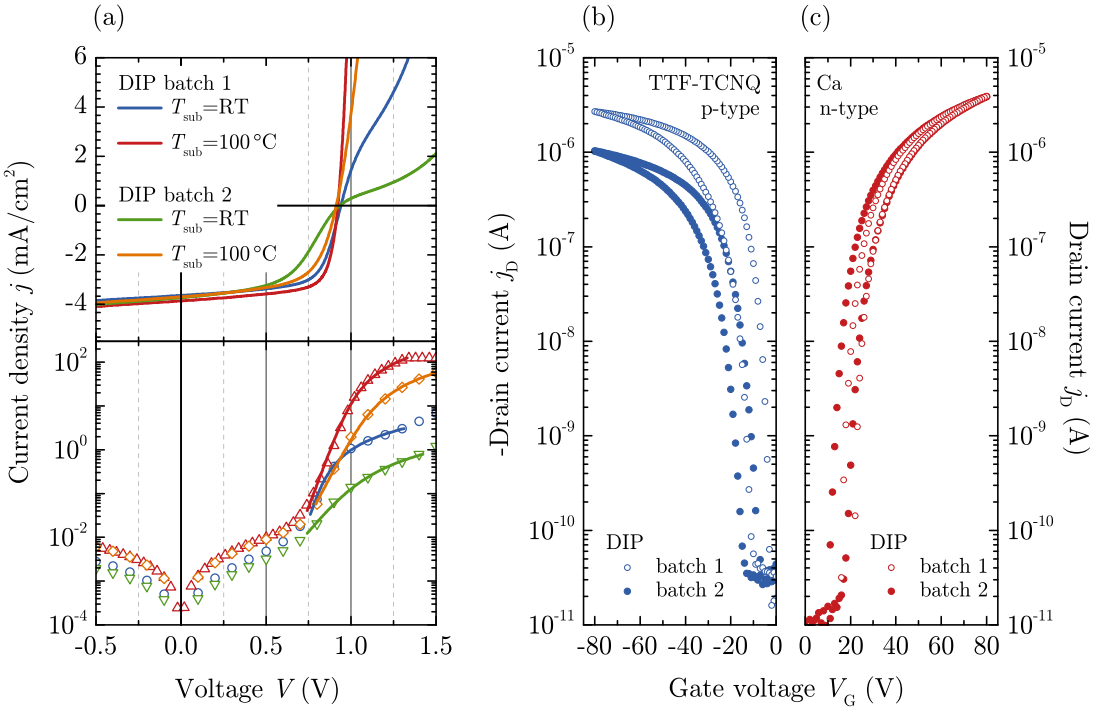

Figure 6.15.: Influence of DIP purity. (a) Current-voltage characteristics of ITO/ PEDOT/ DIP(50 nm)/ C_{60}(50 nm)/ BCP(5 nm)/ Al PHJ cells with different DIP source batches. Upper part: j-V characteristics under white LED illumination. Lower part: Logarithmic plot of the dark j-V characteristics (open symbols). The solid lines are fits based on the modified diode equation. Results of the fits are given in Tab. 6.3. (b) and (c) Transfer characteristics in the linear range for unipolar FETs with different electrode materials (channel length 70 µm) all fabricated on unheated substrates. (b) Hole transport regime (negative gate voltage) at a drain voltage of $V_D = -2$ V and (c) electron transport regime (positive gate voltage) at a given drain voltage of $V_D = +2$ V. Each measurement consists of a forward- and backward voltage sweep, manifesting in a hysteresis.

Table 6.3.: Upper part: Open-circuit voltage V_{oc}, short-circuit current density j_{sc}, fill factor FF, specific series resistance $R_S A$, ideality factor n and dark saturation current density j_0 for ITO/ PEDOT/ DIP(50 nm)/ C_{60}(50 nm)/ BCP(5 nm)/ Al PHJ cells with different DIP source batches (cf. Fig. 6.15). Light illumination was realized with a white LED. As the LED illumination conditions do not fulfill the AM 1.5 g standards, values for power conversion efficiencies are not specified. Lower part: Charge carrier mobilities determined from OFET measurements for different DIP source batches.

Solar cells Substrate treatment	V_{oc} (V)	j_{sc} (mA/cm^2)	FF (%)	$R_S A$ (Ω cm^2)	n	j_0 (mA/cm^2)
PHJ cell with DIP of batch 1 (cf. j-V curves in Fig. 6.15 (a))						
T_{sub} = RT	0.94	-3.75	67.1	133	1.4	$5.4 \cdot 10^{-12}$
T_{sub} = 100 °C	0.92	-3.8	70.4	2	1.8	$8.7 \cdot 10^{-12}$
PHJ cell with DIP of batch 2 (cf. j-V curves in Fig. 6.15 (a))						
T_{sub} = RT	0.93	-3.7	51.9	385	3.9	$3.9 \cdot 10^{-6}$
T_{sub} = 100 °C	0.91	-3.7	61.4	5	2.5	$8.6 \cdot 10^{-8}$

Field-effect transistors DIP batch	μ_h (cm^2/Vs)	μ_e (cm^2/Vs)
OFET with DIP of batch 1 and 2 (cf. transfer characteristics in Fig. 6.15 (b) and (c))		
batch 1	$8 \cdot 10^{-2}$	$1 \cdot 10^{-1}$
batch 2	$5 \cdot 10^{-2}$	$1 \cdot 10^{-1}$

fits as well as the characteristic photovoltaic parameters are summarized in Tab. 6.3. Within the measurement accuracy, all samples show similar values for V_{oc} and j_{sc}. The most noticeable difference is the current in forward direction, which manifests in strongly varying series resistances, and—associated with that—in different fill factors. In accordance with the results of Sec. 5.1, the devices with DIP evaporated on heated substrates show higher currents in forward direction. Thus, elevated substrate temperatures in combination with batch 1 of DIP leads to low specific series resistance of $R_S A = 2\,\Omega\,\text{cm}^2$, resulting in excellent fill factors exceeding 70 %. In contrast, the unheated sample with batch 2 of DIP shows high specific series resistance of almost $400\,\Omega\,\text{cm}^2$, which affects the fill factor in a way that it reaches only 52 %. Contrary to the expectations, V_{oc} stays almost the same even though recombination currents are found to be increased for batch 2. While a slight reduction of V_{oc} is observable for $T_{sub} = 100\,°\text{C}$, the high series resistance

of the unheated cell marks the exponential current regime and hinders a reliable evaluation of the fitted data.

In addition to the influence on OPVCs, the effect of material purity on charge carrier mobility is studied in organic field-effect transistors (OFETs), that have been fabricated as described in Sec. 3.2.2. OFETs were prepared on highly doped silicon wafers with 320 nm thermally grown oxide and a TTC passivation layer followed by a 25 nm thick film of DIP from the different batches. Figure 6.15 (b) and (c) display transfer characteristics of OFETs with top contacts of TTF-TCNQ and Ca for unipolar hole and electron transport, respectively. Charge carrier mobilities were determined by the transmission line method[204,359] using channel lengths between 50 and 150 µm. Figure 6.15 (b) shows the hole transport regime (negative gate voltage) at a drain voltage of $V_\mathrm{D} = -2\,\mathrm{V}$ and Fig. 6.15 (c) the electron transport regime (positive gate voltage) at a drain voltage of $V_\mathrm{D} = +2\,\mathrm{V}$, respectively. It is found that the values of the electron mobilities for the different DIP batches are similar with $\mu_\mathrm{e}(\mathrm{DIP}, \mathrm{batch}\,1) = \mu_\mathrm{e}(\mathrm{DIP}, \mathrm{batch}\,2) = 1 \cdot 10^{-1}\,\mathrm{cm}^2/\mathrm{Vs}$. In contrast, the hole mobilities differ considerably for the two DIP batches: $\mu_\mathrm{h}(\mathrm{DIP}, \mathrm{batch}\,1) = 8 \cdot 10^{-2}\,\mathrm{cm}^2/\mathrm{Vs}$ and $\mu_\mathrm{h}(\mathrm{DIP}, \mathrm{batch}\,2) = 5 \cdot 10^{-2}\,\mathrm{cm}^2/\mathrm{Vs}$. It is important to note that this difference in mobility is clearly beyond the scattering of values obtained on nominally identical samples from different fabrication runs, which was found to be less than 10 %.

When compared to the transport investigations presented in the previous section, it is striking that the charge carrier mobilities from FET measurements are found to be up to five orders of magnitude higher than values determined from SCLC—a phenomenon which has often been reported in literature.[50,69,360–362] The reason is found in the dependence of μ on charger carrier density as well as on molecular packing as described in Sec. 2.2.3: While in diodes the charge carrier transport is perpendicular to the substrate and extends over the whole thickness of the organic film, the transport in OFETs is restricted to the channel, i.e., to the few nanometers next to the insulator-semiconductor interface and is parallel to the substrate. As schematically depicted in Fig. 2.12 the π-orbital overlap in crystalline materials as DIP varies for different directions leading to a directional dependence of charge carrier transport. In addition, charge carrier density inside the active layer of an operating OFET is typically very high as compared to OLEDs or OPVCs. Both effects contribute to the anisotropy between mobilities determined from SCLC measurements and field-effect mobilities—the latter known to be orders of magnitude higher.

Independent of these differences, the results indicate that the performance of a DIP/C_{60} PHJ solar cell is impacted by material's purity. Specifically, the fill factor increases with hole mobility, which is found in turn to depend on material purity.

To assess this quantity in more detail, mass spectrometry measurements of the different DIP batches were performed by our cooperation partners in Würzburg. The obtained spectra (see Ref. 328) allow for an estimation of the purity level of the individual batches. As a result, batch 1 contains about half of the integrated impurity content compared to batch 2, though the total material purity of both batches is very high due to two step gradient sublimation.

In summary, it can be concluded that the device performance strongly correlates to the material's impurity levels estimated by mass spectroscopy. The lower hole mobility measured in the OFET transfer characteristics of batch 2 is a strong indication for impurity-induced hole trapping being also the reason for poor solar cell performance reflected in lower fill factors. For ultra-pure single crystalline reference systems, Probst *et al.*[363] demonstrated a decrease of the hole mobility at room temperature by one order of magnitude in anthracene molecular crystals intentionally doped with tetracene at a relative concentration of only 10^{-7}. Due to the respective HOMO level positions, tetracene acts as bare electrical hole trap in the anthracene matrix. This illustrates that already very small amounts of impurities can strongly affect the charge transport characteristics and thereby increase the series resistance of the studied DIP photovoltaic devices.

Chapter 7

The donor/acceptor interface

Up to now, the studies addressed the interface between anode and donor as well as the donor itself—with the analysis based on morphological, structural, energetic, and electric aspects. In this context, one of the focal points has been the impact of substrate treatment on the properties of the semiconducting layers and, with that, on device performance. In the following, the attention will be shifted one step further within the device stack, namely to the interface between donor and acceptor. The first part will mainly address morphological and structural aspects and their influence on device performance of both planar and bulk heterojunctions studied on a variety of different D/A systems, however, with particular focus on the DIP/C_{60} system. Afterwards, the interface between donor and acceptor will be examined concerning its electronic properties—including the energetics of the charge transfer state and recombination.

7.1. Morphology, structure and energetics of donor/acceptor interfaces

7.1.1. The DIP/C_{60} interface

Morphology and structure of the DIP/C_{60} interface

Morphological and structural studies in Sec. 5.1.1 demonstrate the strong influence of substrate temperature on the film growth of DIP. AFM measurements could reveal a change in surface morphology from round-shaped islands to a terrace-like structure with extended crystallites when going from unheated to heated substrate. Based on these findings, planar heterostructures have been fabricated where DIP films evaporated at different substrate temperatures were covered with C_{60}. In comparison with the AFM results of pure DIP as shown in Fig. 5.1, the covering C_{60} molecules form small domains with diameters of about 25–30 nm, adapting to the underlying morphology of the DIP (see Fig. 7.1).

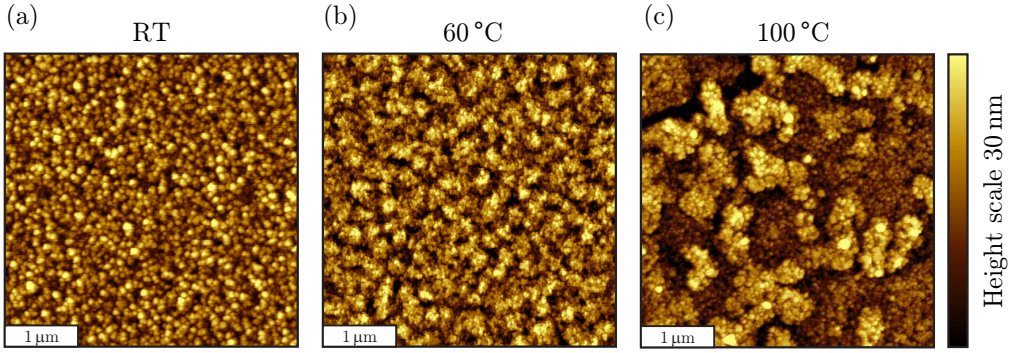

Figure 7.1.: AFM images of C_{60} (80 nm) on ITO/PEDOT/DIP(50 nm), with DIP evaporated at substrate temperatures of (a) RT, (b) 60 °C, and (c) 100 °C. In all cases C_{60} is evaporated without substrate heating. The total image size is $4 \times 4\,\mu m^2$ in all cases.

When coevaporating both materials with the substrate kept at room temperature, the topography is characterized by irregularly shaped domains with high surface roughness (see Fig. 7.2 (a)). However, depositing the mixed film on a heated substrate with $T_{sub} = 100\,°C$ leads to a spongiform basic structure composed of large interconnected features resembling the neat DIP film grown at 100 °C as well a smaller crystallites on top reminiscent of C_{60} grown on top of DIP (see Fig. 7.2 (b)). This observation already points to phase separation in the coevaporated film which will be confirmed by XRS measurement as shown in the following.

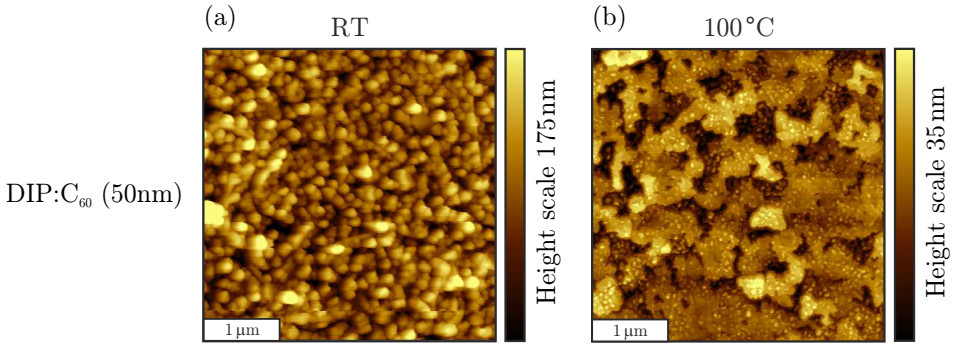

Figure 7.2.: AFM images of mixed films of DIP and C_{60} (mixing ratio 1:1, 50 nm) deposited on ITO/PEDOT at substrate temperature of (a) RT and (b) 100 °C. The total image size is $4 \times 4\,\mu m^2$ in all cases.

In analogy to the investigations on neat DIP films, XRS measurements were performed to detect the structural order and spatial coherence length in both bilayer and mixed films of DIP and C_{60} as well as to give evidence of the mixing behavior inside the blend. Results of specular X-ray scattering and grazing incidence X-ray diffraction are summarized in Fig. 7.3. The DIP films of the bilayer samples as well as the mixed DIP:C_{60} layers were deposited at substrate temperature of 25 °C and 100 °C, respectively. The reflectivity of the PHJ clearly demonstrate that the overall signal is mainly determined by the highly crystalline DIP layer which is characterized by the strong (001) and (002) peaks of the DIP σ-phase. Laue oscillations around the DIP (001) Bragg reflection indicate coherently ordered domains with magnitude corresponding to the whole DIP layer thickness. In contrast to studies on neat C_{60} films evaporated on ITO/PEDOT (as will be shown in Fig. 7.10) the X-ray scattering spectra of C_{60} evaporated on DIP show comparatively pronounced Bragg reflections of C_{60} at $q_z \approx 0.775$ Å^{-1} which are superimposed with the DIP(002) reflection. This exceptional behavior may be attributed to improved growth properties of C_{60} on top of the well ordered DIP structure. Section 2.2.3 introduced the strong influence of charge carrier mobility on grain boundaries, whereas a linear increase of μ with grain size has been reported. Thus, the crystallinity of both DIP and C_{60} are considered as great advantage of this material system for efficient charge carrier extraction when applied in PHJ photovoltaic devices.

Mixed DIP:C_{60} layers show the same DIP Bragg peak positions as neat DIP, which clearly proves that both materials exist in individual phases instead of forming a mutual crystal structure as found for molecularly mixed films. However, there is no measurable C_{60} Bragg reflection in the blends, which indicates low out-of-plane order for C_{60} crystallites. The comparably narrow width Δq_z of the DIP(001) peak in the mixture evaporated at $T_{sub} = 100$ °C (orange line in Fig. 7.3 (a)) corresponds

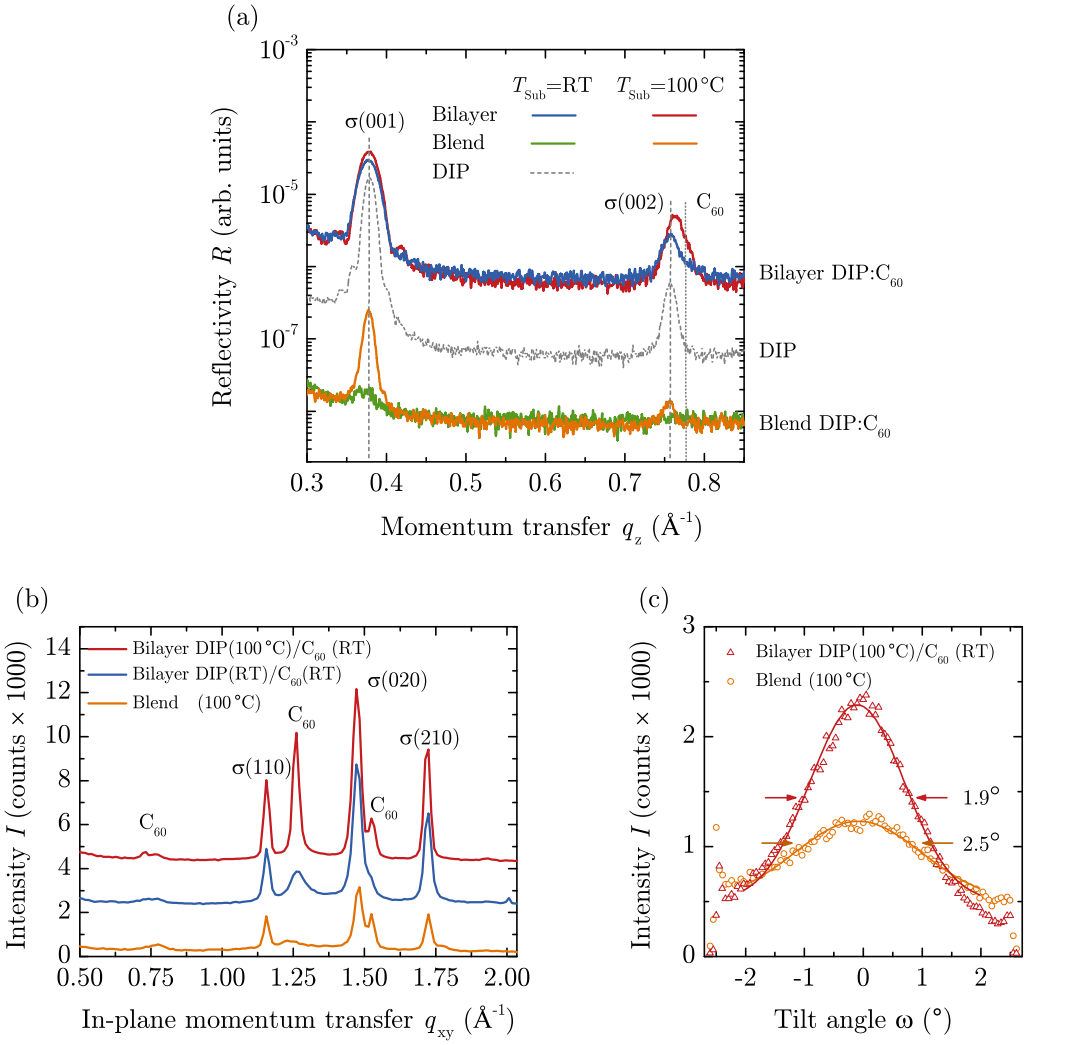

Figure 7.3.: (a) Specular X-ray reflectivity of bilayers of DIP(20 nm) /C_{60}(20 nm) and mixed layers of DIP:C_{60} (40 nm, mixing ratio 1:1) both evaporated on ITO/PEDOT, grown at different temperatures as indicated in the diagram. For comparison the spectrum of the pure DIP film evaporated at T_{sub} = RT is included. Bragg reflections at $q_z = 0.378\,\mathring{A}^{-1}$ can be associated with a lattice plane spacing of $d_{DIP} = 16.6\,\mathring{A}$. (b) In-plane grazing incidence X-ray diffraction data of two DIP(20 nm)/C_{60}(20 nm) bilayers on ITO/PEDOT grown at different substrate temperatures and a mixed film of DIP:C_{60}(40 nm, mixing ratio 1:1) grown at T_{sub} = 100 °C. (c) Rocking scans on the DIP(001) reflections of a DIP(20 nm)/C_{60}(20 nm) bilayer and a mixed layer DIP:C_{60}(40 nm, mixing ratio 1:1), both grown at T_{sub} = 100 °C (taken from Ref. 327).

to a coherence length of $D \approx 45$ nm, which is approximately equal to the entire layer thickness indicating that crystalline DIP domains extend throughout the whole film as has already been deduced from AFM measurements (cf. Fig. 7.2 (b)).

The crystalline DIP domains are much smaller when the substrate is not heated during coevaporation pointing towards less pronounced phase separation in the unheated blend (green curve in Fig. 7.3 (a)), which is found to considerably impact corresponding solar cell performance as will be shown later on.

In addition to specular reflectivity mode, GIXD data has been recorded which probes the lateral crystal structure of the sample. As can be seen from Fig. 7.3 (b), the diffraction spectrum shows several C_{60} Bragg reflections in the DIP/C_{60} bilayers confirming the presence of a crystalline C_{60} layer on DIP. All in-plane DIP reflections can be assigned to the σ-phase, whereas C_{60} Bragg reflections are related to the fcc structure (cf. Sec. 3.1.3).[q] As was already deduced from specular reflectivity and expected from AFM images, the highly crystalline DIP surface improves the growth properties of C_{60} on top—especially when DIP was grown on heated substrate. In accordance with the out-of-plane reflectivity, both DIP as well as C_{60} Bragg peaks are present in the mixed film, confirming a certain degree of phase separation.

Rocking scans at a constant scattering angle at the position of Bragg reflections probe the angular distribution of the lattice planes, i.e., the mosaicity. For the bilayer and mixed DIP/C_{60} film evaporated at substrate temperature of 100 °C a mosaicity (full width at half maximum of the rocking curve) of $\Delta\omega = 1.9°$ and 2.5°, respectively, is found by rocking scans on the (001) reflections (see Fig. 7.3 (c)). This indicates a comparatively small angular spread of the orientations of the crystallites, which was shown to play a non-negligible role on charge carrier mobility.[49]

Electronic structure of the DIP/C_{60} heterojunction

Building on the examined DIP films as shown in Fig. 5.3 and 5.8, thickness dependent UPS spectra of C_{60} deposited both on PEDOT/DIP and HIL1.3/DIP have been recorded (see Fig. 7.4). The valence spectra for C_{60} on 10 nm PEDOT/DIP show that the low binding energy onset of the acceptor HOMO is at 1.50 eV, both for the C_{60} mono- and multi-layer. With the DIP onset situated at 0.45 eV, the HOMO offset between DIP and C_{60} at this interface is 1.05 eV. As was shown in Sec. 5.2.2, the electronic structure of the anode/DIP interface is very much dependent on the hole injection layer, i.e., using a high work function HIL or heating the PEDOT film leads to markedly reduced hole injection barriers. In spite of these differences at the hole injecting contact, the energy level alignment at the DIP/C_{60} interface is unchanged when using the high work function HIL1.3 as electrode. In this case vacuum level alignment prevails and the HOMO offset is 1.05 eV, too.

[q] A more precise classification of the C_{60} peaks can be found in Ref. 200.

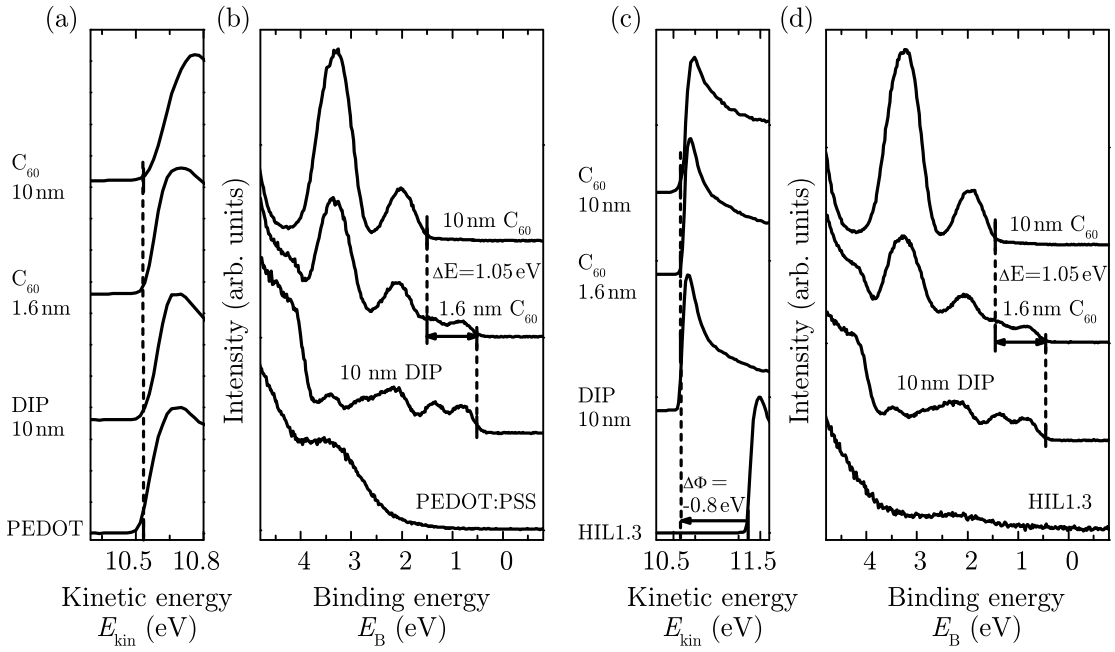

Figure 7.4.: Ultraviolet photoelectron spectra of ITO/PEDOT substrates with different coverage of C_{60} on top of PEDOT/DIP(10 nm) (left part) and HIL1.3/DIP(10 nm) (right part). Secondary electron cutoff (SECO) spectrum (a) and (c) and valence region spectrum (b) and (d) (taken from Ref. 327).

The energy level structure at HIL/DIP/C_{60} interfaces is schematically summarized in Fig. 7.6 (a) where the dashed and shaded energy levels denote the situation when HIL1.3 is used as hole injection layer. The DIP/C_{60} interface energetics relevant for PHJ devices are identical for both PEDOT:PSS formulations. Assuming a transport gap for C_{60}[r] of 2.5 eV and for DIP of 2.5 eV (cf. Tab. 4.1) the interfacial energy gap $E_{DA} = \left|E_{HOMO}^{donor} - E_{LUMO}^{acceptor}\right|$ between the DIP HOMO and the C_{60} LUMO is 1.45 eV, which is an estimate of the maximum achievable open-circuit voltage in organic heterojunction solar cells as was shown in Sec. 2.3.2. A detailed analysis of this topic will be given in Sec. 7.2.1.

Figure 7.5 shows thickness dependent UPS spectra for mixed films of DIP:C_{60} co-deposited on ITO/PEDOT (without substrate heating). As illustrated by the schematic energy level diagram in Fig. 7.6 (b), the energy levels are almost identical to the PHJ case—except for the low binding energy onset of the C_{60} HOMO which is found 0.1 eV closer to E_F, as inferred from a fitting routine of the blend UPS spectrum by summation of pristine C_{60} and DIP spectra depicted in Fig. 7.5 (c).

[r] In contrast to the published data in Ref. 327, where the optical gap of C_{60} was assumed as $E_g = 2.3$ eV,[364] more recent measurements identified $E_g(C_{60})$ to be 2.5 eV.

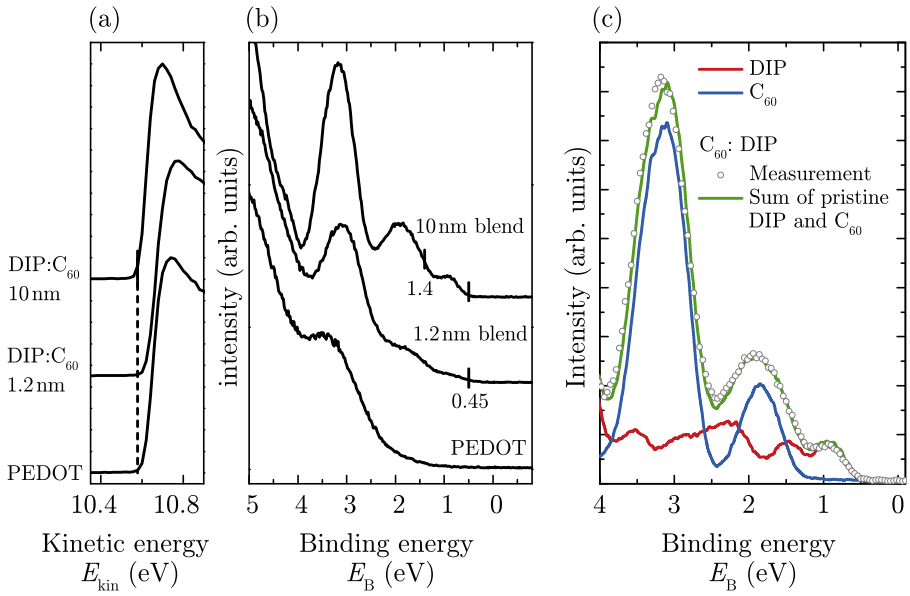

Figure 7.5.: Ultraviolet photoelectron spectra of ITO/PEDOT substrate with different coverage of a DIP:C_{60} blend (mixing ratio approximately 1:1) on top of ITO/PEDOT. Secondary electron cutoff (SECO) spectrum (a) and valence region spectrum (b). (c) Valence region spectra for C_{60}, DIP and the mixed film C_{60}:DIP compared to a summation of the pristine C_{60} and DIP spectra (taken from Ref. 327).

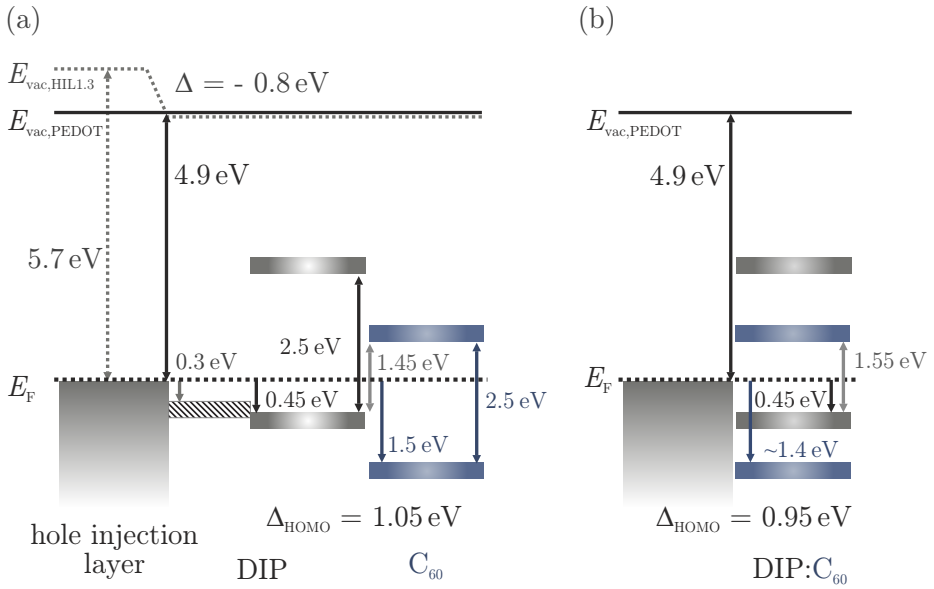

Figure 7.6.: Schematic energy level diagrams for (a) PHJ HIL/DIP/C_{60} with PEDOT or HIL1.3 as hole injection layer (dashed lines and the shaded area mark the levels measured for the HIL1.3) and (b) DIP:C_{60} blend on ITO/PEDOT.

Thus, the interfacial energy gap is deduced to $E_{DA} = 1.55\,eV$ and, consequently, similar values for V_{oc} are expected for planar and bulk heterojunction solar cells based on DIP/C_{60}.

Electrical characterization

Based on these results, planar and bulk heterojunctions with and without substrate heating can be interpreted with regard to the observed morphological, structural and energetic differences. A detailed investigation on PHJ devices with varying substrate temperature and hole injection barrier has already been presented in chapter 5 as part of the analysis of the anode/donor interface. In accordance with the mobility investigations inside the donor, the results demonstrate that the decisive influence of substrate heating can be attributed to a lowering of the hole injection barrier—rather than to a change in film morphology. In addition to the remarkably high crystallinity of DIP films, X-ray scattering data on DIP/C_{60} bilayers showed improved growth properties of C_{60} on the well ordered DIP structure. It is very likely, that this exceptional behavior contributes to an excellent charge extraction efficiency in PHJ devices—ultimately leading to the observed fill factors exceeding 70%.

Concerning the heating effect on mixed DIP:C_{60} films, X-ray scattering technique reveal an enhancement of phase separation when heating the substrate during deposition of the blend. When preparing PM-HJ solar cells, the blend is sandwiched between thin films of pure material. In the heated devices, the neat DIP layer underneath the blend is usually deposited with $T_{sub} = 100\,°C$ as well—while the capping C_{60} is always evaporated without further heating of the substrate. As will be shown in the following, substrate heating during fabrication of PH-HJ devices reveal a clear improvement in photovoltaic parameters—which is mainly manifested in enhanced fill factors. Based on the results of the PHJ cells together with the morphological and structural analysis of the blend, two different effects might be responsible for this improvement: On the one hand heating the sample is accompanied by reduced hole injection barriers at the anode/DIP contact—and on the other hand enlarged phase separation inside the blend suggests facilitating charge carrier extraction. In order to separate both effects the following device series has been fabricated and analyzed concerning their photovoltaic behavior—all based on the structure

ITO/ PEDOT/ DIP(5 nm)/ DIP:C_{60}(50 nm)/ C_{60}(10 nm)/ BCP(5 nm)/ Al.

In addition to a completely unheated cell and one where both the neat DIP as well as the mixed layer were evaporated on heated substrate, one device was pre-

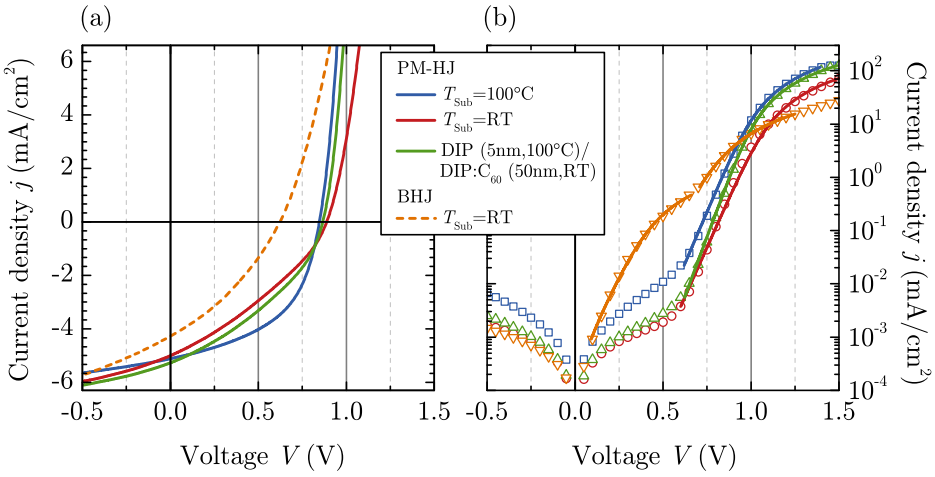

Figure 7.7.: Effect of different substrate temperatures during DIP evaporation of PM-HJ solar cells: j-V characteristics of cells with structure ITO/ PEDOT/ DIP(5 nm)/ DIP:C_{60}(50 nm)/ C_{60}(10 nm)/ BCP(5 nm)/ Al. (a) j-V characteristics under white LED illumination. (b) Logarithmic plot of the dark j-V characteristics (open symbols). The solid lines are fits based on the modified diode equation. Neat C_{60} layers are always deposited with the substrate held at RT. Results of the fits are given in Tab. 7.1.

pared with heated DIP single layer but the blend evaporated at T_{sub} = RT. The j-V characteristics in dark and under illumination are shown in Fig. 7.7 and the photovoltaic parameters are listed in Tab. 7.1. The most obvious difference can be found in the shape of the light j-V curve within the fourth quadrant—quantitatively expressed by the fill factor of the cell: Both the completely unheated cell (red curve) as well as the device with DIP interlayer deposited at T_{sub} = 100 °C (green curve) suffer from low fill factors between 33 and 37%, which can be attributed to impeded charge carrier extraction as result of the small-scale phase separation as shown from the structural analysis. By contrast, substrate heating during blend evaporation enables phase separation with larger domains of pure DIP and C_{60}—ultimately leading to pronounced percolation paths refleted in enhanced fill factors of up to 50% (blue curve).

The PM-HJ concept has been introduced as combination of planar and bulk heterojunction, unifying benefits of both concepts. Thus, it combines enhanced dimension of the D/A interface inside the blend with unhindered charge carrier collection properties of neat organic layers. In the following, the PM-HJ devices is compared with a pure BHJ cell where the neat DIP and C_{60} films encompassing the blend has been omitted. The layer sequence of the BHJ device is

ITO/ PEDOT/ DIP:C_{60}(100 nm)/ BCP(5 nm)/ Al,

Table 7.1.: Open-circuit voltage V_{oc}, short-circuit current density j_{sc}, fill factor FF, specific series resistance $R_S A$, ideality factor n and dark saturation current density j_0 for PM-HJ solar cells with different substrate treatment (cf. Fig. 7.7). Unless explicitly assigned to a certain layer, the substrate temperature refers to the DIP containing films (pure and mixed layer)—all C_{60} capping layers were deposited with T_{sub} = RT. Light illumination was realized with a white LED. As the LED illumination conditions do not fulfill the AM 1.5 g standards, values for power conversion efficiencies are not specified.

Architecture	V_{oc} (V)	j_{sc} (mA/cm^2)	FF (%)	$R_S A$ (Ω cm^2)	n	j_0 (mA/cm^2)
PM-HJ						
$T_{sub} = 100\,°C$	0.85	-5.1	49.6	3	2.2	$3.6 \cdot 10^{-7}$
T_{sub} = RT	0.89	-5.0	33.1	5	2.3	$1.3 \cdot 10^{-7}$
DIP(100 °C)/DIP:C_{60}(RT)	0.87	-5.3	36.6	3	1.9	$1.6 \cdot 10^{-8}$
BHJ						
T_{sub} = RT	0.62	-4.3	33.4			
1st exponential increase				397	2.5	$2.9 \cdot 10^{-4}$
2nd exponential increase				21	2.7	$4.4 \cdot 10^{-5}$

whereas the blend has been evaporated on heated substrate. Current-voltage characteristics are included in Fig. 7.7 (orange dashed curve) and characteristic device parameters are listed in Tab. 7.1. The active layer thickness of the BHJ has to be chosen somewhat larger compared to PM-HJ devices, as the neat BHJ is more susceptible to leakage currents. However, the resulting short-circuit current is even smaller than for the PM-HJ which is actually composed of a smaller overall layer thickness. From the morphological and structural analysis of mixed DIP:C_{60} films as shown in Sec. 7.1.1 it can be deduced that this material combination exhibits phase separation in the blend and forms percolation paths for both carrier types—in particular, if the blend is evaporated at elevated substrate temperature. However, the decrease in j_{sc} with increased thickness of the blend demonstrates the limits of the bulk heterojunction concept: with the increase in layer thickness, recombination losses due to the presence of both phases in close proximity exceed the gain in absorption efficiency and finally reduce j_{sc}.[365,366] A similar reduction in j_{sc} is found for increasing the total layer thickness in PM-HJ devices as has been shown in Ref. 327.

Following from the characteristic device properties of the PM-HJ cells, it is remarkable that all cells reach almost identical open-circuit voltages as the best PHJ devices (cf. Tab. 5.1). By contrast, pure bulk heterojunction devices have substantially lower V_{oc} of only 0.6–0.7 V, even though equal values of the interfacial energy gap have been detected by UPS measurements (cf. Fig. 7.6). This can be seen as a further advantage of the hybrid PM-HJ concept over the pure BHJ device: in the latter V_{oc} may be limited by the built-in voltage V_{bi} because recombination of charge carriers at the interface between an electrode and the mixed layer immediately sets in as soon as the applied voltage exceeds V_{bi}.[333] A similar observation has been found by Foertig *et al.* using transient photovoltage measurements: The authors report on CuPc/C_{60} based solar cells and attribute a lowering of V_{oc} in BHJ cells compared to PHJ (at least at low illumination intensities) to an increase of the active recombination region due to small-scale phase separation within the blend.[367] The neat donor and acceptor layers encompassing the mixed layer in the PM-HJ cell suppress this direct recombination leading to reduced losses in V_{oc}. This possible explanation is confirmed by the immediate increase in dark current density in forward direction for voltages above $V = 0$ V, which is not characterized by a markable onset voltage (see Fig. 7.7 (b)). A further peculiarity of the dark j-V curve can be found in the double exponential increase—a feature which is also observed for CuPc/C_{60} PHJ as will be shown in Sec. 7.2.1. Giebink *et al.* ascribe the double exponential current-voltage characteristic to a concurrent existence of two recombination pathways of different order at a junction.[26] Even though the reason for this behavior of the BHJ cell in dark is not part of the present study, two sets of parameters can be extracted for the first and second increase, respectively—listed in Tab. 7.1. The fitted parameters are rather similar except of the series resistance which strongly decreases for the current density in the higher voltage range. Thus, a possible explanation might be found in different injection barriers for holes into the DIP domains and electrons into the C_{60} domains—ultimately leading to successive charge carrier injection. In any case, j_0 of the BHJ is found to be 3–4 orders of magnitude higher than for PM-HJ cells. This indicates higher recombination losses in pure BHJ devices which is quite conceivable when assuming increased recombination at the electrodes. According to Eq. (2.25) this increase in j_0 is directly related to the loss in V_{oc}. Consequently, the neat donor and acceptor layers encompassing the mixed layer in a PM-HJ cell suppress this direct recombination and thus enable V_{oc} to reach values as high as for PHJ devices.

Based on the above described results both on planar as well as on bulk heterojunctions, a summarizing comparison between heated and unheated PHJ and PM-HJ devices is shown in Fig. 7.8, whereas the extracted device parameters as well as the exact layer sequences are listed in Tab. 7.2. In general, all four devices

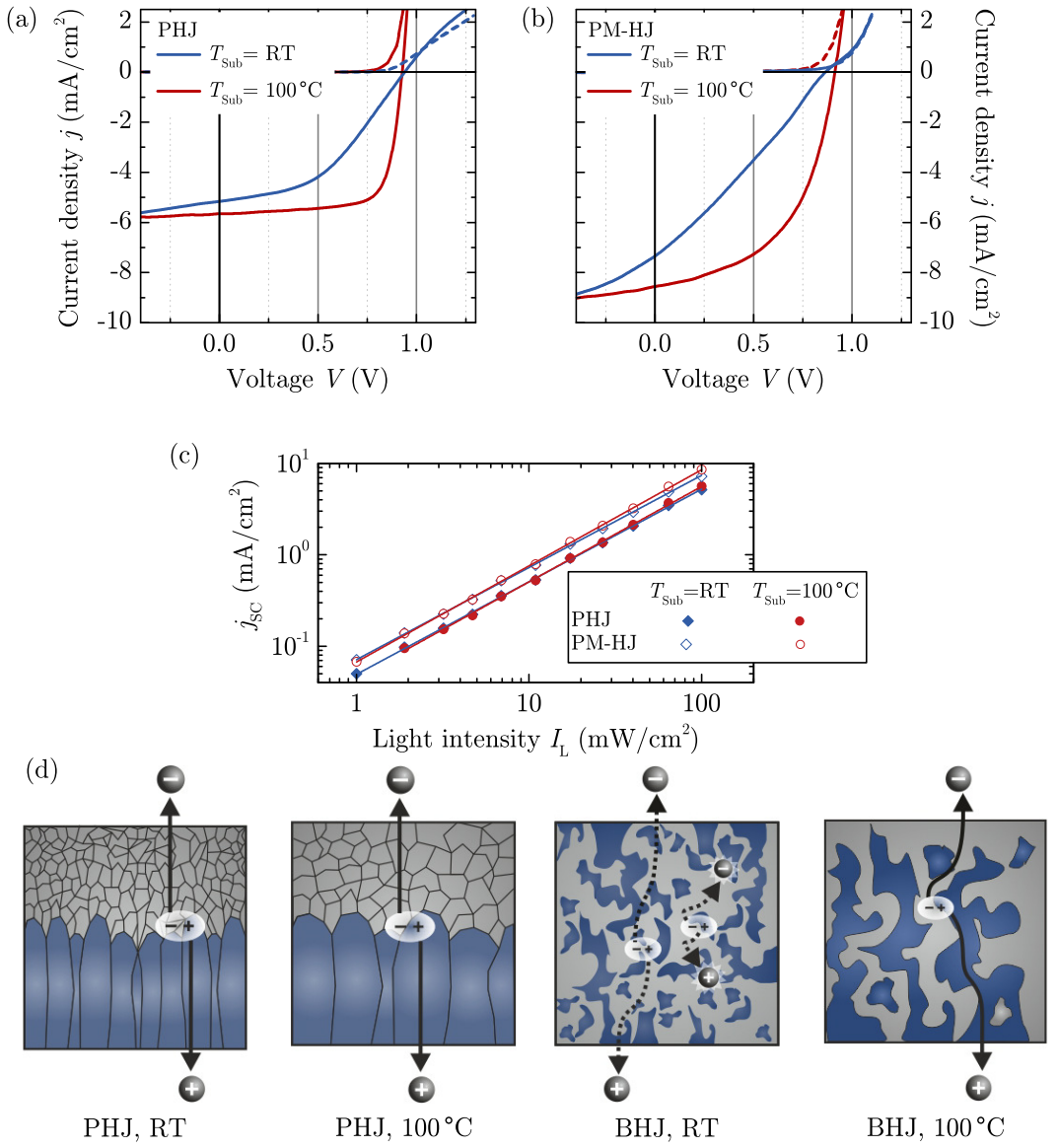

Figure 7.8.: Current density vs. voltage (j-V) characteristics of (a) PHJ and (b) PM-HJ devices with different architectures measured under AM 1.5 g illumination. The organic layers were either deposited on unheated substrates or on heated ones with substrate temperature of 100 °C during DIP evaporation (as neat or mixed film). Characteristic values and exact layer sequences are summarized in Tab. 7.2. (c) Light intensity dependence of the short-circuit current density following a power law $j_{sc} \propto (I_L)^{\alpha}$ with $\alpha \approx 1.0$. (d) Schematic picture of the film morphology in planar and planar-mixed heterojunctions of DIP and C_{60} illustrating the pronounced crystallinity in case of PHJ—which is even improved when heating the substrate during DIP evaporation—and the impact of substrate heating on the scale of phase separation in BHJ.

show almost identical open-circuit voltage and differ only in their short-circuit currents and fill factors. The high open-circuit voltages up to 0.93 V can be ascribed to the high ionization potential of DIP and the favorable energy level alignment with C_{60}—finally leading to high interfacial energy gap which ultimately limits V_{oc}. As discussed above, the PM-HJ concept suppresses the direct recombination of charge carriers at the organic/electrode interface and enables V_{oc} to reach values as high as for PHJ devices.

The short-circuit currents are considerably higher in the PM-HJ solar cells as compared to the corresponding PHJ structures: Excitons which are created in the mixed layer are always in proximity of a donor/acceptor interface and can thus easily be dissociated. Furthermore, excitons created in the adjacent layers of neat DIP and C_{60} may also contribute to the photocurrent, as the layer thicknesses of 5 and 10 nm are well below the exciton diffusion length of DIP[205] and C_{60}.[368]

The second parameter, in which the investigated cells differ in a characteristic way, is the fill factor. Comparing the heated and the unheated devices, respectively, the PHJ cells have a higher FF than the PM-HJ devices, and in particular for the heated PHJ device it reaches exceptionally high values exceeding 74%—being one of the highest fill factors observed for organic small molecule solar cells. It indicates highly efficient charge carrier transport towards the electrical contacts with little recombination losses—despite of comparatively thick layers—as well as unhindered charge carrier extraction without energetic barriers. Inherently higher bulk recombination and lower carrier mobility in the mixed layer probably limit charge collection efficiency and thereby the FF of these devices.

The positive impact of substrate heating on the electrical properties of the solar cells is predominantly reflected in a considerable increase of the fill factor in both device architectures. As discussed before, different origins can be held responsible for the impact of T_{sub} on the j-V characteristics of PHJ and PM-HJ cells: In the PHJ setup the improvement of FF is not so much a result of morphological changes but rather a consequence of reduced hole injection barrier resulting from heating the PEDOT substrate (cf. Sec. 5.1). By contrast, the efficiency enhancement in the PM-HJ cell can be ascribed to morphological differences instead of energetic relations. As deduced from morphological and structural investigations presented in the previous section, substrate heating during evaporation of the blended film causes enhanced phase separation and with that improved carrier extraction to the electrodes. These findings could be further confirmed by a comprehensive morphological and structural study including grazing incidence small angle X-ray scattering (GISAXS) which has the advantage to probe the volume of a film—providing information about domain distances in the bulk.[369] The enhanced phase separation, in turn, leads to an increase of the fill factor from 28% to 52%.

Table 7.2.: Solar cell parameters of PHJ and PM-HJ devices with different substrate temperature during evaporation of DIP containing layers (j-V curves shown in Fig. 7.8). Devices were measured under AM 1.5 g illumination.* V_{oc}: open-circuit voltage, j_{sc}: short-circuit current density, FF: fill factor and η: power conversion efficiency, $R_S A$: specific series resistance, n: diode ideality factor and j_0: dark saturation current density.

Architecture	V_{oc} (V)	j_{sc} (mA/cm^2)	FF (%)	η (%)	$R_S\,A$ ($\Omega\,$cm^2)	n	j_0 (mA/cm^2)
PHJ (cf. j-V curves in Fig. 7.8 (a))							
DIP(50 nm, RT/100 °C)/C_{60}(80 nm, RT)							
T_{sub} = RT	0.94	-5.2	44.3	2.1	120	1.5	$2.9 \cdot 10^{-11}$
T_{sub} = 100 °C	0.93	-5.6	74.3	3.9	3	1.6	$6.3 \cdot 10^{-10}$
PM-HJ (cf. j-V curves in Fig. 7.8 (b))							
DIP(5 nm, RT/100 °C)/DIP:C_{60}(50 nm, RT/100 °C)/C_{60}(10 nm, RT)							
T_{sub} = RT	0.86	-7.4	28.0	1.8	7	3.1	$3.0 \cdot 10^{-6}$
T_{sub} = 100 °C	0.91	-8.6	51.9	4.1	7	2.0	$3.5 \cdot 10^{-8}$

* As already mentioned, the inhomogeneity of the light beam together with a cell area being smaller than the reference cell leads on an overestimation of the power conversion efficiency—however, the setup enables constant measurement conditions allowing for a clear comparison between the cells.

As has been introduced in Sec. 2.3.2, the light intensity dependence of the short-circuit current density can be used to identify the dominant recombination mechanism. Here, j_{sc} follows a power law $j_{sc} \propto (I_L)^{\alpha}$, with a scaling exponent α very close to one for all devices (see Fig. 7.8 (c)). Based on the considerations given in Sec. 2.3.2 this observation could be taken as indication for first order recombination kinetics. However, it has also been mentioned that the reliability of this analysis is only limited and bimolecular recombination losses cannot be excluded. A further discussion on possible prevailing recombination mechanisms—based on the interpretation of the diode ideality factor—is given in Sec. 7.2.4.

The deduced structures of the planar and bulk heterojunctions are summarized in schematic pictures shown in Fig. 7.8 (d): The PHJ, both with and without substrate heating, is characterized by a pronounced crystallinity of the DIP layer as well as its templating effect leading to unusually crystalline C_{60} films—both allowing for efficient charge carrier extraction towards the electrodes. When depositing a blend of DIP and C_{60} without heating the substrate, small-scale phase separation leads

to reduced charge carrier mobility and hindered transport towards the electrodes. By contrast, mixed films evaporated under substrate heating exhibit large-scale phase separation forming a bicontinuous network of both molecular species, which enables efficient exciton dissociation and charge carrier transport. Altogether, the lower current in the planar heterojunction cells is almost completely compensated by their extremely high FF achieving equally high power conversion efficiency.

7.1.2. The CuPc/F_{16}CuPc interface

Fluorination of phthalocyanines can be considered as common method to increase their electron affinity and ionization potential, while having almost no effect on the energy gap.[299,370] As can be seen from the energy level diagram in Fig. 4.2 the electrochemical potentials of the perfluorinated CuPc are shifted in a way, that F_{16}CuPc can act as acceptor in combination with its hydrogenated counterpart. Therefore, bilayers and blends of CuPc and F_{16}CuPc were studied concerning their structural properties and possible suitability as D/A combination for an application in OPVCs.

As shown in Ref. 371 the topography of neat films of CuPc and F_{16}CuPc has a granular structure which changes towards worm-like domains when deposited at elevated substrate temperatures. When mixing both materials, AFM measurements reveal similar morphologies of the blend as compared to the neat films, which already points towards a molecular mixture of both constituents.

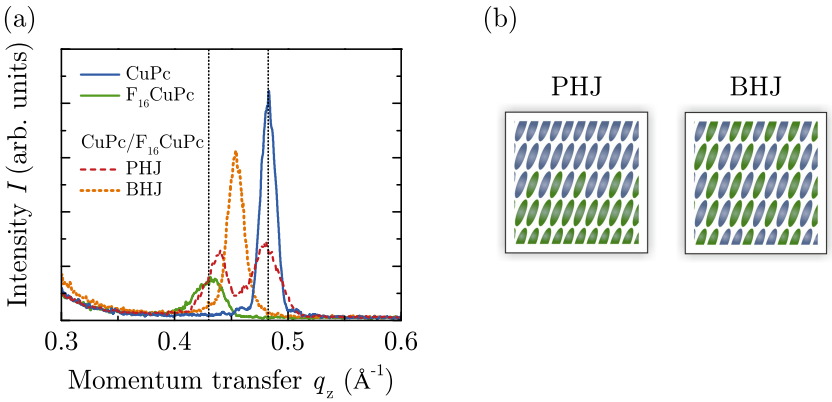

Figure 7.9.: (a) X-ray reflectivity spectra of neat films of CuPc (25 nm) and F_{16}CuPc (25 nm), a bilayer CuPc(25 nm)/F_{16}CuPc(25 nm) and blend of CuPc:F_{16}CuPc(50 nm, mixing ratio 1:1). All films have been deposited on unheated ITO/PEDOT substrates (taken from Ref. 371). (b) Schematic drawing of the planar and mixed heterojunction of CuPc and F_{16}CuPc as revealed from structural investigation.

X-ray scattering technique has been used in order to analyze the molecular arrangement in neat, bilayer and mixed films of CuPc and F_{16}CuPc. The obtained XRR spectra are depicted in Fig. 7.9 (a). Both types of phthalocyanine show pronounced Bragg peaks when deposited on ITO/PEDOT. The signature at $q_z = 0.48$ Å^{-1} corresponds to the (100) reflection of CuPc α-phase, revealing almost upright standing molecules on the substrate (cf. Sec. 3.1.3). Due to the larger terminating atoms in the perfluorinated CuPc, its lattice spacing perpendicular to the substrate is distinctly higher which shifts the Bragg peak to lower values of q_z. As has been discussed in Sec. 3.1.3, F_{16}CuPc appears in two different polymorphs when grown on SiO_2—namely a $\beta_{bilayer}$-structure with upright standing molecules stacked in columns and a β-phase with herringbone arrangement (cf. Fig. 3.5 (b) and (c), respectively). While having different in-plane stacking behavior both polymorphs do not differ significantly in their out-of-plane lattice spacing. Thus, the Bragg reflection at $q_z = 0.43$ Å^{-1} cannot clearly be attributed to either the β- or $\beta_{bilayer}$-structure. The bilayer CuPc/F_{16}CuPc exhibits Bragg peaks of both components—however, with a slight shift of the CuPc reflection, which can be attributed to a certain degree of intermixing at the interface. A more detailed investigation of this feature can be found in Ref. 200. In contrast to the X-ray scattering data of DIP:C_{60}, the mixed CuPc:F_{16}CuPc film shows only one Bragg peak which is located between the ones of the neat materials. This gives clear evidence that both phthalocyanines mix on a molecular level—forming a mixed crystalline film with a lattice spacing $d_\perp$ between those of pure CuPc and F_{16}CuPc. A systematic analysis including different mixing ratios and GIXD data can be found in Ref. 200.

The formation of a molecular mixture within the blend of CuPc and F_{16}CuPc—illustrated in Fig. 7.9 (b)—is related to similar sizes and shapes of both molecules and their similar packing motifs in neat films as has already been shown for pentacene combined with its perfluorinated analogue PFP and other rod-like molecules (see Refs. 372, 373 and 318). Implications on electrical transport within the solid solution of CuPc:F_{16}CuPc were reported in Refs. 371 and 374: While unipolar electron or hole transport is enabled by continuous molecular paths through the mixed complex, a tremendous lowering in current is observed if both charge carrier types are injected simultaneously or if photogenerated by light absorption. This behavior is assigned to the formation of charge transfer states with the hole located on the CuPc molecule and the electron on the F_{16}CuPc molecule.

When applying CuPc and F_{16}CuPc as active semiconductors in PHJ devices the current in reverse direction is higher than under forward biasing, which has been ascribed to the formation of a charge-generation layer at the D/A interface based on tunneling of electrons from the CuPc HOMO to the F_{16}CuPc LUMO.[374] In this case, no measurable effect upon illumination is found for the j-V behavior,

however, the charge generating properties might be of interest in tandem solar cells.[375] As expected from the energy level diagram depicted in Fig. 4.2, small open-circuit voltages were detected in BHJ photovoltaic devices.[374] Here, the formation of self-trapped CT excitons significantly reduces the exciton dissociation efficiency—ultimately making the material combination CuPc/F_{16}CuPc unusable for the application in photovoltaic cells. Altogether, D/A combinations forming molecularly mixed crystalline films within the blend carry the risk of insufficient charge carrier separation eliminating them from successful application as active material in organic BHJ solar cells.

7.1.3. The CuPc/C_{60} interface

The combination of CuPc and C_{60} is a well-known D/A combination and became a kind of prototype small-molecule OPVC system.[124,192,226,376,377] As can be seen from the absorption spectra in Fig. 4.3, this material combination features favorable conditions for light harvesting due to the complementary absorption spectra of both constituents and high absorption coefficient over almost the full visible range. As shown in Ref. 371 neat films of CuPc and C_{60} evaporated at room temperature, display a granular structure with needle-shaped crystallites in the case of CuPc and spherical domains for C_{60}. Mixing both materials by coevaporation yields an irregular film topography which is caused by dissimilar molecular shapes as has been shown in Sec. 3.1.3 and already hints towards phase separation between CuPc and C_{60}.

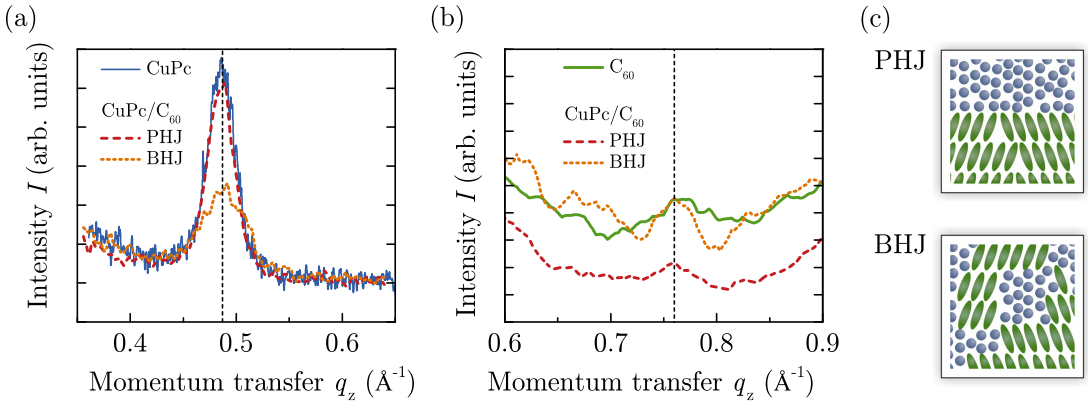

Figure 7.10.: X-ray reflectivity spectra of neat films of (a) CuPc (25 nm) and (b) C_{60} (25 nm). Both figures contain spectra of a bilayer CuPc(25 nm)/C_{60}(25 nm) film and blend of CuPc:C_{60}(50 nm, mixing ratio 1:1). All films have been deposited on unheated ITO/PEDOT substrates (taken from Ref. 371). (c) Suggested molecular arrangement in CuPc/C_{60} bilayers and blends as revealed by structural investigations.

To analyze the molecular arrangement in the pure films and in the heterojunctions, X-ray scattering measurements were performed (see Fig. 7.10 (a) and (b)). The measurements comprise neat films of the pure material as well as heterojunctions in the form of bilayer (C_{60} on top of CuPc) and mixed films—examined concerning their out-of-plane structure. All films have been deposited on ITO/PEDOT without heating the substrate during evaporation. In analogy to the studies presented in the previous section, a pronounced Bragg peak at $q_z = 0.48$ Å^{-1} can be identified as the (100) reflection of CuPc α-phase, which is observable in the pure CuPc film but also in the bilayer. Very weak C_{60} features indicate weak crystalline order of pure C_{60} films on ITO/PEDOT. In contrast to the templating effect which was observed for the PHJ DIP/C_{60} (see Sec. 7.1.1), no improvement of structural order can be found when growing C_{60} on top of CuPc. The mixture of both materials shows Bragg reflections of CuPc α-phase and C_{60} fcc-phase, proving phase separation in blends of CuPc:C_{60}—however, composed of smaller crystalline CuPc domains as compared to pure films. This tendency of phase separation is consistent with the sterically incompatible molecular shape of both components. The analysis of electrical transport properties within blends with varying mixing ratios reveals an exponential decrease of charge carrier mobility upon diluting one component with the respective counterpart.[371] Thus, charge carrier transport in BHJ solar cells is supposed to be limited by the size of single material domains within the mixture as the formation of percolation paths towards the electrodes is a necessary prerequisite for efficient charge extraction. Suggested molecular arrangements within the bilayer and blend of CuPc and C_{60} are illustrated in Fig. 7.10 (c).

Based on these results the material combination CuPc/C_{60} has been studied both in PHJ and PM-HJ photovoltaic cells. j-V curves in dark and under illumination are depicted in Fig. 7.11 (a), whereas characteristic photovoltaic parameters as well as results obtained from fitting the dark j-V curve with the Shockley equation are listed in Tab. 7.3. All devices were fabricated with an ITO/PEDOT anode and BCP/Al cathode and active layer sequences as given in Fig. 7.11 and measured under comparable conditions as the corresponding DIP/C_{60} cells shown in Fig. 7.8. The most prominent difference to the DIP/C_{60} devices is the open-circuit voltage being only about 0.5 V for the presented cells. By estimating the upper limit of V_{oc} via the intermolecular energy gap, a substantial lower value of $E_{DA} \approx 1$ eV can be extracted from UPS data (see schematic energy level diagram based on published data in Ref. 240), being approximately 0.45 eV lower than the corresponding value for DIP/C_{60}. This difference is almost exactly reflected by the difference in open-circuit voltages—a topic which is further addressed in Sec. 7.2.1. According to the electronic structure of the planar and bulk heterojunction, similar values for V_{oc} would be expected. However, j-V characteristics found higher open-circuit voltage

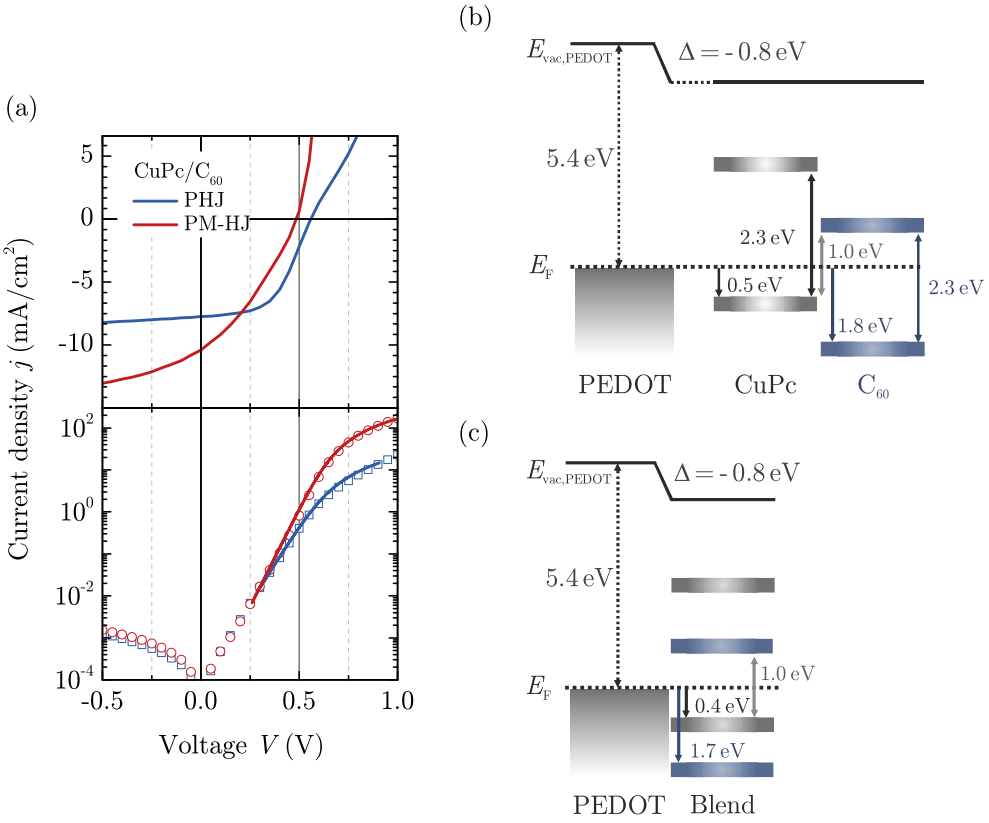

Figure 7.11.: (a) j-V characteristics of solar cells based on CuPc and C_{60}. PHJ of structure ITO/ PEDOT/ CuPc(40 nm)/ C_{60}(60 nm)/ BCP(8 nm)/ Al and PM-HJ of structure ITO/ PEDOT/ CuPc(3.5 nm)/ CuPc:C_{60}(50 nm, mixing ratio 1 : 1)/ C_{60}(5 nm)/ BCP(8 nm)/ Al. Upper parts: j-V characteristics under AM 1.5 g illumination (1 sun). Lower parts: Logarithmic plot of the dark j-V characteristics (open symbols). The solid lines are fits based on the modified diode equation. All layers are deposited with the substrate held at RT. Results of the fits are given in Tab. 7.3. Schematic energy level diagrams of (b) planar and (c) bulk heterojunction of CuPc/C_{60} after Ref. 240.

for the PHJ than for the PM-HJ. Increased recombination losses within the bulk, which would be reflected in significantly differing j_0, seem not to be the case here. Instead, a comparably large hole injection barrier between the bottom contact and the adjacent CuPc layer was found resulting in increased series resistance—and being partly responsible for the appearance of an s-shape in the PHJ device.

Regarding the short-circuit currents both types of CuPc/C_{60} cells are clearly ahead of the corresponding DIP based devices, which is simply related to the larger absorption coefficient of CuPc and the better spectral coverage in the long wavelength range (see Fig. 4.3).

Table 7.3.: Open-circuit voltage V_{oc}, short-circuit current density j_{sc}, fill factor FF, power conversion efficiency η, specific series resistance $R_S A$, ideality factor n and dark saturation current density j_0 for PHJ and PM-HJ solar cells based on CuPc and C_{60} evaporated on unheated substrates (cf. Fig. 7.11). Light illumination was realized with a solar simulator at one sun.

Device architecture	V_{oc} (V)	j_{sc} (mA/cm^2)	FF (%)	η (%)	$R_S\,A$ ($\Omega\,$cm^2)	n	j_0 (mA/cm^2)
PHJ	0.56	-7.7	52.6	2.28	13.8	2.3	$9 \cdot 10^{-5}$
PM-HJ	0.49	-10.6	33.4	1.76	1.6	1.8	$2.5 \cdot 10^{-5}$

The generally lower fill factors for CuPc/C_{60} are indicative for stronger recombination losses in this material system, which is clearly confirmed by significantly higher values of the dark saturation current. The argument of lower hole mobility in neat CuPc than in DIP—as stated in Ref. 327—could not be affirmed by mobility measurement carried out in hole-only diodes (see Sec. 6.2): While for unipolar CuPc diodes a zero-field mobility of $\mu_{h,0} = 1.9 \cdot 10^{-5}\,$mA/cm^2 has been determined in Ref. 378, similar measurements with unipolar DIP diodes reveal an even lower mobility of $\mu_{h,0} \approx 5\text{–}6 \cdot 10^{-7}\,$mA/cm^2 perpendicular to the substrate (cf. Sec. 6.2). Instead, enhanced growth conditions of C_{60} can explain—at least in part—the improved efficiency of charge carrier extraction in PHJ based on DIP/C_{60}: As has been found by structural investigation, DIP has a templating effect on the subsequent C_{60} film leading to comparatively high crystalline order in the C_{60} film. As X-ray scattering data do not indicate a similar behavior for C_{60} grown on CuPc, the fullerene film is supposed to exhibit significantly smaller crystalline domains and with this lower charge carrier mobility and less efficient electron transport towards the electrodes. However, based on the fact that the maximum absorption coefficient of DIP in the visible spectral range is about four times lower than for CuPc, the reduction of the photocurrent by only 25% point towards very efficient charge carrier collection in DIP/C_{60} cells. In BHJ, a reduction in charge carrier mobility has been found upon mixing CuPc and C_{60} as result of nanophase separation on length-scale of a few ten nanometers. By contrast, the morphology of the DIP phase in BHJ architecture is characterized by large, cohesive crystalline structures with DIP domains in the size of the entire film thickness. This allows for favorable transport properties by the formation of pronounced percolation pathways for each of the charge carrier types and thus less recombination losses as compared to the CuPc/C_{60} based devices.

7.2. Electronic properties of donor/acceptor interfaces

7.2.1. Temperature dependence of open-circuit voltage

From the previous chapters it becomes clear that the greatest potential of DIP as donor in organic solar cells can be found in its high ionization potential and the favorable energy level alignment with the C_{60} acceptor leading to high open-circuit voltages of up to 0.93 V. As already stated in Sec. 2.3.2 V_{oc} is ultimately limited by the energy of the charge transfer state E_{CT}. Although the linear relationship between eV_{oc} and E_{CT} is generally accepted, there is an ongoing discussion about the mismatch between both quantities—usually amounting to approximately 0.2–0.5 eV. In order to assess E_{CT}, temperature dependent current-voltage measurements have been carried out under illumination and in dark. A comprehensive description of the measurement data and the corresponding analysis is exemplarily shown on the material system DIP/C_{60}, which is followed by a comparative analysis of a series of different donor/acceptor combinations.

The material system DIP/C_{60}

The measurement data of the DIP/C_{60} material system is recorded for a photovoltaic cell with the following structure:

ITO/ PEDOT/ DIP(50 nm, $T_{sub} = 100\,°C$)/ C_{60}(80 nm)/ BCP(5 nm)/ Al.

The PHJ cell has been illuminated with a white LED at an intensity of approximately 20 mW/cm^2 and was recorded in a temperature range between 350 and 130 K. The obtained j-V curves under illumination are shown in Fig. 7.12 (a). In a wide temperature range, V_{oc} increases linearly with decreasing temperature (see Fig. 7.12 (b)). As can be seen from (c), the short-circuit current density first decreases slightly with decreasing temperature—however, when cooling below $T = 180$ K a strong decline is observed. Based on a temperature independent exciton generation rate, the reasons for the continuously decreasing j_{sc} can on the one hand be found in a reduction of charge carrier extraction efficiency as result of thermally activated charge carrier mobility—an assumption which will be further discussed when analyzing the dark current. On the other hand a decline of exciton transport may contribute to the temperature dependence of j_{sc}. The appearance of an s-shape at temperatures below 230 K can be ascribed to an increasing series resistance as will be discussed further below.

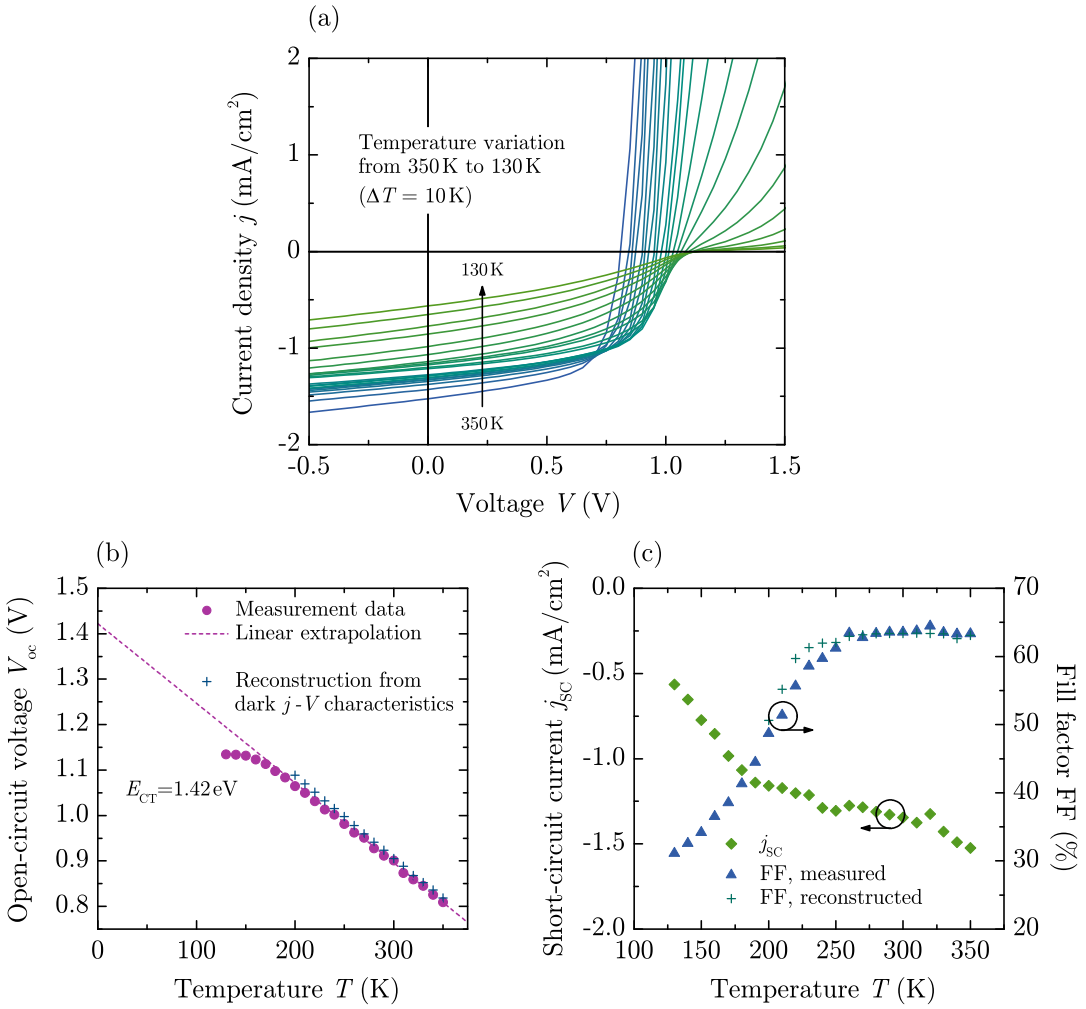

Figure 7.12.: (a) j-V characteristics of a planar heterojunction solar cell under white LED illumination in the temperature range $130\,\mathrm{K} \leq T \leq 350\,\mathrm{K}, \Delta T = 10\,\mathrm{K}$. The device has the following structure: ITO/ PEDOT/ DIP(50 nm, $T_{\mathrm{sub}} = 100\,^{\circ}\mathrm{C}$)/ C_{60}(80 nm)/ BCP(5 nm)/ Al. (b) Open-circuit voltage V_{oc} in dependence on temperature revealed from illuminated j-V data shown in (a) (magenta symbols) with an extrapolation of the linear regime (dashed line) and reconstructed data according to Eq. (7.5) (blue crosses). (c) Respective short-circuit current density j_{sc} and fill factor FF in dependence on temperature (filled symbols). The blue crosses mark reconstructed data based on Eq. (7.2).

Regarding the temperature dependence of the open-circuit voltage as shown in Fig. 7.12 (b), an almost linear increase in V_{oc} with decreasing T is observed in a wide temperature range. A similar relation has experimentally been found for a variety of material systems.[19,141,146] The deviation of the linear behavior for temperatures $T < 150\,\mathrm{K}$ can be attributed to the series resistance which is found to

strongly depend on temperature as will be discussed below. Theoretical considerations by Green predict this approximately linear temperature dependence of eV_{oc}[379]—whereas the 0 K intercept is ascribed to the HOMO-LUMO gap. Thus, an extrapolation of the linear behavior towards $T = 0\,\mathrm{K}$ yield a value of $E_{\mathrm{CT}} = 1.42\,\mathrm{eV}$. Exact calculations on the same material system as shown in Ref. 148 confirm the suitability of the linear extrapolation as reasonable approach: As introduced in Sec. 2.3.2 a refined evaluation has been done based on the modified SQ limit by taking the relative absorption strength of the CT state into account as well as radiative and non-radiative recombination losses. Results show that data fitting with the refined model results in a value of E_{CT} differing only by approximately 2% from the linearly extrapolated value. Moreover, the refined model in Ref. 148 allows for an estimation of the contributions from radiative and non-radiative recombination losses—the latter found to exceed their non-radiative counterpart by orders of magnitude: Based on a CT energy of 1.42 eV, non-avoidable radiative recombination processes lead to a reduction of $\Delta V_{\mathrm{OC}}^{\mathrm{rad}}(300\,\mathrm{K}) = 0.12\,\mathrm{V}$ and a further reduction by non-radiative recombination losses of $\Delta V_{\mathrm{OC}}^{\mathrm{non-rad}}(300\,\mathrm{K}) \approx 0.4\,\mathrm{V}$—resulting in an open-circuit voltage of $V_{\mathrm{oc}} = 0.9\,\mathrm{V}$ at room temperature (cf. Eq. (2.26)).

The injected current density—typically dominated by recombination at the D/A interface—is approximated by Shockley's equation for an ideal diode. Under open-circuit conditions (i.e. $j = 0, V = V_{\mathrm{oc}}$) the recombination rate of charge carriers equals the generation rate of optical charge carriers with its photocurrent equivalent j_{ph}. As shown in Sec. 2.1.6, equalizing both currents and assuming high shunt resistances yield an expression for the open-circuit voltage as given by Eq. (2.8). Under the assumption that $j_{\mathrm{ph}} = j_{\mathrm{sc}}$ and $j_{\mathrm{sc}} \ll j_0$, the open-circuit voltage is given by

$$V_{\mathrm{oc}} \approx n\frac{k_{\mathrm{B}}T}{e}\ln\left(\frac{j_{\mathrm{sc}}}{j_0}\right). \tag{7.1}$$

Based on this relation and referring to the simulations shown in Sec. 2.1.6 it can safely be assumed that the dark saturation current density j_0 has a decisive impact on the open-circuit voltage—and presumably also on its temperature dependence. Moreover, Eq. (7.1) suggests that V_{oc} can be calculated purely from the knowledge of the ideality factor n, the short-circuit current density j_{sc}, and the dark saturation current density j_0. In order to address this question, corresponding dark j-Vcharacteristics have been recorded for the DIP/C_{60} cell.

As demonstrated in the previous chapters, the exponential part of the j-Vcurves can be fitted with a modified Shockley equation (5.1). Figure 7.13 (a) depicts the dark current-voltage characteristics in a temperature range between 350 K and 130 K (open symbols)—the corresponding fits are included as straight lines. For temperatures below $T \approx 200\,\mathrm{K}$, the drift current at high voltages becomes small,

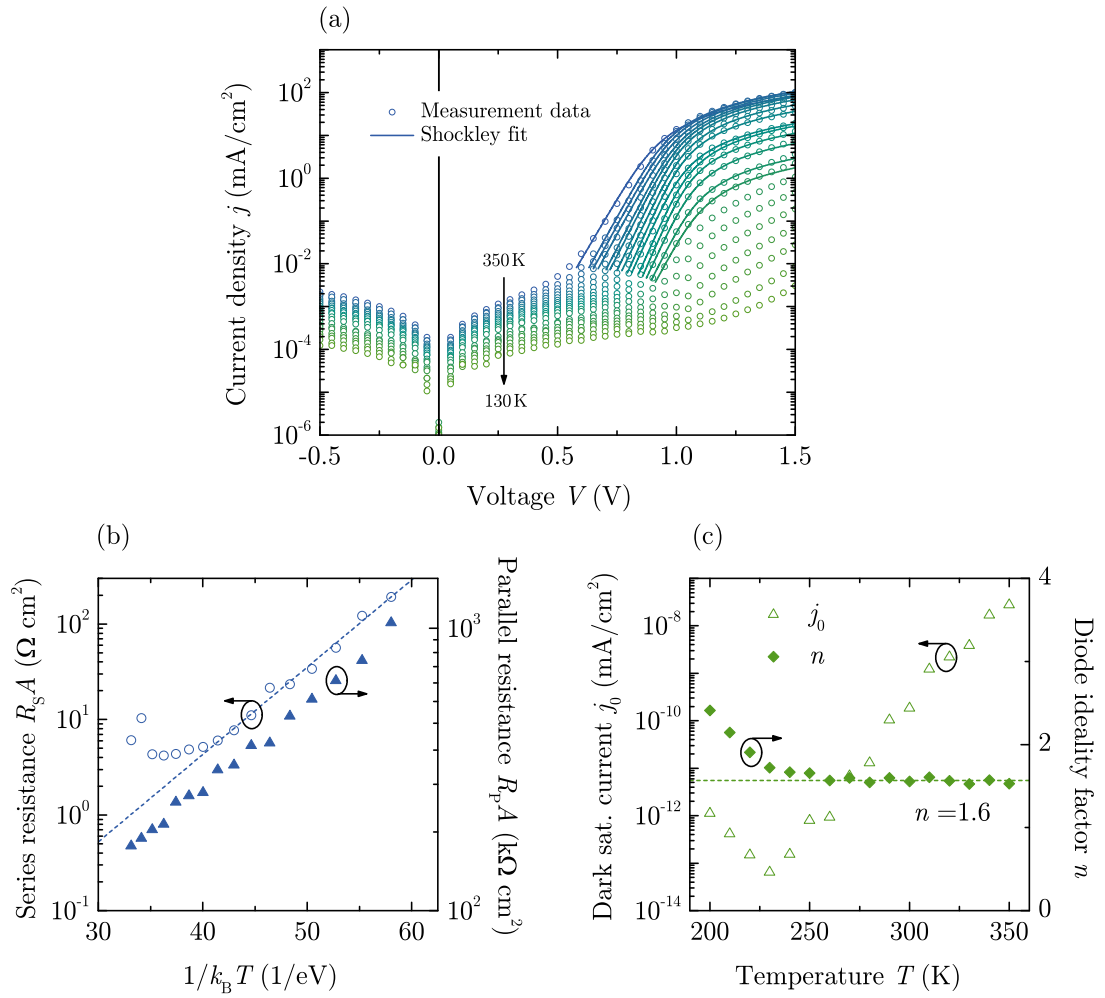

Figure 7.13.: (a) Dark j-V characteristics of the planar heterojunction as shown in Fig. 7.12 for several temperatures ranging from 130 K to 350 K (open symbols). The solid lines are fitted curves in the forward-bias region using the Shockley equation. (b) Specific series and parallel resistance $R_S A$ and $R_P A$. (c) Dark saturation current density j_0 and diode ideality factor n in dependence on temperature, analyzed with the Shockley equation.

so that the diffusion dominated regime is reduced in its extent, not allowing for accurate fitting any more. The fitting parameters are summarized in Fig. 7.13 (b) and (c): Figure 7.13 (b) illustrates the temperature dependence of the specific series resistance $R_S A$: At high temperatures, the values are at an almost constant low level ranging between 4 and 10 Ω cm^2. Below $T \approx 270$ K an exponential temperature dependence is observed for the series resistance with $R_S \propto \exp(E_a/k_B T)$ with an activation energy $E_a \approx 0.21$ eV. This proportionality suggests that the reason for the continuous increase in series resistance with decreasing T can be found in a lowering of charge carrier mobility, characterized by $\mu \propto 1/R_S \propto \exp(-E_a/k_B T)$

(cf. Eq. (2.11)). The specific parallel resistance $R_\mathrm{P}A$ is determined from the linear regime at low positive voltages and is found to follow the same temperature dependence $\ln(R_\mathrm{P}) \propto 1/k_\mathrm{B}T$. Assuming an ohmic behavior as given by Eq. (2.14), R_P is directly proportional to μ and may, thus, be determined by the temperature dependence of the mobility, too. Regarding the influence of R_P and R_S on the fill factor of the illuminated j-V characteristics, a relation can be found in Ref. 19:

$$\mathrm{FF}(R_\mathrm{S}, R_\mathrm{P}) \approx \mathrm{FF}(0, \infty) \cdot \left(1 - \frac{j_\mathrm{sc} R_\mathrm{S} A}{V_\mathrm{oc}} - \frac{V_\mathrm{oc}}{j_\mathrm{sc} R_\mathrm{P} A}\right). \tag{7.2}$$

From Eq. (7.2) it becomes obvious that high series or low shunt resistances negatively affect the fill factor. By means of the extracted values for $V_\mathrm{oc}(T)$, $R_\mathrm{S}(T)$ and $R_\mathrm{P}(T)$, the temperature dependence of FF can be reconstructed as shown in Fig. 7.12 (c) (blue crosses). The reconstructed values show good accordance with the measured data. By separately evaluating the contributions of $V_\mathrm{oc}(T)$, $R_\mathrm{S}(T)$ and $R_\mathrm{P}(T)$, it can be concluded that the thermally activated series resistance can almost exclusively be held responsible for the decrease in FF below $T = 240\,\mathrm{K}$.

Based on the extrapolation of the linear part in the semilogarithmic j-V plot, the ideality factor n and the dark saturation current j_0 are measures of the slope and intercept with the current axis, respectively. The temperature dependencies of n and j_0 are depicted in Fig. 7.13 (c). Down to a temperature of approximately 230 K, the ideality factor shows an almost constant value of $n \approx 1.6$ (dashed line) and the dark saturation current density decreases exponentially with T. For further decreasing temperatures, the value of n increases while, at the same time, j_0 deviates from its continuous decline. This correlation clearly illustrates that both parameters are somehow dependent on each other as has already been shown for inorganic heterojunctions.[380] The temperature dependence of n has recently been discussed in literature: Harada *et al.* found a temperature dependent ideality factor $n \propto 1/T$ in homojunction diodes.[381,382] The authors ascribe their experimental findings to a deviation from the classical Einstein relation $D_\mathrm{cc}/\mu = k_\mathrm{B}T/e$ (with D_cc being the diffusion coefficient of the charge carriers) which describes the balance between drift and diffusion currents in thermal equilibrium. In order to account for the disorder in organic systems, they suggest an adjustment of its classical form expressed by a generalized Einstein relation

$$\frac{D_\mathrm{cc}}{\mu} = g(\rho, T)\frac{k_\mathrm{B}T}{e}. \tag{7.3}$$

The charge density- and temperature-dependent enhancement factor $g(\rho, T)$ considers a Gaussian DOS of organic semiconductors and can be regarded equal to the ideality factor. Although Wetzelaer *et al.* observed that ideality factors in electron-

only devices deviate from unity, suggesting an enhancement of the classical Einstein relation, they neither found any temperature dependence—at least not in the investigated temperature regime between 295 and 215 K—nor could they figure out any relation to the amount of disorder.[383] Instead, the authors see their results as a confirmation of the validity of the classical Einstein relation in disordered organic semiconductors and ascribe $n > 1$ to the presence of energetically deep states within the band gap, which can be discharged by recombination in double-carrier devices. Moreover, they ascribe an apparent increase of n with decreasing temperature to an experimental artifact caused by too large leakage currents in the low voltage regime.[383] As a consequence, the evaluable diffusion regime is limited both by high leakage currents and reduced drift currents, leading to overestimated and temperature-dependent ideality factors.
As has been shown by morphological and structural investigations, DIP/C_{60} solar cells are found to be highly crystalline. Thus, disorder considerations should not play a major role in this material system. Instead, the data seem to confirm the argument given by Wetzelaer *et al.*: Low parallel and high series resistances limit the voltage regime where the diffusion current can be evaluated unambiguously. The general validity of this relation will be further discussed in the subsequent section when comparing different material systems. A statement about the height of the ideality factor concerning prevailing recombination processes will be topic of Sec. 7.2.4, while in the following the discussion will be focused on the temperature dependence of the extracted parameters—and, in particular, on their relation to V_{oc}.

As can be deduced from Eq. (7.1) low dark current densities lead to enhanced open-circuit voltages for a given j_{sc}. The temperature dependence of j_0, resulting from charge carriers thermally generated at the D/A interface or within the bulk,[332] is usually expressed by an Arrhenius equation. However, concerning the exact term describing $j_0(T)$, literature provides partly inconsistent expressions: Work on inorganic heterojunction solar cells revealed the relation

$$j_0 = j_{00} \exp\left(-\frac{\Delta E}{n k_{\mathrm{B}} T}\right), \tag{7.4}$$

with an activation energy ΔE of about half the band gap for many inorganic heterojunctions.[380] Equation (7.4) has been adopted to organic heterojunctions in a variety of recent publications—however, partly with slightly differing interpretations: Thus, Potscavage *et al.* use Eq. (7.4), however, with an ideality factor n' (with $n/n' \approx 1$), whose exact nature is not specified.[21] Forrest and Thompson use the same formula but with an additional factor of 2 in the denominator of the exponent.[19,332,384] They argue that the factor of 2 accounts for the generation

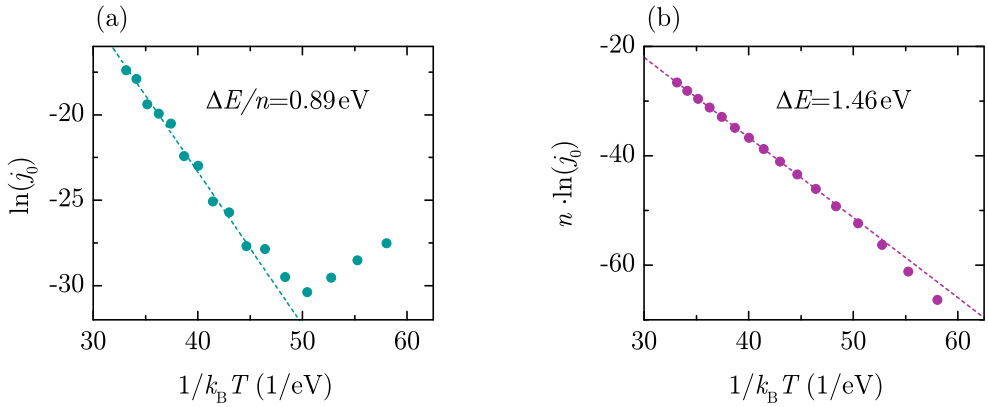

Figure 7.14.: Temperature dependence of the dark saturation current (a) $\ln(j_0)$ versus $1/k_\mathrm{B}T$ and (b) evaluated by studying $n \cdot \ln(j_0)$ plotted versus $1/k_\mathrm{B}T$ in order to estimate the activation energy ΔE from Eq. 7.4.

of both an electron and hole at the D/A interface, giving an activation energy of $\Delta E/2$ for the process.[332] Other authors applied Eq. (7.4) and identified ΔE with the HOMO-LUMO gap E_DA at the D/A interface.[385,386] The following analysis is based on the pristine form of Eq. (7.4)—with the goal to identify the nature of ΔE in the present material combinations.

In the DIP/C_{60} system, the dark saturation current obeys a temperature dependence of the form $\ln(j_0) \propto 1/k_\mathrm{B}T$ in a wide temperature range of $240\,\mathrm{K} \leq T \leq 350\,\mathrm{K}$ (see Fig. 7.14 (a)). According to Eq. (7.4), the slope can be identified with $\Delta E/n = 0.89\,\mathrm{eV}$. Using the plateau value of the ideality factor determined in Fig. 7.13 (c) of $n = 1.6$, an activation energy of $\Delta E = 1.42\,\mathrm{eV}$ can be determined. An almost equal value of $\Delta E = 1.46\,\mathrm{eV}$ is determined when directly fitting $n \cdot \ln(j_0)$ versus $1/k_\mathrm{B}T$. Comparing these results to the value of the energy of the charge transfer state E_CT as gained from the extrapolation of V_oc versus $T = 0\,\mathrm{K}$, an almost perfect accordance is manifested.

Inserting Eq. (7.4) into Eq. (7.1) yields

$$eV_\mathrm{oc} = \Delta E - nk_\mathrm{B}T \cdot \ln\left(\frac{j_{00}}{j_\mathrm{sc}}\right), \tag{7.5}$$

which allows to evaluate the contribution of j_{00} and ΔE to V_oc. Based on Eq. (7.5), the open-circuit voltage can be calculated solely based on ΔE, n and j_{00} extracted from dark j-Vcharacteristics, together with the short-circuit current density j_sc. As can be seen from Fig. 7.12 (b) (blue crosses), a very precise prediction of the open-circuit voltage is obtained. Only at low temperatures the reconstructed data deviate from the measured ones as consequence of the increasing value of n.

In conclusion, the activation energy ΔE as extracted from the temperature dependence of the dark saturation current can be identified with the energy of the CT state E_{CT} as given by the extrapolation of V_{oc} towards 0 K. In this context, it has to be mentioned that ΔV_{oc} extracted from experimental dark j-V curves by $e\Delta V_{\mathrm{oc}} = nk_{\mathrm{B}}T \cdot \ln(j_{00}/j_{\mathrm{sc}})$ (cf. Eq. 7.5) is a result of both radiative and non-radiative recombination current. As mentioned before, an identification of each contribution can be achieved by simulations based on a modified SQ theory.[148] Apart from the experimentally detected accordance between E_{CT} and ΔE, an interfacial energy gap at the DIP/C_{60} HJ of $E_{\mathrm{DA}} = 1.40 \pm 0.15$ eV has recently been determined by Wilke *et al.*,[98] unambiguously revealing the correspondence between E_{CT} (determined from temperature dependence of V_{oc}), ΔE (deduced from thermally activated j_0) and the interfacial energy gap $E_{\mathrm{DA}} = \left|E_{\mathrm{HOMO}}^{\mathrm{donor}} - E_{\mathrm{LUMO}}^{\mathrm{acceptor}}\right|$ for the material system DIP/C_{60}.

Temperature dependent measurements for a series of different donor/acceptor combinations

In order to examine the proposed linear relationship between the intermolecular gap E_{DA} and V_{oc}, a series of different donor/acceptor combinations have been investigated concerning their temperature behavior. All cells have similar device structures with

ITO/ PEDOT(≈ 30 nm)/ donor/ acceptor/ BCP(5 nm)/ Al,

whereas the exact film thicknesses of the active layers as well as possible substrate heating and various device parameters are listed in Tab. 7.4 at the end of this chapter. It has to be noted that neither growth conditions nor film thicknesses have been optimized for all of them. The temperature dependent j-V characteristics of all investigated material systems are found in Appendix B including the analysis of the temperature dependent light and dark curves. The following discussion is mainly concentrated on a comparison of the different systems.

An overview of the different material combinations concerning their current-voltage behavior is given in Fig. 7.15 by means of j-V characteristics measured under illumination and in dark—both recorded at room temperature. For better comparability the current densities of the light curves are normalized to j_{sc}, respectively. From a first optical comparison between the data sets, it becomes obvious that V_{oc} strongly correlates with the onset of dark current flow. However, as can, e.g., be seen from the Pen/DIP system (green symbols) this is not the only determining parameter: from the order of the onset voltage alone, the highest V_{oc} of all systems would be expected—which is obviously not the case. Instead,

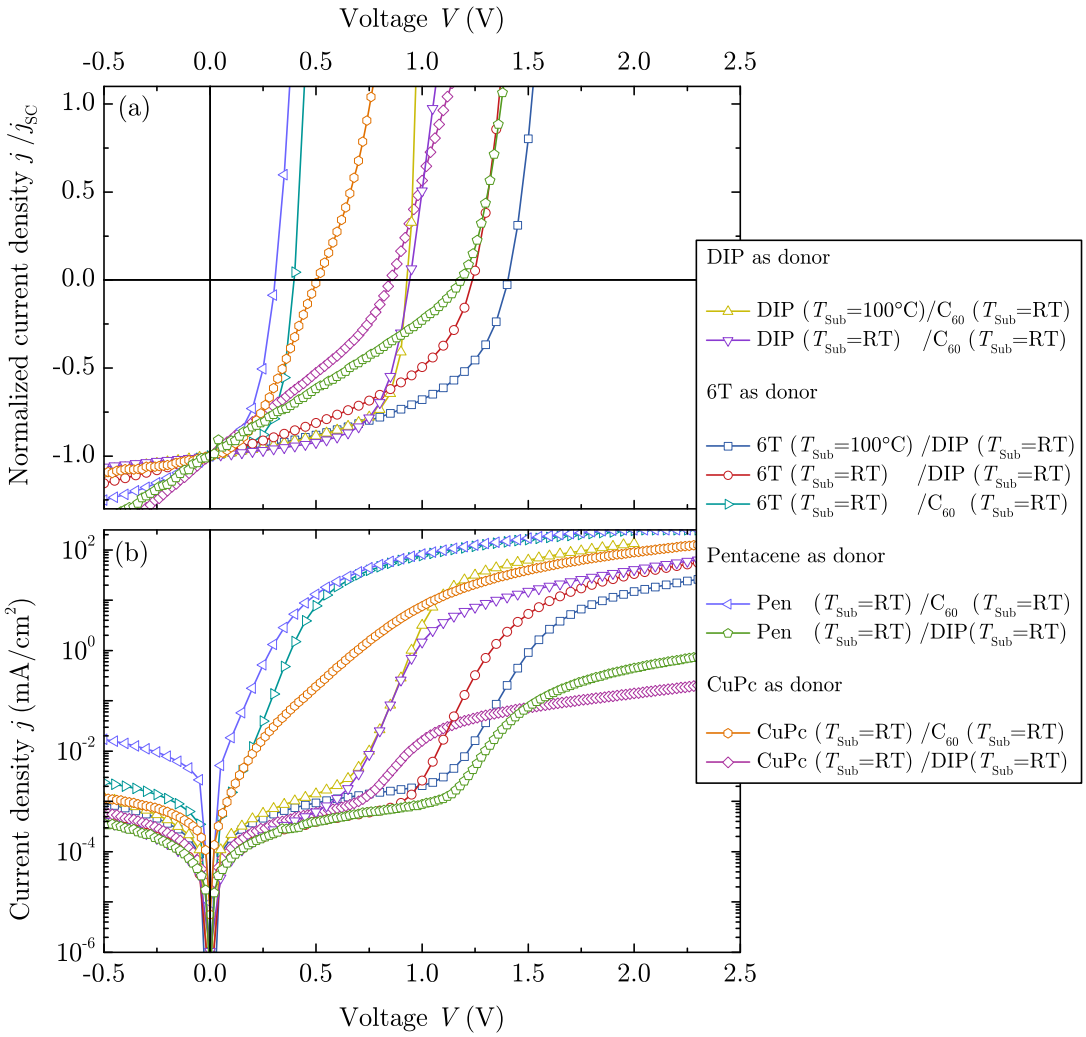

Figure 7.15.: j-V characteristics of a series of PHJ solar cell employing different donor/acceptor combinations (a) under illumination and (b) in dark, both recorded at room temperature. For better comparability the current densities of the light curves are normalized to j_{sc}, respectively. The respective device structures and parameters are summarized in Tab. 7.4.

the shape of the exponential increase of the dark current seems to play an equally important role.

As was shown in the previous section for the DIP/C$_{60}$ system, an estimate of E_{CT} can be extracted from the extrapolation of the temperature dependent V_{oc} towards $T = 0\,\mathrm{K}$ in their linear range. Figure 7.16 depicts the measurement data for the different material systems (symbols) recorded in a temperature range between $110\,\mathrm{K} \lesssim T \lesssim 320\,\mathrm{K}$—including the linear fits (straight lines). Thus, values ranging from $E_{CT} = 0.89\,\mathrm{eV}$ (for Pen/C$_{60}$) to $E_{CT} = 2.11\,\mathrm{eV}$ (for 6T/DIP) are

found. While some of the data show a linear behavior almost over the entire temperature region (e.g. Pen/C_{60}, 6T/C_{60}) others leave the linear range at a certain temperature and bend downwards as has been observed for the DIP/C_{60} system, albeit in alleviated form. Concerning the different illumination intensities, on the average amounting only to approximately 0.3 sun (see Tab. 7.4), it has to be mentioned that independent studies reveal that linear extrapolations of temperature dependent V_{oc} recorded for different light intensities all intersect in a similar point at $T = 0\,\mathrm{K}$,[146,165] as long as light intensities are not too low.[387] Comparable effects in the temperature dependence of V_{oc} can be found in literature, ascribing it to different effects as will be discussed in the following: A theoretical method explaining the curvature by a Gaussian disorder of the semiconductors with no need of taking resistance limitation into account was given by Manor *et al.* showing promising results for bulk heterojunction devices.[388] However, it has been shown that the DIP/C_{60} films are highly crystalline, disorder considerations should not play a major role in this system. By means of macroscopic simulations, Rauh *et al.* identified the saturation of V_{oc} at lower temperatures to be caused by injection barriers for charge carriers at the contact[389] Their results show that even comparatively low barriers of 0.1 eV–0.2 eV cause a saturation behavior at low temperatures—even though energetic barriers of this magnitude are not supposed to reduce V_{oc} for higher temperatures where the contact can still be considered as ohmic. Others attribute the deviation from monotonic increase of V_{oc} with decreasing temperature to the difficulty to accurately measure the sample temperature under illumination due to the limited thermal conductivity of the insulating glass substrate.[26] However, this reason can very likely be excluded in the present samples, as the cells have been given sufficient time to adopt the set temperature and deviations from linearity are too large to be explained by an inaccurate temperature measurement. Instead, this feature can be associated with the dark current in forward direction: The lower the injection current (see Fig. 7.15 (b)) the more pronounced is the kink in V_{oc}. As predicted by Eq. (7.1) V_{oc} directly correlates with the photocurrent—represented by j_{sc}—and the dark injection current, which is parameterized in j_0 and n. The saturation or even decrease of V_{oc} below a certain temperature is accompanied with both, a decrease in j_{sc} and an increase in j_0. As discussed above both parameters are strongly influenced by the series resistance R_S which increases for low temperatures. Generally, R_S is composed of an interfacial part, resulting from energetic injection barriers between electrodes and adjacent organic layers, and a bulk part which is characterized by charge carrier mobility. As it has been shown that even small injection barriers can affect V_{oc} at low temperatures[389] and from the thermally activated charge carrier mobility, it is very likely that in the present material combinations both parts contribute to the increase in series resistance for decreasing T.

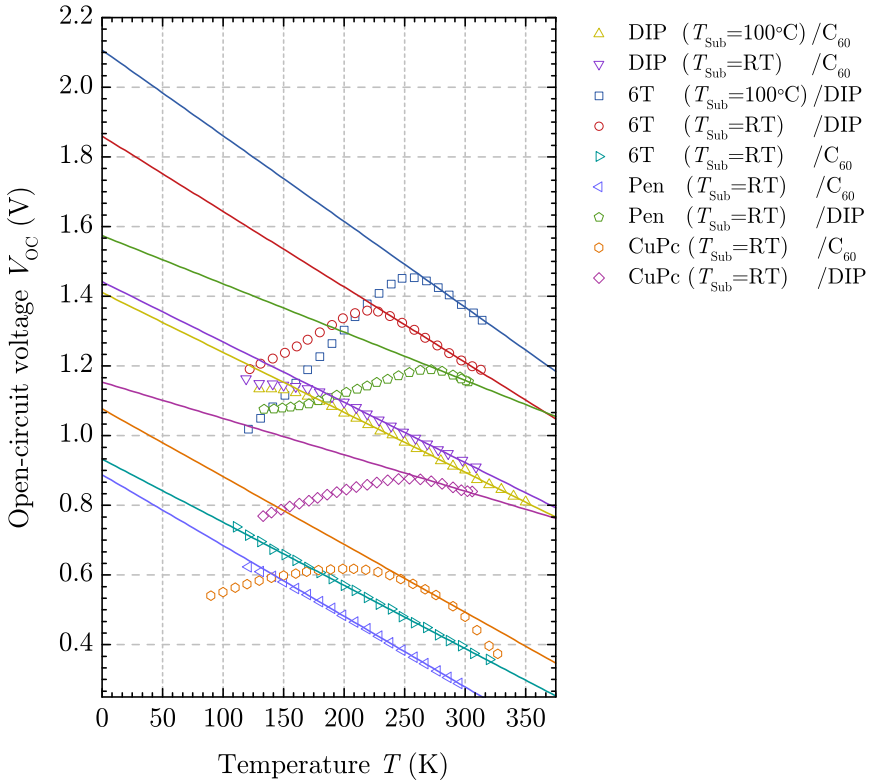

Figure 7.16.: Temperature dependence of V_{oc} of the PHJ solar cells as listed in Tab. 7.4. The extrapolation of the linear regime towards $T = 0\,\mathrm{K}$ gives a measure of the energy of the charge transfer state E_{CT}.

The temperature dependence of j_{sc} and FF are shown in Fig. 7.17 (a) and (b), respectively. As the light intensity of illumination is not the same for all measured devices, the absolute values of j_{sc} are not comparable. However, the results allow for a qualitative analysis concerning the curve shape and striking differences in the absolute values. The Pen/DIP and the CuPc/DIP samples suffer from remarkably low short-circuit currents, which can very likely be assigned to their energetic positions—especially because the absorption coefficients are not extremely low (cf. Fig. 4.3). As can be seen from the energy level diagram in Fig. 4.2, the LUMO offsets are expected to be small[s] not providing enough driving force for efficient exciton dissociation. The devices with the highest short-circuit currents show relatively constant short-circuit currents down to a certain temperature below which the absolute value of j_{sc} continuously decreases. As already mentioned before, constant j_{sc} over the whole temperature range would be expected when assuming

[s] As already mentioned, the literature values of the HOMO and LUMO levels allow only for a rough estimation of the energetic situation of the heterojunction, as long as possibly occurring vacuum level shifts are not taken into account.

temperature independent exciton generation rates. The decreasing j_{sc}—an effect which has been observed for other material systems, too[387]—can be ascribed to impeded exciton and charge carrier transport with decreasing temperature as result of thermally activated charge carrier mobility. This argument is affirmed by the temperature dependent series resistance which basically follows an Arrhenius law in a large temperature range for all material systems (see Fig. 7.17 (e)). Comparing the temperature dependent fill factors again emphasizes the high potential of the material system DIP/C_{60} which demonstrates the highest FF in the present comparison (see Fig. 7.17 (b)). According to Eq. (7.2) and illustrated in the simulations in Fig. 2.5, the fill factor is sensitive to high series or low parallel resistances. Thus, low values of R_P can be made responsible for the comparably low fill factors in the system Pen/C_{60} while otherwise benefiting from low series resistances. Both, high R_S and low R_P, explain the extremely low FF in the material systems Pen/DIP and CuPc/DIP.

The temperature dependence of the different dark saturation current densities j_0 is shown in Fig. 7.17 (c) (for a clearer display of the data, it is referred to Appendix B where the curves are presented individually). From the comparative overview it becomes clear that the temperature dependence of j_0 can take different forms, strongly correlating with the series resistance: Those material systems which are characterized by low R_S (e.g. Pen/C_{60}, CuPc/C_{60}, 6T/C_{60}) demonstrate the expected exponential decrease of j_0 with decreasing temperature according to Eq. (7.4). By contrast, those suffering from high R_S (e.g. CuPc/DIP, Pen/DIP, 6T/DIP) show an opposite trend—at least in the low temperature regime. Moreover, this differentiation is reflected in the temperature dependence of the ideality factor: a linear dependence of $\ln j_0$ on $-1/k_B T$ is accompanied by a temperature independent n—whereas deviations from this proportionality are reflected in increasing ideality factors. This observation confirms on the one hand the strong correlation between j_0 and n and on the other hand it emphasizes the decisive impact of R_S on the analysis of the dark j-V curve which defines the temperature region allowing for a reliable evaluation of the fitted data.

For the quantitative analysis of the dark saturation current density according to Eq. (7.4), the temperature regions characterized by an exponential decrease in j_0 and a constant n serve as guide for a reliable evaluation of $n \cdot \ln(j_0)$ concerning the estimation of ΔE. The results are listed in Tab. 7.4. For most of the heterojunctions remarkably good agreement between ΔE and E_{CT} (as extracted from the linear extrapolation of V_{oc} versus T) is observed. Nevertheless, a few material combinations obviously show large discrepancies between both energies. Thus, the activation energies ΔE of the Pen/DIP and CuPc/C_{60} system are almost exactly twice as high as E_{CT}.

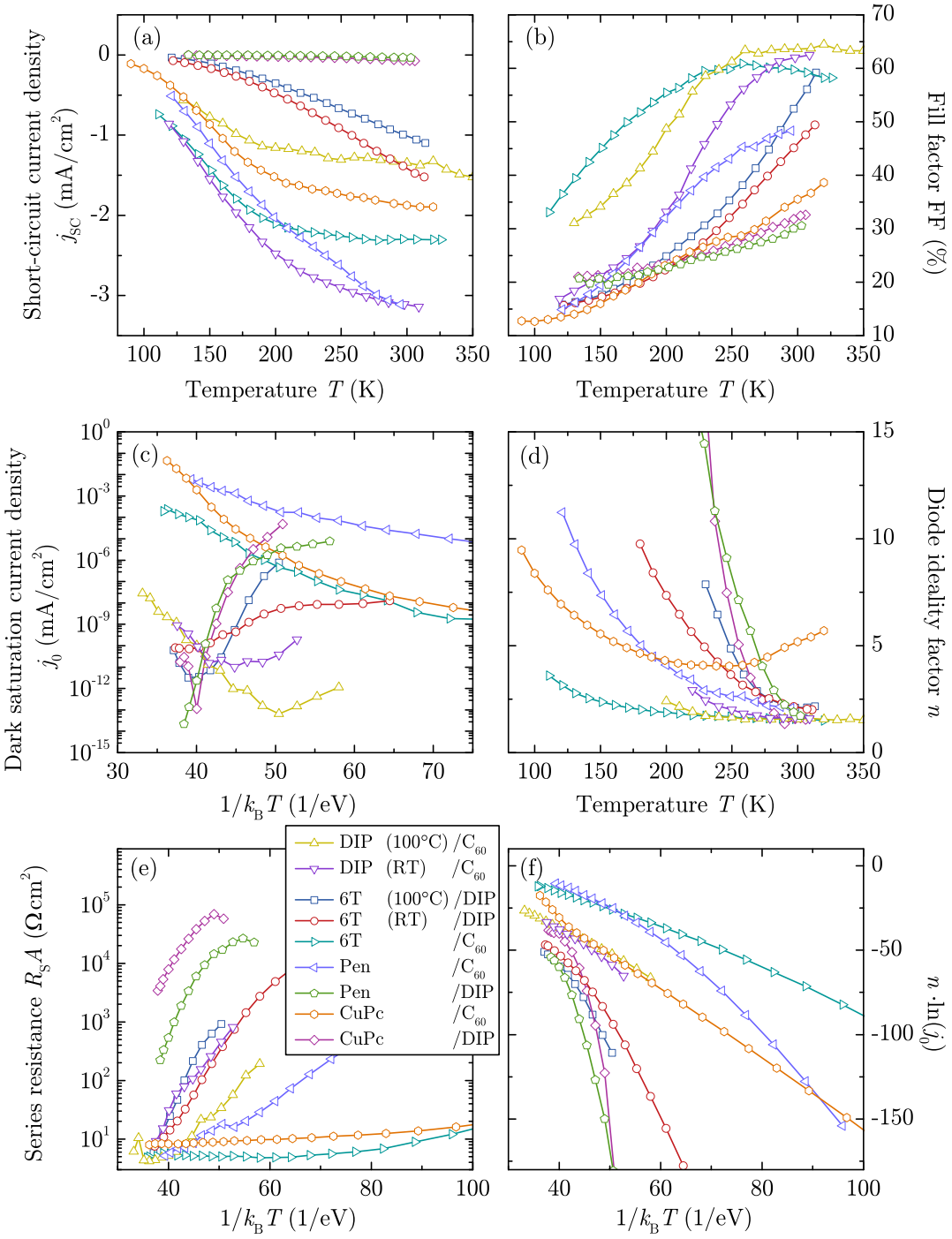

Figure 7.17.: (a) Short-circuit current density j_{sc} and (b) fill factor FF of the illuminated PHJ solar cells as listed in Tab. 7.4 in dependence on temperature. (c) Dark saturation current j_0, (d) diode ideality factor n, and (e) specific series resistance $R_S A$ in dependence on temperature as extracted from the Shockley fits of the dark j-V characteristics (see Appendix B). (f) j_0 and n analyzed with the Shockley equation and evaluated by studying $n \cdot \ln(j_0)$ plotted versus $1/k_B T$ in order to estimate ΔE.

For the Pen/DIP combination the deviation can be assigned to j_0 not following the temperature dependence as required for Eq. (7.4): As can be seen from Fig. B.10 (c) in the Appendix, the dark saturation current continuously increases with decreasing temperature which does not allow for a useful definition of an evaluable temperature regime for fitting $n \cdot \ln(j_0)$. For the CuPc/C_{60} heterojunction, the reasons for the deviation are different: In the temperature regime between 200 and 270 K both requirements for a reasonable fit are fulfilled (i.e. temperature dependence of n and j_0) which are related to low series resistances. The reason of the deviation might rather be found in the shape of the dark j-V curves: As can be seen from Fig. B.13 (b) and (c), the current in the diffusion dominated voltage regime is characterized by two differently steep slopes—a feature which is mainly pronounced at high temperatures. In literature, this double exponential j-V characteristics observed for CuPc/C_{60} has been addressed by the introduction of two independent diode ideality factors which consider the recombination of free acceptor electrons with trapped donor holes and vice versa.[26] In any case, this double exponential feature seems to be a peculiarity of the CuPc/C_{60} system as becomes apparent from the comparative display in Fig. 7.15 (b). In order to account for the double exponential dark current, a second parameter set has been extracted from fits to the Shockley equation in the low voltage region of the high temperature curves (cf. Fig. B.13 and B.14 in the Appendix). However, the high temperature behavior of $n \cdot \ln(j_0)$ exactly resembles the data extracted from the second exponential increase, both characterized by an activation energy of $\Delta E \approx 3.4\,\mathrm{eV}$ (see Fig. B.14 (d)). In any case, these observations suggest that CuPc/C_{60} is not a particularly suitable material combination to investigate the correlation between ΔE and E_{CT}, as the results lead to the probably incorrect assumption of ΔE corresponding to twice the effective band gap as stated in Refs. 19, 332, 384. Instead, the direct correlation of ΔE and E_{CT} as found for most of the investigated material combinations, rather indicates that the activation energy for the dark saturation current ΔE corresponds on a 1:1 manner to the CT energy. In analogy with inorganic pn-diodes, the dark saturation current in an organic heterojunction is assigned to the thermal generation of charge carriers due to an excitation of an electron from the HOMO of a donor molecule to the CT state formed with an acceptor molecule.[21] Based on this consideration, it seems reasonable to associate the characteristic activation energy ΔE for electron excitation with the energy of the charge transfer state E_{CT}.

In conclusion, it is shown that the dark saturation current is based on a thermally activated process with an effective activation energy ΔE identified as the energy of the CT state E_{CT}, which can be extracted from the linear extrapolation of the temperature dependent V_{oc} towards $T = 0\,\mathrm{K}$. The experimentally determined values for V_{oc} and E_{CT} are compared to values of the intermolecular energy

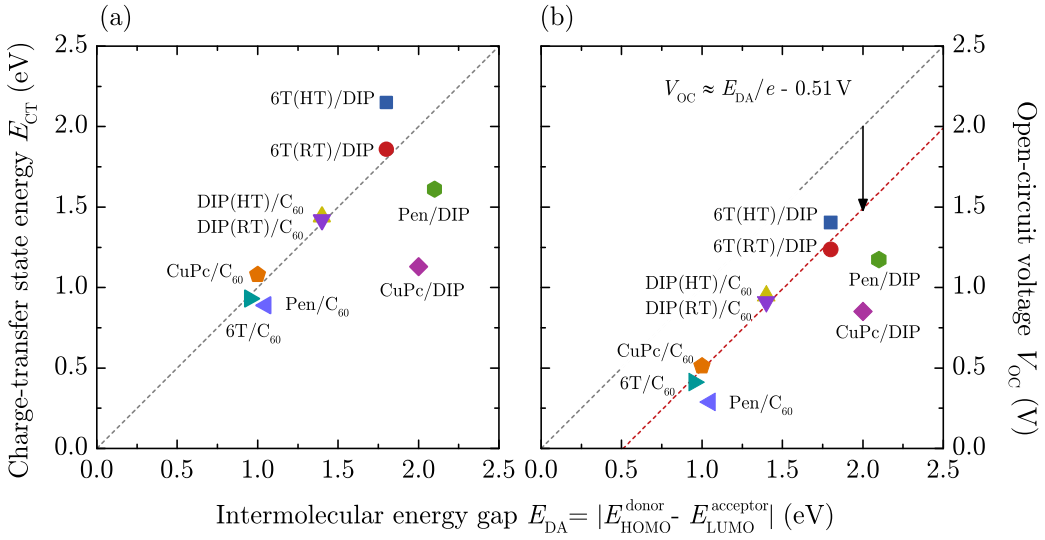

Figure 7.18.: (a) Relation between E_{CT} (as extracted from the linear extrapolation of V_{oc} towards 0 K) and the intermolecular energy gap E_{DA} (deduced from the difference between literature values of HOMO level of donor and LUMO level of acceptor) of the different studied photovoltaic devices as listed in Tab. 7.4. Devices which have been prepared with the donor deposited both at T_{sub} = RT and 100 °C are marked with **RT** and **HT**, respectively. (b) V_{oc} at room temperature versus E_{DA} confirming their linear dependence for the majority of the material combinations according to $V_{oc} = E_{DA}/e - 0.51$ V. The gray lines mark a one-to-one correspondence.

gap $E_{DA} = \left|E^{donor}_{HOMO} - E^{acceptor}_{LUMO}\right|$ as found in literature (cf. Tab. 7.4). Figure 7.18 summarizes the overall results of the present studies. The left part depicts the relation between E_{DA} and E_{CT} of the different devices at room temperature. For most of the material combinations, the extrapolation of the temperature dependent V_{oc} seems to represent a reliable method to determine E_{CT}. The deviation of the system 6T(100 °C)/DIP might have structural reasons—a topic which is currently subject of detailed investigations. Possible origins of the deviations of Pen/DIP and CuPc/DIP will be discussed below. Figure 7.18 (b) shows the relation between V_{oc} and E_{DA}. While for polymer solar cells the linear relationship between V_{oc} and E_{CT} has been confirmed by various independent studies[100,113,139,156] publications on small molecule devices are limited.[19] Here, an excellent correlation is found for most of the material systems clearly affirming that the open-circuit voltage is determined by the energy of the CT state—as has been theoretically predicted by Eq. (2.26). By applying a best fit to the data the linear dependence can be described by $V_{oc} = E_{DA}/e - 0.51$ V. The material combinations Pen/DIP and CuPc/DIP take a special position concerning their extremely high series resistances resulting in a

deviating temperature dependence of V_{oc} (see Fig. 7.16), which suggest the measured open-circuit voltage at RT to be underestimated. At the same time, the values for E_{DA} have only been roughly determined based on literature values of the individual materials without correction for possibly arising vacuum level shifts when applying them in a HJ device, which may lead to an overestimation of E_{DA}. Both arguments can be used to reasonably justify the deviation of both data points from the linear relationship.

As deduced from Eq. (2.26), the difference between measured V_{oc} and maximum obtainable open-circuit voltage determined by the CT state energy can be assigned to a sum of radiative and non-radiative loss paths. The experimental confirmation of Eq. (7.5) emphasizes the necessary prerequisites for highest possible V_{oc} being augmented j_{sc} and ΔE while at the same time suppressing j_{00}. Simulations based on the modified Shockley Queisser limit reveal that suppressed CT state absorption and recombination are essential requirements for maximum achievable organic PV efficiency.[148] Indeed, it has been shown by various authors that weak intermolecular electronic coupling between donor and acceptor molecules is considered to result in low j_{00}—a property which can be modified by varying the strength of the π-interaction.[332,384,390,391] Apart from radiative recombination losses, which are thermodynamically unavoidable, non-radiative losses can be made responsible for the major part of the voltage loss.[146,148] This emphasizes the importance to minimize their extent for maximum possible solar cell efficiency.

Table 7.4.: Characteristic parameters for a series of PHJ photovoltaic devices with different donor/acceptor materials with thicknesses (in nm) as given below. All cells have a similar device structure with ITO/ PEDOT($\approx$ 30 nm)/ donor/ acceptor/ BCP(5 nm)/ Al. If not otherwise stated, the materials are deposited at T_{sub} = RT. Quantities extracted from illuminated j-V characteristics at RT: open-circuit voltage V_{oc} (given in V), short-circuit current density j_{sc} (given in mA/cm^2), and fill factor FF (given in %). Light illumination inside the cryostat was realized with a white LED with an estimated intensity I_{L} (given in mW/cm^2). E_{CT} denotes the energy of the charge transfer state as extracted from a linear extrapolation of the temperature dependent V_{oc} towards $T = 0$ K (given in eV). Quantities extracted from dark j-V characteristics at RT: specific series resistance $R_{\mathrm{S}}A$ (given in $\Omega\,$cm^2) , ideality factor n, and dark saturation current density j_0 (given in mA/cm^2). ΔE denotes the activation energy as deduced from the temperature dependence of the dark saturation current. For comparison, the intermolecular energy gap $E_{\mathrm{DA}} = \left| E^{\mathrm{donor}}_{\mathrm{HOMO}} - E^{\mathrm{acceptor}}_{\mathrm{LUMO}} \right|$ is listed as assumed from literature values, both given in eV.

	Illuminated j-V characteristics					Dark j-V characteristics				Lit.
D/A	V_{oc}	j_{sc}	FF	I_{L}	E_{CT}	$R_{\mathrm{S}}A$	n	j_0	ΔE	E_{DA}
DIP as donor										
DIP(50)/C$_{60}$(80)	0.95	-3.1	61.3	48	1.44	31	1.6	$9.2 \cdot 10^{-11}$	1.62	1.4[i]
DIP(50)*/C$_{60}$(80)	0.91	-1.3	63.6	18	1.42	5	1.6	$1.0 \cdot 10^{-10}$	1.46	1.4[ii]
6T as donor										
6T(60)/DIP(60)	1.24	-1.3	42.5	37	1.86	14	2.3	$8.0 \cdot 10^{-11}$	2.03	1.8[i]
6T(60)*/DIP(60)	1.40	-0.9	48.5	38	2.11	25	2.3	$3.5 \cdot 10^{-12}$	2.10	
6T(40)/C$_{60}$(80)	0.41	-2.3	60.0	32	0.93	6	1.7	$7.1 \cdot 10^{-5}$	0.94	0.95[i]
Pen as donor										
Pen(50)/C$_{60}$(80)	0.29	-3.1	48.3	36	0.89	5	2.1	$6.0 \cdot 10^{-3}$	0.98	1.05[iii]
Pen(25)/DIP(65)	1.17	-0.03	28.9	22	1.57	532	2.2	$2.3 \cdot 10^{-12}$	3.10	2.1[iv]
CuPc as donor										
CuPc(25)/C$_{60}$(50)	0.51	-1.9	34.0	28	1.08	8	4.9	$2.0 \cdot 10^{-3}$	1.98[v]	1.0[iii]
						260	2.9	$1.1 \cdot 10^{-3}$	3.38[v]	
CuPc(25)/DIP(65)	0.85	-0.1	31.0	26	1.13	7911	1.3	$1.1 \cdot 10^{-13}$	1.15	2.0[iv]

* Deposited with $T_{\mathrm{sub}} = 100\,^{\circ}$C.

[i] HOMO and LUMO values are taken from Ref. 98 where they are actually determined from UPS/IPES experiments for the given heterojunction in the present order of deposition.

[ii] Similar E_{DA} as for the unheated case is expected as stated in Sec. 7.1.1.

[iii] Values based on UPS measurements on the given HJ—however, the LUMO is estimated by adding a transport gap to the HOMO. Values for Pen/C$_{60}$ are taken from Refs. 317, 386 and values for CuPc/C$_{60}$ are taken from Ref. 240.

[iv] Rough estimation based on literature values of HOMO levels and transport gaps as given in Tab. 4.1 without correction for possibly arising vacuum level shifts.

[v] Two parameter sets can be extracted from different temperature regimes (cf. Fig. B.14 in the Appendix). Upper row: medium to low temperature regime. Lower row: high temperature regime.

7.2.2. Access to the charge transfer state via PDS

In the previous section, it has been shown that temperature dependent measurements of the open-circuit voltage provide access to the energy of the CT state. As CT absorption features are typically characterized by low absorption coefficients, direct detection requires very sensitive spectroscopic techniques. Among the most common methods is photothermal deflection spectroscopy (PDS), which allows the determination of values for α_{CT} being several orders of magnitude smaller as compared to the bulk material absorption. As explained in Sec. 3.3.7 PDS is based on local heating of the sample which is caused by even very weak absorption of light. In order to assess E_{CT} for the material system DIP/C_{60}, neat and mixed films (ratio approximately 1:1) of DIP and C_{60} were evaporated on quartz glass substrates. Perfluorohexane was used as deflection medium, which assures high transmittance in the energy region of 0.6–6 eV[392] and large changes in index of refraction with small changes in temperature. Moreover, it guarantees for insolubility of both DIP and C_{60}.

Figure 7.19 shows PDS data of a co-evaporated mixed layer of DIP and C_{60} in comparison to the spectra of the single materials. To obtain absolute values of the absorption coefficient, the PDS signal is calibrated using standard reflec-

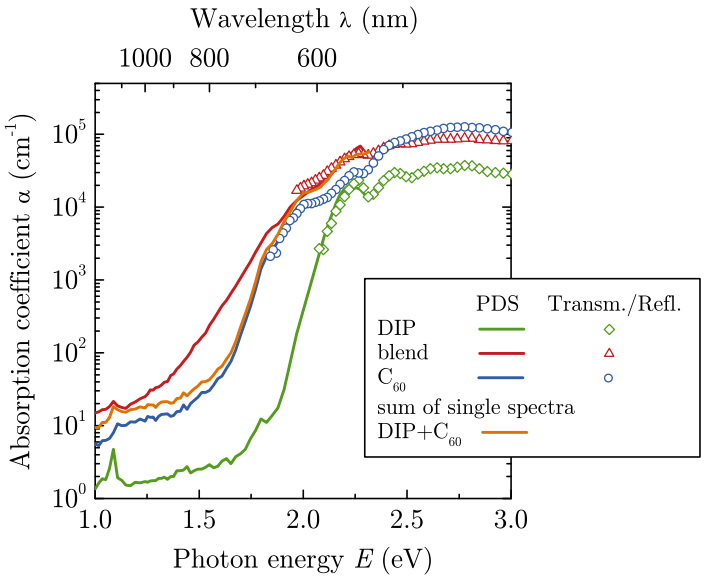

Figure 7.19.: Absorption spectrum for a blend of DIP:C_{60} (lines: photothermal deflection spectroscopy (PDS); open symbols: transmission/reflection measurement). For comparison, the single spectra of both materials as well as their sum are plotted to demonstrate the additional feature caused by the charge transfer state absorption.

tion/transmission measurements in the high energy regime (open symbols), where both measurement ranges overlap.[148]

In the DIP spectrum (green line in Fig. 7.19) a pronounced peak is apparent at an energy $E = 1.1\,\mathrm{eV}$, which can be ascribed to a multiphonon absorption due to vibrational stretching modes of C-H bonds. With increasing energy ($1.5\,\mathrm{eV} < E < 1.8\,\mathrm{eV}$) an absorption tail belonging to a tail of the DOS distribution is observed (for a detailed explanation of this feature it is referred to Ref. 157 and references herein). The high energy range is characterized by Gaussian π–π^* excitations which can be detected by common methods such as transmission measurements. In the neat C_{60} film, the onset of the transition to higher excited states is found to be situated below that of DIP. The spectrum of the mixed film of DIP:C_{60} is characterized by signatures of both materials: While at low energies, the multiphonon absorption of DIP can be detected the high energy region is governed by the characteristic absorption of the fullerene which implies that the main contribution to light absorption in a heterojunction device with comparable layer thickness of both materials will come from the fullerene. However, what clearly distinguishes the simple superposition of the single spectra from the measured spectrum of the blend film is the extra, broad absorption in the energy range between 1.3 eV and 1.7 eV, which cannot be found in any of the neat materials. This extra feature can be considered as direct measure of the CT state as it presents the energetically lowest state to absorb light (cf. schematic energy diagram in Fig. 2.21 (a)).

Based on these results, the energy of the CT state is expected around 1.5 eV. However, for a more precise determination of E_{CT}, the CT absorption spectrum can be quantitatively evaluated together with its luminescence spectrum as was proposed by Vandewal *et al.*[393]—a corresponding analysis will be shown in the end of the subsequent section.

7.2.3. Photoluminescence and Electroluminescence

Photoluminescence spectra based on DIP and C_{60}

The fact that a measurable CT signature is observable in the absorption spectrum of a DIP/C_{60} mixture suggests that its existence might be detectable in the luminescence behavior as well. Indeed, some recent studies on polymer/fullerene blends report on the experimental evidence of the charge transfer state by the presence of a new, long-wavelength photoluminescence band.[136,152] Here, neat and mixed films of DIP and C_{60} have been investigated concerning their photoluminescence (PL) behavior when excited with light of 480 nm wavelength.

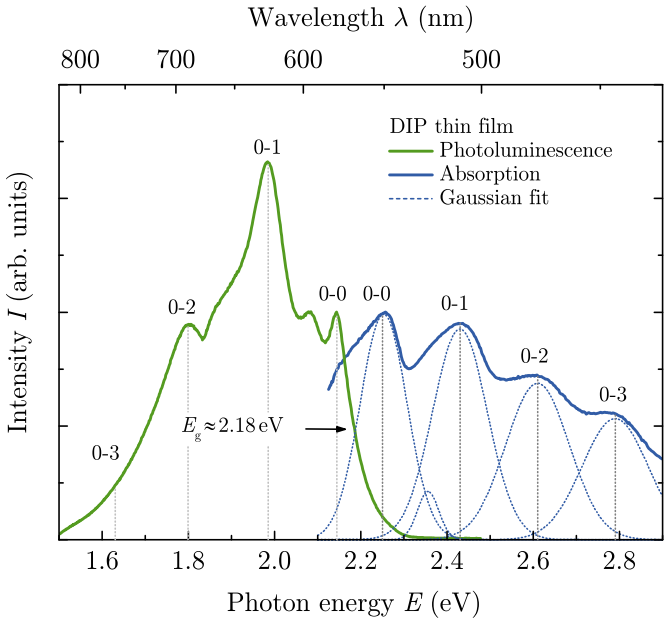

Figure 7.20.: Photoluminescence spectrum of a neat film of DIP (65 nm) evaporated on ITO/PEDOT in comparison to the absorption spectrum. The blue dotted lines show a Gaussian deconvolution of the DIP absorption spectrum.

Figure 7.20 shows the PL spectrum of a pure DIP layer (65 nm) which was evaporated on ITO/PEDOT. A reference spectrum has been recorded to ensure that the substrate does not influence the signature of the DIP thin film. As expected, the emission spectrum is red-shifted compared to the absorption as has been schematically depicted in Fig. 2.8. The absorption spectrum in the shown wavelength range is basically structured by four characteristic peaks, which can be assigned to the HOMO-LUMO transition of DIP. Based on the energetically lowest transition at $E_{00} = 2.25$ eV three further peaks at a distance of approximately 0.18 eV represent its vibronic progression. Comprehensive theoretical and experimental studies by Heinemeyer *et al.* demonstrate that the dielectric function of DIP thin films requires the implementation of a mixed Frenkel-CT model.[394] It considers that the excitation in a highly crystalline thin film of DIP molecules does not only take place on one molecule (Frenkel exciton) but can be extended to two neighboring sites (homo-molecular CT-state[t]) as consequence of the unit cell with two molecules (cf. crystal packing of DIP molecules in Fig. 3.2).

The photoluminescence spectrum of DIP (green line in Fig. 7.20) is characterized by the 0–0 transition at $E \approx 2.14$ eV followed by pronounced vibronic progression

[t]The term "homo-molecular" for a CT-state on two neighboring molecules of the same species is used to emphasize the difference to the "hetero-molecular" CT-state which is relevant for the exciton dissociation process in an organic heterojunction solar cell.

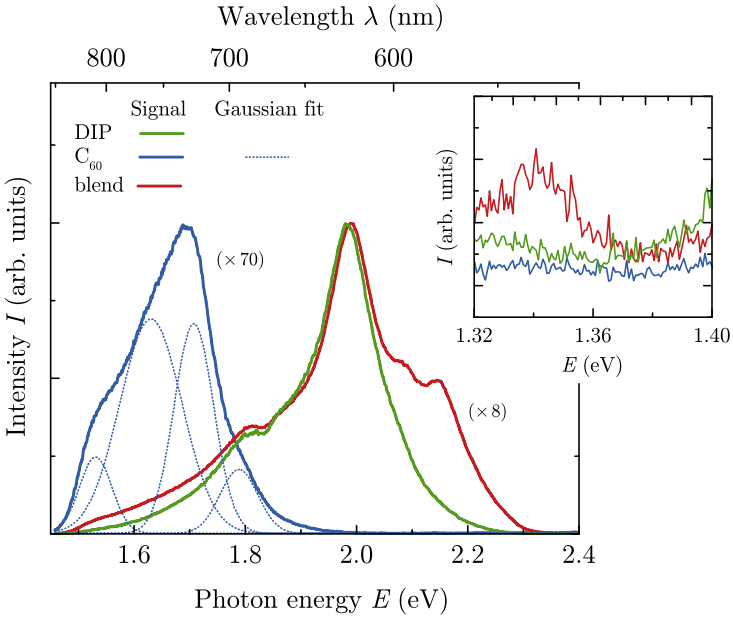

Figure 7.21.: Photoluminescence spectra of a mixed film of DIP and C_{60} in comparison to the spectra of neat films of DIP and C_{60}. The blue dotted lines show a Gaussian deconvolution of the C_{60} PL spectrum. All films were evaporated on quartz glass at substrate temperature of 100 °C with layer thicknesses of 1 µm.

with peak energies of 1.98 and 1.80 eV—similarly reported in literature.[395,396] The origin of the additional features on both edges of the 0–1 transition are unknown—however, a detailed analysis would go beyond the scope of this work. Even though the luminescence is shifted to lower energies as compared to the absorption, it does not resemble a mirror symmetry. Similar deviations have been reported in Ref. 202 and were attributed to different vibrational wave functions of the ground and excited state. In contrast to the ideal case depicted in the schematic absorption and emission diagram in Fig. 2.8, the peaks of the 0–0 transition do not coincide but show a Stokes shift of approximately 110 meV due to interactions with the environment. The intersection between the 0-0 peaks of absorption and emission can serve as estimate for the optical energy gap of the material. As the long-wave absorption peak decreases slowly as a result of neglected reflection, it is fitted by a Gaussian function yielding an intersect with the short-wave peak of the emission spectrum at approximately 2.18 eV. Based on the empirical relation between the optical energy gap E_g and the transport gap E_t found by Djurovich *et al.*,[134] $E_g = 2.18\,\text{eV}$ leads to a transport gap of approximately 2.6 eV.[u] This value is in very

[u]The authors mathematically described the empirical relation by $E_t \approx (1.39 \pm 0.15) \cdot E_g - (0.46 \pm 0.38)\,\text{eV}$.

good agreement with the literature value of $E_t = 2.5\,\mathrm{eV}$[98] (cf. Tab. 4.1) and allows to estimate an exciton binding energy of $E_B^{exc} \approx 0.3\,\mathrm{eV}$.

As a next step, the photoluminescence spectrum of a mixed film of DIP and C_{60} was recorded and compared to the spectra of neat films of DIP and C_{60}. As the signal strength of C_{60} is expected to be comparatively small (due to a dipole forbidden S_0-S_1 transition as will be explained in the subsequent section), all films were prepared with a film thickness of 1 µm deposited on quartz glass. The spectra are shown in Fig. 7.21. As consequence of the relatively thick films the high energy DIP signal in the neat film vanishes almost completely due to reabsorption (cf. Fig. 7.20), while the peak positions of lower energy are identical with those measured for the thin sample. The neat C_{60} spectrum can be best described by four Gaussian peaks with energies of $E = 1.53\,\mathrm{eV}, 1.63\,\mathrm{eV}, 1.71\,\mathrm{eV}$ and $1.79\,\mathrm{eV}$. The results are in very good agreement with literature values for C_{60} deposited on quartz substrate as found in Ref. 397: The authors attribute the main band at $E = 1.71\,\mathrm{eV}$ to the Frenkel excitation within one C_{60} molecule and the two peaks on the low energy side to its vibronic progression. The high energy emission band located around 1.8 eV was assigned to the presence of residual C_{70} in the sublimated powder or to film defects. However, a detailed investigation of the luminescence properties of the neat materials was not part of the present study. The PL signal of the mixed film (red line in Fig. 7.21) is essentially characterized by the emission bands of DIP—including the high energy peaks which are not suppressed by reabsorption. The influence of C_{60} is only weakly defined in the low energy range between 1.5 and 1.8 eV. A photoluminescence signal of the CT state would be expected outside the spectral sensitivity range of the Silicon detector. For that reason, luminescence in the near-infrared region has been recorded using an InGaAs detector. As can be seen in the inset of Fig. 7.21, an additional peak might be identified for the mixed film. However, the poor signal-to-noise ratio resulting from the non-cooled detector system, does not allow for an unambiguous identification. By exciting the materials electrically and detecting the signal with a cooled CCD camera, this drawback could be eliminated as will be shown in the subsequent section.

Electroluminescence spectra of DIP/C_{60} based solar cells

Apart from photoluminescence, DIP shows strong emission spectra when excited electrically—i.e. in a solar cell device operated under forward bias (electroluminescence, EL). This property makes it a suitable material to study spectroscopic signatures of single layer, planar and bulk heterojunction devices. All devices have the following common layer structure:

ITO/ PEDOT($\approx 30\,\mathrm{nm}$)/ active layer/ BCP($5\,\mathrm{nm}$)/ Al,

with either single layers of DIP and C_{60}, bilayer or mixed films as active layer. The precise device structures including layer thickness and substrate temperature are listed in Tab. 7.5. Prior to spectral EL measurements, the devices have been examined concerning their light emission as a function of applied voltage—recorded by a photodiode. Results are shown in Fig. 7.22. When applying a forward bias to each of the cells, electrons are injected from the Al cathode into the LUMO of the adjacent organic layer while at the same time holes are injected from the ITO/PEDOT anode to the HOMO of the adjacent semiconducting layer just as in the case of the dark currents studied in the course of this work. A noticeable current flow of the photodetector—as observed for all investigated devices—indicates that the injected charge carriers recombine—at least partially—by generating light. As the detection capability of the photodiode suffered from capacitive influences of the lead, the onset voltage of light emission V_{EL} cannot accurately be determined from Fig. 7.22. In general, the recombination can either take place at the contacts or inside the active organic film, where it might be accompanied by emission of light. For the single layer devices, the spectral luminescence of the radiative recombination is expected to reflect the fluorescence spectra of the respective organic material. In the heterojunction devices, the charge carrier recombination can either occur on one of the constituents or—and this is what is hoped for—electron on the acceptor and hole on the donor form a CT state and recombine. From an energetic point of view, the CT state is the lowest energetic state which allows for recombination as has been illustrated in Fig. 2.21. Based on this consideration, CT emission is expected to be the prevailing emission path when choosing a voltage just above the open-circuit voltage of the OPV cell. When going to higher voltages, the signal will be more and more dominated by the pure materials.

Table 7.5.: Device structure of the diodes investigated concerning their electroluminescence behavior.

Device	Active layer (thickness/substrate temperature)
DIP single layer	DIP ($100\,\mathrm{nm}$, RT)
C_{60} single layer	C_{60} ($100\,\mathrm{nm}$, RT)
PHJ	DIP ($50\,\mathrm{nm}$, RT) / C_{60} ($80\,\mathrm{nm}$, RT)
PM-HJ, RT	DIP ($5\,\mathrm{nm}$, RT) / DIP:C_{60} ($50\,\mathrm{nm}$, RT) / C_{60} ($10\,\mathrm{nm}$, RT)
PM-HJ, HT	DIP ($5\,\mathrm{nm}$, $100\,^{\circ}\mathrm{C}$) / DIP:C_{60} ($50\,\mathrm{nm}$, $100\,^{\circ}\mathrm{C}$) / C_{60} ($10\,\mathrm{nm}$, RT)

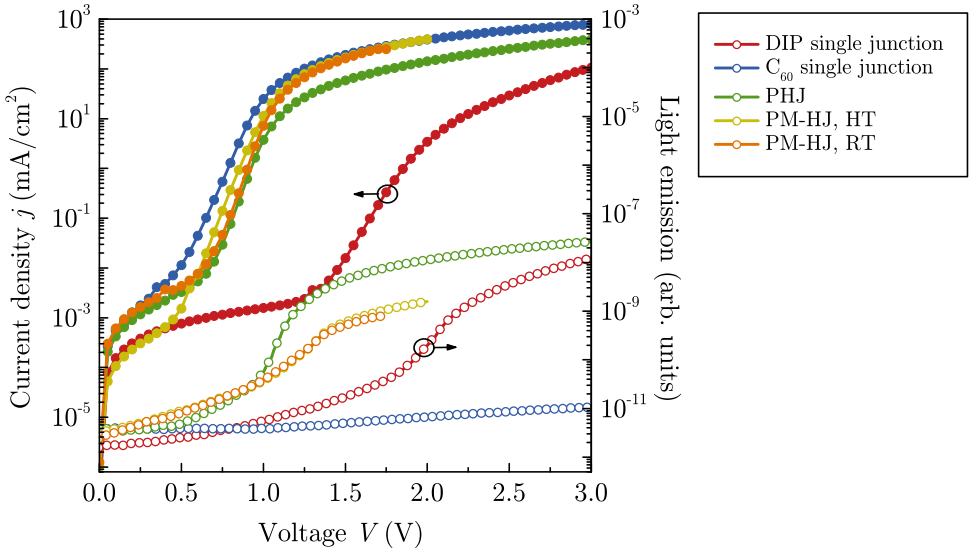

Figure 7.22.: Voltage dependent current densities (closed circles) and light emission (open circles) of different diodes recorded prior to electroluminescence measurements. The layer structures are listed in Tab. 7.5.

As the choice of the electrode materials is equal for all diodes and represents the optimized configuration for the DIP/C_{60} heterojunction devices, the energetic constellation of anode and cathode are naturally not optimized for the single layer cells. Based on the energetic picture given in Sec. 7.1.1, large electron and hole injection barriers are expected for the DIP and C_{60} single layers, respectively. This might be one reason why the light emission of the C_{60} device is almost below the threshold for detection. However, as the current density in forward direction is still rather high, the majority of charge carriers seems to recombine non-radiatively. In this context it has to be mentioned that the HOMO-LUMO transition of C_{60} is dipole forbidden:[398] Both, the ground state S_0 as well as the first excited state S_1 exhibit even parity—being responsible for the forbidden transition from S_1 to S_0. However, vibronic coupling as well as disorder in the film may lead to a certain degree of mixed components of even and odd states which can partially abolish the violation of parity conservation.[399] Another prerequisite for efficiently detecting EL signals from single layer devices are ambipolar properties of the semiconductor allowing to transport both electrons and holes. As was shown in chapter 6, DIP shows both electron and hole transport. By contrast, investigations on OFETs could not observe any hole transport in C_{60} even with TTF-TCNQ as electrode material.[285] However, for the present study a qualitative comparison of the heterojunctions with the single layer devices is of primary importance.

Figure 7.23 and 7.24 show the measured EL for the single layer, planar and

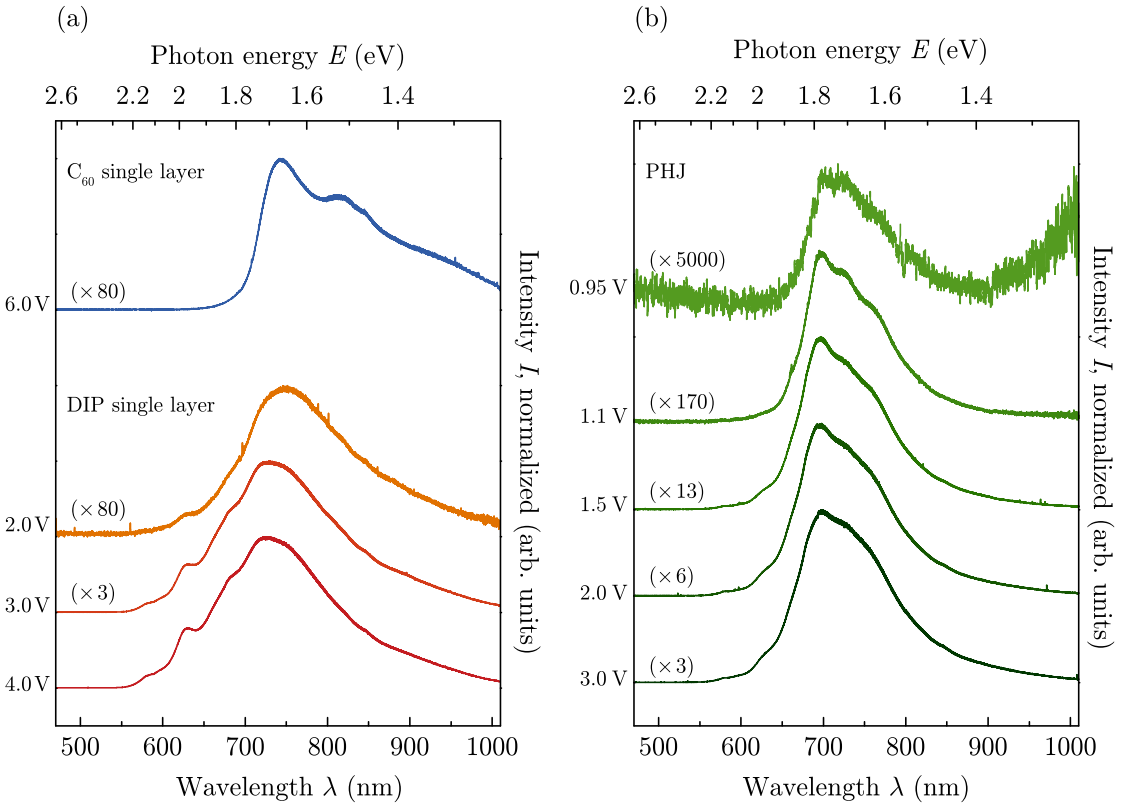

Figure 7.23.: Electroluminescence spectra of (a) single layer C_{60} (blue curve) and DIP (red curves) and (b) PHJ DIP/C_{60} photovoltaic devices (green curves), obtained by applying a forward voltage of given magnitude. For better comparability the curves are normalized to their maximum values—however, the magnification factors are given in brackets to illustrate the strong variations in signal strength.

planar-mixed heterojunction devices. The luminescence signals were corrected for the spectral sensitivity of the detector and normalized to their maximum values, respectively. For an exact calculation of the quantum efficiency, the system would have to be calibrated against a light source with known intensity. However, in the present study the analysis is based on qualitative signal strengths, which are represented by their relative magnification factors (given in brackets besides the respective curves). Due to the detection limit of the CCD camera the spectra are cut off at 1010 nm.

As expected from the extremely small light emission of the C_{60} single layer even with increasing voltage (cf. Fig. 7.22), a clearly visible EL spectrum could only be recorded applying a high voltage of $V = 6\,\mathrm{V}$ and with long integration times. Similar peak positions as found for the PL spectrum are observed, with an additional broad decay in the long wavelength range. For the DIP single layer, the

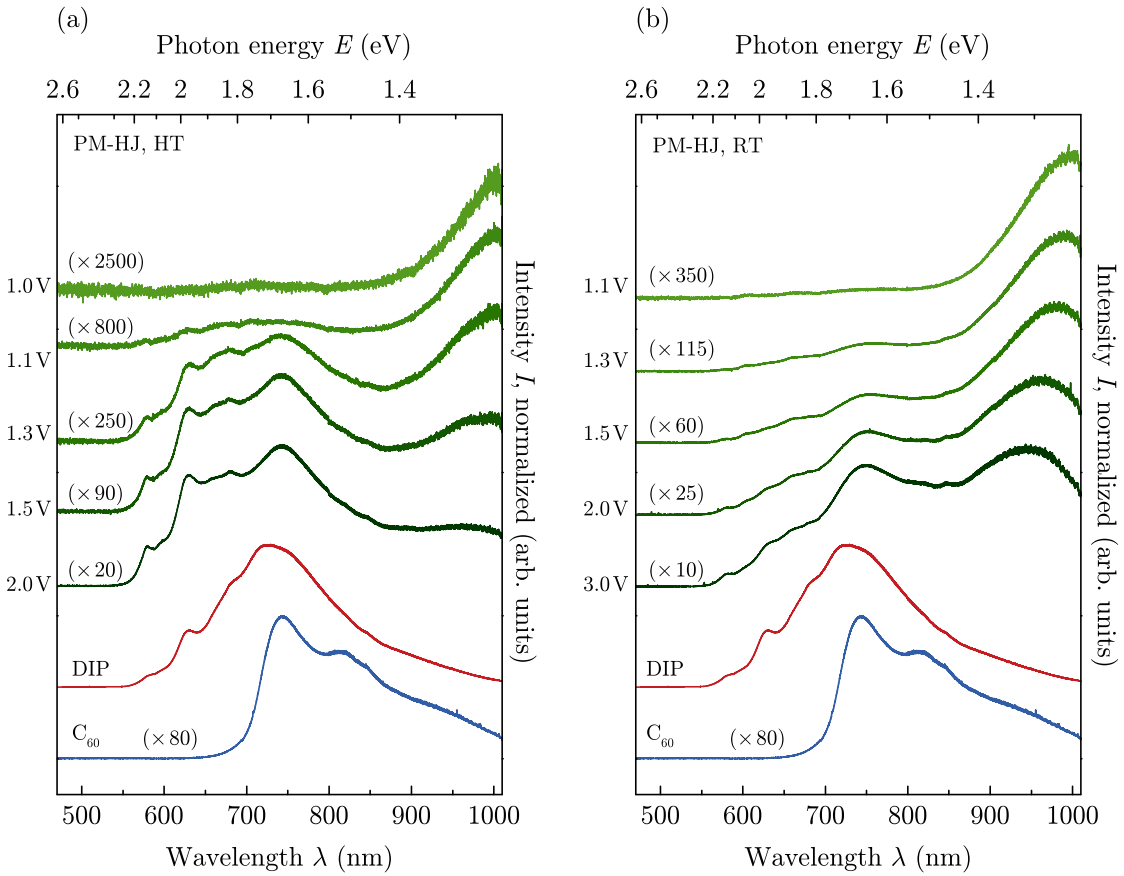

Figure 7.24.: Electroluminescence spectra of PM-HJ solar cells based on DIP:C_{60} with different substrate temperatures of (a) $T_{sub} = 100\,°C$ and (b) $T_{sub} = RT$. The curves are obtained by applying a forward voltage of given magnitude. For better comparability the curves are normalized to their maximum values—however, the magnification factors are given in brackets to illustrate the strong variations in signal strength.

situation is like in C_{60}: The main EL features resemble the PL spectrum, however, with changed height ratios. Figure 7.23 (b) shows the EL spectra for the PHJ device. As expected, luminescence bands of both single materials are identifiable in the wavelength range between 600 and 900 nm, however, relatively smeared out in energy. With decreasing applied voltage, the shape of the spectra remains the same, but with less intensity. At $V = 0.95\,V$, situated just above the open-circuit voltage, the signal is only very weak—however, with an additional feature in the low energy part of the spectrum. Assuming this peak to originate from a luminescent CT state, the weakness is not surprising, as the contact between donor and acceptor molecules in a planar stacked heterojunction is limited to a small volume at the interface. For this reason, a more pronounced CT emission would be expected for a mixed film which is characterized by a strongly increased

D/A interface. According measurement data of the PM-HJ devices are shown in Fig. 7.24 (green curves). The left hand side depicts the spectra of the heated cell and it is conspicuous that the luminescence up to $\lambda = 900\,\mathrm{nm}$ is characterized by very distinct peaks which can be attributed to EL features of the single components (cf. red and blue curves). In contrast to the PHJ, an additional low energy signal can already be observed at high applied voltages. When reducing V, the emission bands in the middle wavelength range are gradually reduced until they are almost completely suppressed at $V = 1.0\,\mathrm{V}$. At the same time, the signal at low energies grows in its relative height and defines the spectrum completely. The unheated PM-HJ device (see Fig. 7.24 (b)) principally shows a similar behavior. The spectrum in the middle wavelength range is less pronounced than in the HT case, which can be ascribed to the morphology of the blend as investigated in Sec. 7.1.1: In both cases the two materials form a phase-separated mixture when evaporating them simultaneously. However, the domains of the single materials are larger when the substrate is heated during evaporation leading to more pronounced luminescence features from the pure materials as could be observed in Fig. 7.24 (a). Due to the refined phase separation in the RT case the DIP/C_{60} interface is even greater, which facilitates the detection of the CT signal. Moreover, a slight red-shift of the CT signature is observed for the heated device as compared to the unheated, a phenomenon attributed to crystallization of the organic components[144,400] which is indeed higher in the heated device as was found by structural investigations shown in Sec. 7.1.1.

Altogether, the additional peak in the low energy part of the PM-HJ EL spectra does not correspond to either of the single constituents and is much more pronounced as compared to the PHJ devices. Moreover, it dominates the emission spectrum when reducing the applied voltage just above the onset of light emission where the recombination is expected to take place via the lowest energy state, namely the CT state. In the voltage dependence of the PM-HJ spectra, a slight red-shift of the CT emission is observed for decreasing applied voltage. This can very likely be attributed to the vanishing influence of the higher energy states which originate from the pure materials.
While the direct correlation between E_{CT} and V_{oc} seems to be undisputed, Ng *et al.* investigated a possible relationship between the intensity of CT emission and photovoltaic performance.[401] However, their studies on Rubrene/C_{60} planar and bulk heterojunction devices did not give any indication for a relation. The present data on DIP/C_{60} diodes could confirm the general trend of improved exciton dissociation when increasing the interfacial D/A area by going from a planar to a bulk heterojunction which is reflected by significantly pronounced CT emission in the electroluminescence signal. However, an even stronger CT signature is observed

for the unheated PM-HJ device which is known to be characterized by a more intimate mixture and less pronounced phase separation, but, which at the same time shows poorer photovoltaic performance as the charge carrier extraction is hindered by missing percolation paths. These findings confirm the necessary trade-off which has to be found between efficient exciton dissociation guaranteed by a possibly highest D/A interface on the one hand and unhindered charge carrier extraction on the other hand. In the EL experiment this limitation seems to play a less important role as the injection current is governed by drift—in contrast to the diffusion dominated region when operated under solar cell condition.

In a recent publication, Tvingstedt *et al.* report electroluminescence from several types of polymer:fullerene BHJ solar cells biased in the forward direction—deducing E_{CT} from the peak energy of the CT emission.[144] According to this concept, a CT energy of $E_{\mathrm{CT}} \approx 1.25\,\mathrm{eV}$ would be extracted from the pronounced low energy peak of the PM-HJ deposited at RT (cf. Fig. 7.24 (b), $V = 1.1\,\mathrm{V}$). However, Vandewal *et al.* proposed an alternative formalism to identify E_{CT}:[393] Based on the framework of Marcus theory, the authors extracted the CT energy E_{CT} by analyzing the absorption and the emission spectra of a series of polymer:PCBM blends. They fitted the CT absorption cross section $\sigma(E)$ by

$$\sigma(E)E = \frac{f_\sigma}{\sqrt{4\pi\lambda_0 k_{\mathrm{B}} T}} \exp\left(\frac{-(E_{\mathrm{CT}} + \lambda_0 - E)^2}{4\lambda_0 k_{\mathrm{B}} T}\right), \tag{7.6}$$

and the CT emission rate I_{f} by

$$\frac{I_{\mathrm{f}}}{E} = \frac{f_{I_{\mathrm{f}}}}{\sqrt{4\pi\lambda_0 k_{\mathrm{B}} T}} \exp\left(\frac{-(E_{\mathrm{CT}} - \lambda_0 - E)^2}{4\lambda_0 k_{\mathrm{B}} T}\right), \tag{7.7}$$

whereas λ_0 denotes the reorganization energy (related to the Stokes shift) and f_σ and $f_{I_{\mathrm{f}}}$ are proportional to the square of the electronic coupling matrix element. The left hand side of both equations is called reduced absorption and emission, respectively.

The reduced absorption and emission spectra for the DIP and C_{60} based devices are shown in Figure 7.25. By fitting both spectra with Eq. (7.6) and (7.7), a reorganization energy of $\lambda_0 \approx 0.26\,\mathrm{eV}$ as well as an energy of the CT state of $E_{\mathrm{CT}} \approx 1.50\,\mathrm{eV}$ can be deduced. However, it has to be mentioned that this determination can only provide an estimation of E_{CT}, as the height of the reduced emission is adjusted to an estimated position of the CT absorption maximum only. The reorganization energy λ_0 corresponds to non-radiative energy losses as a result of relaxation (see schematic picture in Ref. 146) and its magnitude is found to be similar to values determined for a variety of polymer:fullerene blends.[393]

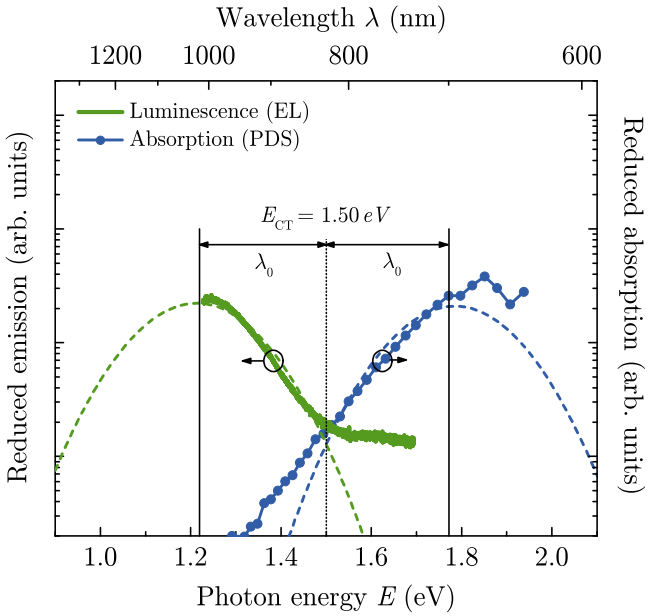

Figure 7.25.: Reduced absorption (from PDS, blue circles—corresponding to the difference between absorption spectrum of the blend and absorption spectrum of the sum of single spectra) and emission (from EL, green straight line) for DIP:C_{60} measured at room temperature. The dashed curves are fits according to Eq. (7.6) and (7.7), using the same values for E_{CT} and λ_0.

For a conceptional consideration of non-radiative recombination losses regarding electronic coupling of the CT state and reorganization energy it is referred to a review article published recently by Schlenker and Thompson.[390] In short, the authors emphasize the demand for materials and architectures that minimize the electronic coupling and maximize the reorganization energy in order to suppress non-radiative recombination and to get highest possible V_{oc}. Comparing the CT energy given by a linear extrapolation of $V_{oc}(T)$ towards $T = 0\,K$ (cf. Sec. 7.2.1), it has been determined to 1.42 eV. Similar deviations are found for a variety of polymer blends—where temperature dependent absorption measurements reveal a redshift of the CT band upon cooling—ultimately resulting in the same E_{CT} when extrapolating towards $T = 0\,K$. The reason is assumed to be found in increased disorder at higher temperature.[393]

To summarize, EL has shown to be a suitable method to directly probe the bimolecular radiative recombination from CT state in DIP/C_{60} solar cells. Its unambiguous detection by alternative methods such as absorption or photoluminescence are often hampered by an overlap of the weak CT luminescence with the fluorescence features of the pure materials. In contrast, EL offers the possibility to suppress the signals of the individual materials by reducing the applied voltage

to a minimum—just above the onset voltage for detectable light emission. By a combined analysis of the CT absorption (as deduced from PDS measurements, cf. Sec. 7.2.2) and CT emission (from EL spectra at smallest possible applied voltage), its energy could be determined to $E_{\mathrm{CT}} = 1.50\,\mathrm{eV}$ for the DIP/C_{60} material combination which is in very good agreement with E_{CT} extracted from the temperature dependent V_{oc} measurements (1.42 eV), the value determined from the activation energy of the dark saturation current (1.46 eV) (both analyzed and discussed in Sec. 7.2.1) as well as the literature value from photoelectron spectroscopy (1.4 eV, see Tab. 4.1).

7.2.4. Charge carrier recombination in solar cells based on DIP and C_{60}

The importance of charge carrier recombination has already been pointed out in various parts within the course of this work. As introduced in Sec. 2.3.2, recombination of photogenerated charge carriers ultimately limits the open-circuit voltage in organic solar cells. The crucial impact of recombination current on V_{oc} has been experimentally confirmed in Sec. 7.2.1. In the following, studies based on impedance spectroscopy will investigate to what extent charge carrier recombination can be made responsible for the shape of the j-V curve which determines the fill factor of a device. Subsequently, results on the diode ideality factor—identified by a variety of different methods—will be compared to each other and associated with the prevailing recombination mechanism.

Recombination current identified by impedance analysis

The general approach to reconstruct j-V curves from IS data. Very recently Boix *et al.* developed a method to reconstruct current-voltage characteristics solely from the analysis of impedance data measured under different illumination intensities.[402] The corresponding model is based on the assumption that the total device current $j(V_F)$ can be decomposed into a (negative) photocurrent j_{ph} and a (positive) contribution which is identified as the recombination current $j_{rec}(V_{oc})$ of separated photogenerated carriers. This relation is visualized in Fig. 7.26. Here, j_{ph}—corresponding to the recombination current density at V_{oc}—is assumed to be voltage-independent and depends on light intensity only.

As shown before, the voltage dependent current behavior of a solar cell can be best described by the Shockley equation

$$j(V_F) = j_0 \left[\exp\left(\beta \frac{eV_F}{k_B T} \right) - 1 \right] - j_{Ph}. \tag{7.8}$$

In accordance with the conventional form given in Eq. (2.1), the parameter β accounts for the deviation from the ideal diode behavior—being the inverse of the diode ideality factor n.[403] Assuming $\exp(\beta e V_F / k_B T) \gg 1$, which is a justified assumption as shown in appendix C, Eq. (7.8) simplifies to

$$j(V_F) \approx \underbrace{j_0 \cdot \exp\left(\beta \frac{eV_F}{k_B T} \right)}_{j_{rec}(V_F)} - j_{Ph}, \tag{7.9}$$

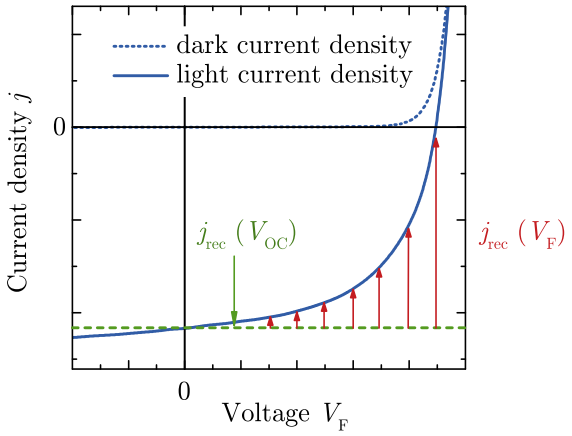

Figure 7.26.: Illustration of the assumptions underlying the model used to reconstruct j-V-curves from IS data: A charge recombination current $j_{rec}(V_F)$ is added to the photocurrent to shape the cell's j-V-characteristics. The photocurrent is assumed to be constant and corresponds to the recombination current at open-circuit condition, i.e. $j_{ph} = j_{rec}(V_{OC})$.

whereas—according to the picture illustrated in Fig. 7.26—the first summand can be interpreted as the voltage dependent recombination current j_{rec}:

$$j_{rec}(V_F) = j_0 \exp\left(\beta \frac{eV_F}{k_B T}\right). \tag{7.10}$$

Here, V_F represents the splitting of electron and hole Fermi levels ($e\,V_F = E_{F,n} - E_{F,p}$) by assuming that good contacts allow for the equilibration of the Fermi levels of the electrodes and the corresponding edge of the organic layer.[347] A justification for Eq. (7.10) is based on the assumption that charge carrier density follows Boltzmann statistics:[26,404,405] $\rho = \rho_0 \exp(e\,V_F/k_B\,T)$ with the equilibrium carrier concentration ρ_0—whereas β represents an effective order of recombination. Leong *et al.* report on a similar expression to Eq. (7.10) which they also applied to interpret IS data in terms of recombination mechanisms.[406] However, their recombination parameter β_{Leong} is found to be twice the β defined here, i.e. $\beta_{Leong} = 2 \cdot \beta$. A comment on the conformity of both approaches will be given in the end of this section.

By ordinary steady-state j-Vmeasurements both contributions, i.e., the voltage independent photocurrent and the voltage-dependent recombination current, cannot be separated. As a great advantage, impedance analysis offers the possibility to determine differential quantities which allows to measure the voltage-dependent term while omitting the constant photocurrent. The specific recombination resistance—determined from the low frequency part of the impedance

spectra—is related to the recombination current density j_{rec} as[407]

$$R_{\mathrm{rec}}A = \left(\frac{\mathrm{d}j_{\mathrm{rec}}}{\mathrm{d}V_{\mathrm{F}}}\right)^{-1}. \tag{7.11}$$

Combining Eq. (7.10) and (7.11) yields

$$\left(\frac{\mathrm{d}j_{\mathrm{rec}}}{\mathrm{d}V_{\mathrm{F}}}\right)^{-1} = \left[j_0 \exp\left(\beta\frac{\mathrm{e}V_{\mathrm{F}}}{k_{\mathrm{B}}T}\right)\cdot\frac{\beta\,\mathrm{e}}{k_{\mathrm{B}}T}\right]^{-1} \tag{7.12}$$

which defines the recombination resistance as

$$R_{\mathrm{rec}}A = \frac{k_{\mathrm{B}}T}{j_0\beta\,\mathrm{e}}\exp\left(-\beta\frac{\mathrm{e}V_{\mathrm{F}}}{k_{\mathrm{B}}T}\right) \tag{7.13}$$

$$= R_0\exp\left(-\beta\frac{\mathrm{e}V_{\mathrm{F}}}{k_{\mathrm{B}}T}\right) \tag{7.14}$$

$$= \frac{k_{\mathrm{B}}T}{\beta\,\mathrm{e}}j_{\mathrm{rec}}^{-1} \tag{7.15}$$

By transposing Eq. (7.15), a general expression for the recombination current in dependence on V_{F} can be derived as

$$j_{\mathrm{rec}}(V_{\mathrm{F}}) = \frac{k_{\mathrm{B}}T}{\beta\,\mathrm{e}\,R_{\mathrm{rec}}(V_{\mathrm{F}})A} \tag{7.16}$$

and correspondingly j_{rec} at V_{OC} is given by

$$j_{\mathrm{rec}}(V_{\mathrm{OC}}) = \frac{k_{\mathrm{B}}T}{\beta\,\mathrm{e}\,R_{\mathrm{rec}}(V_{\mathrm{OC}})A}. \tag{7.17}$$

Under open circuit the total current vanishes, i.e., after Eq. (7.9) the photocurrent j_{Ph} is entirely compensated by the recombination current $j_{\mathrm{rec}}(V_{\mathrm{oc}})$. Moreover, j_{Ph} is considered to be independent of voltage which implies that the exciton dissociation process is not influenced by the electric field and j_{Ph} can be approximated by j_{sc}. Inserting Eq. (7.16) and (7.17) in Eq. (7.9) yields the total current in dependence on the recombination resistance:

$$j(V_{\mathrm{F}}) = \frac{k_{\mathrm{B}}T}{\beta\,\mathrm{e}}\left(\frac{1}{R_{\mathrm{rec}}(V_{\mathrm{F}})A} - \frac{1}{R_{\mathrm{rec}}(V_{\mathrm{oc}})A}\right). \tag{7.18}$$

The parameter β is determined by fitting the high-voltage range of the recombination resistance vs. voltage curve with the expression given in Eq. (7.14) and the specific recombination resistances $R_{\mathrm{rec}}(V_{\mathrm{F}})A$ and $R_{\mathrm{rec}}(V_{\mathrm{oc}})A$ are parameters which can be directly extracted from impedance data as will be shown below.

As was introduced in Sec. 2.1.6 the ideal diode behavior as assumed in Eq. (2.1) is hardly fulfilled in real devices, where series and parallel resistances have to be considered—resulting in a modified form as given by Eq. (2.7). Especially around the maximum power point the series resistance R_S can lead to comparatively pronounced distortions, which show the need for its consideration.[402] Advantageously, R_S can be separately extracted from IS data which enables a correction of the voltage accounting for the potential drop at the series resistance as

$$V_F = V_{app} - j \cdot R_S A. \tag{7.19}$$

Alternatively, the IS measurement can be performed at various open-circuit voltages (modified by different illumination intensities).[348,407] Under these conditions the balance between photocurrent and recombination flux eliminates the need to consider a series resistance.

Recombination currents of DIP/C_{60} PHJ cells with heated substrate. To analyze photovoltaic devices according to the above presented approach a series of impedance measurements have been performed on DIP/C_{60} based solar cells by varying the applied bias voltage under different light intensities (either an LED or a halogen lamp is used as light source). The data analysis will be exemplarily shown by means of a heated PHJ device with the following layer sequence:

ITO/ PEDOT($\approx 30\,$nm)/ DIP($50\,$nm, $100\,^\circ$C)/C_{60}($50\,$nm, RT)/ BCP($6\,$nm)/ Al

Typical j-V curves and the corresponding impedance spectra illustrating the analysis procedure at different applied potentials are shown in Fig. 7.27. At each light intensity impedance spectra have been recorded for bias voltages V_{dc} ranging from $-0.05\,$V to $1\,$V in steps of $50\,$mV (see Fig. 7.27 (a)). Figure 7.27 (b) depicts the corresponding experimental IS data (closed circles) which were fitted (straight lines) to the model represented by the equivalent circuit shown in the inset. The experimental IS analysis allows measuring the recombination resistance R_{rec} as function of the applied voltage for different illumination intensities. To measure under open-circuit condition a bias voltage V_{dc} equal to V_{oc} at each light intensity was applied as illustrated in Fig. 7.27 (c). Additionally the series resistance R_S and chemical capacitance C_μ were directly extracted from the low-frequency arc of the impedance spectra. A detailed definition of the chemical capacitance C_μ can be found in Refs. 408 and 409. In short, C_μ consists of two parts: one part is related to the electrostatic capacitance, which equals the geometric capacitance C_g of a parallel-plate capacitor as defined by Eq. (3.20), and an additional contribution from the density of states. Thus, for mesoscopic systems such as the present solar cells an electric field leads both to an accumulation of excess charge carriers at the

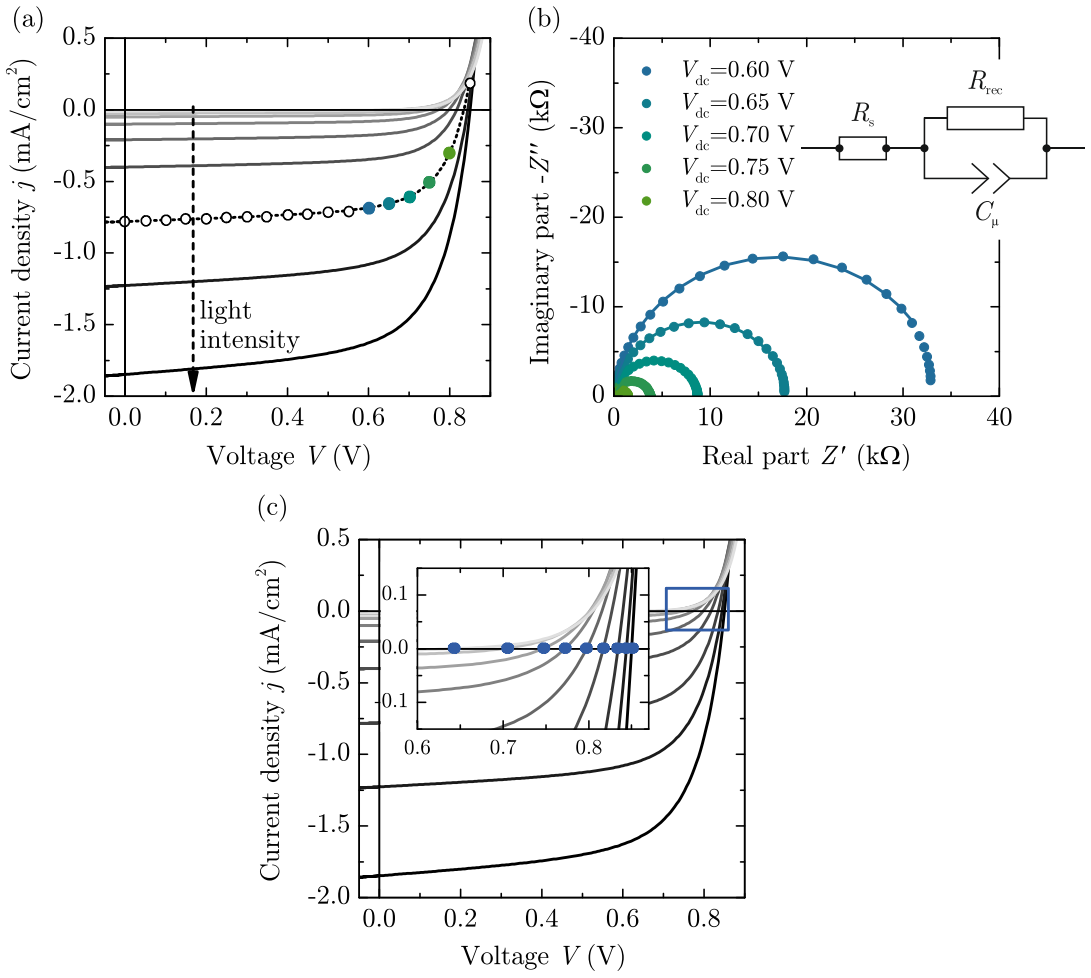

Figure 7.27.: Principle of IS analysis for analysis of recombination current: (a) Current-voltage characteristics of a heated DIP/C_{60} PHJ solar cell for a variety of different light intensities. The highlighted curve exemplarily shows the bias voltage steps V_{dc}—each of the marked voltages was applied to record a frequency scan of impedance. (b) Impedance spectra measured under different bias voltages as marked in (a). The low-frequency response is modeled by means of a parallel RC circuit shown in the inset. (c) Current-voltage characteristics where V_{oc} is varied by illumination with different light intensities. To measure under open circuit a bias voltage V_{dc} equal to V_{oc} is applied at each light intensity.

electrodes as well as to a variation of the Fermi level positions within the organic layers with respect to the Fermi levels of the electrodes.

Figure 7.28 shows the variation of $R_{rec}\,A$, C_μ/A and $R_S A$ as function of V_F at different illumination intensities. The voltage is corrected for the potential drop at the series resistance $R_S A$ as given by Eq. (7.19). For better comparison to the current-voltage characteristics, the respective j-V curves are included in the

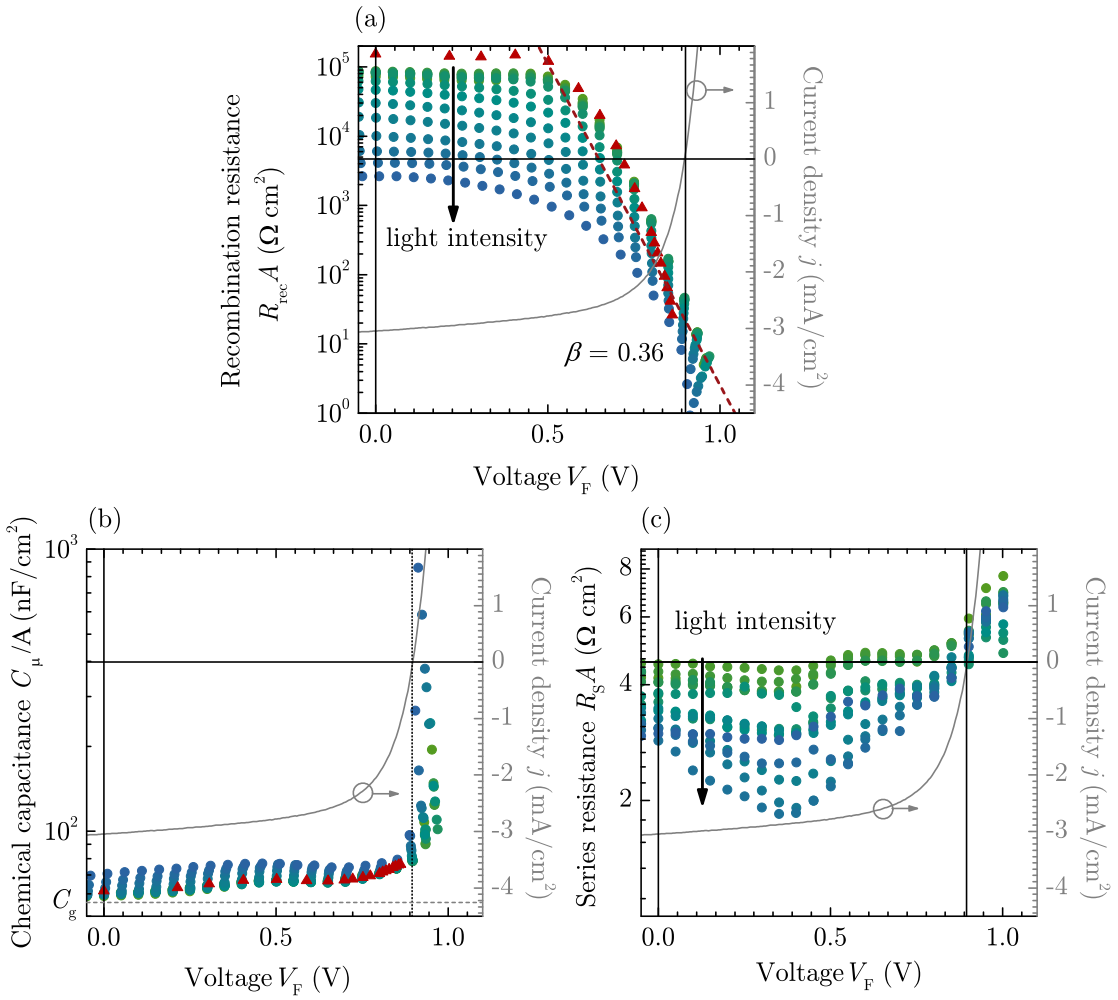

Figure 7.28.: Heated DIP/C_{60} PHJ solar cell: (a) Specific recombination resistance $R_{\mathrm{rec}}\,A$ (b) chemical capacitance C_μ/A and (c) series resistance $R_S A$ extracted from impedance spectroscopy at different illumination intensities. Voltages are corrected for the potential drop at a series resistance following Eq. (7.19). The values obtained at open circuit are included for comparison (red triangles) just as the j-Vcurve recorded for the highest light intensity.

impedance diagrams whenever possible. Moreover, values for V_{oc} are marked by vertical lines. It can be seen that the voltage dependence of the recombination resistance can be separated into two distinct regimes: At low voltages up to $V_{\mathrm{F}} \approx 0.5\,\mathrm{V}$, $R_{\mathrm{rec}}A$ reveals a plateau-like behavior which depends on the illumination intensity: With higher light levels, $R_{\mathrm{rec}}\,A$ decreases covering a range of almost two orders of magnitude. However, as illustrated from the schematic picture in Fig. 7.26 the low voltage region with high recombination resistances is mainly dominated by the photocurrent j_{ph} making the deviations in recombination resistance for the

different light intensities less important for the reconstruction of the j-V curves. At voltages above $V_F \approx 0.5\,V$ the distance between curves for different light intensities is reduced and can approximately be described by Eq. (7.14) with a common β of 0.36. However, this observation is not in full accordance with the results for solution-processed P3HT:PCBM cells[402] where all curves almost perfectly collapse within a comparatively large voltage region. The latter has been viewed as evidence for the assumption made in Eq. (7.10) stating that the illumination intensity does not affect the recombination mechanism in the corresponding voltage range. When fitting $R_{rec}A$ measured at open-circuit condition (red triangles in Fig. 7.28 (a)) a steeper slope is observed with $\beta_{OC} = 0.64$.

The chemical capacitance C_μ/A (see Fig. 7.28 (b)) exhibits almost no voltage-dependence up to the V_{oc}—contradicting the observations for P3HT:PCBM cells.[402] In the polymer cells, C_μ/A is found to follow an exponential behavior in the high voltage range up to V_{oc}, namely $C_\mu = C_0 \exp(\alpha\, V_{oc}/k_B\, T)$ with $\alpha \approx 0.34$, which is attributed to the carrier occupation of electronic density of states.[348] In contrast, the results shown here indicate that the DOS contribution to the chemical capacitance does not seem to play an important role. Instead, C_μ is primarily determined by the geometric capacitance, extracted from dark C-V measurement at reverse bias where the injected charge can be neglected. A steep increase of C_μ is observed only for voltages above V_{oc}. Altogether, the bulk charge density within DIP/C_{60} PHJ devices seems to be independent of voltage—at least up to V_{oc}—and shows only week dependence on light intensity. This indicates that most of the charges reside on the electrodes—in contrast to various polymer-fullerene BHJ devices where the majority of charges is located within the photoactive layer.[169,402,410] Interestingly, similar results were reported by Credgington *et al.* upon charge extraction measurements on a Pen/C_{60} PHJ device,[411] suggesting that this observation can be seen as peculiarity of PHJ cells based on small molecular materials. It becomes conceivable if assuming unhindered charge carrier transport within extraordinarily crystalline layers of pure material which leads to fast removal of charges out of the photoactive material.

The series resistance is observed to vary only within a limited range ($R_S A \approx$ 2–7 $\Omega\,cm^2$, see Fig. 7.28 (c)), exhibiting values which are small compared to polymer cells.[402] The fact, that $R_S A$ is almost constant over the whole voltage range suggests that it can mainly be ascribed to cable and contact (especially ITO) contributions—rather than to transport and interfacial effects as was stated for P3HT:PCBM devices.[402]

Based on the extracted values for $R_{rec}\,A$ and β, the recombination current can be calculated according to Eq. (7.16) and (7.17). A comparison between the measured and calculated values for j_{sc} is shown in Fig. 7.29. Very good correlations can be

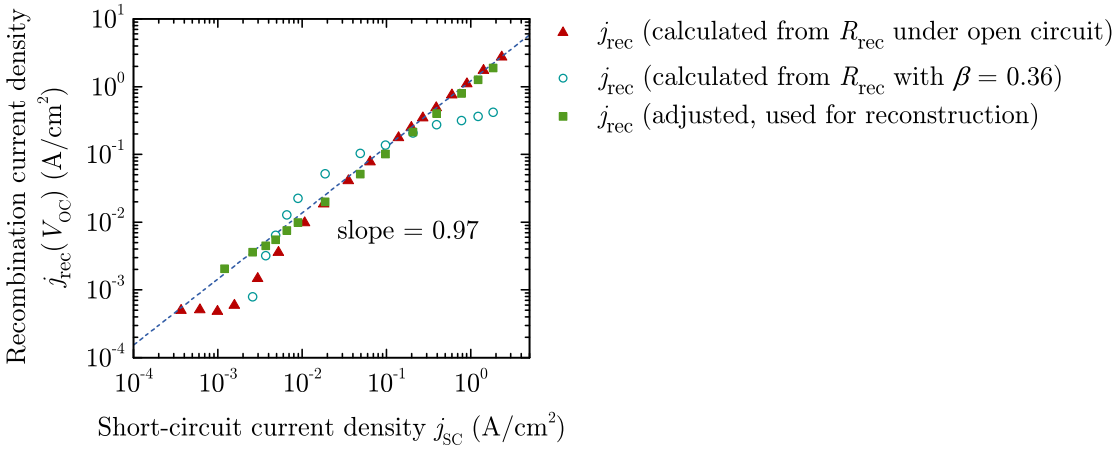

Figure 7.29.: (a) Recombination current density calculated by Eq. (7.17) determined for different irradiation intensities and $\beta = 0.36$ as function of j_{sc} for a heated DIP/C_{60} PHJ cell. Calculated values (blue circles) would not match j_{sc}—instead, adjusted values (green squares) were used for reconstruction.

found between j_{sc} extracted from measured j-V curves and $j_{rec}(V_{oc})$ calculated from R_{rec} under open circuit (red triangles). At high voltages the slope reaches almost unity which agrees with the hypothesis that $j_{rec}(V_{oc}) = j_{ph}$—confirming the basic idea of a constant photocurrent which is balanced by j_{rec} at V_{oc}. In the low-voltage regime Eq. (7.17) seems to underestimate the value for j_{rec}.

However, when calculating $j_{rec}(V_{oc})$ from R_{rec} at the different light intensities with a common β of 0.36 the values show comparatively strong variations around the bisector which would yield partly over-, partly underestimated values of j_{ph} (blue circles). The reason for the deviation can be found in the imperfect collapse of the voltage-dependent recombination resistances at different light intensities as can be seen in Fig. 7.28 (a). While the best fit line perfectly matches the slope in the exponential region only for a few medium light intensities, curves for lower light intensities are steeper while high intensity curves are flatter. This leads to the mentioned deviations and requires the adjustment of j_{ph} for the reconstruction of the j-V characteristics (green squares).

According to Eq. (7.18) and (7.19), the device resistances $R_{rec}\,A$ and $R_S A$ together with the fit parameter β (all solely extracted from IS data) suffice to reconstruct the whole j-V curves. Figure 7.30 (a) shows the results and demonstrates that relatively good correlation between the experimentally determined (lines) and the reconstructed (symbols) current-voltage characteristics can only be found for high light intensities (lower panel) whereas significant deviations are found for low light intensities (upper panel). As was demonstrated in Sec. 2.1.6 the slope near j_{sc} is indicative of the presence of a finite parallel resistance R_P (cf. simulated curves

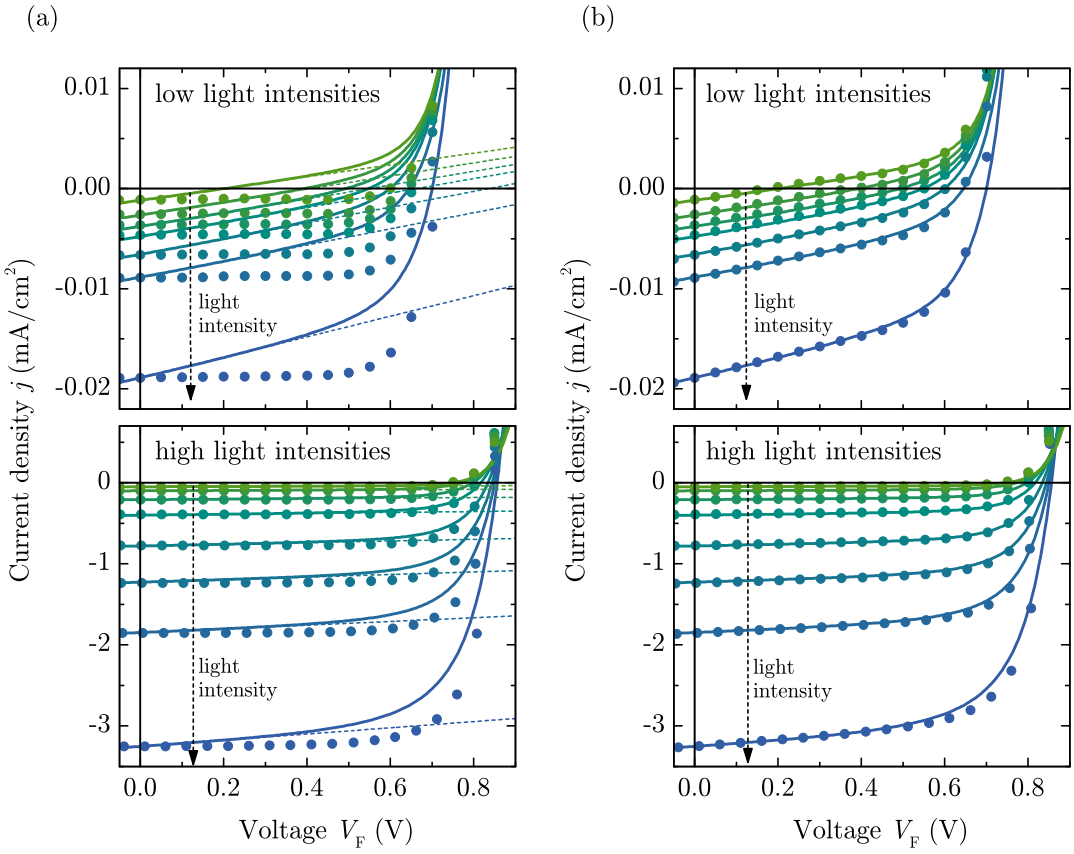

Figure 7.30.: (a) Reconstructed j-V curves (symbols) in comparison to their experimentally determined counterparts (lines) at different low and high light intensities (upper and lower row, respectively) for a heated DIP/C_{60} PHJ solar cell. Voltage is corrected for series resistance drop as $V_F = V_{app} - j\,R_S A$. The reconstructed curves are based on recombination current determined at each illumination intensity and $\beta = 0.36$ (cf. Fig. 7.28). (b) Only by accounting for $R_P A$ and $R_{ph}\,A$ (see linear fits around 0 V in (a) for determination, dashed lines) good agreement between measurement and reconstruction is achieved.

in Fig. 2.5 (b)). The effect of a shunt resistance can be traced back to manufacturing imperfections causing an alternate current path and is expected to play a larger role at low light intensities. It can be extracted from the dark j-V curve at $V = 0\,\mathrm{V}$ and is determined to $R_P A = 740\,\mathrm{k\Omega}$. However, considering $R_P A$ for the reconstruction from IS data for all light intensities does not lead to significant improvements in reproducing the measurement data. This points to an additional voltage dependent loss pathway which is modeled by a second parallel resistance R_{ph}—determined by the slope $\frac{1}{A}\,\frac{\partial V}{\partial j}\Big|_{V=0}$ of the light j-V curves (see dashed lines in Fig. 7.30 (a)).

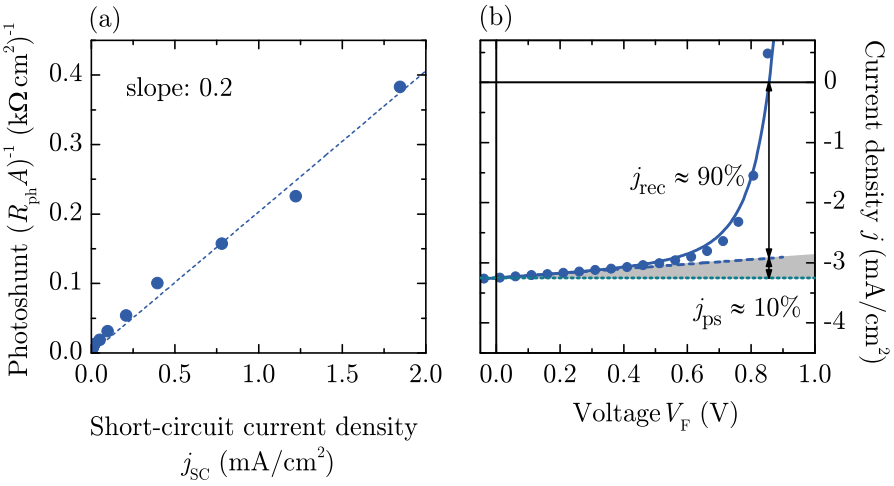

Figure 7.31.: (a) "Photoshunt" (slope $\frac{1}{A}\left.\frac{\partial V}{\partial j}\right|_{V=0}$ of j-V curves depicted in Fig. 7.30) in dependence on the respective short-circuit current (which, in turn, follows a power law $j_{sc} \propto I^{\alpha}$ with I being the light intensity and an exponent α very close to one). A parallel shunt resistance of 740 kΩ, determined from the dark curve at $V = 0$ V, has been taken into account for all light intensities. (b) Reconstruction at highest illumination intensity illustrating the relative contributions of the current j_{ps} due to a "photoshunt" R_{ph} and the recombination current j_{rec}. Both contributions are considered relative to a constant flux at $V = 0$ V.

Based on the modified Shockley equation (7.9) both parallel resistances, i.e., R_P (shunt resistance, measured from dark curve at $V = 0$ V, independent of illumination intensity) and R_{ph} ("photoshunt", determined by slope $\frac{1}{A}\left.\frac{\partial V}{\partial j}\right|_{V=0}$ of light j-Vcurves), can be incorporated into the formula for reconstruction:

$$j(V_F) \approx \underbrace{j_0 \cdot \exp\left(\beta \frac{eV_F}{k_B T}\right)}_{j_{rec}(V_F)} + \frac{V_F}{R_P A} + \frac{V_F}{R_{ph} A} - \underbrace{j_{ph}}_{j_{rec}(V_{oc})} \tag{7.20}$$

By taking both parallel resistances into account excellent agreement to the measurement data is achieved (see Fig. 7.30 (b)).

Figure 7.31 (a) depicts $(R_{ph}A)^{-1}$ in dependence on the respective short-circuit current (which, in turn, follows a power law $j_{sc} \propto I_L^{\alpha}$ with I_L being the light intensity and an exponent α very close to one as was shown in Sec. 7.1.1, Fig. 7.8 (c)). From this, it can be deduced that the voltage dependent contribution to the current as modeled by R_{ph} scales approximately linearly with light intensity. Very recently, Credgington *et al.* reported on a similar observation: Based on charge extraction and transient photovoltage spectroscopy applied to solution-processed,

small molecule solar cells they could identify a field-dependent recombination profile, which was assigned to a geminate contribution to the recombination current.[170] The analysis even allowed them to quantify that approximately 70% of the loss of photocurrent at open-circuit relative to the short-circuit current results from non-geminate recombination and approximately 30% from geminate recombination losses. Based on their results a possible origin of the current due to the "photoshunt" R_{ph} could be found in voltage-dependent geminate recombination. When moving the operation condition from short circuit to open circuit the reduction in internal field might affect the dissociation efficiency of photogenerated charge carriers—leading to a voltage dependence of geminate recombination. This possibility stands in contradiction to the assumption of a constant photocurrent j_{ph} which was assumed in the beginning of this section (see Fig. 7.26) and which is currently subject of significant controversy as already mentioned in Sec. 2.3.1. The existence of field-dependent dissociation[30] is supported by a range of studies,[28,340,412–415] however, other authors report on a negligible dependence of geminate recombination on the applied electric field.[24,189,410,416–421]
If considering the origin of R_{ph} to be found in a field-dependent geminate recombination a similar estimation of both contributions can be made as found in Ref. 170—however, the present IS method does not allow for a distinction between geminate and non-geminate recombination for the j_{rec} contribution. From reconstruction at the highest light intensity the relative contribution of the current j_{ps} due to a "photoshunt" R_{ph} (geminate recombination) can be estimated to be approximately 10% while the recombination current j_{rec} as determined from IS data takes over for the largest part of the current losses at open-circuit (see Fig. 7.31 (b)). Both contributions are considered relative to a constant flux at $V = 0\,\mathrm{V}$.

The disadvantage of this method is that the j-V reconstruction is no longer solely based on values gained by IS but contains information of the measured j-V characteristics itself. For this reason a modified EC was established which accounts for the "photoshunt" by introducing an additional parallel resistance R_{ph} as shown in Fig. 7.32 (a). Exemplarily, the fit was applied to impedance data measured at a medium illumination intensity. As can be seen in Fig. 7.32 (b) the "photoshunt" is constant up to a voltage of approximately 0.8 V with a value of $7\,\mathrm{k\Omega\,cm^2}$—similar to the value extracted from the fit around $V = 0\,\mathrm{V}$. The recombination resistances collapse in the critical voltage region (Fig. 7.32 (c)), leading to the same β of 0.36. However, by taking R_{ph} into account, the characteristic slope of the j-V curve can be correctly described (see Fig. 7.32 (d)). Nevertheless, fitting the IS data with the modified EC becomes ambiguous and reasonable fit results can only be achieved for fixed R_{S}.

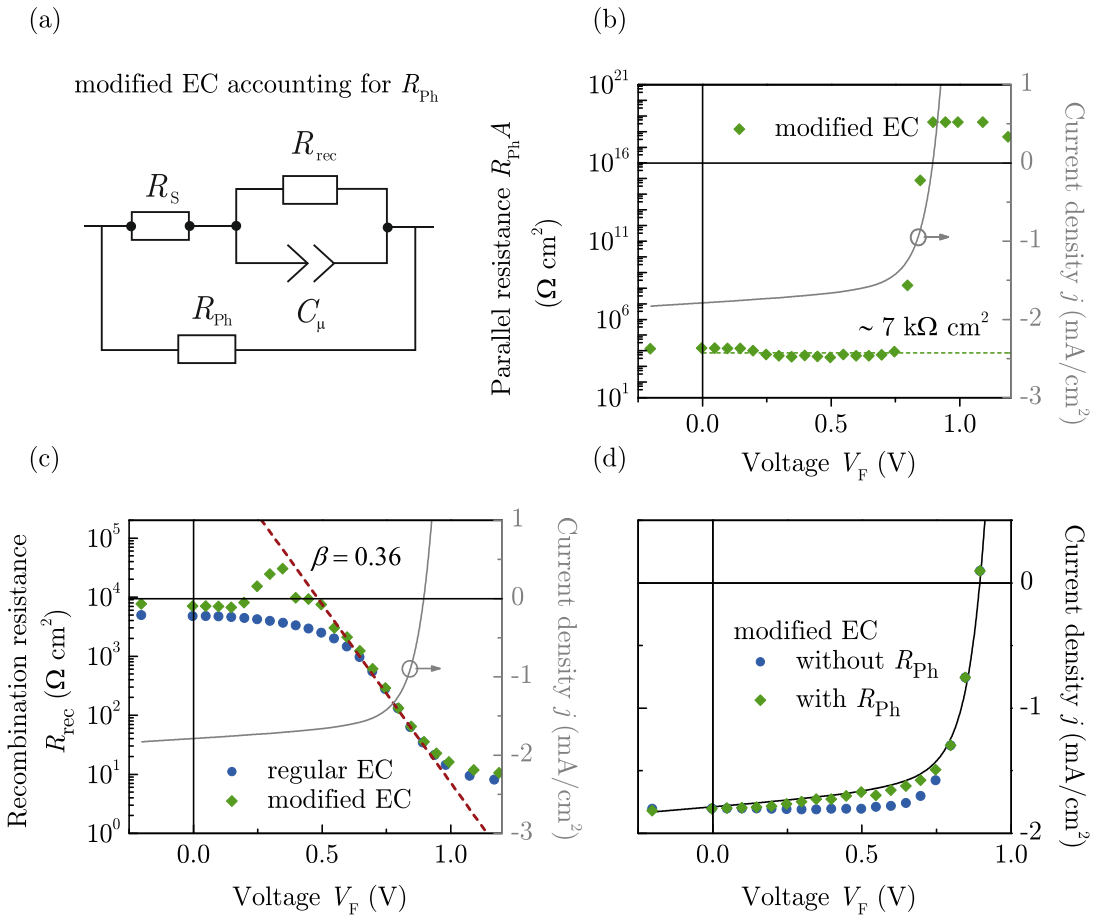

Figure 7.32.: (a) Modified equivalent circuit accounting for an additional parallel resistance R_{Ph}. (b) Specific parallel resistance $R_{\mathrm{Ph}}\,A$ and (c) Recombination resistance R_{rec} extracted from impedance spectroscopy at medium illumination intensity for a heated DIP/C_{60} PHJ solar cell. (d) Reconstructed j-V curve based on the modified EC with and without adding $V_{\mathrm{F}}/(R_{\mathrm{ph}}A)$ to the total current.

Recombination currents of DIP/C_{60} PHJ cells with unheated substrate. When changing the fabrication conditions from heated to non-heated substrate during DIP evaporation—while keeping all other parameters constant—j-V curves with pronounced s-shape are observed. As was discussed in Sec. 5.1 this behavior can be ascribed to an increase of the injection barrier between anode and adjacent organic layer as a result of PEDOT with lower work function. Concerning previously presented methods to analyze the recombination behavior of an OPVC, the equivalent of β can be found in the diode ideality factor n and in the dark saturation current j_0. For a DIP/C_{60} PHJ both parameters are not significantly affected by substrate heating as long as the series resistance is not too high to hinder reasonable data analysis according to the Shockley equation (cf. Tab. 7.2).

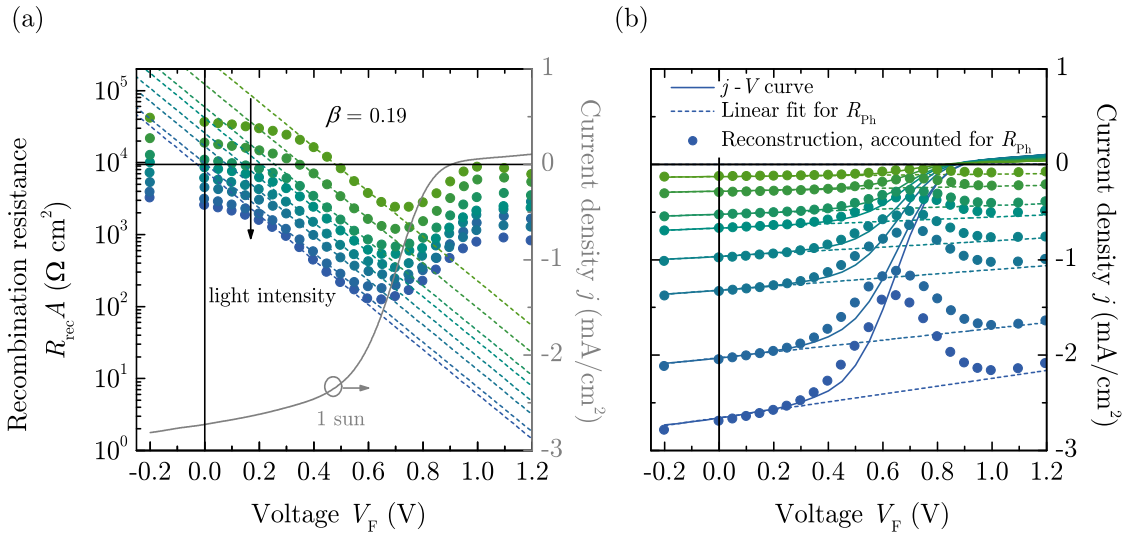

Figure 7.33.: (a) Recombination resistance extracted from impedance spectroscopy at different illumination intensities for a non-heated DIP/C_{60} PHJ solar cell. The voltage is corrected for a potential drop at the series resistance according to Eq. (7.19). (b) Reconstructed j-V curves (symbols) in comparison to their experimentally measured counterparts (lines) based on recombination current determined at each illumination intensity and $\beta = 0.19$. Even by accounting for parallel resistance (see linear fits around $V = 0\,\mathrm{V}$ for determination, dashed lines) strong deviations between measurement and reconstruction are observed.

In order to verify these results, a sample with the following layer sequence was analyzed via IS:

ITO/ PEDOT/ DIP (50 nm, RT)/ C_{60} (50 nm, RT)/ BCP/ Al.

As can be seen in Fig. 7.33 (b) (straight lines), all j-V characteristics measured under different illumination intensities suffer from distinct s-shapes, leading to a reduced slope $\partial j/\partial V$ around V_{oc}—especially at forward bias. The analysis of the recombination current R_{rec} (see Fig. 7.33 (a)) shows constant values at low voltages—but only up to $V_F \approx 0.2\,\mathrm{V}$. In contrast to the device with heated substrate (cf. Fig. 7.28 (a)) the curves for different light intensity do not approach each other in the higher voltage range. Instead, they are going parallel and have to be analyzed by individual fits—but with a common β of 0.19. Furthermore, a second increase in R_{rec} is observed for all curves for $V_F > 0.6\,\mathrm{V}$. The chemical capacitance C_μ does not show a significant increase and the series resistance R_S varies within a small region of $0.1 - 2\,\Omega\,\mathrm{cm}^2$—both not shown here.

Based on the IS data the reconstruction of the j-V curves results in relatively good agreement to the measured data only up to $V_F \approx 0.6\,\mathrm{V}$ (by accounting for

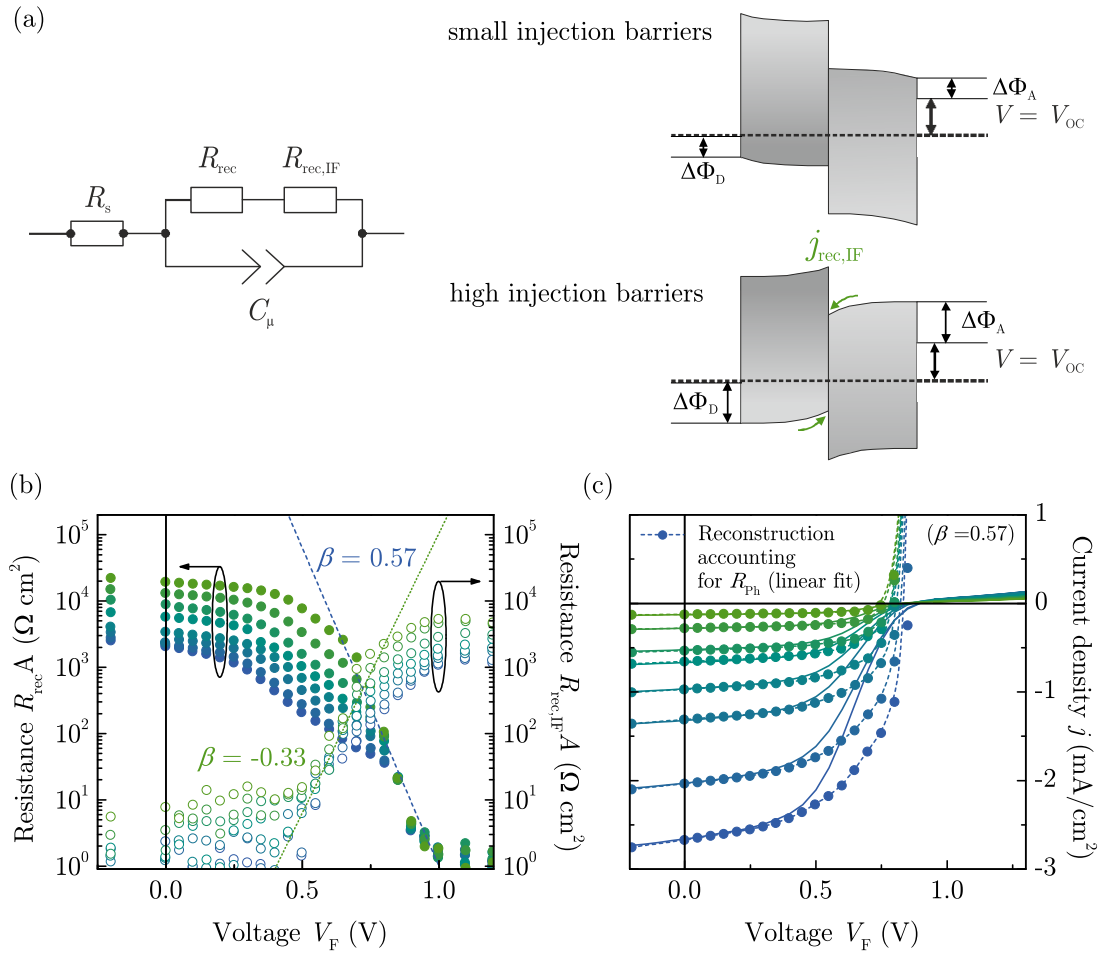

Figure 7.34.: (a) Modified equivalent circuit with two resistances, $R_{\mathrm{rec,inj}}$ and $R_{\mathrm{rec,IF}}$ accounting for injection resistance and recombination at the D/A interface, depending reversely on voltage. The modified EC is based on a band bending model (see schematic) for high injection barriers as adapted from Ref. 422. (b) Recombination and injection resistance extracted from impedance spectroscopy at different illumination intensities based on the modified equivalent circuit for a non-heated DIP/C_{60} PHJ cell. (c) Reconstructed j-V curves (symbols) in comparison to their experimental counterparts (lines) based on recombination current R_{rec} from (b) and $\beta = 0.57$.

R_{P} and R_{ph}, see Fig. 7.33 (b)). However, for higher voltages the reconstructions strongly deviate from the measurement. To account for the increased hole injection barrier between PEDOT and DIP, a modified EC (see Fig. 7.34 (a)) can be used for fitting. An additional resistance $R_{\mathrm{inj,IF}}$ accounts for a recombination current caused by band bending which depends reversely on voltage. The modified EC is based on a drift-diffusion model adapted from Ref. 422 which describes band bending at

a D/A interface in PHJ devices with comparatively high injection barriers from the electrodes to the adjacent organic layers: While the density of photogenerated carriers at the D/A interface is independent of the injection barriers $\Delta\Phi$, the steady-state carrier density is lower in the case of high $\Delta\Phi$, because electrons and holes move towards each other instead of being separated even for flat band condition (schematically shown in right part of Fig. 7.34 (a)). This leads to a higher density of free charge carriers at the interface and subsequently to increased recombination, which is considered by an additional interfacial recombination resistance $R_{\mathrm{rec,IF}}$ within the model.

Figure 7.34 (b) depicts the progress of both recombination resistances: Caused by band bending at the D/A interface $R_{\mathrm{rec,IF}}$ shows small values until $V_{\mathrm{F}} \approx 0.6\,\mathrm{V}$ where it slowly rises as the flux of injected charge carriers form the prevalent recombination current. R_{rec} collapses into a single curve with $\beta = 0.57$, which results in reconstructed j-V curves with high currents in forward direction (cf. Fig. 7.34 (c)). With this method reconstruction of the j-V characteristics as expected without injection barrier becomes possible. However, a complete reconstruction of the curves under consideration of the s-shape has not been established.

On the whole, impedance analysis has been successfully used to determine recombination currents in PHJ solar cells based on DIP/C_{60}. One of the decisive advantages over steady-state measurement results from IS being a differential method which bypasses the influence of constant contributions to the current. The interpretation of the measurement data requires the device to be modeled with a proper equivalent circuit. Thus, by including an additional series resistance, the applied voltage can directly be corrected for R_{S}. By comparing the results on DIP/C_{60} PHJ cells to polymeric BHJ devices as reported in literature, decisive differences were found which might help to identify and understand fundamental differences of both classes of organic semiconductors: In polymeric BHJ cells the chemical capacitance differs significantly from the geometrical value—which can be assigned to a considerable contribution from the bulk charge. By contrast, most of the charge in PHJ cells based on DIP/C_{60} resides on the electrodes. Moreover, for polymeric BHJ cells, a successful reconstruction of illuminated j-V curves is simply based on the assumption of a constant photocurrent which is reduced by a recombination current determined from IS data—in total shaping the cells's j-V behavior.[402] However, a correct reproduction of the measured j-V curves of the DIP/C_{60} PHJ was only possible by introducing an additional "photoshunt", which possibly results from voltage-dependent geminate recombination. Apart from the exact origin of the recombination—be it geminate or non-geminate—it is made clear that its existence significantly influences the shape of the j-V characteristics.

Ideality factor as measure of charge carrier recombination

Understanding and controlling the recombination loss mechanisms is essential for improving the performance of OPVCs—especially since the previous section demonstrated that charge carrier recombination does not only affect V_{oc} but also strongly influences the shape of the j-V curve and therewith the fill factor of the device. Thus, it is of fundamental interest to identify the mechanisms of recombination in order to increase power conversion efficiency. As already addressed in the prevailing sections the diode ideality factor n can serve as useful measure for recombination mechanisms. Based on simulated j-V characteristics, Fig. 2.4 clearly demonstrates the influence of n on the shape of the j-V curve. Concerning the interpretation of the ideality factor, a variety of studies can be found in literature[26,423,424]—all based on charge carrier recombination as dominating factor. Besides the method to determine the ideality factor by fitting the dark j-V characteristics with the Shockley equation or from bias-dependent IS measurements there are several alternative approaches to detect n. Some of those will be presented in the following and their applicability to solar cells based on DIP/C_{60} is evaluated.

Ideality factor determined from derivative of j-V curve. As has already been discussed before, the dark j-V characteristics can be divided into three distinctive regimes (see Fig. 7.35): At negative and small positive voltages, the current is determined by the parallel resistance R_{P}—linearly depending on voltage (ohmic leakage current, I). In an intermediate voltage regime (II), the current is driven by diffusion against the built-in potential V_{bi} and depends exponentially on V. Finally, a deviation from this exponential behavior marks the drift-dominated regime (III) where the current is limited by the series resistance R_{S}. At various parts in the present work, measurement data have been fitted with the modified Shockley equation (5.1) where the diode ideality factor n is a measure of the slope of the exponential regime. In order to prevent erroneous fitting, Wetzelaer *et al.* proposed an alternative determination of n by numerically differentiating the current with respect to V:[425]

$$n = \left(\frac{k_{\mathrm{B}}T}{e} \frac{\partial \ln j}{\partial V} \right)^{-1} . \tag{7.21}$$

The lower part of Fig. 7.35 depicts n as determined by Eq. (7.21). The gray area marks the diffusion regime characterized by a plateau in n, which can be regarded as steepest increase of the exponential regime.

In order to check the accordance between both methods to determine n, i.e., via the Shockley fit and by the derivative, a comparison has been done for the heated PHJ cell based on DIP/C_{60} with layer structure given in Fig. 7.35. Figure 7.36 (a)

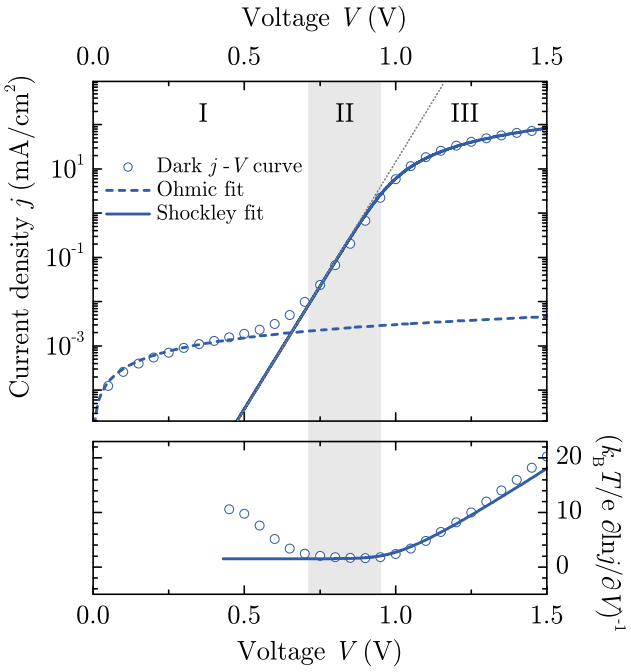

Figure 7.35.: Upper part: Dark j-V characteristics of a PHJ with structure ITO/ PEDOT/ DIP(50 nm, T_{sub} = 100 °C)/ C_{60}(80 nm, T_{sub} = RT)/ BCP/ Al measured at room temperature. The voltage axis is divided into an ohmic (I), diffusion (II) and drift (III) dominated regime. The dashed line describes the linear voltage dependence of the leakage current and the solid line corresponds to the fitted curve in the forward-bias region using the modified Shockley equation (5.1). Lower part: Differential plot of the data (symbols) and the Shockley fit (straight line) according to Eq. (7.21).

depicts the voltage dependence of n determined by Eq. (7.21) for different temperatures. It can be seen that within a wide range of T, the plateau value of n stays constant—in accordance to what has been found in Ref. 425 for double and single-carrier devices. For the deviations at lower temperatures it is referred to the corresponding discussion in Sec. 7.2.1, where it has been found that increasing series resistances which go together with low temperatures gradually restrict the exponential regime. Directly comparing both methods reveals good agreement of n as shown in Fig. 7.36 (b) where even the temperature dependence is almost identical. The plateau value in the high temperature regime is determined to $n = 1.64$ when the ideality factor is extracted from the derivative of the current, and $n = 1.57$ for the analysis with Shockley fit.

Figure 7.37 summarizes typical results of the diode ideality factor n for heated and unheated planar and planar-mixed heterojunction cells based on DIP/C_{60}[v]—

[v]The exact layer sequences as well as the corresponding j-V characteristics under illumination has

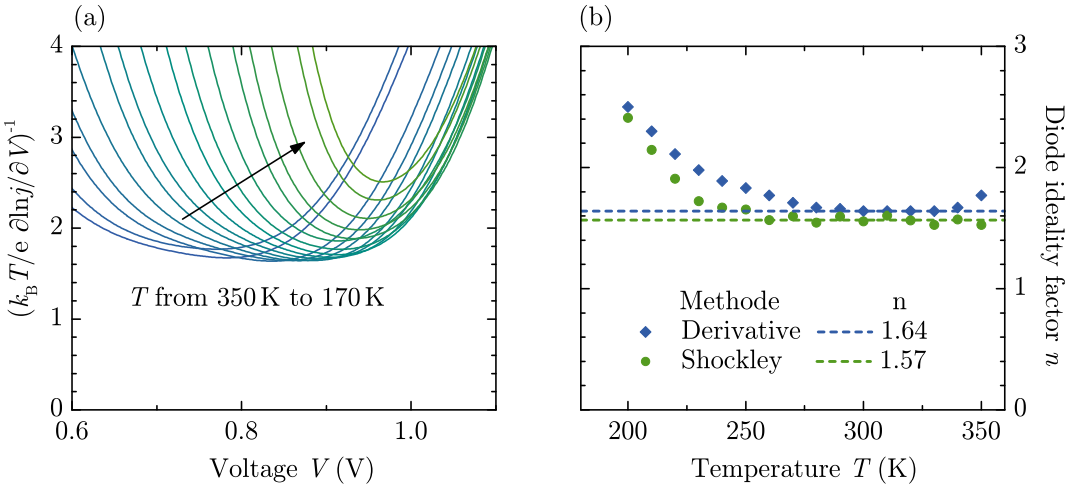

Figure 7.36.: (a) Temperature dependent diode ideality factor of a PHJ shown in Fig. 7.35, determined via the derivative of the dark j-V characteristics according to Eq. (7.21). (b) Comparison between the temperature dependent ideality factor calculated from the derivative and Shockley fit.

determined from the Shockley fit ((a) and (b)) and via the derivative according to Eq. (7.21) ((c) and (d)). The extracted values for the ideality factor are listed in Tab. 7.6. As expected, the ideality factors as deduced from the Shockley fit are similar to those determined from the minimum of the derivative. For a more accurate evaluation according to Eq. (7.21) it would be favorable to record the current within smaller voltage steps. In contrast to other PHJ cells with comparable layer sequence (see, e.g., Tab. 5.1), the ideality factor of the unheated PHJ device seems to be below average, indicating favorable preparation conditions of the PEDOT layer as has been discussed in Sec. 5.1.4. Whereas literature generally agrees in interpreting n in terms of recombination processes, there is an ongoing discussion about the precise classification of the dominant recombination mechanism deduced from the ideality factor: For an ideal pn-diode n is expected to be equal to unity, if charge carrier trapping can be excluded and recombination purely takes place via bimolecular recombination.[423] Based on classic inorganic pn-junctions Sah *et al.* traced a diode ideality factor of $n = 2$ back to trap-assisted recombination[426] (cf. SRH formalism in Sec. 2.3.2). Similar arguments have been used for organic heterojunctions explaining an ideality factor exceeding one by SRH recombination following from the inclusion of disorder which is manifested by an exponential tail of localized states in the DOS of electrons and holes.[171]

When comparing the ideality factors of planar and planar-mixed heterojunction cells based on DIP/C_{60}—including all investigated devices presented within

been shown in Fig. 7.8 on page 156.

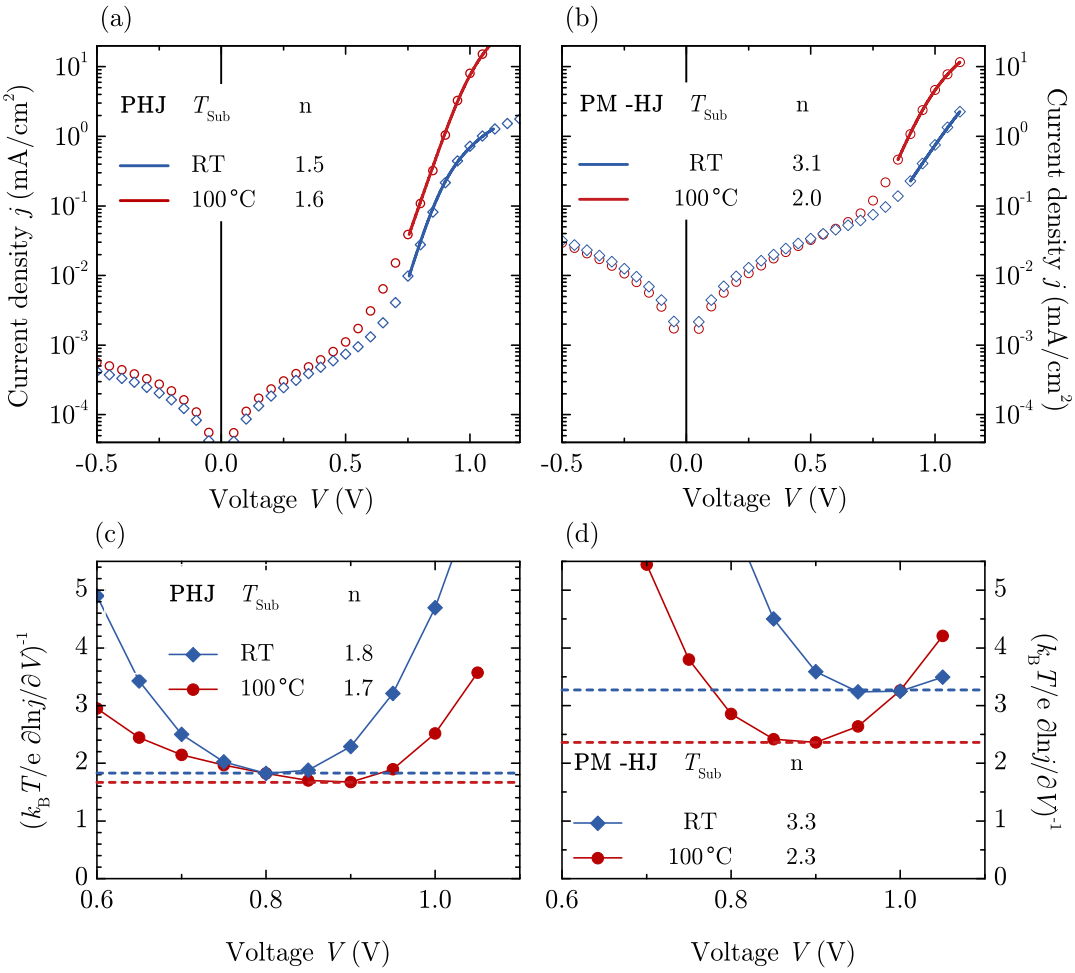

Figure 7.37.: Dark current density vs. voltage characteristics of (a) PHJ and (b) PM-HJ devices with different architecture (light curves depicted in Fig. 7.8). The organic layers were either deposited on unheated substrates or on heated ones with substrate temperature of 100 °C during DIP evaporation (as neat or mixed film). The exact layer sequences are given in Tab. 7.2 on page 156.

different chapters of the present thesis—generally lower ideality factors around $n \approx 1.5$ are found for PHJs while PM-HJ devices are characterized by somewhat higher values of $n \approx 2$. This general trend is especially significant when comparing heated devices, where the influence of energy level misalignment and unfavorable small-scale phase separation can be excluded. According to the above stated interpretations, trap-assisted SRH recombination seems to play a role—both in the planar as well as in the planar-mixed heterojunction. Whereas a combination of bimolecular recombination of the Langevin type and SRH recombination can be deduced from the PHJ ideality factor of $n = 1.5$, purely trap-assisted recombina-

tion is expected in PM-HJ cells, which might result from interfacial defects/traps due to incomplete phase separation in the BHJ. In contrast, the generation of free charge carriers within a planar heterojunction device is restricted to a small area along the D/A interface. IS measurements of the chemical capacitance (see first part of this section) indicate that in DIP/C_{60} PHJ cells most of the charges reside on the electrodes which, in turn, confirm the concept of unhindered transport of photogenerated majority charge carriers through a film with low density of minority carriers. Finally, this leads to longer charge carrier lifetimes and reduced recombination rates. Any larger ideality factors that are observed cannot be explained directly. Kirchartz *et al.* provide a possible explanation of $n > 2$ by recombination of two carriers that are both trapped leading to tail-to-tail recombination.[171] However, in various discussions of this work, it has been stressed that reliable determination of n require at the same time low leakage and high drift currents, which otherwise mask the diffusion dominated exponential current regime (see, e.g., Sec. 7.2.1).

Comparing the PHJ cells with different batches of DIP as presented in Sec. 6.3, it is striking that both parameters—the diode ideality factor n as well as the dark saturation current j_0—are observed to increase significantly when comparing batch 2 to batch 1. At the same time mass spectrometry measurements of the different DIP batches revealed that the impurity content of batch 2 is around twice as much as compared to batch 1. This observation confirms that the addition of trap states by higher impurity levels increases the probability of trap-assisted recombination which reduces the "quality" of the diodes—manifested in increasing n and j_0.

The light ideality factor n^*. In accordance to the above mentioned interpretation of the ideality factor, it has been shown by Wetzelaer *et al.* that the non-ideality of n when deduced from dark j-V measurements can be ascribed to deeply trapped carriers—however, this effect is partly neutralized under illumination.[423] According to these considerations an ideality factor determined from light characteristics would provide a more reliable indication of the recombination mechanism dominant in an operating solar cell. A light ideality factor can either be determined from voltage dependent luminance measurements,[425] or from the slope of the dependence of V_{oc} on the logarithm of the light intensity, that scales linearly with j_{ph}.[415] The latter is based on Eq. (2.8) and defines the light ideality factor n^* as

$$V_{oc} = n^* \frac{k_B T}{e} \ln\left(\frac{j_{sc}}{j_0} + 1\right), \tag{7.22}$$

by equating the photogenerated current density j_{ph} with j_{sc}. The accuracy of this method might be limited when high series resistances of the cell would require to

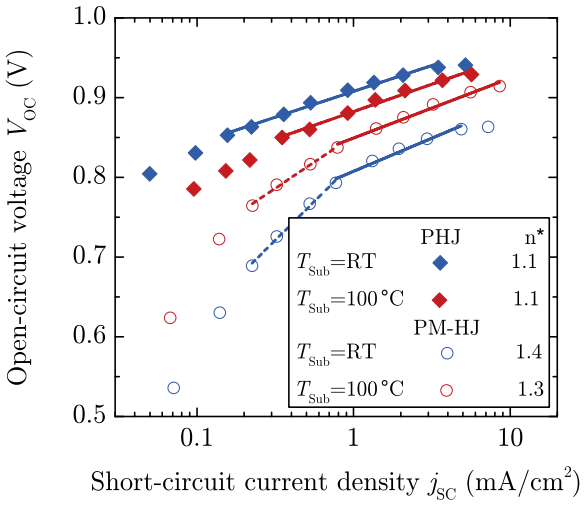

Figure 7.38.: V_{oc} vs. j_{sc} for planar and planar-mixed heterojunction solar cell based on DIP/C_{60} (light curves depicted in Fig. 7.8). According to Eq. (7.22), the light ideality factor n^* can be extracted from the slope of the linear fit.

consider R_S for a correct extraction of V_{oc}.[427]

Following this concept, PHJ and PM-HJ cells based on DIP/C_{60} were analyzed and results are shown in Fig. 7.38. While a linear dependence of V_{oc} on $\ln(j_{sc})$ is found for all devices at high illumination intensities (approximately 1 to 0.1 sun), the PM-HJ devices show a bending at lower intensities. A similar effect has been observed by Zhang *et al.* for small molecule BHJ solar cells—ascribed to a contribution of the density of free charge carriers in the photoactive layer.[428] However, the following discussion is restricted to the high illumination regime. It is found that the light ideality factors n^* for the PHJ extracted from the linear fit of the semi-logarithmic plot according to Eq. (7.22) are significantly smaller than those of the PM-HJ cells. Compared to the dark ideality factors n, the values determined for n^* are considerably lower in both cases—however, following the same tendency. Similar discrepancies between dark and light ideality factors have been observed for polymer:fullerene BHJ solar cells.[423,429] A possible explanation may be found in Ref. 424, where light intensity dependent charge carrier densities were identified as the reason for a crossover from SRH to bimolecular recombination when comparing light and dark ideality factors: As outlined in Sec. 2.3.2, the recombination rate of SRH mechanism depends linearly on charge carrier density while the rate for bimolecular recombination shows a quadratic dependence on charge carrier density. By increasing the carrier density within the cell, be it by increasing voltage from short circuit to open circuit or by increasing light intensity,[165,410] an enhanced probability of recombination is expected—especially for bimolecular recombination as it shows the stronger dependence on charge density. Thus, higher charge carrier

Table 7.6.: Ideality factors of PHJ and PM-HJ devices with different substrate temperature during evaporation of DIP containing layers (Light j-V curves shown in Fig. 7.8).

Substrate temperature	Shockley fit n	Derivative j-V curve n	V_{oc} vs j_{sc} n^*	IS data $1/\beta$
PHJ—DIP(50 nm, RT/100 °C)/C_{60}(80 nm, RT)				
T_{sub} = RT	1.5	1.8	1.1	
T_{sub} = 100 °C	1.6	1.7	1.1	2.8 (1.6)‡
PM-HJ—DIP(5 nm, RT/100 °C)/DIP:C_{60}(50 nm, RT/100 °C)/C_{60}(10 nm, RT)				
T_{sub} = RT	3.1	3.3	1.4 (3.3)†	
T_{sub} = 100 °C	2.0	2.3	1.3 (2.2)†	

‡ Determined from R_{rec} measured at open circuit or in dark.
† Extracted from the low light intensity region.

densities under illumination can explain smaller light ideality factors n^* because of a greater influence of bimolecular recombination—characterized by $n = 1$. Comparing different cell architectures, the DIP/C_{60} PHJs with a light ideality factor of $n^* \approx 1.1$ gives less indication for trap-assisted recombination than PM-HJ with $n^* \approx 1.4$. This result confirms one decisive advantage of the PHJ concept: Compared to their BHJ counterparts, the lower interfacial area hampers recombination losses which ultimately leads to enhanced charge carrier extraction reflected in high fill factors.

Can β from IS measurements serve as indicator of the prevailing recombination mechanism? By means of IS analysis an exponential dependence of the recombination current on voltage has been found in the voltage regime around V_{oc} as predicted by Bisquert and co-workers—both for dye-sensitized solar cells and organic bulk heterojunctions based on polymers.[347,348,402] However, no explicit correlation between the extracted β-parameter and the prevailing recombination mechanism was established. By contrast, Leong *et al.* showed a similar approach based on the differential resistance—with $\beta_{Leong} = 2 \cdot \beta$ as has been mentioned before—but explicitly identifying β_{Leong} with the recombination order parameter.[406] Even though these differences might suggest a contradiction, an agreement between both approaches is found when identifying β with the inverse of the diode ideality factor n. Assuming $n = 1$ indicates second-order ($\kappa = 2$)

bimolecular recombination, the corresponding parameters would be $\beta = 1/n = 1$ and $\beta_{\mathrm{Leong}} = \kappa = 2$. Similarly, first-order ($\kappa = 1$) SRH recombination, which is equated with $n = 2$ yields $\beta = 1/n = 0.5$ and $\beta_{\mathrm{Leong}} = \kappa = 1$.
For the heated DIP/C_{60} PHJ, $1/\beta$ seems to be overestimated when determined from a common fit of the voltage dependent recombination resistance according to Fig. 7.28 (a). When $1/\beta$ is determined from IS measurements under open circuit or in dark, the value is in good agreement with the dark ideality factor n, e.g., extracted by means of the Shockley equation. In any case, the discrepancies between $1/\beta$ and n indicate the necessity to have a critical look at the concept underlying the correlation between β and the recombination resistance. Intentionally introducing charge carrier traps—e.g. by doping of the organic layer—could be one possibility to specifically examine the relation between β as determined by IS measurements and its exact meaning in terms of carrier recombination. As a result of intentional doping, SRH recombination would be expected as predominant recombination mechanism allowing to observe its direct impact on R_{rec}.

To sum up, it has been experimentally verified that recombination losses play a crucial role in device performance, however, an unambiguous identification of the prevailing recombination mechanism has not been investigated in more detail within the scope of the present thesis. Nevertheless, it seems to be a hot topic within current research and would be worth to concentrate on in further studies.

Chapter 8

The top contact

Up to now, the presented studies concentrated on the anode/organic interface, charge carrier transport inside the donor, and finally the donor/acceptor interface. This last chapter will briefly present some investigations carried out on the top contact—including the effect of exciton blocking layers in DIP/C_{60} planar heterojunctions. As has been introduced in Sec. 3.1.4, exciton blocking layers (EBLs) have been exploited to increase longevity and were found to mechanically protect the organic layers—along with successfully hindering exciton quenching at the cathode. In the following chapter, two different exciton blockers will be tested regarding their preferable thickness for optimum device performance as well as their impact on long-term stability. Finally, variations of the metal cathode will be presented including the difference of Sm and Al as top contact and their interplay with the exciton blocking layer BCP.[w]

8.1. Thickness effects of different exciton blocking layers

As has been mentioned in Sec. 3.1.4, BCP is one of the most common exciton blocking materials in OPVCs. Its large bandgap of $E_g \approx 4.7\,\text{eV}$ enables efficient exciton quenching at the organic/cathode contact. As LiF performed worse than BCP when used as EBL in DIP/C_{60} solar cells (see Sec. 5.1.3), it has been replaced

[w]The main results of the second section of this chapter have been published in Ref. 328.

by BCP in the further course of this work. One reason for its limited applicability might be found in its strong sensitivity to the right choice of layer thickness: Owing to its insulating properties, LiF has to be inserted as very thin layer of a few Ångstroms only—otherwise hindering efficient electron extraction (cf. Sec. 3.1.4). In contrast, electron transport through BCP seems to be unhindered, despite of its high lying LUMO which is found to be situated around 2 eV above the LUMO of C_{60}. As sketched in Fig. 3.7 (b) charge transport is supposed to occur via defect states below the LUMO of BCP which are induced by thermal evaporation of the metal top contact.

8.1.1. Degradation effects with BCP as EBL

Concerning the applicability of BCP as exciton blocking layer in solar cells based on DIP/C_{60}, thickness dependent studies have been performed on PHJ devices—including their development over time.

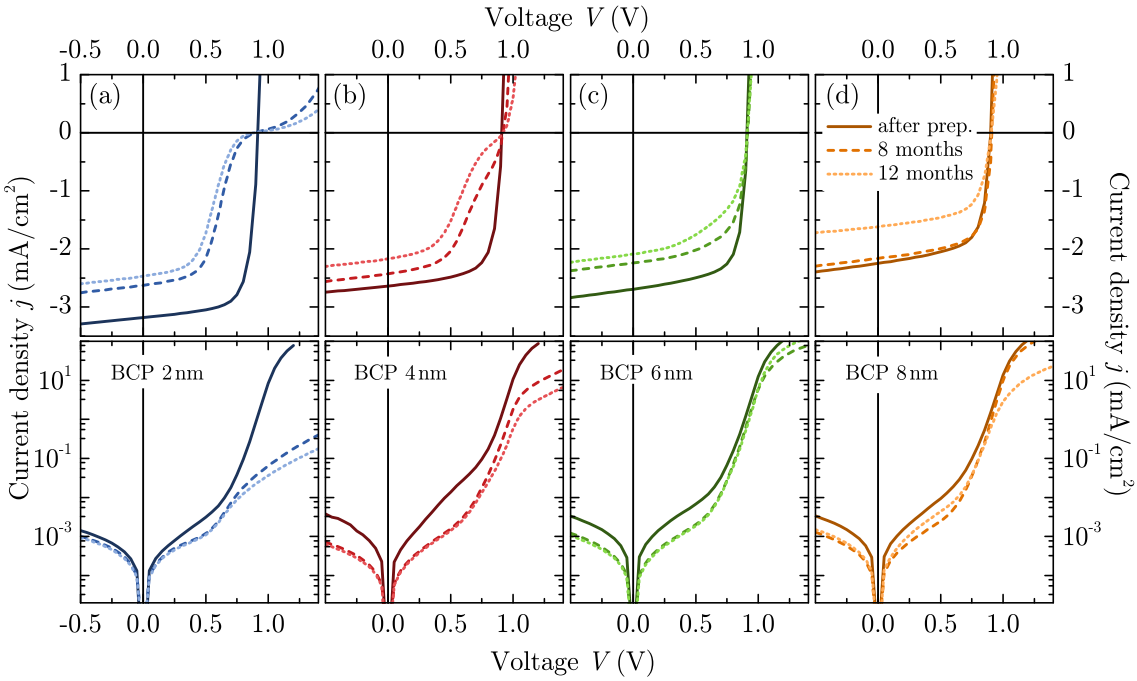

Figure 8.1.: Effect of varying BCP thickness on PHJ solar cells based on DIP/C_{60}. Upper parts: j-V characteristics under white LED illumination. Lower parts: Logarithmic plot of the dark j-V curves—the currents in forward direction are fitted with the Shockley equation and series resistances are extracted. The characteristic cell parameters as well as their development over time are displayed in Fig. 8.2.

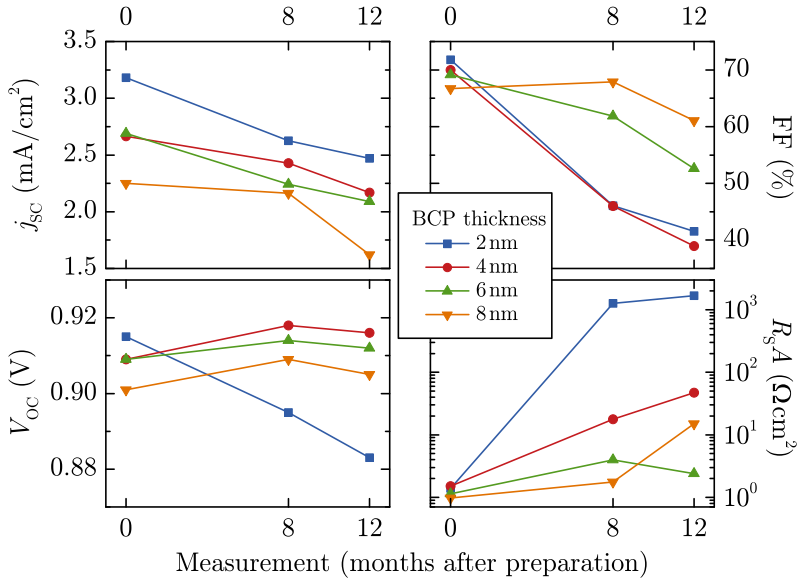

Figure 8.2.: Temporal development of the characteristic cell parameters of PHJ solar cells with varying thickness of BCP inserted as EBL. Short-circuit current density j_{sc}, open-circuit voltage V_{oc} and fill factor FF are extracted from the j-V curves under illumination (upper parts of Fig. 8.1)—the specific series resistance $R_S A$ results from Shockley fits of the dark j-V characteristics (lower parts of Fig. 8.1).

Figure 8.1 shows j-V curves of the devices with structure

ITO/ PEDOT($\approx 30\,\text{nm}$)/ DIP($50\,\text{nm}, 100\,^\circ\text{C}$)/ C_{60}($80\,\text{nm}$, RT)/ BCP/ Al,

with BCP layer thicknesses of 2, 4, 6 and 8 nm. The upper row depicts illuminated j-V curves recorded directly after preparation as well as after 8 and 12 months—stored under inert atmosphere inside the glovebox in dark and without encapsulation. A graphical representation of the characteristic cell parameters and their development over time is shown in Fig. 8.2. Directly after preparation, all BCP layer thicknesses enable cells with high fill factors, which are ascribed to low series resistances as extracted from Shockley fits of the current density in forward direction. With increasing BCP thickness the short-circuit currents are slightly reduced which might be a consequence of limited conductivity through the BCP layer. However, with time passing, the cell with the thinnest BCP layer suffers from increased series resistance—accompanied with significantly reduced fill factors, which might result from insufficient protection against residues of oxygen and moisture or against Al penetration. As this effect strongly depends on the layer thickness of BCP, it seems as if the protective property of BCP is only achieved above a certain thickness. Based on these results, an optimal BCP thickness was

determined to 5–6 nm, which enables reasonable device stability with concurrently high electron-collection efficiency. Similar results were found for solar cells based on CuPc/C_{60} with an optimal layer thickness of 5 nm.[259] The observations agree with studies on OLEDs reporting that a minimum BCP layer thickness of ≈ 6 nm is necessary to form a uniform film.[430]

8.1.2. Degradation effects with NTCDA as EBL

Apart from the undisputed beneficial effect on the device performance of solar cells, one disadvantage of BCP can be seen in its partly observed tendency to crystallize as has been reported in various literature[118,431]—sometimes inducing fast degradation of solar cells.[432] Therefore, alternative materials have been studied as EBL which allow for increased long-term stability.[433–437] Moreover, exciton blockers with improved conductivity have been employed where charge transport does not rely on Al-induced damage but on energy-level alignment. This, in turn, enables the use of thicker EBLs without loosing conductivity.[438]

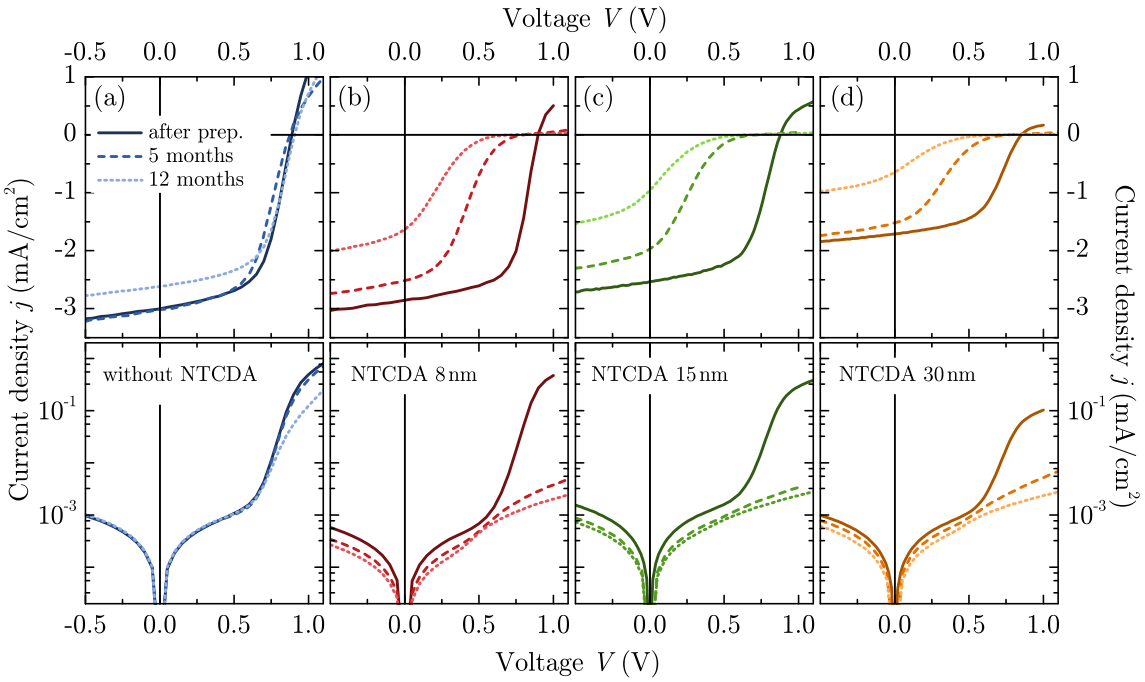

Figure 8.3.: Effect of varying NTCDA thickness on PHJ solar cells based on DIP/C_{60}. Upper parts: j-V characteristics under white LED illumination. Lower parts: Logarithmic plot of the dark j-V curves—the currents in forward direction are fitted with the Shockley equation and series resistances are extracted. The characteristic cell parameters as well as their development over time are displayed in Fig. 8.4.

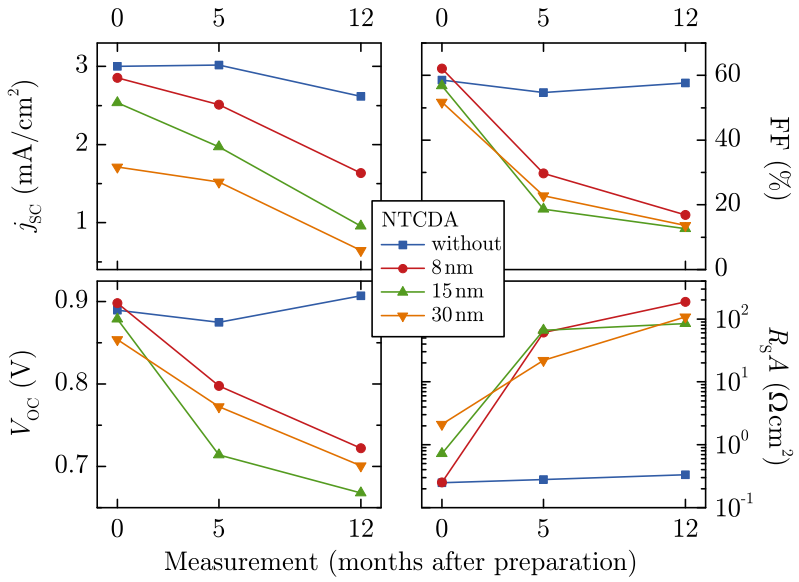

Figure 8.4.: Temporal development of the characteristic cell parameters of PHJ solar cells with varying thickness of NTCDA inserted as EBL. Short-circuit current density j_{sc}, open-circuit voltage V_{oc} and fill factor FF are extracted from the j-V curves under illumination (upper parts of Fig. 8.3)—the specific series resistance R_SA results from Shockley fits of the dark j-V characteristics (lower parts of Fig. 8.3).

Based on these findings, NTCDA has been used as exciton blocking material and studied concerning its effect on solar cell longevity. Planar heterojunctions based on DIP/C_{60} have been investigated—with equal device structure as for the BCP cells in the previous section. The corresponding light and dark j-V characteristics are depicted in Fig. 8.3 and the temporal development of the extracted parameters are summarized in Fig. 8.4. As mentioned in Sec. 3.1.4, studies found in literature suggest that high conductivity of NTCDA and favorable energy level alignment with C_{60} allow for the application of thick layers which accordingly provide a better level of protection against interdiffusion of oxygen and water or damage via metal evaporation. Thus, a thickness variation with 8, 15 and 30 nm of NTCDA has been carried out—compared to a reference cell without blocking layer. According to the thickness variation of BCP, the short-circuit current density is reduced with increasing blocking layer, which already hints towards limited conductivity within the NTCDA film—confirmed by a thickness dependent series resistance. However, in contrast to the results with BCP as exciton blocker, the long-term stability is substantially reduced with increasing NTCDA thickness. These findings indicate that the NTCDA film itself might be responsible for the degradation as its resistivity increases with layer thickness. Investigations on indium-doped NTCDA reveal

high reactivity in atmosphere which result in a strong reduction of conductivity.[439] As opposed to literature, the limited conductivity of NTCDA does not allow for its use as thick, protective exciton blocking layer and no improvement over BCP was found—neither in the cell characteristics recorded after device preparation nor in the devices' long-term stability.

Altogether, the results on different EBLs with varying thickness and their long-term stability finally identified a 5 to 6 nm thick layer of BCP as optimum exciton blocker for the use in DIP/C_{60} based solar cells with Al top contact—a result which has been applied within the course of this work. Very recently, Steindamm *et al.* could show that using an interlayer of the exciton blocking layer bathophenanthroline (BPhen) yield a doubling of the short-circuit current in DIP/C_{60} based PHJ cells with silver as top contact material. The authors could ascribe the positive impact of BPhen to both, an exciton blocking effect at the Ag cathode interface and prevention of metal penetration into the photoactive layer.[440]

8.2. Top contact variations

Beneath their beneficial property to prohibit exciton quenching at the electrode, exciton blocking layers are also known to serve as protection layer for eliminating the creation of Al-induced defect states in C_{60}.[192,257,260] It is known that thermal evaporation of metals on top of organic materials can lead to interdiffusion of metal atoms into the underlying layer and thus to formation of metal clusters inside the organic[441,442] or cathode-induced damage for charge transport.[438] De Castro *et al.* propose that isolated aluminum nanoclusters inside a C_{60} film, which are formed upon evaporation, lead to defect states close to the interface that modify the electric potential drop in the device and thus screen the electric field at the cathode for low forward bias.[346] While the positive effect of BCP as exciton blocking layer in DIP/C_{60} based solar cells seems to be undisputed, it is not clear whether its decisive role is found in its exciton blocking properties or in a protective effect against metal interdiffusion.

In order to discriminate both effects, an alternative metal has been studied as top contact material: With a considerably larger atomic radius compared to aluminum, samarium (Sm) is supposed to show reduced tendency of interdiffusion into an underlying organic film. To investigate the diffusion behavior of Sm into C_{60}, thickness dependent UPS investigations were performed. Figure 8.5 shows the UPS spectra of the interface between Sm and C_{60} with various steps of Sm thickness ranging from approximately 1 Å to 70 Å. The valence region spectra (see Fig. 8.5 (b)) reveal a continuous decrease in intensity of the characteristic C_{60}

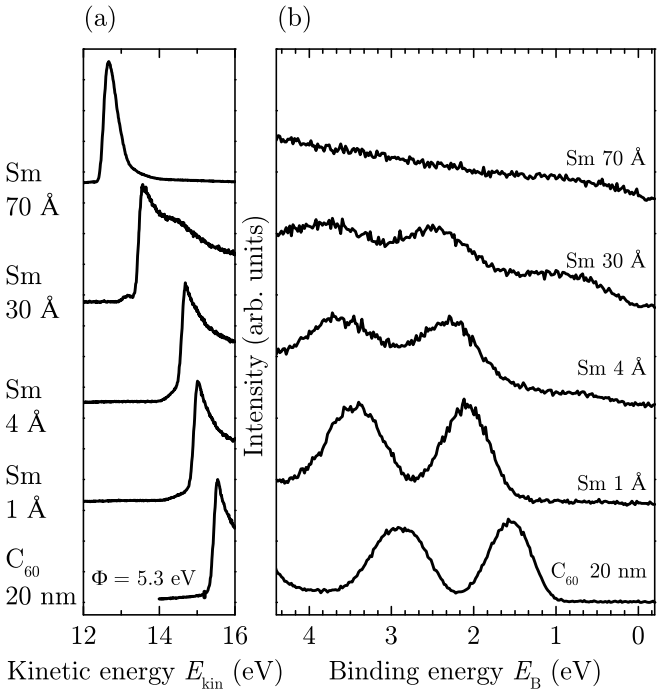

Figure 8.5.: Ultraviolet photoelectron spectra of ITO/HIL1.3/C_{60} substrates with different coverage of Sm. (a) Secondary electron cutoff (SECO) spectrum and (b) valence region spectrum (taken from Ref. 328).

features with increasing Sm coverage, suggesting the formation of a closed film already after a few monolayers.

Based on this result, the protective effect of BCP has been studied in OPVCs comprising the comparison between Al and Sm as cathode material—with and without an interlayer of BCP. The exact layer sequence of the PHJs is

ITO/ (hole injection layer)/ DIP(50 nm)/ C_{60}(50 nm)/ (top contact)

with different top contacts, i.e., with and without BCP (layer thickness 5 nm) covered by Al or Sm. The j-V curves of the corresponding solar cells are shown in Fig. 8.6 (a) for devices with PEDOT as hole injection layer, with the substrate kept at room temperature during DIP evaporation. The photovoltaic parameters are summarized in Tab. 8.1. Independent of the application of BCP, the devices with Sm as top contact exhibit smaller values of j_{sc} than cells with pure Al. Optical transfer matrix calculations for the used device stack comprising a Ca(20 nm)/Al(100 nm) cathode predicts considerably lower photocurrents compared to a pure Al cathode. As Sm shows an even weaker metal reflectance, similar tendencies as for the Ca/Al cathode are expected. Corresponding results can be found in Ref. 443, emphasizing the profound impact of the metal reflectivity on the

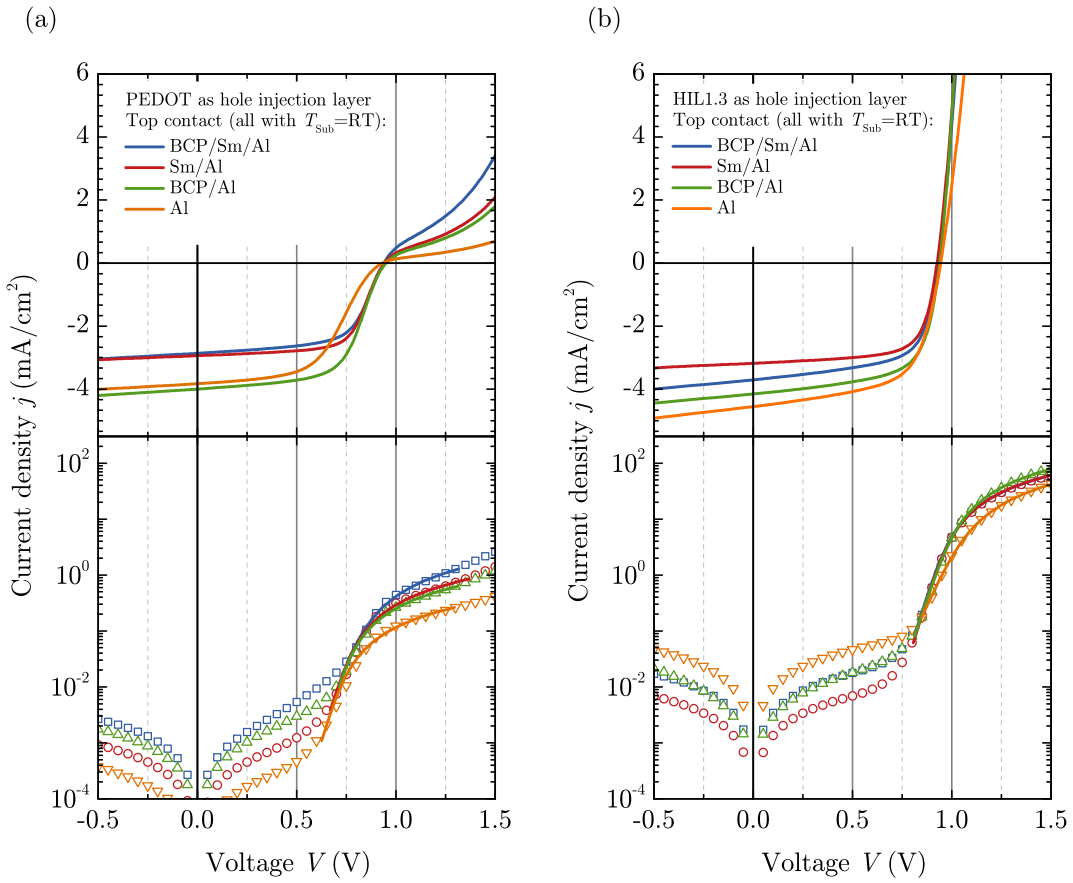

Figure 8.6.: Current voltage characteristics of PHJ solar cells of the structure ITO/ (hole injection layer)/ DIP(50 nm)/ C_{60}(50 nm)/ (top contact) with different top contacts, i.e., with and without BCP(5 nm) covered by Al or Sm (DIP evaporated at room temperature). (a) Devices with PEDOT as hole injection layer, (b) devices with HIL1.3 as hole injection layer. Upper parts: j-V characteristics under white LED illumination. Lower parts: Logarithmic plot of the dark j-V characteristics (open symbols). The solid lines are fits based on the modified diode equation. Results of the fits are given in Tab. 8.1.

electrical field confinement within multilayer device structures. On the whole, the values for the specific series resistances extracted from fits of the Shockley equation are comparatively high. Reasons can be found in enhanced hole injection barriers from the unheated PEDOT as discussed in Sec. 5.1. Nevertheless, devices with Sm as top contact show lower values for $R_S A$ than their counterparts with Al. The most striking variation in the series resistance is observed when BCP is inserted as interlayer underneath Al: $R_S A$ is reduced by a factor of approximately 2.5 from 1.8 kΩ cm^2 to 0.7 kΩ cm^2, whereas the ideality factor stays almost unchanged. This is accompanied by an enhancement of the fill factor from 52% to 61%.

Table 8.1.: Open-circuit voltage V_{oc}, short-circuit current density j_{sc}, fill factor FF, specific series resistance $R_S\,A$, ideality factor n and dark saturation current density j_0 for PHJ solar cells of the structure ITO/ (HIL)/ DIP(50 nm)/ C_{60}(50 nm)/ BCP(5 nm)/ (top contact) with a variation of top contacts—evaporated on different hole injection layers (cf. Fig. 8.6). Light illumination was realized with a white LED. As the LED illumination conditions do not fulfill the AM 1.5 g standards, values for power conversion efficiencies are not specified.

Top contact modification	V_{oc} (V)	j_{sc} (mA/cm^2)	FF (%)	$R_S\,A$ (Ω cm^2)	n	j_0 (mA/cm^2)
PHJ cells – top contact variation and PEDOT as HIL (cf. j-V curves in Fig. 8.6 (a))						
BCP/Sm/Al	0.94	-2.9	62.4	304	2.0	$3.5 \cdot 10^{-9}$
Sm/Al	0.94	-2.9	65.9	590	1.6	$6.2 \cdot 10^{-11}$
BCP/Al	0.94	-3.9	60.8	747	1.4	$4.1 \cdot 10^{-12}$
Al	0.93	-3.8	52.2	1807	1.5	$3.0 \cdot 10^{-11}$
PHJ cells – top contact variation and HIL1.3 as HIL (cf. j-V curves in Fig. 8.6 (b))						
BCP/Sm/Al	0.93	-3.7	64.0	7	1.6	$4.6 \cdot 10^{-11}$
Sm/Al	0.93	-3.2	69.5	7	1.6	$2.3 \cdot 10^{-11}$
BCP/Al	0.94	-4.2	64.2	5	1.7	$3.5 \cdot 10^{-10}$
Al	0.94	-3.7	64.2	9	2.3	$3.0 \cdot 10^{-8}$

Identical variations of the top contact were performed with HIL1.3 as hole injection layer. The j-V curves of the solar cells are shown in Fig.8.6 (b). The open circuit voltages are almost identical for all devices and the short-circuit currents follow the same trend as with PEDOT as hole injection layer. In general, values for the series resistance are two orders of magnitude lower than the devices with PEDOT. In the case of Al-devices, a reduction in $R_S A$ by a factor of three is found when inserting BCP as blocking layer. Even though the relative change is similar to the case with PEDOT as hole injection layer, there is no effect on the fill factor, which stays constant at a value of FF $\approx 64\%$ indicating that it might be limited by other factors like material's purity in this case (see Sec. 6.3). In the ideal case, the cathode should form an ohmic contact to the adjacent electron acceptor, while the holes should be blocked. In this context Brabec *et al.* stated that the interaction between C_{60} and many kinds of metal cathodes is large enough that Fermi level pinning (cf. Sec. 2.2.4) of the C_{60} LUMO takes place for almost all common metal contacts.[139] Regarding the values of the work function this condition seems to be fulfilled for both kinds of top contacts, due to their low values ($\Phi_{Al} \approx 4.3$ eV and

$\Phi_{\mathrm{Sm}} \approx 2.7\,\mathrm{eV}$, cf. Sec. 3.1.5) compared to the LUMO level of the fullerene. However, vacuum deposition of metals does not lead to a well-defined interface between semiconductor and metal film. Penetration of metal atoms or clusters into the organic layer can change the effective work function of the metal compared to a free surface. Nevertheless, the differences in work function do not significantly influence the open-circuit voltage. This is in accordance with the theory extensively discussed in Sec. 7.2.1 stating that V_{oc} is mainly controlled by the energy-level offset at the donor/acceptor heterojunction and nearly invariant on electrodes with different work function values. Similar results have been obtained by Cheyns *et al.*:[405] By means of an analytical model based on the continuity equation, they derive an expression for the open-circuit voltage for planar heterojunction solar cells. It indicates that V_{oc} does not depend on injection barriers and thus on the work functions of the metal contacts. However, extensions of their model show that the work function of the cathode metal leads to changes in the charge carrier concentration profie, which influences the shape of the j-V curve around V_{oc}.

Using PEDOT as hole injection layer, the comparison of Sm or Al as metal top contact and their interplay with the exciton blocking layer BCP clearly reveal that there is no need for an exciton blocking layer when Sm is used as top contact, whereas its usage is indispensable for achieving high FFs with Al as metal cathode. Based on the results from UPS measurements it is expected that samarium—in contrast to aluminum—does not diffuse into C_{60} but, in fact, forms a closed film already after a few monolayers. This emphasizes the protective effect of BCP from metal penetration rather than its role as exciton diffusion barrier. Moreover, it has been shown that by using HIL1.3 as hole injection layer, the series resistances can be reduced by two orders of magnitude compared to the devices with PEDOT—which is in accordance with the observations reported in Sec. 5.2. Concerning the effect of BCP on the solar cells with HIL1.3 and pure Al cathode, there is no measurable influence on the FF, in spite of similar relative changes in $R_{\mathrm{S}}A$ compared to the PEDOT-based samples. From this it can be stated that as long as the series resistance is comparatively low, changes in its value have only a minor effect on the fill factor.

Chapter 9

Summary and Outlook

The aim of this work was to develop a detailed understanding of the correlation between macroscopic parameters, such as growth condition, material choice and type of heterojunction, on the one hand and film structure, energetic alignment and transport properties on the other hand—and, one step further, their impact and significance on solar cell device characteristics. The following section summarizes the main results of this work and gives an outlook on possible extensions and promising future investigations.

9.1. Main results and conclusions

The decisive role of energy level alignment at the bottom contact

Firstly, it should be noted that the comprehensive studies on the donor/acceptor combination DIP/C_{60} can be considered as pioneering work concerning its application in organic photovoltaic cells—at least in this comprehensiveness.[x] The extensive analysis on DIP as donor covers growth studies, energy level alignment as well as charge and exciton transport properties and finally led to its successful application in organic solar cells. The studies emphasize the crucial influence of the substrate temperature during DIP film growth on morphology and overall

[x] Preliminary work on DIP as absorber in OPVCs can be found in Ref. 444.

performance of DIP based photovoltaic cells. Detailed investigations revealed that the positive impact of substrate heating can mostly be attributed to a lowering of the hole injection barrier between the Fermi level of PEDOT and the HOMO of DIP in consequence of increased PEDOT work function—manifested in markedly reduced series resistance. Similar results could be achieved with alternative hole injection materials, which exhibit high initial work functions even without substrate heating. This leads to pinning of the positive polaron level of DIP and ultimately results in low hole injection barriers. Conversely, the studies clearly indicated that non-negligible hole injection barriers at the anode/donor interface can be made responsible for the appearance of s-shaped j-V curves which lead to reduced fill factors.

Charge carrier mobilities in DIP thin films

Transport properties of both excitons and charges are strongly correlated to the crystalline order of the involved materials. By separately studying single-carrier devices of DIP, the identification of the dominant current-limiting mechanism has been possible. Even if the charge carrier mobility is characterized by a strong field dependence, the thickness dependence of the current provides a unique criterion to distinguish different limiting cases. It is has been shown that the electron current in DIP is space-charge limited with an electron mobility of $\mu_{e,0} \approx 2 \cdot 10^{-4}\,\mathrm{cm}^2/\mathrm{Vs}$. The mobility of holes is lower by almost three orders of magnitude. While the ITO/PEDOT contact was found to be injection limiting when DIP is deposited onto the unheated substrate, the current limitation changes to SCLC behavior when the substrate is heated during evaporation of the organic. This observation is in perfect agreement with the barrier lowering for holes observed by UPS measurements. For a correct analysis the results emphasize that a consideration of possibly occurring high series resistances is essential as—depending on the material—they may reach values of up to a few kΩ. In this context, impedance analysis offers the possibility of detecting the voltage drop at the series resistance which can play a significant role for a correct analysis. In conclusion, the combination of steady-state j-V measurements and IS provides a unique method to analyze transport mechanism with supplementary information given by each of the characterization techniques.

Morphology and energetics at the D/A interface

Representing the decisive environment for exciton dissociation and charge carrier recombination, the donor/acceptor interface takes a crucial role in the functional-

ity of an OPVC. As organic semiconductors usually suffer from comparatively low exciton diffusion lengths, the morphology of the active layers is a crucial parameter as it determines the photoactive volume where excitons can be efficiently dissociated. On the other hand, even in a blend with large interfacial area the successful formation of percolation paths in the donor and acceptor material is a prerequisite for efficient charge carrier collection towards the electrodes. Besides a favorable morphology, the energy level alignment at the donor/acceptor interface plays an equally important role as the interfacial energy gap should be as large as possible to maximize V_{oc}—while at the same time exciton dissociation requires a certain energy offset. Thus, a detailed understanding of the correlation between structure, energetics and transport properties is indispensable to achieve favorable conditions for exciton and charge transport in both the donor and acceptor phase and efficient charge carrier separation and extraction at the involved interfaces. Owing to the respective molecular shapes, different growth scenarios have been identified leading to largely different interface morphologies—eventually influencing device performance.

The DIP/C_{60} interface. Planar and bulk heterojunctions of DIP and C_{60} have been analyzed in terms of structure, energetics and solar cell performance. It has been shown that growth at elevated temperature leads to the formation of a cohesive network of large crystalline DIP domains, yielding a large surface area that can be covered with C_{60} molecules in planar heterojunctions. The planar stacking, both with and without substrate heating, is characterized by a pronounced crystallinity of the DIP layer as well as its templating effect which leads to unusually crystalline C_{60} films. The crystallinity of both allows for efficient charge carrier extraction towards the electrodes yielding remarkably high fill factors up to 74% even in simply stacked PHJ devices devoid of doped transport layers. Comparatively low absorption coefficients of neat DIP films are consistent with the upright standing arrangement of the DIP molecules, as the transition dipole moment of the fundamental molecular absorption is aligned along the long molecular axis and thus unfavorably oriented for efficient absorption of light under normal incidence. However, absorption spectra of DIP and C_{60} thin films indicate that the main contribution to light harvesting in a heterojunction device with comparable layer thickness of both materials can be assigned to the fullerene. Coevaporating the molecules without substrate heating leads to small-scale phase separation with reduced charge carrier mobility and hindered transport towards the electrodes. By contrast, mixed films evaporated under substrate heating exhibit large-scale phase separation forming a bicontinuous network of both molecular species, which enables efficient exciton dissociation and charge carrier transport. Apart from fa-

vorable film morphology, one of the greatest potentials of DIP as donor in organic solar cells can be found in its high ionization potential and the favorable energy level alignment with both the PEDOT electrode and the C_{60} acceptor leading to high open-circuit voltages of up to 0.93 V.

The CuPc/F_{16}CuPc interface. In contrast to the phase separation observed in mixtures of the differently shaped DIP and C_{60} molecules, the combination of CuPc with its perfluorinated analogue F_{16}CuPc leads to the formation of a solid solution of both constituents. This molecular mixture is related to the similar sizes and shapes of both molecules and their similar packing motifs in neat films. However, it has been demonstrated that such an intimate mixing is not favorable for charge separation in photovoltaic cells as the primarily formed charge transfer states are Coulombically bound, which tremendously reduces charge carrier collection efficiency. When applied in PHJ devices, the absence of measurable effect upon illumination excludes its suitability as photoactive material combination—however, its property as charge-generation layer offers a possibility to be applied in tandem solar cells.

The CuPc/C_{60} interface. The material system CuPc and C_{60} shows very favorable spectral properties for light harvesting over the whole visible range which surely contributed to its development towards a kind of prototype small molecule OPVC system. However, limitations in the transport properties of this material system were found: Comparatively high crystalline order in thin films of C_{60} has been found when deposited onto DIP, which was assigned to a templating effect. By contrast, structural investigations revealed significantly smaller crystalline domains of C_{60} when evaporated on CuPc which leads to lower charge carrier mobility and less efficient electron transport towards the electrodes. These limitations on charge carrier transport manifests in reduced fill factors and pronounced s-shaped j-V characteristics when applied in PHJ devices. In consequence of the sterically incompatible molecular shape of both constituents, blends of CuPc and C_{60} show nanophase separation on a length-scale of a few ten nanometers, being spatially separated not too far from the expected exciton diffusion range. Thus, charge carrier transport in BHJ solar cells is supposed to be limited by the size of single material domains as the formation of percolation paths towards the electrodes is a necessary prerequisite for efficient charge extraction. Significantly higher dark saturation currents are indicative for stronger recombination losses compared to DIP/C_{60}—ultimately leading to lower fill factors. The comparatively small interfacial energy gap at the CuPc/C_{60} heterojunction limits the maximum achievable open-circuit voltage to approximately 0.5 V. This fact represents the strongest

limitation of this material combination as it originates from an intrinsic material property which can hardly be modified.[y]

General remarks on morphology and energy level alignment at the D/A interface. To conclude, the route towards high-efficiency molecular solar cells still holds many challenges. Even if finding an energetically favorable D/A pair, morphological aspects—both in planar as well as in bulk heterojunctions—can hinder the successful application in solar cell devices. It could be experimentally verified that the control of film morphology is a crucial parameter for device performance as it has strong influence on almost all processes involved in light-to-current conversion in organic solar cells: Transport properties of both excitons and charges are strongly correlated to the crystalline order of the involved materials, having a crucial impact on charge extraction properties manifested in the fill factor of a device. In bulk heterojunctions, the right scale of phase separation—which has to be considered in relation to the exciton diffusion lengths within the respective materials—decides on the successful formation of percolation paths which are indispensable for efficient charge carrier extraction.

Energetics of the charge transfer complex and its role on cell parameters

CT energy as upper limit for V_{oc}. While a certain energy level offset at the D/A interface is essential to enable photo-induced charge transfer between both partners, the introduction of such a heterojunction is accompanied with additional energy losses as compared to an inorganic homojunction cell. In order to find a trade-off between efficient exciton dissociation and minimal loss of photon energy, it is important to gain detailed understanding of the elementary processes determining the relation between CT state and solar cell parameters. It is by now well established in polymer BHJ cells that the energy of the CT state sets an upper limit for the achievable open-circuit voltage, however, the actual V_{oc} in polymer devices at room temperature is typically by about 0.5 V lower than E_{CT} which is ascribed to a sum of radiative and non-radiative recombination losses. For molecular OPV cells, such a general understanding has so far been lacking as there have been no direct spectroscopic signatures of CT states so far. Within this work, a comparative analysis on a series of different molecular D/A combinations has been carried out, which unambiguously confirms the linear dependence of V_{oc} on the

[y] One way to overcome the material-related limitation of the open-circuit voltage can be found in a (partial) fluorination of molecules as has e.g. been demonstrated for fluorinated ZnPc in Ref. 445.

energy of the CT state with a similar offset as found for polymer cells. Although it is important to fully distinguish between forward bias and solar cell operation, it has been shown that the relevance of the charge transfer state is not only restricted to the solar cell operation but plays a significant and partly similar role under LED operation: Beside its role as intermediate state to facilitate exciton dissociation the CT state also acts as interfacial recombination center for both geminate and bimolecular recombination. While it is generally accepted to consider the dark saturation current j_0 as measure for charge carrier recombination, its exact description differs in existing literature. Here, it has been experimentally confirmed that the activation energy of the temperature dependent j_0 can be identified with the energy of the CT state. The results emphasize the necessary prerequisites for highest possible V_{oc} being augmented j_{sc} and E_{CT} while at the same time suppressing j_{00}. This can be practically realized by the search for suitable D/A pairs with efficient light absorption, high interfacial energy gap, and reduced intermolecular electronic coupling.

Spectroscopic signature of the CT state. The direct detection of the CT state requires very sensitive spectroscopic techniques as light emission from CT states in organic devices is comparatively weak and often superimposed by bulk emission from the neat donor or acceptor phases. Their unambiguous detection has thus far only been reported in polymer-fullerene BHJ cells, but not in molecular D/A systems. In this work, CT features of the DIP/C_{60} material system could be detected by means of photothermal deflection spectroscopy and electroluminescence—providing an estimate for the CT state energy at the DIP/C_{60} interface.

Detecting and identifying recombination losses

Charge carrier recombination shaping the j-V curve. Besides its significant influence on V_{oc}, recombination currents in DIP/C_{60} PHJ have been found to strongly impact the shape of the j-V curve as was visualized by impedance spectroscopy. Being a differential technique, it bypasses the influence of constant contributions to the total current and provides a direct measure of the recombination current. Even if field-dependent charge carrier separation cannot be excluded in the DIP/C_{60} PHJ cells, its contribution to the overall recombination losses at V_{oc} is expected to be comparatively small. Pronounced differences have been figured out when compared to polymer BHJ cells: Results of studies on the chemical capacitance indicate that most of the charges reside on the electrodes—which is in contrast to various polymer-fullerene BHJ devices where the majority of charges is

located within the photoactive layer. This pronounced difference to polymer BHJ cells can likely be ascribed to unhindered charge carrier transport within extraordinarily crystalline layers of pure material which leads to fast removal of charges out of the photoactive material. This observation highlights one difficulty arising from the bulk heterojunction concept: in spite of its obvious advantage to facilitate exciton dissociation and charge carrier generation—which is otherwise limited by small exciton diffusion lengths—blends of electronically different materials often show reduced charge carrier mobility as compared to the neat materials and enhanced recombination losses—ultimately reducing the fill factor and open-circuit voltage in solar cells.

Diode ideality factor as measure for recombination mechanism. Following the decisive impact of charge carrier recombination both on V_{oc} and the fill factor, understanding and controlling the recombination loss mechanisms are essential for improving the performance of OPVCs. This requires a fundamental interest to identify the mechanisms of recombination in order to increase power conversion efficiency. In this context, the diode ideality factor n can serve as useful measure for the prevailing recombination mechanism. Different approaches to determine n have been compared to each other and evaluated concerning their applicability to solar cells based on DIP/C_{60}. In line with expectations, ideality factors n extracted from dark j-Vmeasurements yield similar results—while differing from n^* as determined from data recorded under illumination. The deviations can be attributed to the distinct recombination mechanisms depending differently on charge carrier density, which—in turn—is influenced by light intensity. The concrete evaluation of the ideality factor in planar and bulk heterojunction devices based on DIP/C_{60} revealed a certain influence of trap-assisted SRH recombination in both types of architectures, however, its extent in planar heterojunctions has been found to be less pronounced. The small interfacial area and unhindered charge carrier extraction in crystalline PHJ solar cells are made responsible for longer charge carrier lifetimes and reduced recombination rates. By contrast, interfacial defects or traps due to incomplete phase separation in the BHJ lead to enhanced recombination losses.

Benefits of molecular materials over polymeric semiconductors. In this context, molecular semiconductors—if deposited by thermal evaporation—have a major benefit over their polymeric counterparts, as this fabrication technique allows for much more freedom to adjusting the device architecture as compared to solution-processed polymer/fullerene blends. Heterojunctions based on DIP/C_{60} revealed highly crystalline films which typically exhibit lower energetic disorder

compared to polymeric BHJ, allowing for higher mobilities. Strictly planar D/A interfaces might suffer from limited exciton dissociation efficiencies but their smaller interfacial area has been shown to slow down nongeminate recombination losses which enables remarkably high fill factors. Moreover, it has been demonstrated that highly purified materials are indispensable as impurities were identified to enhance recombination losses. This stresses the importance of material purification (e.g. by vacuum sublimation) which facilitates maximized device performance under prevailing energetic and morphological circumstances.

Exciton blocking materials and their role as protection layer.

Finally, the influence of Sm and Al as metal top contacts and their interplay with the exciton blocking layer BCP has been investigated. Measurements showed that Sm—in contrast to Al—does not diffuse into the C_{60} but, in fact, forms a closed film already after a few monolayers. Solar cell characteristics of the used cathode materials with and without an additional layer of BCP reveal the crucial role of BCP as a protective layer which hinders interdiffusion of metal clusters—rather than its role as exciton diffusion barrier. Altogether, the studies emphasize that a careful consideration of both, interfacial effects at the bottom and top contact as well as the photoactive semiconductor itself, is indispensable to achieve highest possible fill factors—and with that highest possible power conversion efficiencies.

9.2. Outlook

The experience and findings gained from the present work imply possible extensions and ideas for further research some of which will be presented in the following.

Tailoring the D/A interface. A variety of results emphasizes the vital impact on solar cell performance emanating from the morphological quality of the D/A interface. However, it is obvious that the vision of tailoring this interface, as indicated in Fig. 2.20, is not straightforward and for sure not possible with one single material combination only. Besides molecular self-assembly and thermodynamically driven phase separation followed so far, there are currently increasing efforts to create artificial phase separation by glancing angle deposition[446–448] or by stamping techniques.[449–451] Preliminary experiments on nanoimprint lithography applied to P3HT/C_{60} and DIP/C_{60} heterojunctions have been carried out within the scope of this work. While the basic feasibility of this technology could be demonstrated, its

successful application with the objective to increase the cell's efficiency still requires dealing with new difficulties arising from modified sample preparation: amongst others the imprint step entails a breaking of the vacuum. Moreover, optimization of diverse parameters such as film thickness, press-in pressure and the appropriate mold profile is currently under investigation.

Taking advantage of planar heterojunctions. Putting aside the pursuit of a deliberately molded interface, advantage can be taken of the benefits arising with planar heterojunctions as has been clearly demonstrated at various parts within the present work. Thus, the search for well-ordered materials with better charge and exciton transport properties could be a viable alternative to the BHJ concept. In this context, preliminary studies using 6T as donor in combination with both C_{60} and DIP as acceptors, show promising results as reported in Ref. 376. There is experimental evidence for the strong impact of growth conditions on film morphology, such as the degree of crystallinity and the dominant molecular orientation, which are expected to have consequences for OPV devices.

DIP as acceptor. DIP has been successfully applied as donor in organic heterojunction solar cells when combined with the acceptor C_{60}. Following a recent approach, DIP can also serve as acceptor, providing particularly enhanced open-circuit voltage and thus an interesting alternative to the almost omnipresent C_{60}.[213] This feature opens up a bunch of new possible D/A combinations, including 6T/DIP, Pen/DIP or even CuPc/DIP, which have partly been introduced within the present thesis. Aside from their bare viability these new material systems appear highly promising and would be worth to be studied systematically.

Enhanced light harvesting. One of the main obstacles of DIP as photoactive layer can be seen in its poor capability for light absorption, owing to the fact that molecules are mostly standing upright on the substrate with their optical transition dipole moment being aligned parallel to the long molecular axis. Conceivable possibilities to enhance light absorption can therefore be found in suitable growth techniques yielding flat-lying molecules or slightly enhanced degree of disorder in the films. Alternatively, multilayer structures with additional absorber layers could provide supplementary absorption in the near-infrared region of the sunlight spectrum. A similar effect could be achieved by the tandem solar cell concept,[452] which combines two or more sub-cells with different absorption ranges. It obviously provides a very attractive way to improve power conversion efficiencies as it significantly enhances photon absorption by simultaneously summing up the

open-circuit voltages of the individual cells. However, one of the emerging difficulties is the right choice of a suitable recombination layer which is needed in order to prevent build-up of charge at the interface between the sub-cells.

Detecting the CT complex in molecular D/A pairs. The experimental evidence of the CT state has been successfully provided in case of the DIP/C_{60} heterojunction by means of highly sensitive techniques such as photothermal deflection spectroscopy and electroluminescence studies with a cooled near-infrared detector. Following this approach, which is encouraged by promising results from preliminary investigations, similar studies should be transfered to further material systems including 6T/C_{60} and 6T/DIP in order to detect spectroscopic signatures of the respective CT state.

Reducing recombination losses. The present thesis experimentally validated the correlation between E_{CT} and V_{oc} in molecular OPVCs. Apart from radiative recombination losses, which are thermodynamically unavoidable, non-radiative losses can be made responsible for the major part of the voltage loss. This emphasizes the importance to minimize their extent for maximum possible solar cell efficiency. In order to address these requirements it would be of great interest to quantify both radiative and non-radiative losses in dependence of the particular material features, such as molecular orientation, crystallinity or interface morphology. By means of a comparative study on a variety of different D/A systems guidelines could be worked out for achieving V_{oc} as close as possible to the limit for a given material pair.

Spectroscopic identification of the dominant recombination mechanism. Concerning recombination, the presented work emphasizes its tremendous relevance for device performance. However, the methods used here did not allow for an unambiguous spectroscopic detection of the prevailing recombination mechanism, i.e., whether it is geminate or nongeminate. In this context, transient photoconductivity or photovoltage measurements provide information about carrier kinetics and recombination time—employed to identify the magnitude of geminate and nongeminate decay pathways.[411,419] Both are small-perturbation methods and their functionality is based on the fact that geminate decays are based on charge-neutral polaron pairs which are not affected by an electrical field. In the present work, the potential of impedance analysis to identify recombination losses has been pointed out—however, the interpretation of the measurement data is by far not straightforward and requires targeted and consecutive experiments to exploit the full potential of this complex measuring method. A possible approach could be to

find a correlation between controlled parameter changes, e.g. by intentional doping of the photoactive layers, and the subsequent changes in measurement data and associated parameters such as the recombination parameter β.

Benefiting from the peculiarities of molecular materials. Altogether, future studies should deliberately exploit the advantages which arise from small molecules when applied as photoactive semiconductor in organic solar cells. In contrast to their polymeric counterparts, the processing allows for better control of the interface morphology and quality and typical features associated with polymer bulk heterojunctions such as the influence of considerable disorder effects can be considered as minimal. These peculiarities do not only offer new possibilities for cell design but also imply the opportunity to identify crucial features of organic solar cells which are associated with disorder.

Appendix A

Nomenclature

Materials:

Alq_3	tris(8-hydroxyquinolinato)aluminum
BCP	Bathocuproine
CuPc	Protonated copper-phthalocyanine
C_{60}	Buckminsterfullerene
DIP	Diindenoperylene
$F_{16}CuPc$	Perfluorinated copper-phthalocyanine
HIL1.3	Clevios^{TM} HIL1.3 (PEDOT:PSS formulation)
HIl1.3 N	Clevios^{TM} HIL1.3 N (PEDOT:PSS formulation)
ITO	Indium tin oxide
LiF	Lithium-fluoride
NTCDA	Naphthalene-tetracarboxylic-dianhydride
PCBM	[6,6]-phenyl-C_{61}-butyric acid methyl ester
PEDOT	poly(3,4-ethylenedioxythiophene):poly(styrenesulfonate) (PEDOT:PSS)
Pen	Pentacene
P3HT	Poly(3-hexylthiophene-2,5-diyl)
TPD	N, N'-diphenyl-N, N'-bis(3-methylphenyl)- -1,1'-biphenyl-4,4'-diamine
TTF-TCNQ	Tetracyanoquinodimethane-tetrathiafulvalene
α-6T	α-sexithiophene

Experimental techniques:

AFM	Atomic force microscopy
EL	Electroluminescence
GIXD	Grazing incidence X-ray diffraction
IS	Impedance spectroscopy
PDS	Photothermal deflection spectroscopy
PL	Photoluminescence
UPS	Ultraviolet photoelectron spectroscopy
XRS	X-ray scattering
XRR	X-ray reflectivity

Miscellaneous:

BHJ	Bulk heterojunction
CPE	Constant phase element
CT	Charge transfer
DOS	Density of states
EC	Equivalent circuit
EIB	Electron injection barrier
EQE	External quantum efficiency
FF	Fill factor
HIB	Hole injection barrier
HIL	Hole injection layer
HJ	Heterojunction
HOMO	Highest occupied molecular orbital
IP	Ionization potential
IPCE	Incident photon to current efficiency
j-V	Current-voltage
LUMO	Lowest unoccupied molecular orbital
MPP	Maximum power point
OLED	Organic light-emitting diode
OPVC	Organic photovoltaic cell
OSC	Organic semiconductor
PHJ	Planar heterojunction
PM-HJ	Planar-mixed heterojunction
RT	Room temperature
SCLC	Space charge limited current
SQ	Shockley-Queisser
TCLC	Trap charge limited current

Characteristic values:

A	Area
c	Speed of light
C_μ	Chemical capacitance
C_g	Geometric capacitance
D	Vertical domain size
d	Layer thickness
$d_\perp$	Out-of-plane lattice spacing
E_{CT}	Energy of charge transfer state
E_g	Optical energy gap
E_t	Transport gap
E_B^{exc}	Exciton binding energy
E_B^{CT}	Binding energy of CT state
E_F	Fermi energy
E_{vac}	Vacuum level energy
E_{trap}	Energy of trap level
e	Elementary charge
F	Electrical field
G_0	Generation rate of bound polaron-pairs
h	Planck constant
I_L	Light power density
j_{dark}	Current density of a solar cell measured in dark
j_{ph}	Photocurrent density
j_{sc}	Short-circuit current density
j_0	Dark saturation current density
k_B	Boltzmann's constant
N_A	Doping density
N_c	Density of states at transport level
N_t	Trap density
n	Ideality factor
q_{xy}	Momentum transfer parallel to the sample plane
q_z	Momentum transfer perpendicular to the sample plane
R_{bi}	Bimolecular recombination rate
R_{mono}	Monomolecular recombination rate
$R_P A$	Specific parallel resistance
R_{rec}	Recombination resistance
$R_S A$	Specific series resistance
r_C	Coulomb radius
T_{sub}	Substrate temperature
V_{bi}	Built-in voltage
V_F	Voltage corrected for potential drop at a series resistance
V_{oc}	Open-circuit voltage

Symbols:

η	Power conversion efficiency
η_{int}	Internal quantum efficiency
ρ	Charge carrier density
μ	Charge carrier mobility
Φ	Work function
χ	Electron affinity
Δ	Vacuum level shift
γ	Field activation parameter (SCLC)
τ	Lifetime
ε_{r}	Dielectric constant
ε_0	Permittivity of free space
λ	Wavelength
$\mathscr{V}$	Applied voltage corrected for the built-in potential
γ	Langevin recombination strength
κ	Order of recombination

Appendix B

Temperature dependent measurements

B.1. DIP($T_{\mathrm{sub}} = \mathrm{RT}$)/$C_{60}$

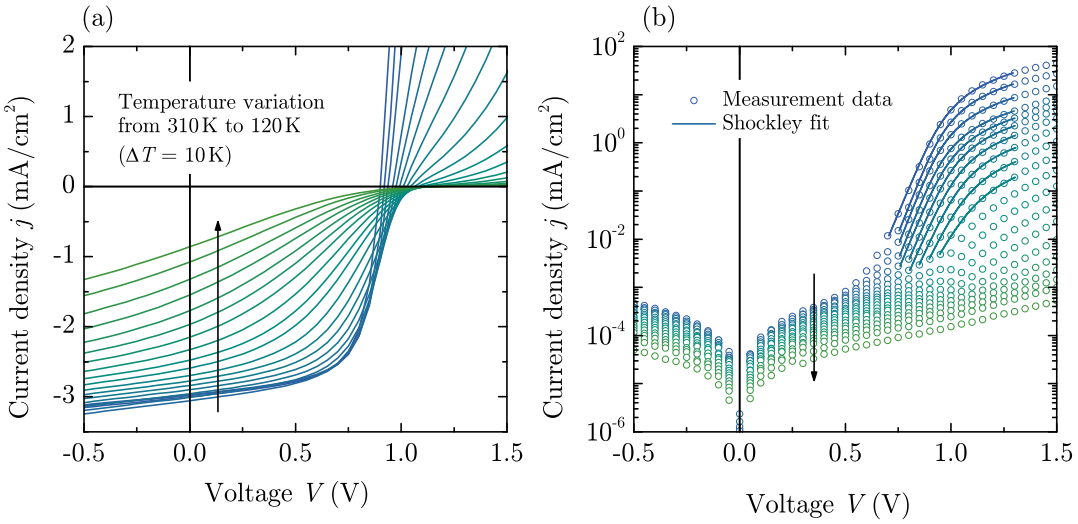

Figure B.1.: j-V characteristics of a planar heterojunction solar cell under white LED illumination in the temperature range 120 K $\leq T \leq$ 310 K. The device has the following structure: ITO/ PEDOT/ DIP(50 nm, T_{sub} = RT)/ C_{60}(80 nm)/ BCP(5 nm)/ Al (a) under white LED illumination and (b) in dark. Solid lines are fits in the forward-bias region using the Shockley equation.

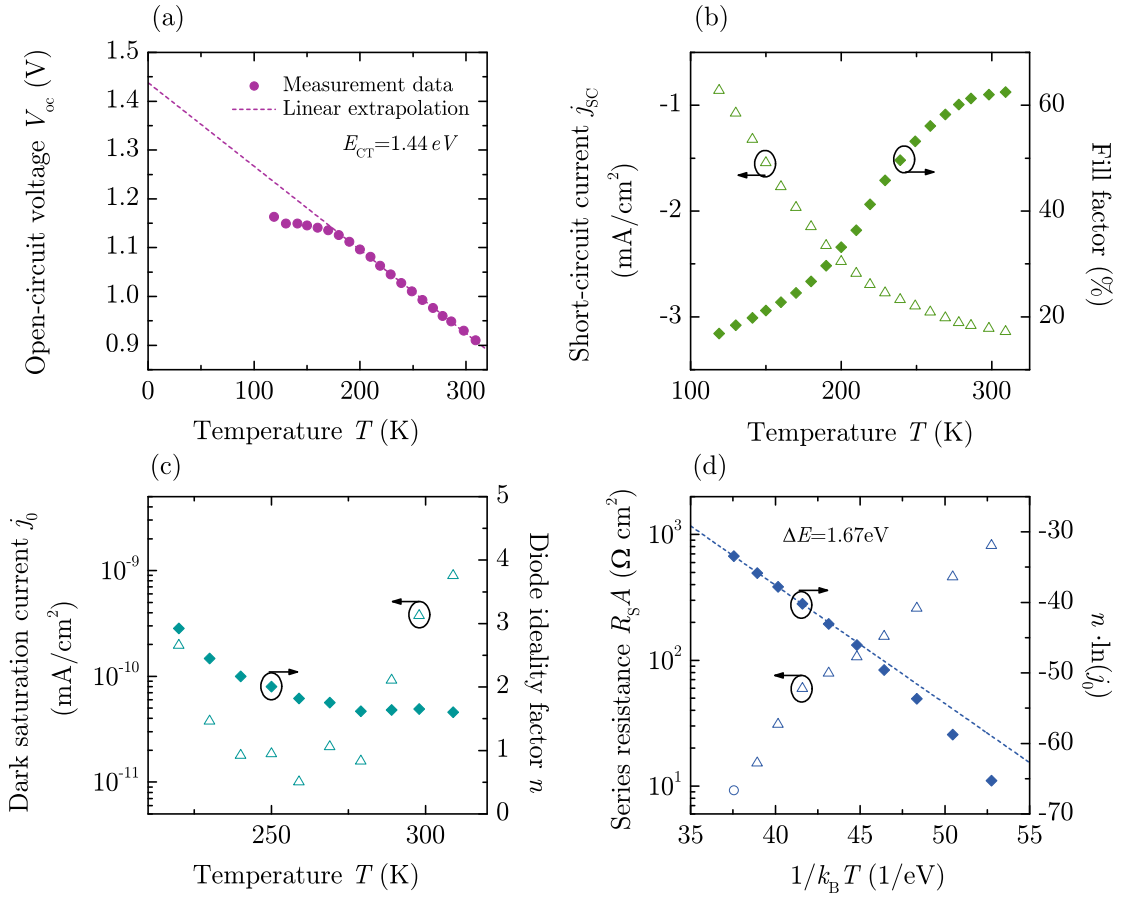

Figure B.2.: (a) and (b) Open circuit voltage V_{oc}, short circuit current density j_{sc}, and fill factor FF in dependence on temperature revealed from illuminated j-Vdata shown in Fig. B.1 (a). (c) and (d) Dark saturation current j_0, diode ideality factor n, and series resistance R_S in dependence on temperature, analyzed with the Shockley equation and evaluated by studying $n \cdot \ln(j_0)$ plotted versus $1/k_B T$ in order to estimate the activation energy ΔE.

B.2. 6T(T_{sub} = RT)/C_{60}

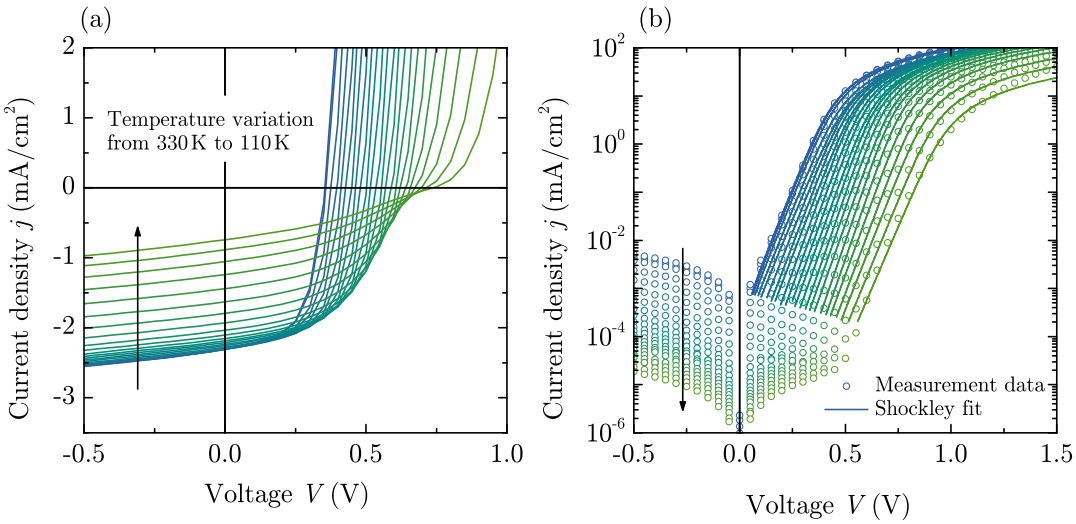

Figure B.3.: j-V characteristics of a planar heterojunction solar cell under white LED illumination in the temperature range 110 K $\leq T \leq$ 330 K. The device has the following structure: ITO/ PEDOT/ 6T(40 nm, T_{sub} = RT)/ C_{60}(80 nm)/ BCP(5 nm)/ Al (a) under white LED illumination and (b) in dark. Solid lines are fits in the forward-bias region using the Shockley equation.

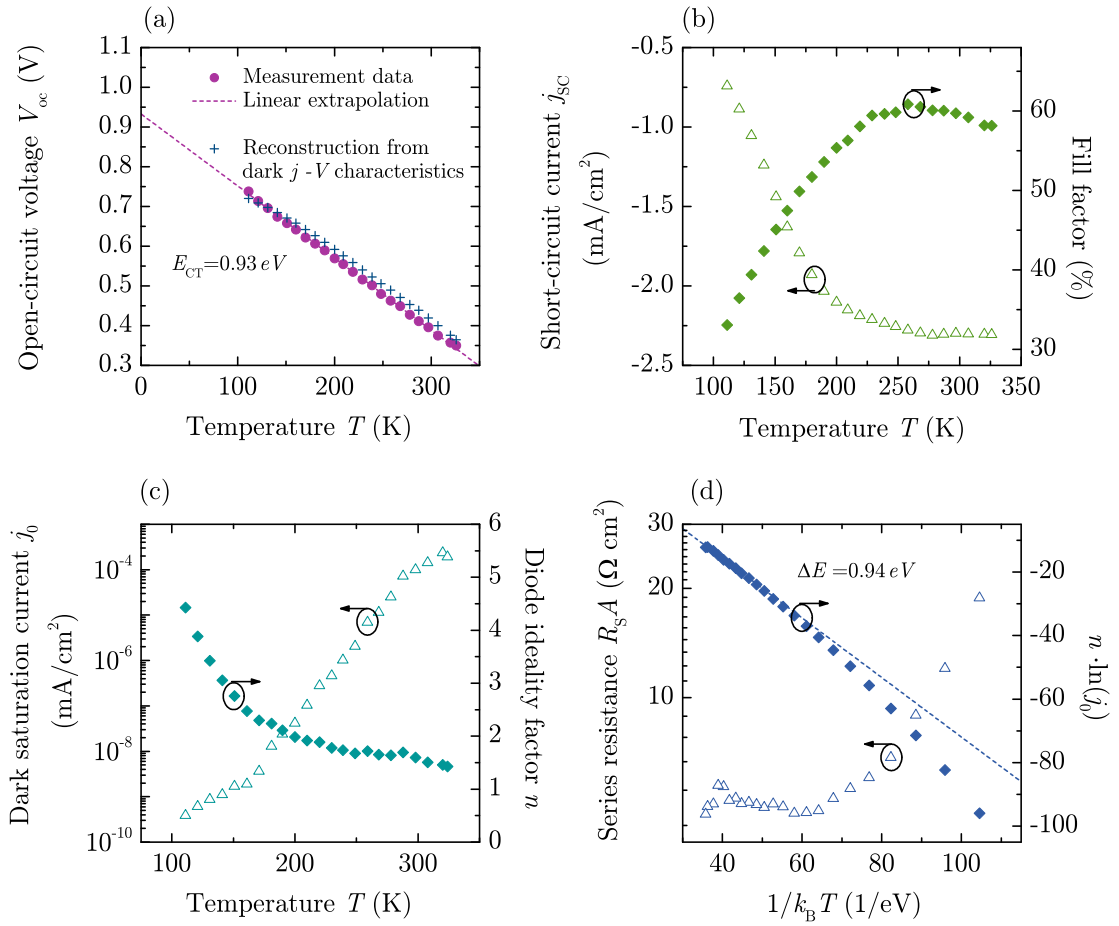

Figure B.4.: (a) and (b) Open circuit voltage V_{oc}, short circuit current density j_{sc}, and fill factor FF in dependence on temperature revealed from illuminated j-Vdata shown in Fig. B.3 (a). (c) and (d) Dark saturation current j_0, diode ideality factor n, and series resistance R_{S} in dependence on temperature, analyzed with the Shockley equation and evaluated by studying $n \cdot \ln(j_0)$ plotted versus $1/k_{\mathrm{B}}T$ in order to estimate the activation energy ΔE.

B.3. 6T(T_{sub} = RT)/DIP

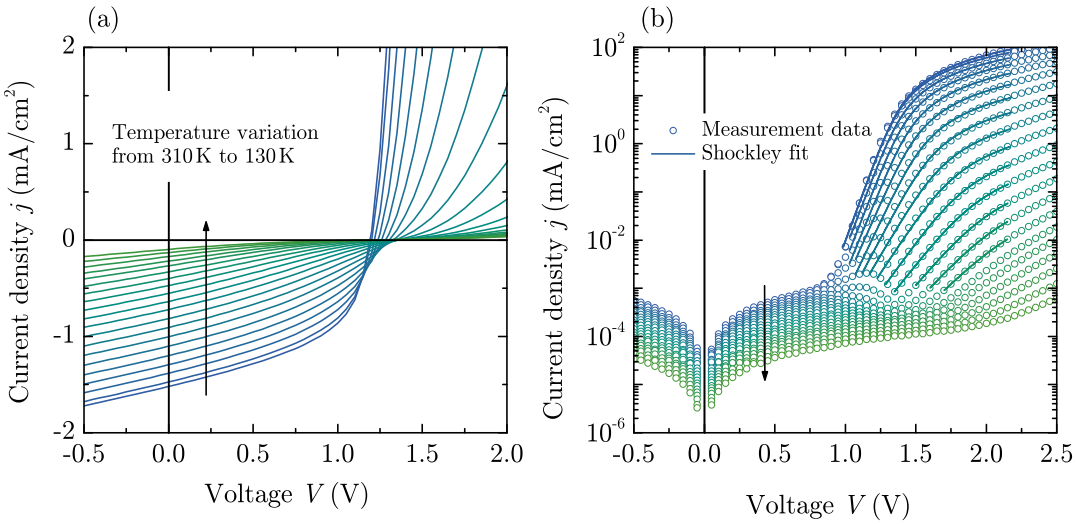

Figure B.5.: j-V characteristics of a planar heterojunction solar cell under white LED illumination in the temperature range 130 K $\leq T \leq$ 310 K. The device has the following structure: ITO/ PEDOT/ 6T(60 nm, T_{sub} = RT)/ DIP(60 nm)/ BCP(5 nm)/ Al (a) under white LED illumination and (b) in dark. Solid lines are fits in the forward-bias region using the Shockley equation.

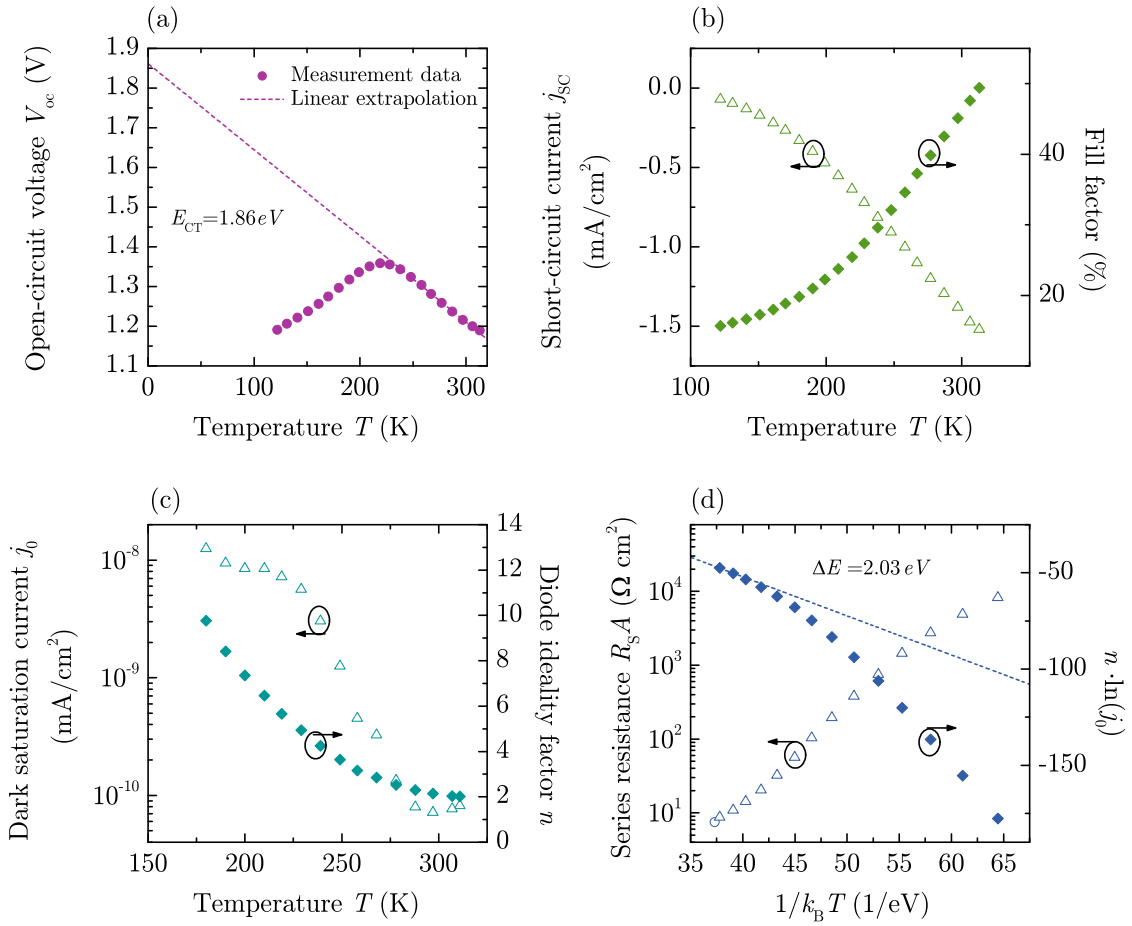

Figure B.6.: (a) and (b) Open circuit voltage V_{oc}, short circuit current density j_{sc}, and fill factor FF in dependence on temperature revealed from illuminated j-Vdata shown in Fig. B.5 (a). (c) and (d) Dark saturation current j_0, diode ideality factor n, and series resistance R_{S} in dependence on temperature, analyzed with the Shockley equation and evaluated by studying $n \cdot \ln(j_0)$ plotted versus $1/k_{\mathrm{B}}T$ in order to estimate the activation energy ΔE.

B.4. 6T($T_{\mathrm{sub}} = 100\,^{\circ}\mathrm{C}$)/DIP

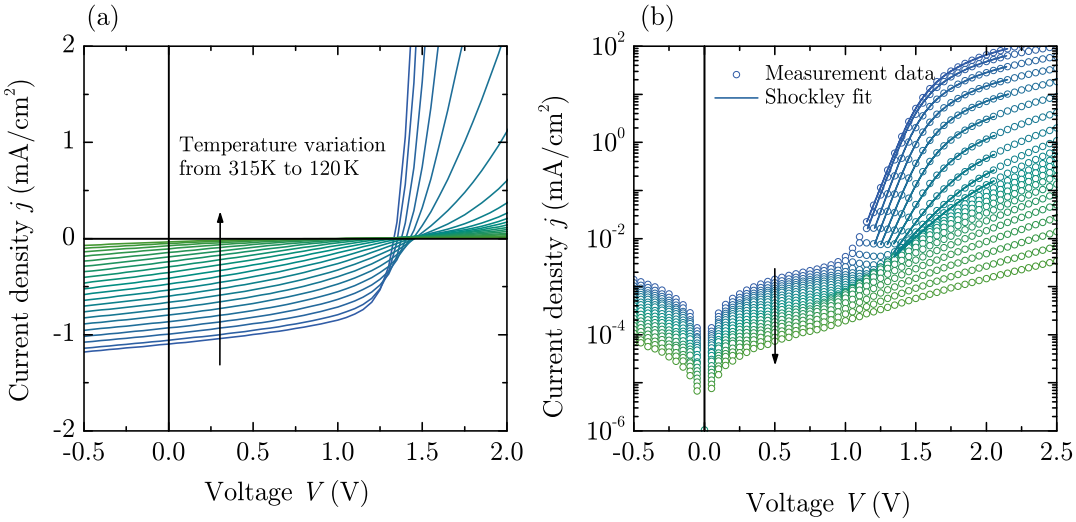

Figure B.7.: j-V characteristics of a planar heterojunction solar cell under white LED illumination in the temperature range $120\,\mathrm{K} \leq T \leq 315\,\mathrm{K}$. The device has the following structure: ITO/ PEDOT/ 6T(60 nm, $T_{\mathrm{sub}} = 100\,^{\circ}\mathrm{C}$)/ DIP(60 nm)/ BCP(5 nm)/ Al (a) under white LED illumination and (b) in dark. Solid lines are fits in the forward-bias region using the Shockley equation.

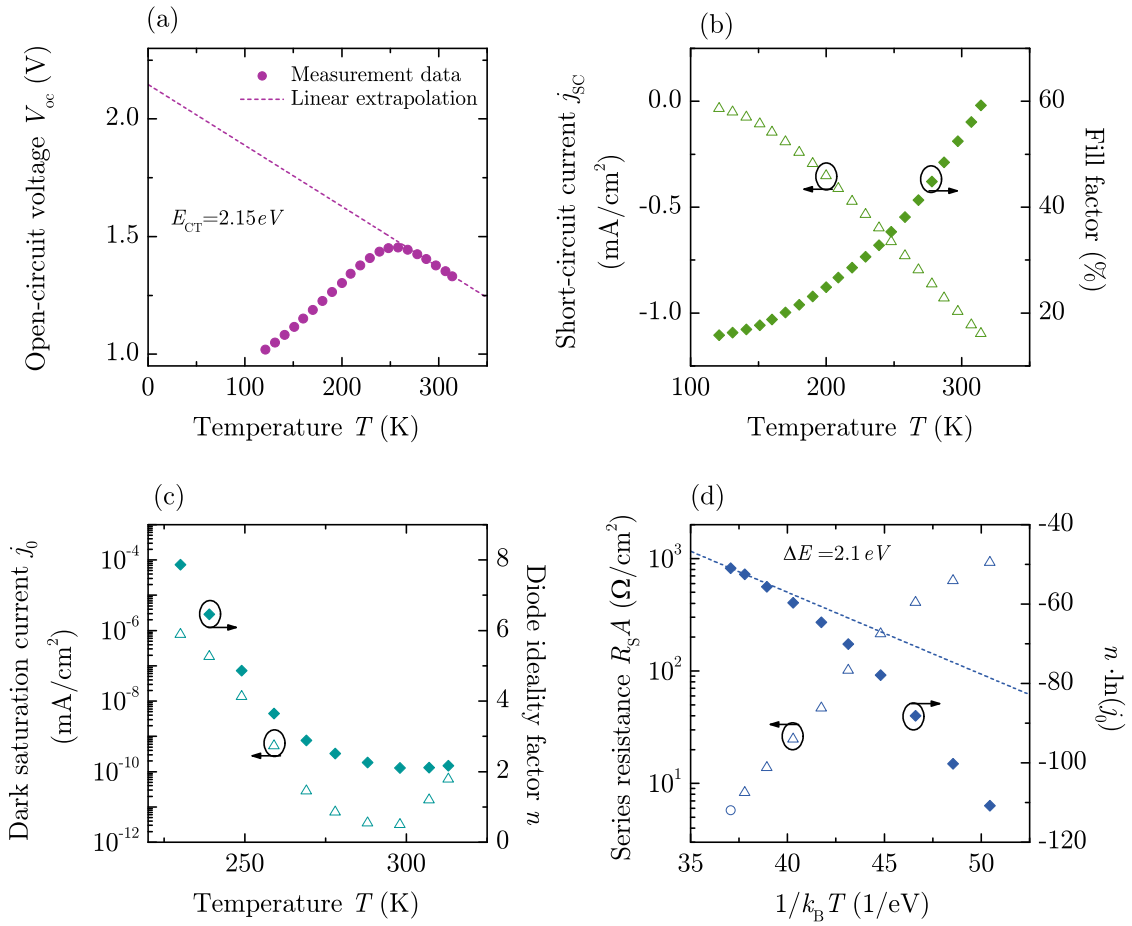

Figure B.8.: (a) and (b) Open circuit voltage V_{oc}, short circuit current density j_{sc}, and fill factor FF in dependence on temperature revealed from illuminated j-V data shown in Fig. B.7 (a). (c) and (d) Dark saturation current j_0, diode ideality factor n, and series resistance R_S in dependence on temperature, analyzed with the Shockley equation and evaluated by studying $n \cdot \ln(j_0)$ plotted versus $1/k_B T$ in order to estimate the activation energy ΔE.

B.5. Pen(T_{sub} = RT)/DIP

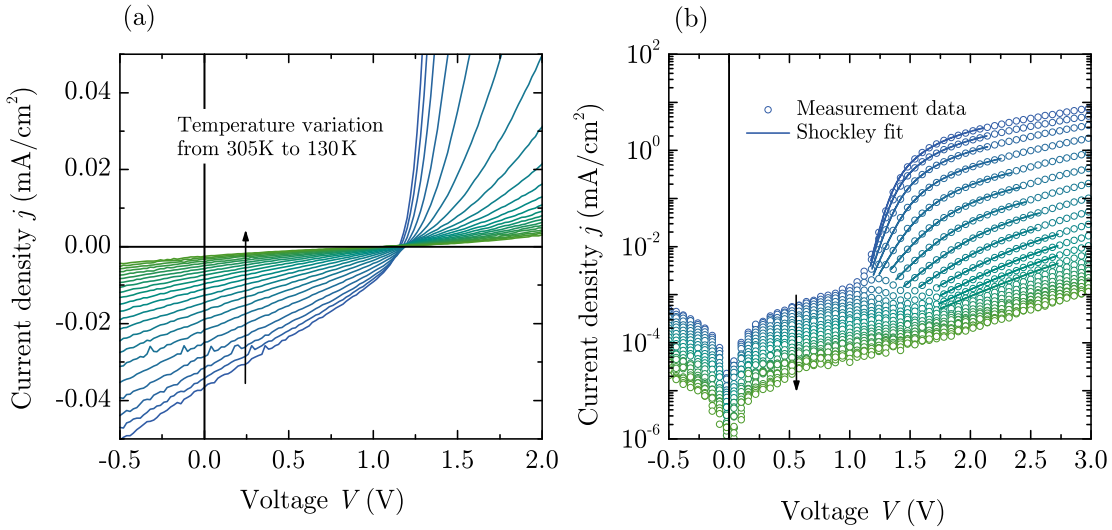

Figure B.9.: j-V characteristics of a planar heterojunction solar cell under white LED illumination in the temperature range 130 K $\leq T \leq$ 305 K. The device has the following structure: ITO/ PEDOT/ Pen(25 nm, T_{sub} = RT)/ DIP(65 nm)/ BCP(5 nm)/ Al (a) under white LED illumination and (b) in dark. Solid lines are fits in the forward-bias region using the Shockley equation.

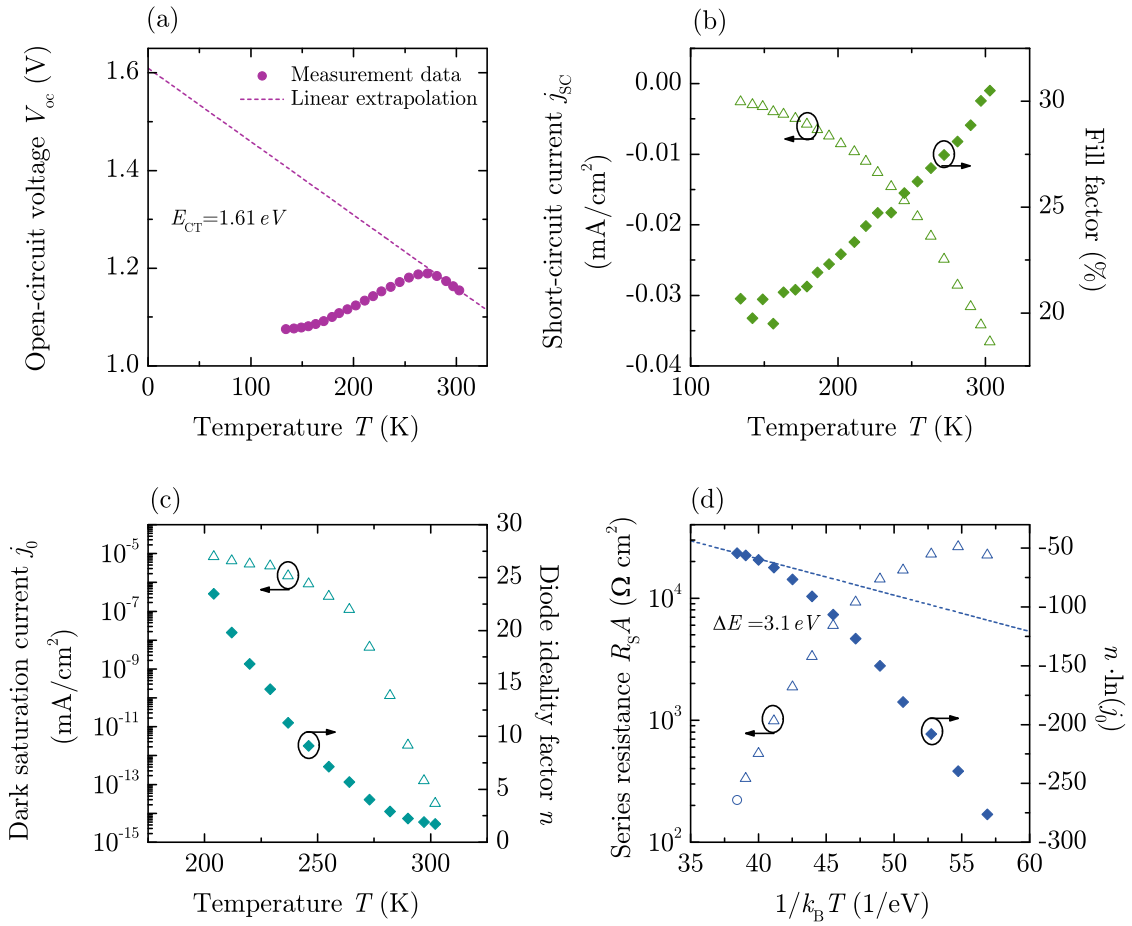

Figure B.10.: (a) and (b) Open circuit voltage V_{oc}, short circuit current density j_{sc}, and fill factor FF in dependence on temperature revealed from illuminated j-V data shown in Fig. B.9 (a). (c) and (d) Dark saturation current j_0, diode ideality factor n, and series resistance R_S in dependence on temperature, analyzed with the Shockley equation and evaluated by studying $n \cdot \ln(j_0)$ plotted versus $1/k_B T$ in order to estimate the activation energy ΔE.

B.6. Pen(T_{sub} = RT)/C_{60}

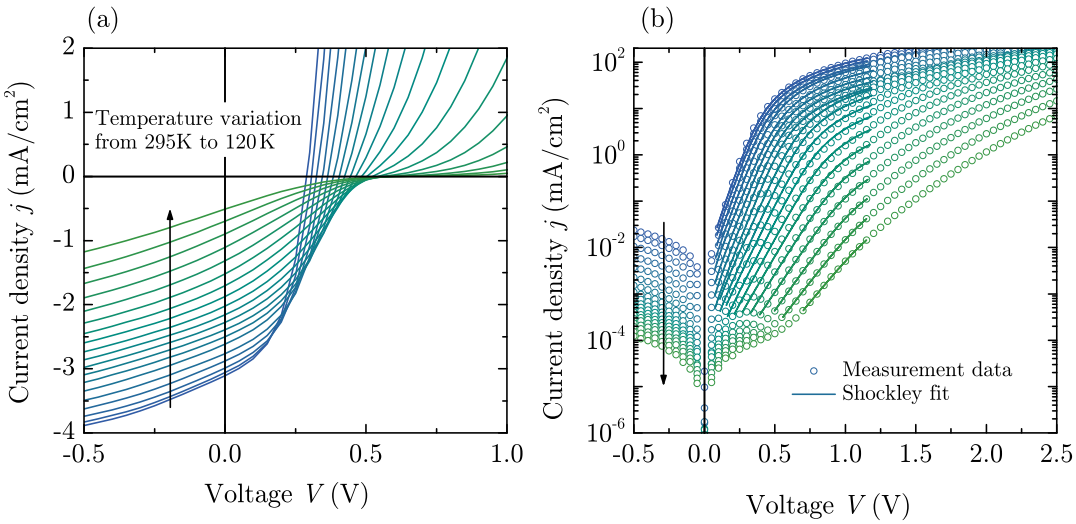

Figure B.11.: j-V characteristics of a planar heterojunction solar cell under white LED illumination in the temperature range 120 K $\leq T \leq$ 295 K. The device has the following structure: ITO/ PEDOT/ Pen(50 nm, T_{sub} = RT)/ C_{60}(80 nm)/ BCP(5 nm)/ Al (a) under white LED illumination and (b) in dark. Solid lines are fits in the forward-bias region using the Shockley equation.

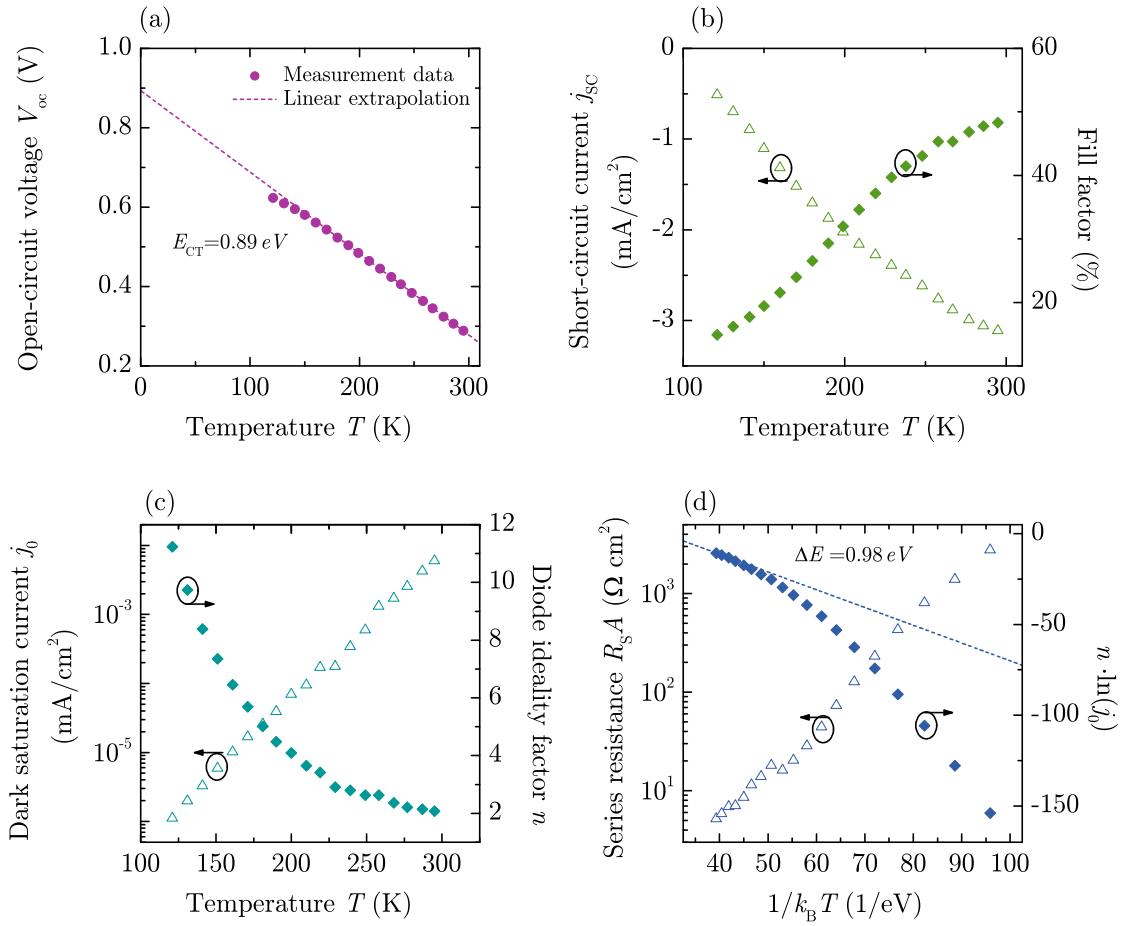

Figure B.12.: (a) and (b) Open circuit voltage V_{oc}, short circuit current density j_{sc}, and fill factor FF in dependence on temperature revealed from illuminated j-Vdata shown in Fig. B.11 (a). (c) and (d) Dark saturation current j_0, diode ideality factor n, and series resistance R_S in dependence on temperature, analyzed with the Shockley equation and evaluated by studying $n \cdot \ln(j_0)$ plotted versus $1/k_B T$ in order to estimate the activation energy ΔE.

B.7. CuPc(T_{sub} = RT)/C_{60}

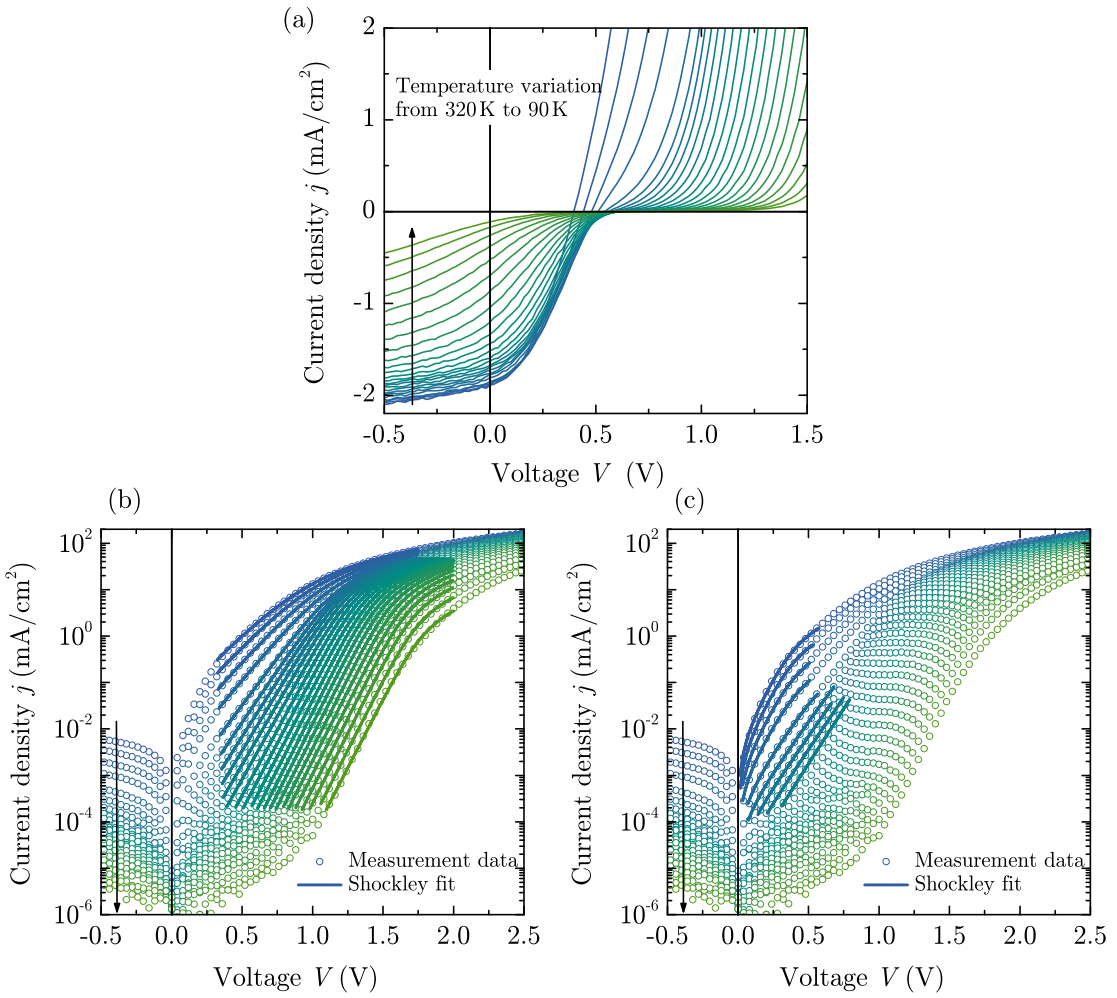

Figure B.13.: j-V characteristics of a planar heterojunction solar cell under white LED illumination in the temperature range 120 K $\leq T \leq$ 295 K. The device has the following structure: ITO/ PEDOT/ CuPc(25 nm, T_{sub} = RT)/ C_{60}(50 nm)/ BCP(5 nm)/ Al (a) under white LED illumination and (b) and (c) in dark. Solid lines are fits in the forward-bias region using the Shockley equation. According to the peculiarity in the form of a double exponential dark current, the curves are fitted both in the higher voltage range (b) as well as in the lower voltage range (c). Both parameter sets are depicted in Fig. B.14—those extracted from (c) are marked in red.

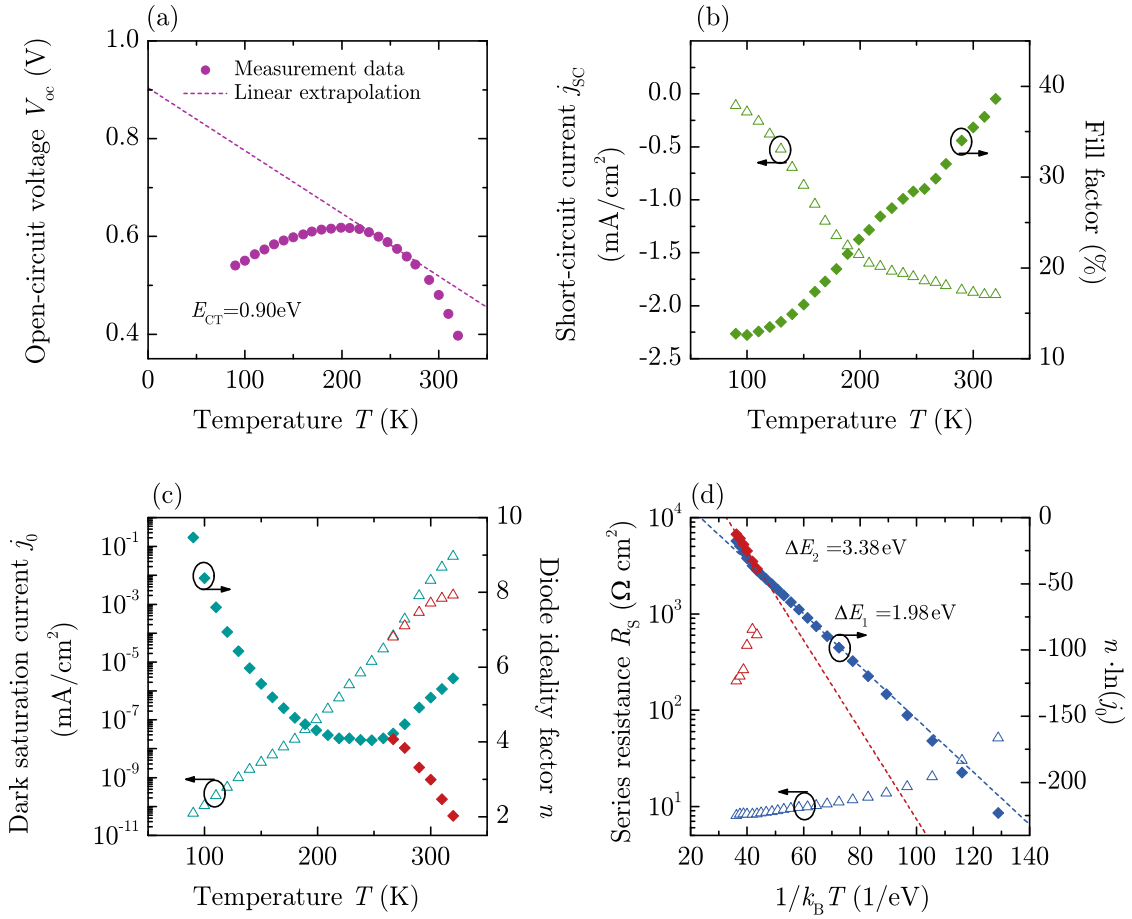

Figure B.14.: (a) and (b) Open circuit voltage V_{oc}, short circuit current density j_{sc}, and fill factor FF in dependence on temperature revealed from illuminated j-Vdata shown in Fig. B.13 (a). (c) and (d) Dark saturation current j_0, diode ideality factor n, and series resistance R_S in dependence on temperature, analyzed with the Shockley equation and evaluated by studying $n \cdot \ln(j_0)$ plotted versus $1/k_B T$ in order to estimate the activation energy ΔE. The red symbols mark the parameters as extracted from the separately fitted low voltage region (cf. Fig. B.13 (c)).

B.8. CuPc(T_{sub} = RT)/DIP

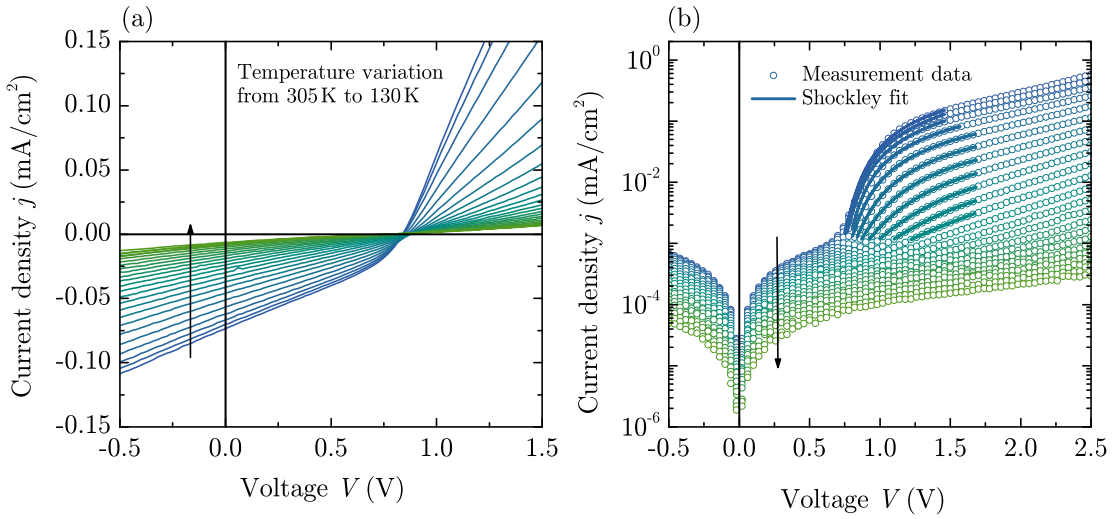

Figure B.15.: j-V characteristics of a planar heterojunction solar cell under white LED illumination in the temperature range 120 K $\leq T \leq$ 295 K. The device has the following structure: ITO/ PEDOT/ CuPc(25 nm, T_{sub} = RT)/ DIP(65 nm)/ BCP(5 nm)/ Al (a) under white LED illumination and (b) in dark. Solid lines are fits in the forward-bias region using the Shockley equation.

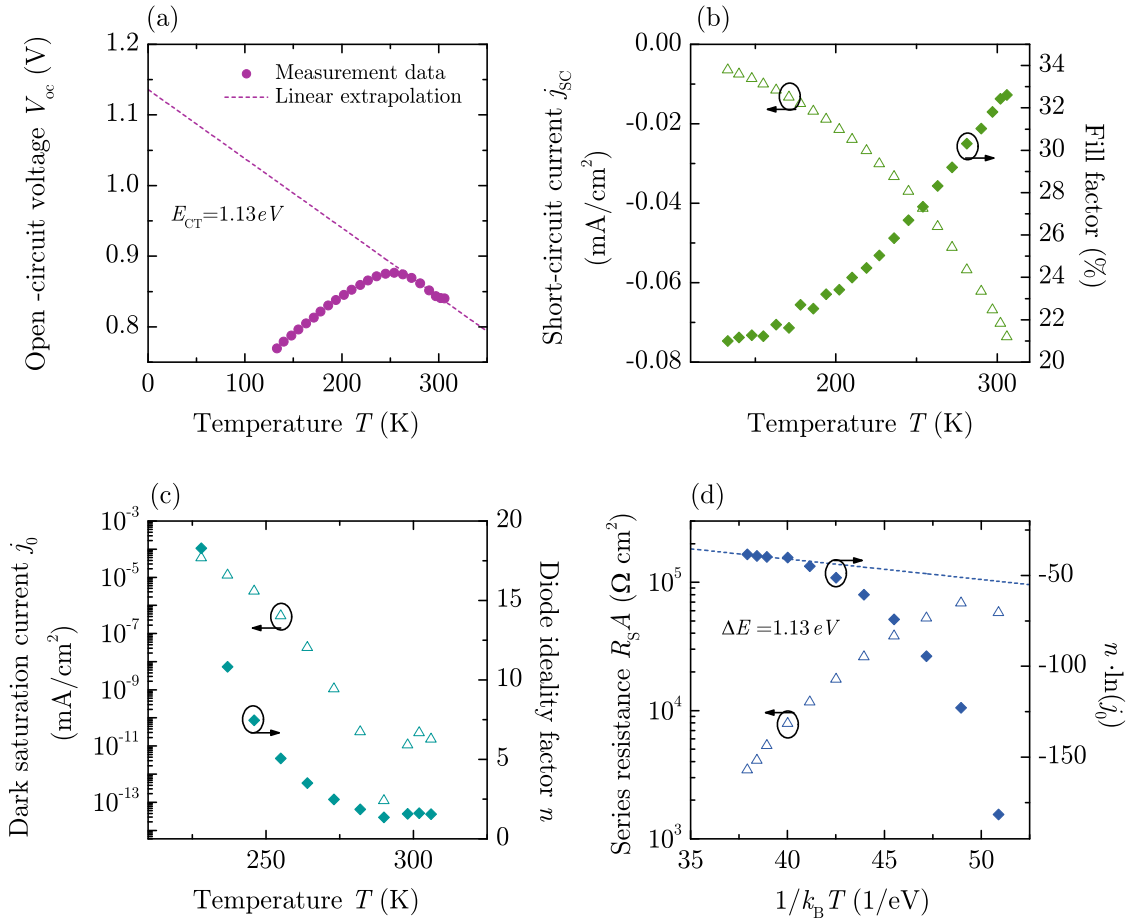

Figure B.16.: (a) and (b) Open circuit voltage V_{oc}, short circuit current density j_{sc}, and fill factor FF in dependence on temperature revealed from illuminated j-V data shown in Fig. B.15 (a). (c) and (d) Dark saturation current j_0, diode ideality factor n, and series resistance R_S in dependence on temperature, analyzed with the Shockley equation and evaluated by studying $n \cdot \ln(j_0)$ plotted versus $1/k_B T$ in order to estimate the activation energy ΔE.

Appendix C

On the approximation within the Shockley equation

Figure C.1 shows the impact of the approximation which is made in the Shockley equation

$$j(V) = j_0 \left[\exp\left(\frac{eV}{nk_\mathrm{B}T} \right) - 1 \right] - j_\mathrm{ph} \tag{C.1}$$

$$\approx j_0 \left[\exp\left(\frac{eV}{nk_\mathrm{B}T} \right) \right] - j_\mathrm{ph}, \tag{C.2}$$

by assuming $\exp\left(\frac{eV_\mathrm{F}}{nk_\mathrm{B}T}\right) \gg 1$. It can be seen that—except for comparatively high values of the dark saturation current—the j-V curves with and without "-1" are virtually identical. Realistic values for j_0 usually range between $5 \cdot 10^{-10}$ and $1 \cdot 10^{-5}\,\mathrm{mA/cm^2}$ (see Refs. 19, 453, 454 and 18 as well as various cells discussed within the present work), which justifies this approximation.

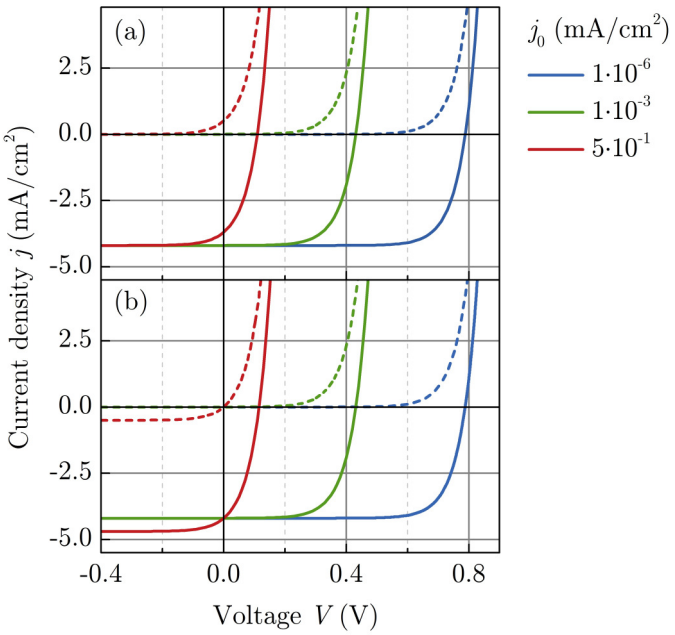

Figure C.1.: Effect of the approximation in the Shockley equation on the j-V characteristics of a solar cell shown for different values of dark saturation current j_0. (a) Simulation without "-1" in Shockley equation (b) Simulation with "-1" in Shockley equation. Only for very large values of j_0 (cf. red curves with $j_0 = 5 \cdot 10^{-1}\,\mathrm{mA/cm^2}$), the approximation leads to deviations in the characteristics. The following parameters have been used for simulation: $R_\mathrm{S}A = 0$, $R_\mathrm{P}A = \infty$, $\mathrm{T} = 300\,\mathrm{K}$, $n = 1$, $j_\mathrm{ph} = 4.2\,\mathrm{mA/cm^2}$.

Bibliography

[1] www.iea.org, downloaded on 23.03.2012.

[2] http://www.nrel.gov/ncpv/, downloaded on 30.03.2013.

[3] T. Kirchartz and U. Rau, "Detailed balance and reciprocity in solar cells," *Phys. Status Solidi A*, vol. 205, pp. 2737–2751, 2008.

[4] C. Brabec, N. Sariciftci, and J. Hummelen, "Plastic solar cells," *Adv. Funct. Mater.*, vol. 11, pp. 15–26, 2001.

[5] K. M. Coakley and M. D. McGehee, "Conjugated polymer photovoltaic cells," *Chem. Mater.*, vol. 16, pp. 4533–4542, 2004.

[6] M. A. Green, K. Emery, Y. Hishikawa, W. Warta, and E. D. Dunlop, "Solar cell efficiency tables (version 41)," *Prog. Photovolt. Res. Appl.*, vol. 21, pp. 1–11, 2013.

[7] F. Padinger, R. Rittberger, and N. Sariciftci, "Effects of postproduction treatment on plastic solar cells," *Adv. Funct. Mater.*, vol. 13, pp. 85–88, 2003.

[8] G. Li, V. Shrotriya, Y. Yao, J. Huang, and Y. Yang, "Manipulating regioregular poly(3-hexylthiophene) : [6,6]-phenyl-C_{61}-butyric acid methyl ester blends-route towards high efficiency polymer solar cells," *J. Mater. Chem.*, vol. 17, pp. 3126–3140, 2007.

[9] www.spp1355.de.

[10] P. Würfel, *Physics of Solar Cells - From Basic Principles to Advanced Concepts*. Wiley-VCH, Weinheim, 2009.

[11] C. Deibel and V. Dyakonov, "Polymer-fullerene bulk heterojunction solar cells," *Rep. Prog. Phys.*, vol. 73, p. 096401, 2010.

[12] R. F. Bailey-Salzman, B. P. Rand, and S. R. Forrest, "Near-infrared sensitive small molecule organic photovoltaic cells based on chloroaluminum phthalo-

cyanine," *Appl. Phys. Lett.*, vol. 91, p. 013508, 2007.

[13] F. Zhang, W. Mammo, L. M. Andersson, S. Admassie, M. R. Andersson, and O. Inganäs, "Low-bandgap alternating fluorene copolymer/methanofullerene heterojunctions in efficient near-infrared polymer solar cells," *Adv. Mater.*, vol. 18, pp. 2169–2173, 2006.

[14] J. Meiss, M. Hummert, H. Ziehlke, K. Leo, and M. Riede, "Organic solar cells with very high fill factor and voltage using tetrapropyl-tetraphenyl-diindenoperylene as green donor," *Phys. Status Solidi Rapid Res. Lett.*, vol. 4, pp. 329–331, 2010.

[15] V. Shrotriya, G. Li, Y. Yao, T. Moriarty, K. Emery, and Y. Yang, "Accurate measurement and characterization of organic solar cells," *Adv. Funct. Mater.*, vol. 16, pp. 2016–2023, 2006.

[16] DIN EN 60904-3, Messgrundsätze für terrestrische photovoltaische (PV) Einrichtungen mit Angaben über die spektrale Strahlungsverteilung.

[17] A. K. Ghosh and T. Feng, "Rectification, space-charge-limited current, photovoltaic and photoconductive properties of Al/tetracene/Au sandwich cell," *J. Appl. Phys.*, vol. 44, pp. 2781–2788, 1973.

[18] S. Yoo, B. Domercq, and B. Kippelen, "Intensity-dependent equivalent circuit parameters of organic solar cells based on pentacene and C_{60}," *J. Appl. Phys.*, vol. 97, p. 103706, 2005.

[19] B. P. Rand, D. P. Burk, and S. R. Forrest, "Offset energies at organic semiconductor heterojunctions and their influence on the open-circuit voltage of thin-film solar cells," *Phys. Rev. B*, vol. 75, p. 115327, 2007.

[20] J. Nelson, "Diffusion-limited recombination in polymer-fullerene blends and its influence on photocurrent collection," *Phys. Rev. B*, vol. 67, p. 155209, 2003.

[21] W. J. Potscavage, A. Sharma, and B. Kippelen, "Critical interfaces in organic solar cells and their influence on the open-circuit voltage," *Acc. Chem. Res.*, vol. 42, pp. 1758–1767, 2009.

[22] E. Lorenzo, *Solar Electricity: Engineering of Photovoltaic Systems*. Progensa, 1994.

[23] R. Sokel and R. C. Hughes, "Numerical analysis of transient photoconductivity in insulators," *J. Appl. Phys.*, vol. 53, pp. 7414–7424, 1982.

[24] V. D. Mihailetchi, L. J. A. Koster, J. C. Hummelen, and P. W. M. Blom, "Photocurrent generation in polymer-fullerene bulk heterojunctions," *Phys.*

Rev. Lett., vol. 93, p. 216601, 2004.

[25] J. Nelson, J. Kirkpatrick, and P. Ravirajan, "Factors limiting the efficiency of molecular photovoltaic devices," *Phys. Rev. B*, vol. 69, p. 035337, 2004.

[26] N. C. Giebink, G. P. Wiederrecht, M. R. Wasielewski, and S. R. Forrest, "Ideal diode equation for organic heterojunctions. I. Derivation and application," *Phys. Rev. B*, vol. 82, p. 155305, 2010.

[27] C. K. Renshaw, C. W. Schlenker, M. E. Thompson, and S. R. Forrest, "Reciprocal carrier collection in organic photovoltaics," *Phys. Rev. B*, vol. 84, p. 045315, 2011.

[28] L. J. A. Koster, E. C. P. Smits, V. D. Mihailetchi, and P. W. M. Blom, "Device model for the operation of polymer/fullerene bulk heterojunction solar cells," *Phys. Rev. B*, vol. 72, p. 085205, 2005.

[29] L. Onsager, "Initial recombination of ions," *Phys. Rev.*, vol. 54, pp. 554–557, 1938.

[30] C. L. Braun, "Electric field assisted dissociation of charge transfer states as a mechanism of photocarrier production," *J. Chem. Phys.*, vol. 80, pp. 4157–4161, 1984.

[31] W. Brütting, ed., *Physics of Organic Semiconductors*. Wiley-VCH, Weinheim, 2005.

[32] M. Schwoerer and H. C. Wolf, *Organic Molecular Crystals*. Wiley-VCH, Weinheim, 2007.

[33] W. Brütting, M. Bronner, M. Götzenbrugger, and A. Opitz, "Ambipolar blends of CuPc and C_{60}: charge carrier mobility, electronic structure and its implications for solar cell applications," *Macromol. Symp.*, vol. 268, pp. 38–42, 2008.

[34] J. Franck and E. G. Dymond, "Elementary processes of photochemical reactions," *Trans. Faraday Soc.*, vol. 21, pp. 536–542, 1926.

[35] E. Condon, "A theory of intensity distribution in band systems," *Phys. Rev.*, vol. 28, pp. 1182–1201, 1926.

[36] H. Mustroph and S. Ernst, "Das Franck-Condon-Prinzip," *Chemie in unserer Zeit*, vol. 45, pp. 256–269, 2011.

[37] B. A. Gregg, "Excitonic solar cells," *J. Phys. Chem. B*, vol. 107, pp. 4688–4698, 2003.

[38] B. A. Gregg and M. C. Hanna, "Comparing organic to inorganic photovoltaic

cells: Theory, experiment, and simulation," *J. Appl. Phys.*, vol. 93, pp. 3605–3614, 2003.

[39] I. Hill, A. Kahn, Z. Soos, and R. Pascal, "Charge-separation energy in films of π-conjugated organic molecules," *Chem. Phys. Lett.*, vol. 327, pp. 181–188, 2000.

[40] C. Deibel, D. Mack, J. Gorenflot, A. Schöll, S. Krause, F. Reinert, D. Rauh, and V. Dyakonov, "Energetics of excited states in the conjugated polymer poly(3-hexylthiophene)," *Phys. Rev. B*, vol. 81, p. 085202, 2010.

[41] B. A. Gregg, S.-G. Chen, and R. A. Cormier, "Coulomb forces and doping in organic semiconductors," *Chem. Mater.*, vol. 16, pp. 4586–4599, 2004.

[42] S. E. Gledhill, B. Scott, and B. A. Gregg, "Organic and nano-structured composite photovoltaics: An overview," *J. Mater. Res.*, vol. 20, pp. 3167–3179, 2005.

[43] K. H. Bhuiyan and T. Mieno, "Modification of dielectric properties of C_{60}, C_{70} and C_{84} thin films by oxygen absorption," *Thin Solid Films*, vol. 506-507, pp. 239–243, 2006.

[44] C. Kittel, *Introduction to solid state physics.* Oldenbourg Verlag München Wien, 13^{th} ed., 2002.

[45] Y. Maeda, N. Tsukamoto, Y. Yazawa, Y. Kanemitsu, and Y. Masumoto, "Visible photoluminescence of Ge microcrystals embedded in SiO_2 glassy matrices," *Appl. Phys. Lett.*, vol. 59, pp. 3168–3170, 1991.

[46] T. G. Pedersen, "Excitons on the surface of a sphere," *Phys. Rev. B*, vol. 81, p. 233406, 2010.

[47] N. Chopra, J. Lee, Y. Zheng, S.-H. Eom, J. Xue, and F. So, "Effect of the charge balance on high-efficiency blue-phosphorescent organic light-emitting diodes," *ACS Appl. Mater. Interfaces*, vol. 1, pp. 1169–1172, 2009.

[48] N. Karl, K.-H. Kraft, J. Marktanner, M. Münch, F. Schatz, R. Stehle, and H.-M. Uhde, "Fast electronic transport in organic molecular solids?," *J. Vac. Sci. Technol. A*, vol. 17, pp. 2318–2328, 1999.

[49] N. Karl, "Charge carrier transport in organic semiconductors," *Synth. Met.*, vol. 133-134, pp. 649–657, 2003.

[50] T. Sakanoue and H. Sirringhaus, "Band-like temperature dependence of mobility in a solution-processed organic semiconductor," *Nature Mater.*, vol. 9, pp. 736–740, 2010.

[51] F. Ortmann, F. Bechstedt, and K. Hannewald, "Charge transport in organic

crystals: interplay of band transport, hopping and electron–phonon scattering," *New J. Phys.*, vol. 12, p. 023011, 2010.

[52] H. Bässler and A. Köhler, "Charge transport in organic semiconductors," in *Unimolecular and Supramolecular Electronics I* (R. M. Metzger, ed.), vol. 312 of *Topics in Current Chemistry*, pp. 1–65, Springer Berlin Heidelberg, 2012.

[53] H. Ishii, K. Sugiyama, E. Ito, and K. Seki, "Energy level alignment and interfacial electronic structures at organic/metal and organic/organic interfaces," *Adv. Mater.*, vol. 11, pp. 605–625, 1999.

[54] W. Brütting and W. Ries, "Grundlagen der organischen Halbleiter," *Physik Journal*, vol. 7, pp. 33–38, 2008.

[55] A. Opitz, *Charge carrier generation and transport at interfaces in organic semiconductor devices*. Habilitation thesis, University of Augsburg, 2009.

[56] V. Coropceanu, J. Cornil, D. A. da Silva Filho, Y. Olivier, R. Silbey, and J. L. Brédas, "Charge transport in organic semiconductors," *Chem. Rev.*, vol. 107, pp. 926–952, 2007.

[57] M. Jaiswal and R. Menon, "Polymer electronic materials: a review of charge transport," *Polym. Int.*, vol. 55, pp. 1371–1384, 2006.

[58] H. Bässler, "Charge transport in disordered organic photoconductors - a monte-carlo simulation study," *Phys. Status Solidi B*, vol. 175, pp. 15–56, 1993.

[59] W. D. Gill, "Drift mobilities in amorphous charge-transfer complexes of trinitrofluorenone and poly-n-vinylcarbazole," *J. Appl. Phys.*, vol. 43, pp. 5033–5040, 1972.

[60] R. M. Hill, "Poole-frenkel conduction in amorphous solids," *Philos. Mag.*, vol. 23, pp. 59–86, 1971.

[61] D. Hertel and H. Bässler, "Photoleitung in Polymeren," *Physik Journal*, vol. 5, pp. 39–45, 2006.

[62] G. Horowitz and M. Hajlaoui, "Mobility in polycrystalline oligothiophene field-effect transistors dependent on grain size," *Adv. Mater.*, vol. 12, pp. 1046–1050, 2000.

[63] A. Miller and E. Abrahams, "Impurity conduction at low concentrations," *Phys. Rev.*, vol. 120, pp. 745–755, 1960.

[64] C. Tanase, E. J. Meijer, P. W. M. Blom, and D. M. de Leeuw, "Unification of the hole transport in polymeric field-effect transistors and light-emitting diodes," *Phys. Rev. Lett.*, vol. 91, p. 216601, 2003.

[65] B. Hartenstein and H. Bässler, "Transport energy for hopping in a gaussian density of states distribution," *J. Non-Cryst. Solids*, vol. 190, pp. 112–116, 1995.

[66] S. D. Baranovskii, H. Cordes, F. Hensel, and G. Leising, "Charge-carrier transport in disordered organic solids," *Phys. Rev. B*, vol. 62, pp. 7934–7938, 2000.

[67] R. Coehoorn, W. F. Pasveer, P. A. Bobbert, and M. A. J. Michels, "Charge-carrier concentration dependence of the hopping mobility in organic materials with gaussian disorder," *Phys. Rev. B*, vol. 72, p. 155206, 2005.

[68] D. Braun, "Electronic injection and conduction processes for polymer devices," *J. Poly. Sci. B*, vol. 41, pp. 2622–2629, 2003.

[69] J. L. Brédas, J. P. Calbert, D. A. da Silva Filho, and J. Cornil, "Organic semiconductors: A theoretical characterization of the basic parameters governing charge transport," *P. Natl. Acad. Sci. USA*, vol. 99, pp. 5804–5809, 2002.

[70] L. G. Kaake, P. F. Barbara, and X.-Y. Zhu, "Intrinsic charge trapping in organic and polymeric semiconductors: A physical chemistry perspective," *J. Phys. Chem. Lett.*, vol. 1, pp. 628–635, 2010.

[71] P. Mark and W. Helfrich, "Space-charge-limited currents in organic crystals," *J. Appl. Phys.*, vol. 33, pp. 205–215, 1962.

[72] S. C. Jain, W. Geens, A. Mehra, V. Kumar, T. Aernouts, J. Poortmans, R. Mertens, and M. Willander, "Injection- and space charge limited-currents in doped conducting organic materials," *J. Appl. Phys.*, vol. 89, pp. 3804–3810, 2001.

[73] P. W. M. Blom, C. Tanase, D. M. de Leeuw, and R. Coehoorn, "Thickness scaling of the space-charge-limited current in poly(p-phenylene vinylene)," *Appl. Phys. Lett.*, vol. 86, p. 092105, 2005.

[74] P. W. M. Blom, V. D. Mihailetchi, L. J. A. Koster, and D. E. Markov, "Device physics of polymer:fullerene bulk heterojunction solar cells," *Adv. Mater.*, vol. 19, pp. 1551–1566, 2007.

[75] M. Lampert and P. Mark, *Current injection in solids*. Electrical science series, Academic Press, 1970.

[76] M. Pope and C. E. Swenberg, *Electronic processes in organic crystals and polymers*. Oxford university press, New York, 1999.

[77] J. Reynaert, V. I. Arkhipov, G. Borghs, and P. Heremans, "Current–voltage

characteristics of a tetracene crystal: Space charge or injection limited conductivity?," *Appl. Phys. Lett.*, vol. 85, pp. 603–605, 2004.

[78] A. W. Hains, Z. Liang, M. A. Woodhouse, and B. A. Gregg, "Molecular semiconductors in organic photovoltaic cells," *Chem. Rev.*, vol. 110, pp. 6689–6735, 2010.

[79] B. A. Gregg, S. E. Gledhill, and B. Scott, "Can true space-charge-limited currents be observed in π-conjugated polymers?," *J. Appl. Phys.*, vol. 99, p. 116104, 2006.

[80] I. D. Parker, "Carrier tunneling and device characteristics in polymer light-emitting diodes," *J. Appl. Phys.*, vol. 75, pp. 1656–1666, 1994.

[81] P. Murgatroyd, "Theory of space-charge limited current enhanced by Frenkel effect," *J. Phys. D: Appl. Phys.*, vol. 3, pp. 151–156, 1970.

[82] A. C. Dürr, N. Koch, M. Kelsch, A. Rühm, J. Ghijsen, R. L. Johnson, J.-J. Pireaux, J. Schwartz, F. Schreiber, H. Dosch, and A. Kahn, "Interplay between morphology, structure, and electronic properties at diindenoperylene-gold interfaces," *Phys. Rev. B*, vol. 68, p. 115428, 2003.

[83] R. Farchioni and G. Grosso, *Organic Electronic Materials – Conjugated Polymers and Low Molecular Weight Organic Solids*. Berlin: Springer-Verlag, 2001.

[84] S. Berleb, *Raumladungsbegrenzte Ströme und Hoppingtransport in organischen Leuchtdioden aus Tris-(8-hydroxyquinolin)-Aluminium (Alq_3)*. PhD thesis, University of Bayreuth, 2001.

[85] W. Brütting, S. Berleb, and A. G. Mückl, "Device physics of organic light-emitting diodes based on molecular materials," *Org. Electron.*, vol. 2, pp. 1–36, 2001.

[86] W. Brütting, S. Berleb, and A. G. Mückl, "Space-charge limited conduction with a field and temperature dependent mobility in Alq light-emitting devices," *Synth. Met.*, vol. 122, pp. 99–104, 2001.

[87] G. L. J. A. Rikken, D. Braun, E. G. J. Staring, and R. Demandt, "Schottky effect at a metal-polymer interface," *Appl. Phys. Lett.*, vol. 65, pp. 219–221, 1994.

[88] N. Koch, "Organic electronic devices and their functional interfaces," *ChemPhysChem*, vol. 8, pp. 1438–1455, 2007.

[89] I. G. Hill, A. Rajagopal, A. Kahn, and Y. Hu, "Molecular level alignment at organic semiconductor-metal interfaces," *Appl. Phys. Lett.*, vol. 73, pp. 662–

664, 1998.

[90] K. Seki, N. Hayashi, H. Oji, E. Ito, Y. Ouchi, and H. Ishii, "Electronic structure of organic/metal interfaces," *Thin Solid Films*, vol. 393, pp. 298–303, 2001.

[91] K. Seki, E. Ito, and H. Ishii, "Energy level alignment at organic/metal interfaces studied by UV photoemission," *Synth. Met.*, vol. 91, pp. 137–142, 1997.

[92] H. Ishii, N. Hayashi, E. Ito, Y. Washizu, K. Sugi, Y. Kimura, M. Niwano, O. Ouchi, and K. Seki, "Kelvin probe study of band bending at organic semiconductor/metal interfaces: Examination of fermi level alignment," in *Physics of Organic Semiconductors* (W. Brütting, ed.), pp. 69–94, Wiley-VCH Verlag, Weinheim, 2005.

[93] M. Knupfer and H. Peisert, "Electronic properties of interfaces between model organic semiconductors and metals," in *Physics of Organic Semiconductors* (W. Brütting, ed.), pp. 41–67, Wiley-VCH Verlag, Weinheim, 2005.

[94] N. Hayashi, H. Ishii, Y. Ouchi, and K. Seki, "Examination of band bending at buckminsterfullerene (C_{60})/metal interfaces by the kelvin probe method," *J. Appl. Phys.*, vol. 92, pp. 3784–3793, 2002.

[95] A. Kahn, N. Koch, and W. Gao, "Electronic structure and electrical properties of interfaces between metals and π-conjugated molecular films," *J. Poly. Sci. B*, vol. 41, pp. 2529–2548, 2003.

[96] X. Crispin, V. Geskin, A. Crispin, J. Cornil, R. Lazzaroni, W. R. Salaneck, and J.-L. Brédas, "Characterization of the interface dipole at organic/metal interfaces," *J. Am. Chem. Soc.*, vol. 124, pp. 8131–8141, 2002.

[97] S. Braun, W. Osikowicz, Y. Wang, and W. R. Salaneck, "Energy level alignment regimes at hybrid organic-organic and inorganic-organic interfaces," *Org. Electron.*, vol. 8, pp. 14–20, 2007.

[98] A. Wilke, J. Endres, U. Hörmann, J. Niederhausen, R. Schlesinger, J. Frisch, P. Amsalem, J. Wagner, M. Gruber, A. Opitz, A. Vollmer, W. Brütting, A. Kahn, and N. Koch, "Correlation between interface energetics and open circuit voltage in organic photovoltaic cells," *Appl. Phys. Lett.*, vol. 101, p. 233301, 2012.

[99] A. Opitz, J. Frisch, R. Schlesinger, A. Wilke, and N. Koch, "Energy level alignment at interfaces in organic photovoltaic devices," *J. Electron Spec.*, 2012.

[100] M. C. Scharber, D. Mühlbacher, M. Koppe, P. Denk, C. Waldauf, A. J.

Heeger, and C. J. Brabec, "Design rules for donors in bulk-heterojunction solar cells—towards 10% energy-conversion efficiency," *Adv. Mater.*, vol. 18, pp. 789–794, 2006.

[101] G. Dennler, M. C. Scharber, T. Ameri, P. Denk, K. Forberich, C. Waldauf, and C. J. Brabec, "Design rules for donors in bulk-heterojunction tandem solar cells–towards 15% energy-conversion efficiency," *Adv. Mater.*, vol. 20, pp. 579–583, 2008.

[102] P. Peumans, S. Uchida, and S. Forrest, "Efficient bulk heterojunction photovoltaic cells using small-molecular-weight organic thin films," *Nature*, vol. 425, pp. 158–162, 2003.

[103] J. Koenigsberger and K. Schilling, "Über Elektrizitätsleitung in festen Elementen und Verbindungen. I. Minima des Widerstandes, Prüfung auf Elektronenleitung, Anwendung der Dissoziationsformeln," *Ann. Phys.*, vol. 337, pp. 179–230, 1910.

[104] M. Volmer, "Die verschiedenen lichtelektrischen Erscheinungen am Anthracen, ihre Beziehungen zueinander, zur Fluoreszenz und Dianthracenbildung," *Ann. Phys.*, vol. 345, pp. 775–796, 1913.

[105] W. E. Pauli, "Lichtelektrische Untersuchungen an fluoreszierenden Substanzen," *Ann. Phys.*, vol. 345, pp. 677–700, 1913.

[106] M. Pope, H. P. Kallmann, and P. Magnante, "Electroluminescence in organic crystals," *J. Chem. Phys.*, vol. 38, pp. 2042–2043, 1963.

[107] W. Helfrich and W. G. Schneider, "Recombination radiation in anthracene crystals," *Phys. Rev. Lett.*, vol. 14, pp. 229–231, 1965.

[108] H. Shirakawa, E. J. Louis, A. G. MacDiarmid, C. K. Chiang, and A. J. Heeger, "Synthesis of electrically conducting organic polymers: halogen derivatives of polyacetylene, $(CH)_x$," *J. Chem. Soc., Chem. Commun.*, vol. 16, pp. 578–580, 1977.

[109] C. K. Chiang, C. R. Fincher, Y. W. Park, A. J. Heeger, H. Shirakawa, E. J. Louis, S. C. Gau, and A. G. MacDiarmid, "Electrical conductivity in doped polyacetylene," *Phys. Rev. Lett.*, vol. 39, pp. 1098–1101, 1977.

[110] C. W. Tang, "Two-layer organic photovoltaic cell," *Appl. Phys. Lett.*, vol. 48, pp. 183–185, 1986.

[111] Konarka (press release), "Konarka verkündet Verfügbarkeit von Solarzellen für portable Ladegeräte auf der European Photovoltaic Solar Energy Conference." www.konarka.com, accessed 08.03.2012.

[112] G. Dennler, M. C. Scharber, and C. J. Brabec, "Polymer-Fullerene Bulk-Heterojunction Solar Cells," *Adv. Mater.*, vol. 21, pp. 1323–1338, 2009.

[113] D. Veldman, S. C. J. Meskers, and R. A. J. Janssen, "The energy of charge-transfer states in electron donor-acceptor blends: Insight into the energy losses in organic solar cells," *Adv. Funct. Mater.*, vol. 19, pp. 1939–1948, 2009.

[114] J.-L. Brédas, J. E. Norton, J. Cornil, and V. Coropceanu, "Molecular understanding of organic solar cells: The challenges," *Acc. Chem. Res.*, vol. 42, pp. 1691–1699, 2009.

[115] N. S. Sariciftci, L. Smilowitz, A. J. Heeger, and F. Wudl, "Photoinduced electron-transfer from a conducting polymer to buckminsterfullerene," *Science*, vol. 258, pp. 1474–1476, 1992.

[116] T. M. Clarke and J. R. Durrant, "Charge photogeneration in organic solar cells.," *Chem. Rev.*, vol. 110, pp. 6736–6767, 2010.

[117] S. Forrest, "The limits to organic photovoltaic cell efficiency," *MRS Bull.*, vol. 30, pp. 28–32, 2005.

[118] P. Peumans, A. Yakimov, and S. R. Forrest, "Small molecular weight organic thin-film photodetectors and solar cells," *J. Appl. Phys.*, vol. 93, pp. 3693–3723, 2003.

[119] S.-B. Rim and P. Peumans, "The effects of optical interference on exciton diffusion length measurements using photocurrent spectroscopy," *J. Appl. Phys.*, vol. 103, p. 124515, 2008.

[120] R. R. Lunt, N. C. Giebink, A. A. Belak, J. B. Benziger, and S. R. Forrest, "Exciton diffusion lengths of organic semiconductor thin films measured by spectrally resolved photoluminescence quenching," *J. Appl. Phys.*, vol. 105, p. 053711, 2009.

[121] M. Hiramoto, H. Fujiwara, and M. Yokoyama, "Three-layered organic solar cell with a photoactive of codeposited pigments interlayer," *Appl. Phys. Lett.*, vol. 58, pp. 1062–1064, 1991.

[122] J. J. M. Halls, C. A. Walsh, N. C. Greenham, E. A. Marseglia, R. H. Friend, S. C. Moratti, and A. B. Holmes, "Efficient photodiodes from interpenetrating polymer networks," *Nature*, vol. 376, pp. 498–500, 1995.

[123] G. Yu, J. Gao, J. C. Hummelen, F. Wudl, and A. J. Heeger, "Polymer photovoltaic cells: Enhanced efficiencies via a network of internal donor-acceptor heterojunctions," *Science*, vol. 270, pp. 1789–1791, 1995.

[124] S. Heutz, P. Sullivan, B. M. Sanderson, S. M. Schultes, and T. S. Jones, "Influence of molecular architecture and intermixing on the photovoltaic, morphological and spectroscopic properties of CuPc-C_{60} heterojunctions," *Sol. Energy Mater. Sol. Cells*, vol. 83, pp. 229–245, 2004.

[125] J. Xue, B. Rand, S. Uchida, and S. Forrest, "A hybrid planar-mixed molecular heterojunction photovoltaic cell," *Adv. Mater.*, vol. 17, pp. 66–71, 2005.

[126] S. Pfuetzner, J. Meiss, A. Petrich, M. Riede, and K. Leo, "Improved bulk heterojunction organic solar cells employing C_{70} fullerenes," *Appl. Phys. Lett.*, vol. 94, p. 223307, 2009.

[127] T. Tsuzuki, Y. Shirota, J. Rostalski, and D. Meissner, "The effect of fullerene doping on photoelectric conversion using titanyl phthalocyanine and a perylene pigment," *Sol. Energy Mater. Sol. Cells*, vol. 61, pp. 1–8, 2000.

[128] C. Deibel, T. Strobel, and V. Dyakonov, "Role of the charge transfer state in organic donor-acceptor solar cells," *Adv. Mater.*, vol. 22, pp. 4097–4111, 2010.

[129] D. R. Zahn, G. N. Gavrila, and M. Gorgoi, "The transport gap of organic semiconductors studied using the combination of direct and inverse photoemission," *Chem. Phys.*, vol. 325, pp. 99–112, 2006.

[130] C. H. Lee, G. Yu, D. Moses, and A. J. Heeger, "Picosecond transient photoconductivity in poly(*p* -phenylenevinylene)," *Phys. Rev. B*, vol. 49, pp. 2396–2407, 1994.

[131] K. C. Yee and R. R. Chance, "Synthesis and properties of a new polydiacetylene: Poly[1,6-di(N-carbazolyl)-2,4-hexadiyne]," *J. Poly. Sci. - Polymer Physics Edition*, vol. 16, pp. 431–441, 1978.

[132] L. Sebastian and G. Weiser, "One-dimensional wide energy bands in a polydiacetylene revealed by electroreflectance," *Phys. Rev. Lett.*, vol. 46, pp. 1156–1159, 1981.

[133] D. Moses, J. Wang, A. J. Heeger, N. Kirova, and S. Brazovski, "Singlet exciton binding energy in poly(phenylene vinylene)," *P. Natl. Acad. Sci. USA*, vol. 98, pp. 13496–13500, 2001.

[134] P. I. Djurovich, E. I. Mayo, S. R. Forrest, and M. E. Thompson, "Measurement of the lowest unoccupied molecular orbital energies of molecular organic semiconductors," *Org. Electron.*, vol. 10, pp. 515–520, 2009.

[135] H. Ohkita, S. Cook, Y. Astuti, W. Duffy, S. Tierney, W. Zhang, M. Heeney, I. McCulloch, J. Nelson, D. D. C. Bradley, and J. R. Durrant, "Charge carrier formation in polythiophene/fullerene blend films studied by transient

absorption spectroscopy," *J. Am. Chem. Soc.*, vol. 130, pp. 3030–3042, 2008.

[136] M. Hallermann, S. Haneder, and E. D. Como, "Charge-transfer states in conjugated polymer/fullerene blends: Below-gap weakly bound excitons for polymer photovoltaics," *Appl. Phys. Lett.*, vol. 93, p. 053307, 2008.

[137] M. Muntwiler, Q. Yang, W. A. Tisdale, and X.-Y. Zhu, "Coulomb barrier for charge separation at an organic semiconductor interface," *Phys. Rev. Lett.*, vol. 101, p. 196403, 2008.

[138] K. Vandewal, K. Tvingstedt, and O. Inganäs, "Chapter 8 - charge transfer states in organic donor–acceptor solar cells," in *Quantum Efficiency in Complex Systems, Part II From Molecular Aggregates to Organic Solar Cells* (M. T. Uli Würfel and E. R. Weber, eds.), vol. 85 of *Semiconductors and Semimetals*, pp. 261–295, Elsevier, 2011.

[139] C. J. Brabec, A. Cravino, D. Meissner, N. S. Sariciftci, T. Fromherz, M. T. Rispens, L. Sanchez, and J. C. Hummelen, "Origin of the open circuit voltage of plastic solar cells," *Adv. Funct. Mater.*, vol. 11, pp. 374–380, 2001.

[140] C. M. Ramsdale, J. A. Barker, A. C. Arias, J. D. MacKenzie, R. H. Friend, and N. C. Greenham, "The origin of the open-circuit voltage in polyfluorene-based photovoltaic devices," *J. Appl. Phys.*, vol. 92, pp. 4266–4270, 2002.

[141] V. D. Mihailetchi, P. W. M. Blom, J. C. Hummelen, and M. T. Rispens, "Cathode dependence of the open-circuit voltage of polymer:fullerene bulk heterojunction solar cells," *J. Appl. Phys.*, vol. 94, pp. 6849–6854, 2003.

[142] K. Vandewal, K. Tvingstedt, A. Gadisa, O. Inganäs, and J. V. Manca, "On the origin of the open-circuit voltage of polymer–fullerene solar cells," *Nature Mater.*, vol. 8, pp. 904–909, 2009.

[143] W. Shockley and H. J. Queisser, "Detailed balance limit of efficiency of p-n junction solar cells," *J. Appl. Phys.*, vol. 32, pp. 510–519, 1961.

[144] K. Tvingstedt, K. Vandewal, A. Gadisa, F. Zhang, J. Manca, and O. Inganäs, "Electroluminescence from charge transfer states in polymer solar cells," *J. Am. Chem. Soc.*, vol. 131, pp. 11819–11824, 2009.

[145] U. Rau, "Reciprocity relation between photovoltaic quantum efficiency and electroluminescent emission of solar cells," *Phys. Rev. B*, vol. 76, p. 085303, 2007.

[146] K. Vandewal, K. Tvingstedt, J. Manca, and O. Inganäs, "Charge-Transfer States and Upper Limit of the Open-Circuit Voltage in Polymer:Fullerene Organic Solar Cells ," *IEEE J. Sel. Top. Quant.*, vol. 16, pp. 1676–1684, 2010.

[147] K. Vandewal, W. D. Oosterbaan, S. Bertho, V. Vrindts, A. Gadisa, L. Lutsen, D. Vanderzande, and J. V. Manca, "Varying polymer crystallinity in nanofiber poly(3-alkylthiophene): PCBM solar cells: Influence on charge-transfer state energy and open-circuit voltage," *Appl. Phys. Lett.*, vol. 95, p. 123303, 2009.

[148] M. Gruber, J. Wagner, K. Klein, U. Hörmann, A. Opitz, M. Stutzmann, and W. Brütting, "Thermodynamic efficiency limit of molecular donor-acceptor solar cells and its application to diindenoperylene/C_{60} based planar heterojunction devices," *Adv. Energy Mater.*, vol. 2, pp. 1100–1108, 2012.

[149] A. C. Morteani, P. Sreearunothai, L. M. Herz, R. H. Friend, and C. Silva, "Exciton regeneration at polymeric semiconductor heterojunctions," *Phys. Rev. Lett.*, vol. 92, p. 247402, 2004.

[150] T. Offermans, P. A. van Hal, S. C. J. Meskers, M. M. Koetse, and R. A. J. Janssen, "Exciplex dynamics in a blend of π-conjugated polymers with electron donating and accepting properties: MDMO-PPV and PCNEPV," *Phys. Rev. B*, vol. 72, p. 045213, 2005.

[151] C. Yin, T. Kietzke, D. Neher, and H.-H. Hörhold, "Photovoltaic properties and exciplex emission of polyphenylenevinylene-based blend solar cells," *Appl. Phys. Lett.*, vol. 90, p. 092117, 2007.

[152] M. A. Loi, S. Toffanin, M. Muccini, M. Forster, U. Scherf, and M. Scharber, "Charge transfer excitons in bulk heterojunctions of a polyfluorene copolymer and a fullerene derivative," *Adv. Funct. Mater.*, vol. 17, pp. 2111–2116, 2007.

[153] H. Kim, J. Y. Kim, S. H. Park, K. Lee, Y. Jin, J. Kim, and H. Suh, "Electroluminescence in polymer-fullerene photovoltaic cells," *Appl. Phys. Lett.*, vol. 86, p. 183502, 2005.

[154] Y. Zhou, K. Tvingstedt, F. Zhang, C. Du, W.-X. Ni, M. R. Andersson, and O. Inganäs, "Observation of a charge transfer state in low-bandgap polymer/fullerene blend systems by photoluminescence and electroluminescence studies," *Adv. Funct. Mater.*, vol. 19, pp. 3293–3299, 2009.

[155] T. Drori, C.-X. Sheng, A. Ndobe, S. Singh, J. Holt, and Z. V. Vardeny, "Below-gap excitation of π-conjugated polymer-fullerene blends: Implications for bulk organic heterojunction solar cells," *Phys. Rev. Lett.*, vol. 101, p. 037401, 2008.

[156] K. Vandewal, A. Gadisa, W. D. Oosterbaan, S. Bertho, F. Banishoeib, I. Van Severen, L. Lutsen, T. J. Cleij, D. Vanderzande, and J. V. Manca, "The Relation Between Open-Circuit Voltage and the Onset of Photocurrent

Generation by Charge-Transfer Absorption in Polymer:Fullerene Bulk Heterojunction Solar Cells," *Adv. Funct. Mater.*, vol. 18, pp. 2064–2070, 2008.

[157] L. Goris, K. Haenen, M. Nesládek, P. Wagner, D. Vanderzande, L. Schepper, J. D'haen, L. Lutsen, and J. Manca, "Absorption phenomena in organic thin films for solar cell applications investigated by photothermal deflection spectroscopy," *J. Mater. Sci.*, vol. 40, pp. 1413–1418, 2005.

[158] P. Würfel, "Photovoltaic principles and organic solar cells," *Chimia*, vol. 61, pp. 770–774, 2007.

[159] R. T. Ross, "Thermodynamic limitations on the conversion of radiant energy into work," *J. Chem. Phys.*, vol. 45, pp. 1–7, 1966.

[160] S. C. J. Meskers, P. A. van Hal, A. J. H. Spiering, J. C. Hummelen, A. F. G. van der Meer, and R. A. J. Janssen, "Time-resolved infrared-absorption study of photoinduced charge transfer in a polythiophene-methanofullerene composite film," *Phys. Rev. B*, vol. 61, pp. 9917–9920, 2000.

[161] S. De, T. Pascher, M. Maiti, K. G. Jespersen, T. Kesti, F. Zhang, O. Inganäs, A. Yartsev, and V. Sundström, "Geminate charge recombination in alternating polyfluorene copolymer/fullerene blends," *J. Am. Chem. Soc.*, vol. 129, pp. 8466–8472, 2007.

[162] V. Gulbinas, D. Hertel, A. Yartsev, and V. Sundström, "Charge carrier photogeneration and recombination in ladder-type poly(*para*-phenylene): Interplay between impurities and external electric field," *Phys. Rev. B*, vol. 76, p. 235203, 2007.

[163] A. A. Bakulin, D. S. Martyanov, D. Y. Paraschuk, M. S. Pshenichnikov, and P. H. M. van Loosdrecht, "Ultrafast charge photogeneration dynamics in ground-state charge-transfer complexes based on conjugated polymers," *J. Phys. Chem. B*, vol. 112, pp. 13730–13737, 2008.

[164] I.-W. Hwang, D. Moses, and A. J. Heeger, "Photoinduced Carrier Generation in P3HT/PCBM Bulk Heterojunction Materials," *J. Phys. Chem. C*, vol. 112, pp. 4350–4354, 2008.

[165] S. R. Cowan, A. Roy, and A. J. Heeger, "Recombination in polymer-fullerene bulk heterojunction solar cells," *Phys. Rev. B*, vol. 82, p. 245207, 2010.

[166] W. Shockley and W. T. Read, "Statistics of the recombinations of holes and electrons," *Phys. Rev.*, vol. 87, pp. 835–842, 1952.

[167] R. N. Hall, "Electron-hole recombination in germanium," *Phys. Rev.*, vol. 87, pp. 387–387, 1952.

[168] C. G. Shuttle, B. O'Regan, A. M. Ballantyne, J. Nelson, D. D. C. Bradley, and J. R. Durrant, "Bimolecular recombination losses in polythiophene: Fullerene solar cells," *Phys. Rev. B*, vol. 78, p. 113201, 2008.

[169] A. Maurano, R. Hamilton, C. G. Shuttle, A. M. Ballantyne, J. Nelson, B. O'Regan, W. Zhang, I. McCulloch, H. Azimi, M. Morana, C. J. Brabec, and J. R. Durrant, "Recombination dynamics as a key determinant of open circuit voltage in organic bulk heterojunction solar cells: A comparison of four different donor polymers," *Adv. Mater.*, vol. 22, pp. 4987–4992, 2010.

[170] D. Credgington, F. C. Jamieson, B. Walker, T.-Q. Nguyen, and J. R. Durrant, "Quantification of geminate and non-geminate recombination losses within a solution-processed small-molecule bulk heterojunction solar cell," *Adv. Mater.*, vol. 24, pp. 2135–2141, 2012.

[171] T. Kirchartz, B. E. Pieters, J. Kirkpatrick, U. Rau, and J. Nelson, "Recombination via tail states in polythiophene:fullerene solar cells," *Phys. Rev. B*, vol. 83, p. 115209, 2011.

[172] A. J. Mozer, G. Dennler, N. S. Sariciftci, M. Westerling, A. Pivrikas, R. Österbacka, and Juška, "Time-dependent mobility and recombination of the photoinduced charge carriers in conjugated polymer/fullerene bulk heterojunction solar cells," *Phys. Rev. B*, vol. 72, p. 035217, 2005.

[173] C. Deibel, A. Baumann, and V. Dyakonov, "Polaron recombination in pristine and annealed bulk heterojunction solar cells," *Appl. Phys. Lett.*, vol. 93, p. 163303, 2008.

[174] P. Langevin, "Recombinaison et mobilité des ions gazeux," *Ann. Chim. Phys.*, vol. 28, pp. 433–530, 1903.

[175] P. W. M. Blom, M. J. M. de Jong, and S. Breedijk, "Temperature dependent electron-hole recombination in polymer light-emitting diodes," *Appl. Phys. Lett.*, vol. 71, pp. 930–932, 1997.

[176] L. J. A. Koster, V. D. Mihailetchi, H. Xie, and P. W. M. Blom, "Origin of the light intensity dependence of the short-circuit current of polymer/fullerene solar cells," *Appl. Phys. Lett.*, vol. 87, p. 203502, 2005.

[177] R. A. Street, M. Schoendorf, A. Roy, and J. H. Lee, "Interface state recombination in organic solar cells," *Phys. Rev. B*, vol. 81, p. 205307, 2010.

[178] C. Deibel and A. Wagenpfahl, "Comment on "interface state recombination in organic solar cells"," *Phys. Rev. B*, vol. 82, p. 207301, 2010.

[179] R. A. Street, "Reply to "comment on 'interface state recombination in organic solar cells'"," *Phys. Rev. B*, vol. 82, p. 207302, 2010.

[180] J. A. Barker, C. M. Ramsdale, and N. C. Greenham, "Modeling the current-voltage characteristics of bilayer polymer photovoltaic devices," *Phys. Rev. B*, vol. 67, p. 075205, 2003.

[181] I. Riedel, J. Parisi, V. Dyakonov, L. Lutsen, D. Vanderzande, and J. C. Hummelen, "Effect of temperature and illumination on the electrical characteristics of polymer–fullerene bulk-heterojunction solar cells," *Adv. Funct. Mater.*, vol. 14, pp. 38–44, 2004.

[182] I. Riedel and V. Dyakonov, "Influence of electronic transport properties of polymer-fullerene blends on the performance of bulk heterojunction photovoltaic devices," *Phys. Status Solidi A*, vol. 201, pp. 1332–1341, 2004.

[183] A. Moulé and K. Meerholz, "Intensity-dependent photocurrent generation at the anode in bulk-heterojunction solar cells," *Appl. Phys. B - Lasers. O.*, vol. 92, pp. 209–218, 2008.

[184] V. D. Mihailetchi, J. Wildeman, and P. W. M. Blom, "Space-charge limited photocurrent," *Phys. Rev. Lett.*, vol. 94, p. 126602, 2005.

[185] J. R. Tumbleston, Y. Liu, E. T. Samulski, and R. Lopez, "Interplay between bimolecular recombination and carrier transport distances in bulk heterojunction organic solar cells," *Adv. Energy Mater.*, vol. 2, pp. 477–486, 2012.

[186] J. C. Byers, S. Ballantyne, K. Rodionov, A. Mann, and O. A. Semenikhin, "Mechanism of recombination losses in bulk heterojunction P3HT:PCBM solar cells studied using intensity modulated photocurrent spectroscopy," *ACS Appl. Mater. Interfaces*, vol. 3, pp. 392–401, 2011.

[187] L. Liu and G. Li, "Investigation of recombination loss in organic solar cells by simulating intensity-dependent current–voltage measurements," *Sol. Energy Mater. Sol. Cells*, vol. 95, pp. 2557–2563, 2011.

[188] L. J. A. Koster, M. Kemerink, M. M. Wienk, K. Maturová, and R. A. J. Janssen, "Quantifying bimolecular recombination losses in organic bulk heterojunction solar cells," *Adv. Mater.*, vol. 23, pp. 1670–1674, 2011.

[189] G. F. A. Dibb, T. Kirchartz, D. Credgington, J. R. Durrant, and J. Nelson, "Analysis of the relationship between linearity of corrected photocurrent and the order of recombination in organic solar cells," *J. Phys. Chem. Lett.*, vol. 2, pp. 2407–2411, 2011.

[190] M. M. de Kok, M. Buechel, S. I. E. Vulto, P. van de Weijer, E. A. Meulenkamp, S. H. P. M. de Winter, A. J. G. Mank, H. J. M. Vorstenbosch, C. H. L. Weijtens, and V. van Elsbergen, "Modification of PEDOT:PSS as hole injection layer in polymer LEDs," *Phys. Status Solidi A*, vol. 201,

pp. 1342–1359, 2004.

[191] J. Huang, P. F. Miller, J. S. Wilson, A. J. de Mello, J. C. de Mello, and D. D. C. Bradley, "Investigation of the effects of doping and post-deposition treatments on the conductivity, morphology, and work function of poly(3,4-ethylenedioxythiophene)/poly(styrene sulfonate) films," *Adv. Funct. Mater.*, vol. 15, pp. 290–296, 2005.

[192] P. Peumans and S. R. Forrest, "Very-high-efficiency double-heterostructure copper phthalocyanine/C_{60} photovoltaic cells," *Appl. Phys. Lett.*, vol. 79, pp. 126–128, 2001.

[193] A. Wilke, P. Amsalem, J. Frisch, B. Bröker, A. Vollmer, and N. Koch, "Electric fields induced by energy level pinning at organic heterojunctions," *Appl. Phys. Lett.*, vol. 98, p. 123304, 2011.

[194] Product datasheet available at www.clevios.com.

[195] Product datasheet available at www.plextronics.com.

[196] M. Münch, *Strukturelle Beeinflussung der elektrischen Transporteigenschaften dünner organischer Schichten.* PhD thesis, Universität Stuttgart, 2001.

[197] J. von Braun and G. Manz, "Verfahren zur Herstellung von Kondensationsprodukten des Fluoranthens," 1934. Patent Num. 595 024, Deutsches Reichspatentamt, Berlin.

[198] S. Kowarik, A. Gerlach, S. Sellner, F. Schreiber, L. Cavalcanti, and O. Konovalov, "Real-time observation of structural and orientational transitions during growth of organic thin films," *Phys. Rev. Lett.*, vol. 96, p. 125504, 2006.

[199] A. C. Dürr, F. Schreiber, K. A. Ritley, V. Kruppa, J. Krug, H. Dosch, and B. Struth, "Rapid roughening in thin film growth of an organic semiconductor (diindenoperylene)," *Phys. Rev. Lett.*, vol. 90, p. 016104, 2003.

[200] A. Hinderhofer, *Growth studies of organic heterostructures for photovoltaic application.* PhD thesis, Eberhard-Karls-Universität zu Tübingen, 2011.

[201] N. Koch, A. C. Dürr, J. Ghijsen, R. L. Johnson, J. J. Pireaux, J. Schwartz, F. Schreiber, H. Dosch, and A. Kahn, "Optically induced electron transfer from conjugated organic molecules to charged metal clusters," *Thin Solid Films*, vol. 441, pp. 145–149, 2003.

[202] U. Heinemeyer, *Optical properties of organic semiconductor thin films: Static spectra and real-time growth studies.* PhD thesis, Eberhard-Karls-Universität zu Tübingen, 2009.

[203] A. K. Tripathi and J. Pflaum, "Correlation between ambipolar transport and structural phase transition in diindenoperylene single crystals," *Appl. Phys. Lett.*, vol. 89, p. 082103, 2006.

[204] M. Horlet, M. Kraus, W. Brütting, and A. Opitz, "Diindenoperylene as ambipolar semiconductor: Influence of electrode materials and mobility asymmetry in organic field-effect transistors," *Appl. Phys. Lett*, vol. 98, p. 233304, 2011.

[205] D. Kurrle and J. Pflaum, "Exciton diffusion length in the organic semiconductor diindenoperylene," *Appl. Phys. Lett.*, vol. 92, p. 133306, 2008.

[206] S. Banerjee, A. P. Parhi, S. S. K. Iyer, and S. Kumar, "Method of determining the exciton diffusion length using optical interference effect in Schottky diode," *Appl. Phys. Lett.*, vol. 94, p. 223303, 2009.

[207] M. A. Heinrich, J. Pflaum, A. K. Tripathi, W. Frey, M. L. Steigerwald, and T. Siegrist, "Enantiotropic polymorphism in di-indenoperylene," *J. Phys. Chem. C*, vol. 111, pp. 18878–18881, 2007.

[208] D. G. de Oteyza, E. Barrena, M. Ruiz-Oses, I. Silanes, B. P. Doyle, J. E. Ortega, A. Arnau, H. Dosch, and Y. Wakayama, "Crystallographic and electronic structure of self-assembled DIP monolayers on Au(111) substrates," *J. Phys. Chem. C*, vol. 112, pp. 7168–7172, 2008.

[209] A. Dürr, B. Nickel, V. Sharma, U. Täffner, and H. Dosch, "Observation of competing modes in the growth of diindenoperylene on SiO_2," *Thin Solid Films*, vol. 503, pp. 127 – 132, 2006.

[210] Y. L. Huang, W. Chen, H. Huang, D. C. Qi, S. Chen, X. Y. Gao, J. Pflaum, and A. T. S. Wee, "Ultrathin films of diindenoperylene on graphite and SiO_2," *J. Phys. Chem. C*, vol. 113, pp. 9251–9255, 2009.

[211] A. Hinderhofer, T. Hosokai, K. Yonezawa, A. Gerlach, K. Kato, K. Broch, C. Frank, J. Novák, S. Kera, N. Ueno, and F. Schreiber, "Post-growth surface smoothing of thin films of diindenoperylene," *Appl. Phys. Lett.*, vol. 101, p. 033307, 2012.

[212] R. R. Lunt, J. B. Benziger, and S. R. Forrest, "Relationship between crystalline order and exciton diffusion length in molecular organic semiconductors," *Adv. Mater.*, vol. 22, pp. 1233–1236, 2010.

[213] U. Hörmann, J. Wagner, M. Gruber, A. Opitz, and W. Brütting, "Approaching the ultimate open circuit voltage in thiophene based single junction solar cells by applying diindenoperylene as acceptor," *Phys. Status Solidi Rapid Res. Lett.*, vol. 5, pp. 241–243, 2011.

[214] H. W. Kroto, O. S. C. Heath, J. R. and, R. F. Curl, and R. E. Smalley, "C_{60}: Buckminsterfullerene," *Nature*, vol. 318, p. 162, 1985.

[215] P. A. Heiney, J. E. Fischer, A. R. McGhie, W. J. Romanow, A. M. Denenstein, J. P. McCauley Jr., A. B. Smith, and D. E. Cox, "Orientational ordering transition in solid C_{60}," *Phys. Rev. Lett.*, vol. 66, pp. 2911–2914, 1991.

[216] W. Krätschmer, L. D. Lamb, K. Fostiropoulos, and D. R. Huffman, "Solid C_{60}: a new form of carbon," *Nature*, vol. 347, p. 354, 1990.

[217] W. I. F. David, R. M. Ibberson, T. J. S. Dennis, J. P. Hare, and K. Prassides, "Structural phase transitions in the fullerene C_{60}," *Europhys. Lett.*, vol. 18, p. 219, 1992.

[218] J. L. de Boer, S. van Smaalen, V. Petricek, M. Dusek, M. A. Verheijen, and G. Meijer, "Hexagonal close-packed C_{60}," *Chem. Phys. Lett.*, vol. 219, pp. 469–472, 1994.

[219] M. Bronner, A. Opitz, and W. Brütting, "Ambipolar charge carrier transport in organic semiconductor blends of phthalocyanine and fullerene," *Phys. Status Solidi A*, vol. 205, pp. 549–563, 2008.

[220] A. F. Hebard, R. C. Haddon, R. M. Fleming, and A. R. Kortan, "Deposition and characterization of fullerene films," *Appl. Phys. Lett.*, vol. 59, pp. 2109–2111, 1991.

[221] H. Kataura, Y. Endo, Y. Achiba, K. Kikuchi, T. Hanyu, and S. Yamaguchi, "Dielectric constants of C_{60} and C_{70} thin films," *J. Phys. Chem. Solids*, vol. 58, pp. 1913–1917, 1997.

[222] J. Ortiz-López and R. Gómez-Aguilar, "Dielectric permittivity and AC conductivity in polycrystalline and amorphous C_{60}," *Rev. Mex. Fis.*, vol. 49, pp. 529–536, 2003.

[223] D. F. Kronholm and J. C. Hummelen, *Organic Photovoltaics*. Wiley-VCH, Weinheim, 2008.

[224] P. H. Lippel, R. J. Wilson, M. D. Miller, C. Wöll, and S. Chiang, "High-resolution imaging of copper-phthalocyanine by scanning-tunneling microscopy," *Phys. Rev. Lett.*, vol. 62, pp. 171–174, 1989.

[225] C. C. Leznoff and A. B. P. Lever, eds., *Phthalocyanines - Properties and Applications*. VCH Publishers Inc., New York, 1989.

[226] S. M. Schultes, P. Sullivan, S. Heutz, B. M. Sanderson, and T. S. Jones, "The role of molecular architecture and layer composition on the properties and performance of CuPc-C_{60} photovoltaic devices," *Mat. Sci. Eng. C - Biomim.*,

vol. 25, pp. 858–865, 2005.

[227] Y.-S. Hsiao, W.-T. Whang, S.-C. Suen, J.-Y. Shiu, and C.-P. Chen, "Morphological control of CuPc and its application in organic solar cells," *Nanotechnology*, vol. 19, p. 415603, 2008.

[228] W. Rieß, T. A. Beierlein, and H. Riel, "Optimizing OLED Structures for a-Si Display Applications via Combinatorial Methods and Enhanced Outcoupling," *Phys. Status Solidi A*, vol. 201, pp. 1360–1371, 2004.

[229] M. Bronner, *Ambipolarer Ladungstransport in organischen Halbleiter-Mischschichten bestehend aus C_{60} und CuPc*. PhD thesis, University of Augsburg, 2008.

[230] A. Opitz, M. Bronner, and W. Brütting, "Charge carrier injection and ambipolar transport in C_{60}/CuPc organic semiconductor blends," *J. Phys.: Conf. Series*, vol. 100, p. 082043, 2008.

[231] M. Kraus, S. Richler, A. Opitz, W. Brütting, S. Haas, T. Hasegawa, A. Hinderhofer, and F. Schreiber, "High-mobility copper-phthalocyanine field-effect transistors with tetratetracontane passivation layer and organic metal contacts," *J. Appl. Phys.*, vol. 107, p. 094503, 2010.

[232] P. Erk, H. Hengelsberg, M. F. Haddow, and R. van Gelder, "The innovative momentum of crystal engineering," *CrystEngComm*, vol. 6, pp. 474–483, 2004.

[233] J. Gardener, J. Owen, K. Miki, and S. Heutz, "A scanning tunnelling microscopy investigation into the initial stages of copper phthalocyanine growth on passivated silicon surfaces," *Surf. Sci.*, vol. 602, pp. 843–851, 2008.

[234] A. Hoshino, Y. Takenaka, and H. Miyaji, "Redetermination of the crystal structure of alpha-copper phthalocyanine grown on KCl," *Acta Crystallogr. B*, vol. 59, pp. 393–403, 2003.

[235] I. Bruder, J. Schöneboom, R. Dinnebier, A. Ojala, S. Schäfer, R. Sens, P. Erk, and J. Weis, "What determines the performance of metal phthalocyanines (MPc, M = Zn, Cu, Ni, Fe) in organic heterojunction solar cells? A combined experimental and theoretical investigation," *Org. Electron.*, vol. 11, pp. 377–387, 2010.

[236] C. J. Brown, "Crystal structure of β-copper phthalocyanine," *J. Chem. Soc. A*, vol. 47, pp. 2488–2493, 1968.

[237] M. Ashida, N. Uyeda, and E. Suito, "Unit cell metastable-form constants of various phthalocyanines," *B. Chem. Soc. Jpn.*, vol. 39, pp. 2616–2624, 1966.

[238] R. Prabakaran, R. Kesavamoorthy, G. Reddy, and F. Xavier, "Structural investigation of copper phthalocyanine thin films using X-ray diffraction, Raman scattering and optical absorption measurements," *Phys. Status Solidi B*, vol. 229, pp. 1175–1186, 2002.

[239] W. Chen, H. Huang, S. Chen, Y. L. Huang, X. Y. Gao, and A. T. S. Wee, "Molecular orientation-dependent ionization potential of organic thin films," *Chem. Mater.*, vol. 20, pp. 7017–7021, 2008.

[240] A. Wilke, T. Mizokuro, R.-P. Blum, J. P. Rabe, and N. Koch, "Electronic Properties of Cu-Phthalocyanine/Fullerene Planar and Bulk Hetereojunctions on PEDOT:PSS," *IEEE J. Sel. Top. Quant.*, vol. 16, pp. 1732–1737, 2010.

[241] D. G. de Oteyza, E. Barrena, J. O. Ossó, S. Sellner, and H. Dosch, "Thickness-dependent structural transitions in fluorinated copper-phthalocyanine (F_{16}CuPc) films," *J. Am. Chem. Soc.*, vol. 128, pp. 15052–15053, 2006.

[242] J. Ossó, F. Schreiber, M. Alonso, M. Garriga, E. Barrena, and H. Dosch, "Structure, morphology, and optical properties of thin films of F_{16}CuPc grown on silicon dioxide," *Org. Electron.*, vol. 5, pp. 135–140, 2004.

[243] T. Basova, E. Kol'tsov, A. Hassan, A. Tsargorodskaya, A. Ray, and I. Igumenov, "Thin films of copper hexadecafluorophthalocyanine $CuPcF_{16}$," *Phys. Status Solidi B*, vol. 242, pp. 822–827, 2005.

[244] M. I. Alonso, M. Garriga, J. O. Ossó, F. Schreiber, E. Barrena, and H. Dosch, "Strong optical anisotropies of F_{16}CuPc thin films studied by spectroscopic ellipsometry," *J. Chem. Phys.*, vol. 119, pp. 6335–6340, 2003.

[245] C. Dimitrakopoulos and P. Malenfant, "Organic thin film transistors for large area electronics," *Adv. Mater.*, vol. 14, pp. 99–117, 2002.

[246] R. Ruiz, D. Choudhary, B. Nickel, T. Toccoli, K.-C. Chang, A. C. Mayer, P. Clancy, J. M. Blakely, R. L. Headrick, S. Iannotta, and G. G. Malliaras, "Pentacene thin film growth," *Chem. Mater.*, vol. 16, pp. 4497–4508, 2004.

[247] A. C. Mayer, A. Kazimirov, and G. G. Malliaras, "Dynamics of bimodal growth in pentacene thin films," *Phys. Rev. Lett.*, vol. 97, p. 105503, 2006.

[248] M. Muccini, E. Lunedei, C. Taliani, D. Beljonne, J. Cornil, and J. L. Brédas, "Interchain interaction in a prototypical conjugated oligomer from polarized absorption at 4.2 K: α-sexithienyl single crystal," *J. Chem. Phys.*, vol. 109, pp. 10513–10520, 1998.

[249] M. Muccini, E. Lunedei, A. Bree, G. Horowitz, F. Garnier, and C. Taliani,

"Polarized fluorescence in alpha-sexithienyl single crystal at 4.2 K," *J. Chem. Phys.*, vol. 108, pp. 7327–7333, 1998.

[250] M. A. Loi, C. Martin, H. R. Chandrasekhar, M. Chandrasekhar, W. Graupner, F. Garnier, A. Mura, and G. Bongiovanni, "Primary optical excitations and excited-state interaction energies in sexithiophene," *Phys. Rev. B*, vol. 66, p. 113102, 2002.

[251] G. Horowitz, D. Fichou, X. Peng, Z. Xu, and F. Garnier, "A field-effect transistor based on conjugated alpha-sexithienyl," *Solid State Commun.*, vol. 72, pp. 381–384, 1989.

[252] B. Servet, S. Ries, M. Trotel, P. Alnot, G. Horowitz, and F. Garnier, "X-ray determination of the crystal structure and orientation of vacuum evaporated sexithiophene films," *Adv. Mater.*, vol. 5, pp. 461–464, 1993.

[253] M. A. Loi, E. da Como, F. Dinelli, M. Murgia, R. Zamboni, F. Biscarini, and M. Muccini, "Supramolecular organization in ultra-thin films of α-sexithiophene on silicon dioxide," *Nature Mater.*, vol. 4, pp. 81–85, 2005.

[254] S. Schiefer, M. Huth, A. Dobrinevski, and B. Nickel, "Determination of the crystal structure of substrate-induced pentacene polymorphs in fiber structured thin films," *J. Am. Chem. Soc.*, vol. 129, pp. 10316–10317, 2007.

[255] P. Parisse, S. Picozzi, M. Passacantando, and L. Ottaviano, "Experiments and theory on pentacene in the thin film phase: structural, electronic, transport properties, and gas response to oxygen, nitrogen, and ambient air," *Thin Solid Films*, vol. 515, pp. 8316–8321, 2007.

[256] J. Enderlein, "Single-molecule fluorescence near a metal layer," *Chem. Phys.*, vol. 247, pp. 1–9, 1999.

[257] P. Peumans, V. Bulović, and S. R. Forrest, "Efficient photon harvesting at high optical intensities in ultrathin organic double-heterostructure photovoltaic diodes," *Appl. Phys. Lett.*, vol. 76, pp. 2650–2652, 2000.

[258] M. Vogel, S. Doka, C. Breyer, M. C. Lux-Steiner, and K. Fostiropoulos, "On the function of a bathocuproine buffer layer in organic photovoltaic cells," *Appl. Phys. Lett.*, vol. 89, p. 163501, 2006.

[259] Z. Hong, Z. Huang, and X. Zeng, "Utilization of copper phthalocyanine and bathocuproine as an electron transport layer in photovoltaic cells with copper phthalocyanine/buckminsterfullerene heterojunctions: Thickness effects on photovoltaic performances," *Thin Solid Films*, vol. 515, pp. 3019–3023, 2007.

[260] H. Gommans, B. Verreet, B. P. Rand, R. Muller, J. Poortmans, P. Heremans, and J. Genoe, "On the role of bathocuproine in organic photovoltaic cells,"

Adv. Funct. Mater., vol. 18, pp. 3686–3691, 2008.

[261] Y. Hirose, A. Kahn, V. Aristov, P. Soukiassian, V. Bulovic, and S. R. Forrest, "Chemistry and electronic properties of metal-organic semiconductor interfaces: Al, Ti, In, Sn, Ag, and Au on PTCDA," *Phys. Rev. B*, vol. 54, pp. 13748–13758, 1996.

[262] B. E. Lassiter, G. Wei, S. Wang, J. D. Zimmerman, V. V. Diev, M. E. Thompson, and S. R. Forrest, "Organic photovoltaics incorporating electron conducting exciton blocking layers," *Appl. Phys. Lett.*, vol. 98, p. 243307, 2011.

[263] C. K. Chan, E.-G. Kim, J.-L. Brédas, and A. Kahn, "Molecular n-Type Doping of 1,4,5,8-Naphthalene Tetracarboxylic Dianhydride by Pyronin B Studied Using Direct and Inverse Photoelectron Spectroscopies," *Adv. Funct. Mater.*, vol. 16, pp. 831–837, 2006.

[264] K. Suemori, T. Miyata, M. Yokoyama, and M. Hiramoto, "Organic solar cells protected by very thick naphthalene tetracarboxylic anhydride films," *Appl. Phys. Lett.*, vol. 85, pp. 6269–6271, 2004.

[265] K. Suemori, T. Miyata, M. Yokoyama, and M. Hiramoto, "Three-layered organic solar cells incorporating a nanostructure-optimized phthalocyanine:fullerene codeposited interlayer," *Appl. Phys. Lett.*, vol. 86, p. 063509, 2005.

[266] K. Suemori, Y. Matsumura, M. Yokoyama, and M. Hiramoto, "Large area organic solar cells with thick and transparent protection layers," *Jpn. J. Appl. Phys.*, vol. 45, pp. L472–L474, 2006.

[267] R. Schlaf, B. A. Parkinson, P. A. Lee, K. W. Nebesny, G. Jabbour, B. Kippelen, N. Peyghambarian, and N. R. Armstrong, "Photoemission spectroscopy of LiF coated Al and Pt electrodes," *J. Appl. Phys.*, vol. 84, pp. 6729–6736, 1998.

[268] G. E. Jabbour, Y. Kawabe, S. E. Shaheen, J. F. Wang, M. M. Morrell, B. Kippelen, and N. Peyghambarian, "Highly efficient and bright organic electroluminescent devices with an aluminum cathode," *Appl. Phys. Lett.*, vol. 71, pp. 1762–1764, 1997.

[269] L. S. Hung, C. W. Tang, M. G. Mason, P. Raychaudhuri, and J. Madathil, "Application of an ultrathin LiF/Al bilayer in organic surface-emitting diodes," *Appl. Phys. Lett.*, vol. 78, pp. 544–546, 2001.

[270] L. S. Hung, C. W. Tang, and M. G. Mason, "Enhanced electron injection in organic electroluminescence devices using an Al/LiF electrode," *Appl. Phys.*

Lett., vol. 70, pp. 152–154, 1997.

[271] S. E. Shaheen, G. E. Jabbour, M. M. Morrell, Y. Kawabe, B. Kippelen, N. Peyghambarian, M.-F. Nabor, R. Schlaf, E. A. Mash, and N. R. Armstrong, "Bright blue organic light-emitting diode with improved color purity using a LiF/Al cathode," *J. Appl. Phys.*, vol. 84, pp. 2324–2327, 1998.

[272] T. M. Brown and F. Cacialli, "Contact optimization in polymer light-emitting diodes," *J. Poly. Sci. B*, vol. 41, pp. 2649–2664, 2003.

[273] J.-H. Lee and J.-J. Kim, "Interfacial doping for efficient charge injection in organic semiconductors," *Phys. Status Solidi A*, vol. 209, pp. 1399–1413, 2012.

[274] C. J. Brabec, S. E. Shaheen, C. Winder, N. S. Sariciftci, and P. Denk, "Effect of lif/metal electrodes on the performance of plastic solar cells," *Appl. Phys. Lett.*, vol. 80, pp. 1288–1290, 2002.

[275] M. G. Helander, Z. B. Wang, L. Mordoukhovski, and Z. H. Lu, "Comparison of Alq_3/alkali-metal fluoride/Al cathodes for organic electroluminescent devices," *J. Appl. Phys.*, vol. 104, p. 094510, 2008.

[276] S. Günes, H. Neugebauer, and N. S. Sariciftci, "Conjugated polymer-based organic solar cells," *Chem. Rev.*, vol. 107, pp. 1324–1338, 2007.

[277] D. Grozea, A. Turak, X. D. Feng, Z. H. Lu, D. Johnson, and R. Wood, "Chemical structure of Al/LiF/Alq interfaces in organic light-emitting diodes," *Appl. Phys. Lett.*, vol. 81, pp. 3173–3175, 2002.

[278] C. J. Huang, D. Grozea, A. Turak, and Z. H. Lu, "Passivation effect of Al/LiF electrode on C_{60} diodes," *Appl. Phys. Lett.*, vol. 86, p. 033107, 2005.

[279] K. Kawano and C. Adachi, "Reduced initial degradation of bulk heterojunction organic solar cells by incorporation of stacked fullerene and lithium fluoride interlayers," *Appl. Phys. Lett.*, vol. 96, p. 053307, 2010.

[280] H. B. Michaelson, "The work function of the elements and its periodicity," *J. Appl. Phys.*, vol. 48, pp. 4729–4733, 1977.

[281] N. Koch, J. Ghijsen, R. L. Johnson, J. Schwartz, J.-J. Pireaux, and A. Kahn, "Physisorption-like interaction at the interfaces formed by pentacene and samarium," *J. Phys. Chem. B*, vol. 106, pp. 4192–4196, 2002.

[282] G. Saito and J. P. Ferraris, "Requirements for an "Organic Metal"," *B. Chem. Soc. Jpn.*, vol. 53, pp. 2141–2145, 1980.

[283] K. Shibata, K. Ishikawa, H. Takezoe, H. Wada, and T. Mori, "Contact resistance of dibenzotetrathiafulvalene-based organic transistors with metal and

organic electrodes," *Appl. Phys. Lett.*, vol. 92, p. 023305, 2008.

[284] A. Opitz, M. Kraus, M. Bronner, J. Wagner, and W. Brütting, "Bipolar transport in organic field-effect transistors: Organic semiconductor blends versus contact modification," *New. J. Phys.*, vol. 10, p. 065006, 2008.

[285] A. Opitz, M. Horlet, M. Kiwull, J. Wagner, M. Kraus, and W. BrÃfÂ¼tting, "Bipolar charge transport in organic field-effect transistors: Enabling high mobilities and transport of photo-generated charge carriers by a molecular passivation layer," *Org. Electron.*, vol. 13, pp. 1614–1622, 2012.

[286] Z. Y. Zhong and Y. D. Jiang, "Surface treatments of indium-tin oxide substrates for polymer electroluminescent devices," *Phys. Status Solidi A*, vol. 203, pp. 3882–3892, 2006.

[287] M. Jørgensen, K. Norrman, and F. C. Krebs, "Stability/degradation of polymer solar cells," *Sol. Energy Mater. Sol. Cells*, vol. 92, pp. 686–714, 2008.

[288] S. Ogawa, Y. Kimura, M. Niwano, and H. Ishii, "Trap elimination and injection switching at organic field effect transistor by inserting an alkane (C_{44} H_{90}) layer," *Appl. Phys. Lett*, vol. 90, p. 033504, 2007.

[289] M. Kraus, *Charge carrier transport in organic field-effect devices based on copper-phthalocyanine*. PhD thesis, Universität Augsburg, 2011.

[290] G. Horowitz, "Organic field-effect transistors," *Adv. Mater.*, vol. 10, pp. 365–377, 1998.

[291] G. Binnig, C. F. Quate, and C. Gerber, "Atomic force microscope," *Phys. Rev. Lett.*, vol. 56, pp. 930–933, 1986.

[292] http://gwyddion.net/.

[293] A. C. Boccara, D. Fournier, and J. Badoz, "Thermo-optical spectroscopy: Detection by the "mirage' effect'," *Appl. Phys. Lett.*, vol. 36, pp. 130–132, 1980.

[294] W. B. Jackson, N. M. Amer, A. C. Boccara, and D. Fournier, "Photothermal deflection spectroscopy and detection," *Appl. Opt.*, vol. 20, pp. 1333–1344, 1981.

[295] W. B. Jackson and N. M. Amer, "Direct measurement of gap-state absorption in hydrogenated amorphous silicon by photothermal deflection spectroscopy," *Phys. Rev. B*, vol. 25, pp. 5559–5562, 1982.

[296] M. Tzolov, W. Brütting, V. Petrova-Koch, J. Gmeiner, and M. Schwoerer, "Subgap absorption in poly(p-phenylene vinylene)," *Synth. Met.*, vol. 122, pp. 55–57, 2001.

[297] M. Birkholz, P. Fewster, and C. Genzel, *Thin Film Analysis By X-Ray Scattering*. Wiley-VCH, 2006.

[298] S. Krause, M. B. Casu, A. Scholl, and E. Umbach, "Determination of transport levels of organic semiconductors by UPS and IPS," *New J. Phys.*, vol. 10, p. 085001, 2008.

[299] M. Knupfer and H. Peisert, "Electronic properties of interfaces between model organic semiconductors and metals," *Phys. Status Solidi A*, vol. 201, pp. 1055–1074, 2004.

[300] S. C. Veenstra and H. T. Jonkman, "Energy-level alignment at metal-organic and organic-organic interfaces," *J. Poly. Sci. B*, vol. 41, pp. 2549–2560, 2003.

[301] H. Ishii, H. Oji, E. Ito, N. Hayashi, D. Yoshimura, and K. Seki, "Energy level alignment and band bending at model interfaces of organic electroluminescent devices," *J. Lumin.*, vol. 87-89, pp. 61–65, 2000.

[302] N. Koch and A. Vollmer, "Electrode-molecular semiconductor contacts: Work-function-dependent hole injection barriers versus fermi-level pinning," *Appl. Phys. Lett.*, vol. 89, p. 162107, 2006.

[303] S. Duhm, G. Heimel, I. Salzmann, H. Glowatzki, R. L. Johnson, A. Vollmer, J. P. Rabe, and N. Koch, "Orientation-dependent ionization energies and interface dipoles in ordered molecular assemblies," *Nature Mater.*, vol. 7, pp. 326 – 332, 2008.

[304] F. Reinert and S. Hüfner, "Photoemission spectroscopy—from early days to recent applications," *New J. Phys.*, vol. 7, p. 97, 2005.

[305] J. R. Macdonald, *Impedance Spectroscopy*. John Wiley and Sons, New York, 1987.

[306] S. Scheinert and G. Paasch, "Fabrication and analysis of polymer field-effect transistors," *Phys. Status Solidi A*, vol. 201, pp. 1263–1301, 2004.

[307] A. Pitarch, G. Garcia-Belmonte, J. Bisquert, and H. J. Bolink, "Impedance of space-charge-limited currents in organic light-emitting diodes with double injection and strong recombination," *J. Appl. Phys.*, vol. 100, p. 084502, 2006.

[308] http://www.scribner.com.

[309] F. Baumann, *Oxygen reduction kinetics on mixed conducting SOFC model cathodes*. PhD thesis, Fakultät für Chemie der Universität Stuttgart, 2006.

[310] D. M. Taylor and H. L. Gomes, "Electrical characterization of the rectifying contact between aluminium and electrodeposited poly(3-methylthiophene),"

J. Phys. D: Appl. Phys., vol. 28, pp. 2554–2568, 1995.

[311] S. Nowy, *Understanding losses in OLEDs: optical device simulation and electrical characterization using impedance spectroscopy.* PhD thesis, University of Augsburg, 2010.

[312] G. Brug, A. van den Eeden, M. Sluyters-Rehbach, and J. Sluyters, "The analysis of electrode impedances complicated by the presence of a constant phase element," *J. Electroanal. Chem.*, vol. 176, pp. 275 – 295, 1984.

[313] J.-B. Jorcin, M. E. Orazem, N. Pébère, and B. Tribollet, "CPE analysis by local electrochemical impedance spectroscopy," *Electrochim. Acta*, vol. 51, pp. 1473–1479, 2006.

[314] A. Lasia, "Electrochemical impedance spectroscopy and its applications," in *Modern Aspects of Electrochemistry* (R. White, B. Conway, and J. Bockris, eds.), vol. 32, (New York), p. 143, Kluwer Academic/Plenum Publishers, 1999.

[315] B. Hirschorn, M. E. Orazem, B. Tribollet, V. Vivier, I. Frateur, and M. Musiani, "Determination of effective capacitance and film thickness from constant-phase-element parameters," *Electrochim. Acta*, vol. 55, pp. 6218–6227, 2010.

[316] A. Hinderhofer and F. Schreiber, "Organic–Organic Heterostructures: Concepts and Applications," *ChemPhysChem*, vol. 13, pp. 628–643, 2012.

[317] I. Salzmann, S. Duhm, R. Opitz, R. L. Johnson, J. P. Rabe, and N. Koch, "Structural and electronic properties of pentacene-fullerene heterojunctions," *J. Appl. Phys.*, vol. 104, p. 114518, 2008.

[318] A. Hinderhofer, C. Frank, T. Hosokai, A. Resta, A. Gerlach, and F. Schreiber, "Structure and morphology of coevaporated pentacene-perfluoropentacene thin films," *J. Chem. Phys.*, vol. 134, p. 104702, 2011.

[319] A. Hinderhofer, T. Hosokai, C. Frank, J. Novák, A. Gerlach, and F. Schreiber, "Templating effect for organic heterostructure film growth: Perfluoropentacene on diindenoperylene," *J. Phys. Chem. C*, vol. 115, pp. 16155–16160, 2011.

[320] S. Duhm, I. Salzmann, G. Heimel, M. Oehzelt, A. Haase, R. L. Johnson, J. P. Rabe, and N. Koch, "Controlling energy level offsets in organic/organic heterostructures using intramolecular polar bonds," *Appl. Phys. Lett.*, vol. 94, p. 033304, 2009.

[321] W. Chen, D.-C. Qi, H. Huang, X. Gao, and A. T. S. Wee, "Organic–organic heterojunction interfaces: Effect of molecular orientation," *Adv.*

Funct. Mater., vol. 21, pp. 410–424, 2011.

[322] R. Schueppel, K. Schmidt, C. Uhrich, K. Schulze, D. Wynands, J. L. Brédas, E. Brier, E. Reinold, H.-B. Bu, P. Baeuerle, B. Maennig, M. Pfeiffer, and K. Leo, "Optimizing organic photovoltaics using tailored heterojunctions: A photoinduced absorption study of oligothiophenes with low band gaps," *Phys. Rev. B*, vol. 77, p. 085311, 2008.

[323] M. Svensson, F. Zhang, S. Veenstra, W. Verhees, J. Hummelen, J. Kroon, O. Inganäs, and M. Andersson, "High-performance polymer solar cells of an alternating polyfluorene copolymer and a fullerene derivative," *Adv. Mater.*, vol. 15, pp. 988–991, 2003.

[324] J. C. Bijleveld, R. A. M. Verstrijden, M. M. Wienk, and R. A. J. Janssen, "Maximizing the open-circuit voltage of polymer: Fullerene solar cells," *Appl. Phys. Lett.*, vol. 97, p. 073304, 2010.

[325] T. Kietzke, D. A. M. Egbe, H.-H. Hörhold, and D. Neher, "Comparative Study of M3EH-PPV-Based Bilayer Photovoltaic Devices," *Macromolecules*, vol. 39, pp. 4018–4022, 2006.

[326] Y. Zou, Z. Deng, W. J. Potscavage, M. Hirade, Y. Zheng, and C. Adachi, "Very high open-circuit voltage of 5.89 V in organic solar cells with 10-fold-tandem structure," *Appl. Phys. Lett.*, vol. 100, p. 243302, 2012.

[327] J. Wagner, M. Gruber, A. Hinderhofer, A. Wilke, B. Bröker, J. Frisch, P. Amsalem, A. Vollmer, A. Opitz, N. Koch, F. Schreiber, and W. Brütting, "High fill factor and open circuit voltage in organic photovoltaic cells with diindenoperylene as donor material," *Adv. Funct. Mater.*, vol. 20, pp. 4295–4303, 2010.

[328] J. Wagner, M. Gruber, A. Wilke, Y. Tanaka, K. Topczak, A. Steindamm, U. Hörmann, A. Opitz, Y. Nakayama, H. Ishii, J. Pflaum, N. Koch, and W. Brütting, "Identification of different origins for s-shaped current voltage characteristics in planar heterojunction organic solar cells," *J. Appl. Phys.*, vol. 111, p. 054509, 2012.

[329] B. Friedel, P. E. Keivanidis, T. J. K. Brenner, A. Abrusci, C. R. McNeill, R. H. Friend, and N. C. Greenham, "Effects of layer thickness and annealing of PEDOT:PSS layers in organic photodetectors," *Macromolecules*, vol. 42, pp. 6741–6747, 2009.

[330] S. Sze, *Physics of Semiconductor Devices*. Wiley, New York, 1982.

[331] J. D. Servaites, S. Yeganeh, T. J. Marks, and M. A. Ratner, "Efficiency enhancement in organic photovoltaic cells: Consequences of optimizing series

resistance," *Adv. Funct. Mater.*, vol. 20, pp. 97–104, 2010.

[332] M. D. Perez, C. Borek, S. R. Forrest, and M. E. Thompson, "Molecular and morphological influences on the open circuit voltages of organic photovoltaic devices," *J. Am. Chem. Soc.*, vol. 131, pp. 9281–9286, 2009.

[333] C. Uhrich, D. Wynands, S. Olthof, M. K. Riede, K. Leo, S. Sonntag, B. Maennig, and M. Pfeiffer, "Origin of open circuit voltage in planar and bulk heterojunction organic thin-film photovoltaics depending on doped transport layers," *J. Appl. Phys.*, vol. 104, p. 043107, 2008.

[334] A. Kumar, S. Sista, and Y. Yang, "Dipole induced anomalous S-shape *I–V* curves in polymer solar cells," *J. Appl. Phys.*, vol. 105, p. 094512, 2009.

[335] K. Schulze, C. Uhrich, R. Schüppel, K. Leo, M. Pfeiffer, E. Brier, E. Reinold, and P. Bäuerle, "Efficient Vacuum-Deposited Organic Solar Cells Based on a New Low-Bandgap Oligothiophene and Fullerene C_{60}," *Adv. Mater.*, vol. 18, pp. 2872–2875, 2006.

[336] W. Tress, K. Leo, and M. Riede, "Influence of Hole-Transport Layers and Donor Materials on Open-Circuit Voltage and Shape of *I-V* Curves of Organic Solar Cells," *Adv. Funct. Mater.*, vol. 21, pp. 2140–2149, 2011.

[337] D. Gupta, S. Mukhopadhyay, and K. Narayan, "Fill factor in organic solar cells," *Sol. Energy Mater. Sol. Cells*, vol. 94, pp. 1309–1313, 2010.

[338] H. Jin, M. Tuomikoski, J. Hiltunen, P. Kopola, A. Maaninen, and F. Pino, "Polymer–Electrode Interfacial Effect on Photovoltaic Performances in Poly(3-hexylthiophene):Phenyl-C_{61}-butyric Acid Methyl Ester Based Solar Cells," *J. Phys. Chem. C*, vol. 113, pp. 16807–16810, 2009.

[339] M.-S. Kim, B.-G. Kim, and J. Kim, "Effective variables to control the fill factor of organic photovoltaic cells," *ACS Appl. Mater. Interfaces*, vol. 1, pp. 1264–1269, 2009.

[340] L. M. Andersson, C. Müller, B. H. Badada, F. Zhang, U. Würfel, and O. Inganäs, "Mobility and fill factor correlation in geminate recombination limited solar cells," *J. Appl. Phys.*, vol. 110, p. 024509, 2011.

[341] W. Tress, A. Petrich, M. Hummert, M. Hein, K. Leo, and M. Riede, "Imbalanced mobilities causing S-shaped IV curves in planar heterojunction organic solar cells," *Appl. Phys. Lett*, vol. 98, p. 063301, 2011.

[342] I. H. Campbell, P. S. Davids, D. L. Smith, N. N. Barashkov, and J. P. Ferraris, "The schottky energy barrier dependence of charge injection in organic light-emitting diodes," *Appl. Phys. Lett.*, vol. 72, pp. 1863–1865, 1998.

[343] S. Braun, W. R. Salaneck, and M. Fahlman, "Energy-level alignment at organic/metal and organic/organic interfaces," *Adv. Mater.*, vol. 21, pp. 1450–1472, 2009.

[344] R. Steyrleuthner, S. Bange, and D. Neher, "Reliable electron-only devices and electron transport in n-type polymers," *J. Appl. Phys.*, vol. 105, p. 064509, 2009.

[345] S. Berleb, W. Brütting, and G. Paasch, "Interfacial charges and electric field distribution in organic hetero-layer light-emitting devices," *Org. Electron.*, vol. 1, pp. 41–47, 2000.

[346] F. de Castro, J. Heier, F. Nüesch, and R. Hany, "Origin of the kink in current-density versus voltage curves and efficiency enhancement of polymer-C_{60} heterojunction solar cells," *IEEE J. Sel. Top. Quant.*, vol. 16, pp. 1690–1699, 2010.

[347] J. Bisquert and G. Garcia-Belmonte, "On voltage, photovoltage, and photocurrent in bulk heterojunction organic solar cells," *J. Phys. Chem. Lett.*, vol. 2, pp. 1950–1964, 2011.

[348] F. Fabregat-Santiago, G. Garcia-Belmonte, I. Mora-Seró, and J. Bisquert, "Characterization of nanostructured hybrid and organic solar cells by impedance spectroscopy," *Phys. Chem. Chem. Phys.*, vol. 13, pp. 9083–9118, 2011.

[349] T. Kirchartz, W. Gong, S. A. Hawks, T. Agostinelli, R. C. I. MacKenzie, Y. Yang, and J. Nelson, "Sensitivity of the Mott–Schottky analysis in organic solar cells," *J. Phys. Chem. C*, vol. 116, pp. 7672–7680, 2012.

[350] S. L. M. van Mensfoort and R. Coehoorn, "Determination of injection barriers in organic semiconductor devices from capacitance measurements," *Phys. Rev. Lett.*, vol. 100, p. 086802, 2008.

[351] Y. Gao, "Surface analytical studies of interfaces in organic semiconductor devices," *Mat. Sci. Eng. R*, vol. 68, pp. 39–87, 2010.

[352] N. Koch, "Electronic structure of interfaces with conjugated organic materials," *Phys. Status Solidi Rapid Res. Lett.*, vol. 6, pp. 277–293, 2012.

[353] C. Crowell and S. Sze, "Current transport in metal-semiconductor barriers," *Solid State Electron.*, vol. 9, pp. 1035–1048, 1966.

[354] Y. Gartstein and E. Conwell, "Field-dependent thermal injection into a disordered molecular insulator," *Chem. Phys. Lett.*, vol. 255, pp. 93–98, 1996.

[355] V. I. Arkhipov, E. V. Emelianova, Y. H. Tak, and H. Bässler, "Charge in-

jection into light-emitting diodes: Theory and experiment," *J. Appl. Phys.*, vol. 84, pp. 848–856, 1998.

[356] U. Wolf, V. I. Arkhipov, and H. Bässler, "Current injection from a metal to a disordered hopping system. i. monte carlo simulation," *Phys. Rev. B*, vol. 59, pp. 7507–7513, 1999.

[357] S. Nowy, W. Ren, A. Elschner, W. Lövenich, and W. Brütting, "Impedance spectroscopy as a probe for the degradation of organic light-emitting diodes," *J. Appl. Phys.*, vol. 107, p. 054501, 2010.

[358] R. F. Salzman, J. Xue, B. P. Rand, A. Alexander, M. E. Thompson, and S. R. Forrest, "The effects of copper phthalocyanine purity on organic solar cell performance," *Org. Electron.*, vol. 6, pp. 242–246, 2005.

[359] S. Luan and G. W. Neudeck, "An experimental study of the source/drain parasitic resistance effects in amorphous silicon thin film transistors," *J. Appl. Phys.*, vol. 72, pp. 766–772, 1992.

[360] R. Steyrleuthner, M. Schubert, F. Jaiser, J. C. Blakesley, Z. Chen, A. Facchetti, and D. Neher, "Bulk electron transport and charge injection in a high mobility n-type semiconducting polymer," *Adv. Mater.*, vol. 22, pp. 2799–2803, 2010.

[361] H. Sirringhaus, T. Sakanoue, and J.-F. Chang, "Charge-transport physics of high-mobility molecular semiconductors," *Phys. Status Solidi B*, vol. 249, pp. 1655–1676, 2012.

[362] S. Grecu, M. Bronner, A. Opitz, and W. Brütting, "Characterization of polymeric metal-insulator-semiconductor diodes," *Synth. Met.*, vol. 146, pp. 359–363, 2004.

[363] K. H. Probst and N. Karl, "Energy levels of electron and hole traps in the band gap of doped anthracene crystals," *Phys. Status Solidi A*, vol. 27, pp. 499–508, 1975.

[364] R. W. Lof, M. A. Vanveenendaal, B. Koopmans, H. T. Jonkman, and G. A. Sawatzky, "Band-gap, excitons, and coulomb interaction in solid C_{60}," *Phys. Rev. Lett.*, vol. 68, pp. 3924–3927, 1992.

[365] J. G. Xue, B. P. Rand, S. Uchida, and S. R. Forrest, "Mixed donor-acceptor molecular heterojunctions for photovoltaic applications. II. Device performance," *J. Appl. Phys.*, vol. 98, p. 124903, 2005.

[366] T. Kirchartz, B. E. Pieters, K. Taretto, and U. Rau, "Mobility dependent efficiencies of organic bulk heterojunction solar cells: Surface recombination and charge transfer state distribution," *Phys. Rev. B*, vol. 80, p. 035334,

2009.

[367] A. Foertig, A. Wagenpfahl, T. Gerbich, D. Cheyns, V. Dyakonov, and C. Deibel, "Nongeminate recombination in planar and bulk heterojunction organic solar cells," *Adv. Energy Mater.*, vol. 2, pp. 1483–1489, 2012.

[368] D. Qin, P. Gu, R. S. Dhar, S. G. Razavipour, and D. Ban, "Measuring the exciton diffusion length of C_{60} in organic planar heterojunction solar cells," *Phys. Status Solidi A*, vol. 208, pp. 1967–1971, 2011.

[369] M. Gruber, M. Rawolle, J. Wagner, D. Magerl, U. Hörmann, J. Perlich, S. V. Roth, A. Opitz, F. Schreiber, P. Müller-Buschbaum, and W. Brütting, "Correlating structure and morphology to device performance of molecular organic donor–acceptor photovoltaic cells based on diindenoperylene (DIP) and C_{60}," *Adv. Energy Mater.*, p. n/a, 2013. early view.

[370] H. Brinkmann, C. Kelting, S. Makarov, O. Tsaryova, G. Schnurpfeil, D. Wöhrle, and D. Schlettwein, "Fluorinated phthalocyanines as molecular semiconductor thin films," *Phys. Status Solidi A*, vol. 205, pp. 409–420, 2008.

[371] A. Opitz, J. Wagner, M. Bronner, W. Brütting, A. Hinderhofer, and F. Schreiber, "Molecular semiconductor blends: microstructure, charge carrier transport and application in photovoltaic cells," *Phys. Status Solidi A*, vol. 206, pp. 2683–2694, 2009.

[372] J.-O. Vogel, I. Salzmann, R. Opitz, S. Duhm, B. Nickel, J. P. Rabe, and N. Koch, "Sub-nanometer control of the interlayer spacing in thin films of intercalated rodlike conjugated molecules," *J. Phys. Chem. B*, vol. 111, pp. 14097–14101, 2007.

[373] I. Salzmann, S. Duhm, G. Heimel, J. P. Rabe, N. Koch, M. Oehzelt, Y. Sakamoto, and T. Suzuki, "Structural order in perfluoropentacene thin films and heterostructures with pentacene," *Langmuir*, vol. 24, pp. 7294–7298, 2008.

[374] A. Opitz, B. Ecker, J. Wagner, A. Hinderhofer, F. Schreiber, J. Manara, J. Pflaum, and W. Brütting, "Mixed crystalline films of co-evaporated hydrogen- and fluorine-terminated phthalocyanines and their application in photovoltaic devices," *Org. Electron.*, vol. 10, pp. 1259–1267, 2009.

[375] B. Yu, F. Zhu, H. Wang, G. Li, and D. Yan, "All-organic tunnel junctions as connecting units in tandem organic solar cell," *J. Appl. Phys.*, vol. 104, p. 114503, 2008.

[376] A. Opitz, J. Wagner, W. Brütting, I. Salzmann, N. Koch, J. Manara,

J. Pflaum, A. Hinderhofer, and F. Schreiber, "Charge separation at molecular donor-acceptor interfaces: Correlation between morphology and solar cell performance," *IEEE J. Sel. Top. Quant.*, vol. 16, pp. 1707–1717, 2010.

[377] P. Sullivan, S. Heutz, S. M. Schultes, and T. S. Jones, "Influence of codeposition on the performance of CuPc-C_{60} heterojunction photovoltaic devices," *Appl. Phys. Lett.*, vol. 84, pp. 1210–1212, 2004.

[378] A. Opitz, M. Bronner, J. Wagner, M. Götzenbrugger, and W. Brütting, "Ambipolar organic semiconductor blends for photovoltaic cells," *Proc. SPIE*, vol. 7002, p. 70020J, 2008.

[379] M. A. Green, "General temperature dependence of solar cell performance and implications for device modelling," *Prog. Photovolt. Res. Appl.*, vol. 11, pp. 333–340, 2003.

[380] A. Fahrenbruch and J. Aranovich, "Heterojunction phenomena and interfacial defects in photovoltaic converters," in *Solar Energy Conversion* (B. Seraphin, ed.), vol. 31 of *Topics in Applied Physics*, pp. 257–326, Springer Berlin Heidelberg, 1979.

[381] K. Harada, A. G. Werner, M. Pfeiffer, C. J. Bloom, C. M. Elliott, and K. Leo, "Organic homojunction diodes with a high built-in potential: Interpretation of the current-voltage characteristics by a generalized Einstein relation," *Phys. Rev. Lett.*, vol. 94, p. 036601, 2005.

[382] K. Harada, M. Riede, K. Leo, O. R. Hild, and C. M. Elliott, "Pentacene homojunctions: Electron and hole transport properties and related photovoltaic responses," *Phys. Rev. B*, vol. 77, p. 195212, 2008.

[383] G. A. H. Wetzelaer, L. J. A. Koster, and P. W. M. Blom, "Validity of the Einstein relation in disordered organic semiconductors," *Phys. Rev. Lett.*, vol. 107, p. 066605, 2011.

[384] P. Erwin and M. E. Thompson, "Elucidating the interplay between dark current coupling and open circuit voltage in organic photovoltaics," *Appl. Phys. Lett.*, vol. 98, p. 223305, 2011.

[385] C. Waldauf, M. C. Scharber, P. Schilinsky, J. A. Hauch, and C. J. Brabec, "Physics of organic bulk heterojunction devices for photovoltaic applications," *J. Appl. Phys.*, vol. 99, p. 104503, 2006.

[386] J. C. Nolasco, A. Sánchez-Díaz, R. Cabré, J. Ferré-Borrull, L. F. Marsal, E. Palomares, and J. Pallarès, "Relation between the barrier interface and the built-in potential in pentacene/C_{60} solar cell," *Appl. Phys. Lett.*, vol. 97, p. 013305, 2010.

[387] A. K. Thakur, G. Wantz, G. Garcia-Belmonte, J. Bisquert, and L. Hirsch, "Temperature dependence of open-circuit voltage and recombination processes in polymer–fullerene based solar cells," *Sol. Energy Mater. Sol. Cells*, vol. 95, pp. 2131–2135, 2011.

[388] A. Manor and E. A. Katz, "Open-circuit voltage of organic photovoltaics: Implications of the generalized einstein relation for disordered semiconductors," *Sol. Energy Mater. Sol. Cells*, vol. 97, pp. 132–138, 2012.

[389] D. Rauh, A. Wagenpfahl, C. Deibel, and V. Dyakonov, "Relation of open circuit voltage to charge carrier density in organic bulk heterojunction solar cells," *Appl. Phys. Lett.*, vol. 98, p. 133301, 2011.

[390] C. W. Schlenker and M. E. Thompson, "The molecular nature of photovoltage losses in organic solar cells," *Chem. Commun.*, vol. 47, pp. 3702–3716, 2011.

[391] S. Yamamoto, A. Orimo, H. Ohkita, H. Benten, and S. Ito, "Molecular understanding of the open-circuit voltage of polymer:fullerene solar cells," *Adv. Energy Mater.*, vol. 2, pp. 229–237, 2012.

[392] T. Gotoh, S. Nonomura, S. Hirata, and S. Nitta, "Photothermal bending spectroscopy and photothermal deflection spectroscopy of C_{60} thin films," *Appl. Surf. Sci.*, vol. 113-114, pp. 278–281, 1997.

[393] K. Vandewal, K. Tvingstedt, A. Gadisa, O. Inganäs, and J. V. Manca, "Relating the open-circuit voltage to interface molecular properties of donor:acceptor bulk heterojunction solar cells," *Phys. Rev. B*, vol. 81, p. 125204, 2010.

[394] U. Heinemeyer, R. Scholz, L. Gisslén, M. I. Alonso, J. O. Ossó, M. Garriga, A. Hinderhofer, M. Kytka, S. Kowarik, A. Gerlach, and F. Schreiber, "Exciton-phonon coupling in diindenoperylene thin films," *Phys. Rev. B*, vol. 78, p. 085210, 2008.

[395] M. Heilig, M. Domhan, and H. Port, "Optical properties and morphology of thin diindenoperylene films," *J. Lumin.*, vol. 110, pp. 290–295, 2004.

[396] D. Zhang, A. Horneber, J. Mihaljevic, U. Heinemeyer, K. Braun, F. Schreiber, R. Scholz, and A. Meixner, "Plasmon resonance modulated photoluminescence and raman spectroscopy of diindenoperylene organic semiconductor thin film," *J. Lumin.*, vol. 131, pp. 502–505, 2011.

[397] V. Capozzi, G. Casamassima, G. Lorusso, A. Minafra, R. Piccolo, T. Trovato, and A. Valentini, "Optical spectra and photoluminescence of C_{60} thin films," *Solid State Commun.*, vol. 98, pp. 853–858, 1996.

[398] N. Sariciftci, "Role of buckminsterfullerene, C_{60}, in organic photoelectric de-

vices," *Prog. Quant. Electron.*, vol. 19, pp. 131–159, 1995.

[399] M. Fox, *Optische Eigenschaften von Festkörpern.* Oldenbourg Wissenschaftsverlag, 2012.

[400] A. Kabakchiev, K. Kuhnke, T. Lutz, and K. Kern, "Electroluminescence from individual pentacene nanocrystals," *ChemPhysChem*, vol. 11, pp. 3412–3416, 2010.

[401] A. M. C. Ng, A. B. Djurišić, W.-K. Chan, and J.-M. Nunzi, "Near infrared emission in rubrene:fullerene heterojunction devices," *Chem. Phys. Lett.*, vol. 474, pp. 141–145, 2009.

[402] P. P. Boix, A. Guerrero, L. F. Marchesi, G. Garcia-Belmonte, and J. Bisquert, "Current-voltage characteristics of bulk heterojunction organic solar cells: Connection between light and dark curves," *Adv. Energy Mater.*, vol. 1, pp. 1073–1078, 2011.

[403] J. Bisquert and I. Mora-Seró, "Simulation of steady-state characteristics of dye-sensitized solar cells and the interpretation of the diffusion length," *J. Phys. Chem. Lett.*, vol. 1, pp. 450–456, 2010.

[404] F. Fabregat-Santiago, J. Bisquert, G. Garcia-Belmonte, G. Boschloo, and A. Hagfeldt, "Influence of electrolyte in transport and recombination in dye-sensitized solar cells studied by impedance spectroscopy," *Sol. Energy Mater. Sol. Cells*, vol. 87, pp. 117–131, 2005.

[405] D. Cheyns, J. Poortmans, P. Heremans, C. Deibel, S. Verlaak, B. P. Rand, and J. Genoe, "Analytical model for the open-circuit voltage and its associated resistance in organic planar heterojunction solar cells," *Phys. Rev. B*, vol. 77, p. 165332, 2008.

[406] W. L. Leong, S. R. Cowan, and A. J. Heeger, "Differential resistance analysis of charge carrier losses in organic bulk heterojunction solar cells: Observing the transition from bimolecular to trap-assisted recombination and quantifying the order of recombination," *Adv. Energy Mater.*, vol. 1, pp. 517–522, 2011.

[407] G. Garcia-Belmonte, P. P. Boix, J. Bisquert, M. Sessolo, and H. J. Bolink, "Simultaneous determination of carrier lifetime and electron density-of-states in P3HT:PCBM organic solar cells under illumination by impedance spectroscopy," *Sol. Energy Mater. Sol. Cells*, vol. 94, pp. 366–375, 2010.

[408] J. Bisquert, "Chemical capacitance of nanostructured semiconductors: its origin and significance for nanocomposite solar cells," *Phys. Chem. Chem. Phys.*, vol. 5, pp. 5360–5364, 2003.

[409] M. Büttiker, H. Thomas, and A. Prêtre, "Mesoscopic capacitors," *Phys. Lett. A*, vol. 180, pp. 364–369, 1993.

[410] C. G. Shuttle, R. Hamilton, B. C. O'Regan, J. Nelson, and J. R. Durrant, "Charge-density-based analysis of the current–voltage response of polythiophene/fullerene photovoltaic devices," *Proc. Natl. Acad. Sci. U.S.A.*, vol. 107, pp. 16448–16452, 2010.

[411] D. Credgington, Y. Kim, J. Labram, T. D. Anthopoulos, and J. R. Durrant, "Analysis of Recombination Losses in a Pentacene/C_{60} Organic Bilayer Solar Cell," *J. Phys. Chem. Lett.*, vol. 2, pp. 2759–2763, 2011.

[412] P. Peumans and S. R. Forrest, "Separation of geminate charge-pairs at donor–acceptor interfaces in disordered solids," *Chem. Phys. Lett.*, vol. 398, pp. 27–31, 2004.

[413] D. Veldman, Ö. İpek, S. C. J. Meskers, J. Sweelssen, M. M. Koetse, S. C. Veenstra, J. M. Kroon, S. S. v. Bavel, J. Loos, and R. A. J. Janssen, "Compositional and electric field dependence of the dissociation of charge transfer excitons in alternating polyfluorene copolymer/fullerene blends," *J. Am. Chem. Soc.*, vol. 130, pp. 7721–7735, 2008.

[414] Z. E. Ooi, T. L. Tam, A. Sellinger, and J. C. deMello, "Field-dependent carrier generation in bulk heterojunction solar cells," *Energy Environ. Sci.*, vol. 1, pp. 300–309, 2008.

[415] M. M. Mandoc, W. Veurman, L. J. A. Koster, B. de Boer, and P. W. M. Blom, "Origin of the Reduced Fill Factor and Photocurrent in MDMO-PPV:PCNEPV All-Polymer Solar Cells," *Adv. Funct. Mater.*, vol. 17, pp. 2167–2173, 2007.

[416] D. Credgington, R. Hamilton, P. Atienzar, J. Nelson, and J. R. Durrant, "Non-geminate recombination as the primary determinant of open-circuit voltage in polythiophene:fullerene blend solar cells: an analysis of the influence of device processing conditions," *Adv. Funct. Mater.*, vol. 21, pp. 2744–2753, 2011.

[417] S. Inal, M. Schubert, A. Sellinger, and D. Neher, "The relationship between the electric field-induced dissociation of charge transfer excitons and the photocurrent in small molecular/polymeric solar cells," *J. Phys. Chem. Lett.*, vol. 1, pp. 982–986, 2010.

[418] F. C. Jamieson, T. Agostinelli, H. Azimi, J. Nelson, and J. R. Durrant, "Field-Independent Charge Photogeneration in PCPDTBT/PC_{70}BM Solar Cells," *J. Phys. Chem. Lett.*, vol. 1, pp. 3306–3310, 2010.

[419] R. A. Street, S. Cowan, and A. J. Heeger, "Experimental test for geminate recombination applied to organic solar cells," *Phys. Rev. B*, vol. 82, p. 121301, 2010.

[420] F. Etzold, I. A. Howard, R. Mauer, M. Meister, T.-D. Kim, K.-S. Lee, N. S. Baek, and F. Laquai, "Ultrafast Exciton Dissociation Followed by Nongeminate Charge Recombination in PCDTBT:PCBM Photovoltaic Blends," *J. Am. Chem. Soc.*, vol. 133, pp. 9469–9479, 2011.

[421] K. Tvingstedt, K. Vandewal, F. Zhang, and O. Inganäs, "On the dissociation efficiency of charge transfer excitons and frenkel excitons in organic solar cells: A luminescence quenching study," *J. Phys. Chem. C*, vol. 114, pp. 21824–21832, 2010.

[422] P. Heremans, D. Cheyns, and B. P. Rand, "Strategies for increasing the efficiency of heterojunction organic solar cells: Material selection and device architecture," *Acc. Chem. Res.*, vol. 42, pp. 1740–1747, 2009.

[423] G. A. H. Wetzelaer, M. Kuik, M. Lenes, and P. W. M. Blom, "Origin of the dark-current ideality factor in polymer:fullerene bulk heterojunction solar cells," *Appl. Phys. Lett.*, vol. 99, p. 153506, 2011.

[424] S. R. Cowan, W. L. Leong, N. Banerji, G. Dennler, and A. J. Heeger, "Identifying a threshold impurity level for organic solar cells: Enhanced first-order recombination via well-defined $PC_{84}BM$ traps in organic bulk heterojunction solar cells," *Adv. Funct. Mater.*, vol. 21, pp. 3083–3092, 2011.

[425] G. A. H. Wetzelaer, M. Kuik, H. T. Nicolai, and P. W. M. Blom, "Trap-assisted and langevin-type recombination in organic light-emitting diodes," *Phys. Rev. B*, vol. 83, p. 165204, 2011.

[426] R.-Y. Sah, R. N. Noyce, and W. Shockley, "Carrier generation and recombination in p-n junctions and p-n junction characteristics," *Proceedings of the IRE*, vol. 45, pp. 1228–1243, 1957.

[427] R. Street, K. Song, and S. Cowan, "Influence of series resistance on the photocurrent analysis of organic solar cells," *Org. Electron.*, vol. 12, pp. 244–248, 2011.

[428] Y. Zhang, X.-D. Dang, C. Kim, and T.-Q. Nguyen, "Effect of charge recombination on the fill factor of small molecule bulk heterojunction solar cells," *Adv. Energy Mater.*, vol. 1, pp. 610–617, 2011.

[429] L. J. A. Koster, V. D. Mihailetchi, R. Ramaker, and P. W. M. Blom, "Light intensity dependence of open-circuit voltage of polymer:fullerene solar cells," *Appl. Phys. Lett.*, vol. 86, p. 123509, 2005.

[430] M. A. Baldo, S. Lamansky, P. E. Burrows, M. E. Thompson, and S. R. Forrest, "Very high-efficiency green organic light-emitting devices based on electrophosphorescence," *Appl. Phys. Lett.*, vol. 75, pp. 4–6, 1999.

[431] Q. Song, F. Li, H. Yang, H. Wu, X. Wang, W. Zhou, J. Zhao, X. Ding, C. Huang, and X. Hou, "Small-molecule organic solar cells with improved stability," *Chem. Phys. Lett.*, vol. 416, pp. 42–46, 2005.

[432] A. S. Yapi, L. Toumi, Y. Lare, G. M. Soto, L. Cattin, K. Toubal, A. Djafri, M. Morsli, A. Khelil, M. A. Del Valle, and J.-C. Bernède, "On the influence of the exciton-blocking layer on the organic multilayer cells properties," *Eur. Phys. J. - Appl. Phys.*, vol. 50, 2010.

[433] Q. L. Song, M. L. Wang, E. G. Obbard, X. Y. Sun, X. M. Ding, X. Y. Hou, and C. M. Li, "Degradation of small-molecule organic solar cells," *Appl. Phys. Lett.*, vol. 89, p. 251118, 2006.

[434] Z. Hong, Z. Huang, and X. Zeng, "Investigation into effects of electron transporting materials on organic solar cells with copper phthalocyanine/C_{60} heterojunctions," *Chem. Phys. Lett.*, vol. 425, pp. 62–65, 2006.

[435] Y. Berredjem, N. Karst, A. Boulmokh, A. Drici, and J. C. Bernède, "Optimisation of the interface organic "material/aluminium" of CuPc/C_{60} based photovoltaic cells," *Eur. Phys. J. - Appl. Phys.*, vol. 40, pp. 163–167, 2007.

[436] V. Tripathi, D. Datta, G. Samal, A. Awasthi, and S. Kumar, "Role of exciton blocking layers in improving efficiency of copper phthalocyanine based organic solar cells," *J. Non-Cryst. Solids*, vol. 354, pp. 2901– 2904, 2008.

[437] Y. Lare, B. Kouskoussa, K. Benchouk, S. O. Djobo, L. Cattin, M. Morsli, F. Diaz, M. Gacitua, T. Abachi, M. del Valle, F. Armijo, G. A. East, and J. Bernède, "Influence of the exciton blocking layer on the stability of layered organic solar cells," *J. Phys. Chem. Solids*, vol. 72, pp. 97–103, 2011.

[438] B. Rand, J. Li, J. Xue, R. Holmes, M. Thompson, and S. Forrest, "Organic Double-Heterostructure Photovoltaic Cells Employing Thick Tris(acetylacetonato)ruthenium(III) Exciton-Blocking Layers," *Adv. Mater.*, vol. 17, pp. 2714–2718, 2005.

[439] H. Tachikawa and H. Kawabata, "A density functional theory study on the degradation mechanism of thin film of organic semiconductor by water molecules," *Thin Solid Films*, vol. 516, pp. 3287–3293, 2008.

[440] A. Steindamm, M. Brendel, A. K. Topczak, and J. Pflaum, "Thickness dependent effects of an intermediate molecular blocking layer on the optoelectronic characteristics of organic bilayer photovoltaic cells," *Appl. Phys. Lett.*,

vol. 101, p. 143302, 2012.

[441] A. C. Dürr, F. Schreiber, M. Kelsch, and H. Dosch, "Optimized preparation of cross-sectional tem specimens of organic thin films," *Ultramicroscopy*, vol. 98, pp. 51–55, 2003.

[442] M. Scharnberg, J. Hu, J. Kanzow, K. Rätzke, R. Adelung, F. Faupel, C. Pannemann, U. Hilleringmann, S. Meyer, and J. Pflaum, "Radiotracer measurements as a sensitive tool for the detection of metal penetration in molecular-based organic electronics," *Appl. Phys. Lett.*, vol. 86, p. 024104, 2005.

[443] A. K. Pandey, P. E. Shaw, I. D. W. Samuel, and J.-M. Nunzi, "Effect of metal cathode reflectance on the exciton-dissociation efficiency in heterojunction organic solar cells," vol. 94, no. 10, p. 103303, 2009.

[444] T. Roller, *Diindeno-Perylen als Absorber in organischen photovoltaischen Zellen*. PhD thesis, Universität Stuttgart, 2010.

[445] J. Meiss, A. Merten, M. Hein, C. Schuenemann, S. Schäfer, M. Tietze, C. Uhrich, M. Pfeiffer, K. Leo, and M. Riede, "Fluorinated zinc phthalocyanine as donor for efficient vacuum-deposited organic solar cells," *Adv. Funct. Mater.*, vol. 22, pp. 405–414, 2012.

[446] J. Zhang, I. Salzmann, S. Rogaschewski, J. P. Rabe, N. Koch, F. Zhang, and Z. Xu, "Arrays of crystalline C_{60} and pentacene nanocolumns," *Appl. Phys. Lett.*, vol. 90, p. 193117, 2007.

[447] M. M. Hawkeye and M. J. Brett, "Glancing angle deposition: Fabrication, properties, and applications of micro- and nanostructured thin films," *J. Vac. Sci. Technol. A*, vol. 25, p. 1317, 2007.

[448] N. Li and S. R. Forrest, "Tilted bulk heterojunction organic photovoltaic cells grown by oblique angle deposition," *Appl. Phys. Lett*, vol. 95, p. 123309, 2009.

[449] M.-S. Kim, J.-S. Kim, J. C. Cho, M. Shtein, L. J. Guo, and J. Kim, "Flexible conjugated polymer photovoltaic cells with controlled heterojunctions fabricated using nanoimprint lithography," *Appl. Phys. Lett.*, vol. 90, p. 123113, 2007.

[450] D. Cheyns, K. Vasseur, C. Rolin, J. Genoe, J. Poortmans, and P. Heremans, "Nanoimprinted semiconducting polymer films with 50 nm features and their application to organic heterojunction solar cells," *Nanotechnology*, vol. 19, p. 424016, 2008.

[451] W. Zeng, K. S. L. Chong, H. Y. Low, E. L. Williams, T. L. Tam, and A. Sellinger, "The use of nanoimprint lithography to improve efficiencies of bilayer

organic solar cells based on p3ht and a small molecule acceptor," *Thin Solid Films*, vol. 517, pp. 6833–6836, 2009.

[452] T. Ameri, G. Dennler, C. Lungenschmied, and C. J. Brabec, "Organic tandem solar cells: A review," *Energy Environ. Sci.*, vol. 2, pp. 347–363, 2009.

[453] P. Schilinsky, C. Waldauf, and C. J. Brabec, "Performance analysis of printed bulk heterojunction solar cells," *Adv. Funct. Mater.*, vol. 16, pp. 1669–1672, 2006.

[454] R. O. Loutfy, J. H. Sharp, C. K. Hsiao, and R. Ho, "Phthalocyanine organic solar cells: Indium/x-metal free phthalocyanine Schottky barriers," *J. Appl. Phys.*, vol. 52, pp. 5218–5230, 1981.

List of publications

- A. Opitz, M. Kraus, M. Bronner, J. Wagner, and W. Brütting
  "Bipolar transport in organic field-effect transistors: Organic semiconductor blends versus contact modification"
  New. J. Phys., vol. 10, p. 065006, 2008.
- A. Opitz, M. Bronner, J. Wagner, M. Götzenbrugger, and W. Brütting
  "Ambipolar organic semiconductor blends for photovoltaic cells"
  Proc. SPIE, vol. 7002, p. 70020J, 2008.
- A. Opitz, J. Wagner, B. Ecker, U. Hörmann, M. Kraus, M. Bronner, W. Brütting, A. Hinderhofer, and F. Schreiber
  "Microstructure and charge carrier transport in phthalocyanine based semiconductor blends"
  MRS Symp. Proc., vol. 1154, p. B09–12, 2009.
- S. Nowy, W. Ren, J. Wagner, J. A. Weber, and W. Brütting
  "Impedance spectroscopy of organic hetero-layer oleds as a probe for charge carrier injection and device degradation"
  Proc. SPIE, vol. 7415, p. 74150G, 2009.
- A. Opitz, B. Ecker, J. Wagner, A. Hinderhofer, F. Schreiber, J. Manara, J. Pflaum, and W. Brütting
  "Mixed crystalline films of co-evaporated hydrogen- and fluorine-terminated phthalocyanines and their application in photovoltaic devices"
  Org. Electron., vol. 10, pp. 1259–1267, 2009.
- A. Opitz, J. Wagner, M. Bronner, W. Brütting, A. Hinderhofer, and F. Schreiber
  "Molecular semiconductor blends: microstructure, charge carrier transport and application in photovoltaic cells"
  Phys. Status Solidi A, vol. 206, pp. 2683–2694, 2009.

- A. Opitz, J. Wagner, W. Brütting, I. Salzmann, N. Koch, J. Manara, J. Pflaum, A. Hinderhofer, and F. Schreiber
"Charge separation at molecular donor-acceptor interfaces: Correlation between morphology and solar cell performance"
IEEE J. Sel. Top. Quant., vol. 16, pp. 1707–1717, 2010.

- J. Wagner, M. Gruber, A. Hinderhofer, A. Wilke, B. Bröker, J. Frisch, P. Amsalem, A. Vollmer, A. Opitz, N. Koch, F. Schreiber, and W. Brütting
"High fill factor and open circuit voltage in organic photovoltaic cells with diindenoperylene as donor material"
Adv. Funct. Mater., vol. 20, pp. 4295–4303, 2010.

- K. Akaike, A. Opitz, J. Wagner, W. Brütting, K. Kanai, Y. Ouchi, and K. Seki
"Unoccupied states in copper phthalocyanine/fullerene blended films determined by inverse photoemission spectroscopy"
Org. Electron., vol. 11, pp. 1853–1857, 2010.

- U. Hörmann, J. Wagner, M. Gruber, A. Opitz, and W. Brütting
"Approaching the ultimate open circuit voltage in thiophene based single junction solar cells by applying diindenoperylene as acceptor"
Phys. Status Solidi Rapid Res. Lett., vol. 5, pp. 241–243, 2011.

- J. Wagner, M. Gruber, A. Wilke, Y. Tanaka, K. Topczak, A. Steindamm, U. Hörmann, A. Opitz, Y. Nakayama, H. Ishii, J. Pflaum, N. Koch, and W. Brütting
"Identification of different origins for s-shaped current voltage characteristics in planar heterojunction organic solar cells,"
J. Appl. Phys., vol. 111, p. 054509, 2012.

- A. Opitz, M. Horlet, M. Kiwull, J. Wagner, M. Kraus, and W. Brütting
"Bipolar charge transport in organic field-effect transistors: Enabling high mobilities and transport of photo-generated charge carriers by a molecular passivation layer"
Org. Electron., vol. 13, pp. 1614–1622, 2012.

- M. Gruber, J. Wagner, K. Klein, U. Hörmann, A. Opitz, M. Stutzmann, and W. Brütting
"Thermodynamic efficiency limit of molecular donor-acceptor solar cells and its application to diindenoperylene/C_{60} based planar hetero-junction devices"
Adv. Energy Mater., vol. 2, pp. 1100–1108, 2012.

- A. Wilke, J. Endres, U. Hörmann, J. Niederhausen, R. Schlesinger, J. Frisch, P. Amsalem, J. Wagner, M. Gruber, A. Opitz, A. Vollmer, W. Brütting,

A. Kahn, and N. Koch
"Correlation between interface energetics and open circuit voltage in organic photovoltaic cells"
Appl. Phys. Lett., vol. 101, p. 233301, 2012.

- M. Gruber, M. Rawolle, J. Wagner, D. Magerl, U. Hörmann, J. Perlich, S.V. Roth, A. Opitz, F. Schreiber, P. Müller-Buschbaum, W. Brütting
"Correlating structure and morphology to device performance of molecular organic donor–acceptor photovoltaic cells based on diindenoperylene (DIP) and C_{60}"
Adv. Energy Mater., early view, 2013.

Danksagung – Acknowledgments

Letztendlich möchte ich mich bei allen bedanken, die mich bei meiner Arbeit unterstützt und zum Gelingen der Arbeit beigetragen haben.

- **Prof. Dr. Wolfgang Brütting** danke ich herzlichst für die Möglichkeit, meine Promotion in seiner Arbeitsgruppe "Organische Halbleiter" durchführen zu können – insbesondere für das mir entgegengebrachte Vertrauen und die Freiheit, mit der ich meine eigenen Forschungsinteressen verfolgen konnte, für die gute Betreuung und Unterstützung während meiner Arbeit sowie die Ermöglichung mehrerer Auflandsaufenthalte im Rahmen der Promotion.
- Ich danke **Prof. Dr. Bernd Stritzker** für die freundliche Aufnahme an seinen Lehrstuhl.
- **PD Dr. Andreas Opitz** danke ich für die Betreuung und fachliche Unterstützung während seiner Zeit in Augsburg, seine zahlreichen Ideen und seine Hilfsbereitschaft. Insbesondere danke ich ihm für das sorgfältige Korrekturlesen der Arbeit.
- Der **Deutschen Forschungsgesellschaft** danke ich für die Förderung im Rahmen des Schwerpunktprogrammes SPP 1355 "Elementarprozesse der Organischen Photovoltaik" und für die darüber hinausgehende finanzielle Unterstützung des Aufenthaltes an der Universität Jaume I in Spanien.
- Im Rahmen des Schwerpunktprogrammes danke ich für die wunderbare Kooperation mit den Projektpartnern. Mein Dank gilt insbesondere **Prof. Dr. Norbert Koch** und **Andreas Wilke** der Humboldt-Universität Berlin, **Prof. Dr. Jens Pflaum**, **Katharina Topczak** und **Andreas Steindamm** der Universität Würzburg sowie **Prof. Dr. Frank Schreiber** – dem mein besonderer Dank für seine Bereitschaft zur Erstellung des Zweitgutachtens gilt – sowie **Dr. Alexander Hinderhofer** und **Christopher Lorch** der Universität Tübingen. Ihnen allen danke ich ganz herzlich für die inspirierende,

bereichernde und unkomplizierte Zusammenarbeit sowie zahlreiche Messungen und Diskussionen, die entscheidend zum Verständnis der vorgestellten Materialsysteme beigetragen haben.

- A research stay at the University of Chiba, Japan, was made possible by the **Japan Society for the Promotion of Science** (JSPS) by means of an excellently organized scholarship. I would like to express my appreciation to **Prof. Dr. Hisao Ishii**, **Assist. Prof. Dr. Yasuo Nakayama**, **Assist. Prof. Dr. Yutaka Noguchi**, **Dr. Yuya Tanaka**, **Dr. Machida Shin-ichi** and **Kuniko Ito** as well as all employees and students of the "Ishii Laboratory for organic electronics" for their technical support and the warm welcome to the work group.
- Mein Dank gilt auch dem **Förderprogramm "Chancengleicheit"** für das Promotionsstipendium in der Abschlussphase.
- **Dr. Hubert Krenner** und **Stephan Kapfinger** vom Lehrstuhl EPI danke ich für die hervorragende Zusammenarbeit im Rahmen der Elektrolumineszenz-Untersuchungen.
- I thank **Prof. Dr. Juan Bisquert**, **Prof. Dr. Germà Garcia-Belmonte**, **Dr. Antonio Guerrero Castillejo** and **Dr. Luís Fernando Marchesi** as well as all members of the "Grup de dispositius fotovoltaics i optoelectrònics" at the University Jaume I in Castellón, Spain, for their help and expertise concerning impedance spectroscopy.
- **PD Dr. Giuseppe Scarpa** und **Alaa Abdellah** am Lehrstuhl für Nanoelektronik (Technische Universität München) danke ich für die ersten Versuche zur Nanoimprint-Lithographie.
- Für die Einführung in den Photolumineszenz-Messplatz danke ich **Dr. Alexandre Santos Abreu** und **Prof. Dr. Siegfried Horn** vom Lehrstuhl EPII.
- Ein besonderer Dank geht auch an **Konrad Klein** und **Prof. Dr. Martin Stutzmann** vom Walter Schottky Institut (TU München) für die Unterstützung bei den PDS-Messungen.
- Ich danke **Dr. Jan Hanss** und **Andreas Kalytta-Mewes** für die Hilfestellungen bei chemischen Fragen.
- Der **Feinmechanischen und Elektronik-Werkstatt** danke ich für die rasche Hilfe in technischen Angelegenheiten.
- Ich danke **Dr. Bernhard Ecker**, **Sebastian Schiefer**, **Ulrich Hörmann**, **Mark Gruber**, **Christoph Schuhmair** und **Theresa Linderl**, die mich während ihrer Bachelor-, Master- oder Diplomarbeiten bei der Durchführung

zahlreicher Messungen unterstützten und mit ihrer Arbeit, Zeit und Kreativität deutlich zum Gelingen der Arbeit beigetragen haben.

- **Dr. Stefan Gsell** und **Dr. Jörg Frischeisen** danke ich für die Einweisung in diverse Messmethoden, ihren fachlichen Rat und für eine wunderbare Zeit als Bürokollegen.
- Ich danke meinen Kollegen aus der Organik-Arbeitsgruppe, insbesondere **Stefan Grob**, **Christian Mayr**, **Dr. Stefan Nowy**, **Dr. Tobias Schmidt**, **Bert Scholz** und **Dr. Thomas Wehlus** für die gute Zusammenarbeit, die freundschaftliche Atmosphäre und die Hilfsbereitschaft – insbesondere danke ich meinen OPV-Mitstreitern **Mark Gruber** und **Ulrich Hörmann** für ihre aussergewöhnliche Unterstützung in technischen und wissenschaftlichen Belangen, für ihre Ideen und die Freude am gemeinsamen Arbeiten.
- Allen anderen **Mitgliedern des Lehrstuhls für Experimentalphysik IV** danke ich für das angenehme Arbeitsklima – insbesondere möchte ich mich bei **Maria Fuso**, **Sybille Heidemeyer**, **Birgit Knoblich** und **Wolfgang Reiber** bedanken für ihre Unterstützung hinsichtlich jeglicher administrativer und technischer Belange.
- Schließlich danke ich **meinen Eltern und Brüdern** von Herzen für ihre immerwährende liebevolle Unterstützung und meinem Mann **Michael** für das sorgfältige Korrekturlesen der Arbeit, die fachliche Hilfe, seine Rücksichtnahme und Geduld aber auch – und vor allem – für eine wunderbare Zeit fernab der Wissenschaft.

Curriculum vitae

Julia Katharina Kraus, geb. Wagner
geboren am 24. September 1982 in Mitwitz

Universität	
08/2008 – 03/2013	Wissenschaftlicher Mitarbeiter Lehrstuhl für Experimentalphysik IV Universität Augsburg
10/2005 – 08/2008	Studium: Materials Science (M. Sc.) Abschluss: Master of Science Masterarbeit: „Electronic properties of interfaces in organic devices studied by Kelvin probe and impedance spectroscopy“ an der Universität Augsburg (Prof. Wolfgang Brütting)
10/2002 – 11/2005	Studium: Materialwissenschaften (B. Sc.) Abschluss: Bachelor of Science Bachelorarbeit: „Atomarer Transport durch Eisenchlorid-Schichten“ an der Universität Augsburg (Prof. Ferdinand Haider)
Schule	
09/1993 – 06/2002	Frankenwald-Gymnasium Kronach Abschluss: Allgemeine Hochschulreife
09/1989 – 07/1993	Grundschule Mitwitz

Regensburg, Juli 2013